



**FACULTY
OF MATHEMATICS
AND PHYSICS**
Charles University

DOCTORAL THESIS

RNDr. Ondřej Chrenko

**Early phases of formation and evolution
of planetary systems**

Astronomical Institute of Charles University

Supervisor of the doctoral thesis: doc. Mgr. Miroslav Brož, Ph.D.

Study programme: Physics

Study branch: Theoretical Physics, Astronomy
and Astrophysics

Prague 2019

I declare that I carried out this doctoral thesis independently, and only with the cited sources, literature and other professional sources.

I understand that my work relates to the rights and obligations under the Act No. 121/2000 Sb., the Copyright Act, as amended, in particular the fact that the Charles University has the right to conclude a license agreement on the use of this work as a school work pursuant to Section 60 subsection 1 of the Copyright Act.

In date

signature of the author

First and foremost, I would like to express my gratitude to my future wife Barunka for her neverending support, love and patience. I am grateful to my family for encouraging me during my doctoral studies. I thank my supervisor Miroslav Brož for his guidance and motivating discussions. I would also like to thank my collaborators David Nesvorný and Michiel Lambrechts for sharing their profound knowledge with me.

Title: Early phases of formation and evolution of planetary systems

Author: RNDr. Ondřej Chrenko

Institute: Astronomical Institute of Charles University

Supervisor: doc. Mgr. Miroslav Brož, Ph.D.,
Astronomical Institute of Charles University

Abstract: We study orbital evolution of multiple Earth-mass protoplanets in their natal protoplanetary disk. Our aim is to explore the interplay between migration of protoplanets driven by the disk gravity, their growth by pebble accretion, and accretion heating which affects gas in their neighbourhood. Radiation hydrodynamic (RHD) simulations in 2D and 3D are used to model the problem. We find that the heating torque, i.e. the torque exerted by asymmetric hot underdense gas near accreting protoplanets, significantly changes the migration. Specifically, it excites orbital eccentricities of migrating protoplanets, thus preventing their capture in chains of mean-motion resonances. The protoplanets then undergo numerous close encounters and form giant planet cores by mutual collisions. Additionally, if inclinations also become excited, we describe a new mechanism that can form binary planets by means of consecutive two-body and three-body encounters, with the assistance of the disk gravity. Finally, our 3D RHD simulations reveal a complex distortion of the gas flow near an accreting protoplanet, driven by baroclinic perturbations and convection. For specific temperature-dependent opacities of the disk, an instability is triggered which redistributes gas around the protoplanet and leads to an oscillatory migration, consisting of alternating inward/outward excursions. All of these major findings are summarised in a series of papers reprinted in this thesis.

Keywords: protoplanetary disks, planet formation, planet-disk interactions, hydrodynamics

Contents

Introduction	3
1 Overview of planet formation and gas-driven migration	7
1.1 Protoplanetary disks	7
1.1.1 Observational constraints and relevant physics	7
1.1.2 Radiation hydrodynamic (RHD) disk model	19
1.2 From dust to planets	31
1.2.1 Coagulation of dust to pebbles	32
1.2.2 Planetesimal formation induced by turbulence	36
1.2.3 Growth of planets by pebble accretion	40
1.3 Types of planetary migration	46
1.4 Type I migration	48
1.4.1 Lindblad torque	52
1.4.2 Corotation torque	58
1.4.3 Migration maps	68
1.4.4 Orbital eccentricity and inclination	70
1.4.5 Thermal torques	73
2 Migration of accreting low-mass protoplanets	75
2.1 Paper I: Eccentricity excitation and merging of planetary embryos heated by pebble accretion	75
2.1.1 Reprint	79
2.1.2 Corrigendum	105
2.2 Paper II: Dynamics of multiple protoplanets embedded in gas and pebble disks and its dependence on Σ and ν parameters	107
2.3 Paper III: Binary planet formation by gas-assisted encounters of planetary embryos	111
2.3.1 Reprint	113
2.4 Paper IV: Oscillatory migration of accreting protoplanets driven by a 3D distortion of the gas flow	128
2.4.1 Reprint	131
Conclusions	151
Bibliography	155
List of publications	167

Introduction

Preface

Understanding the origin of life goes hand in hand with understanding the origin and evolution of planet Earth, its neighbourhood, and also other distant planets observed in the Universe. Theory of planet formation has thrived over the recent years thanks to groundbreaking discoveries that were made not only within our Solar System but also far beyond its borders.

Thrilling findings were enabled by several space missions launched towards unexplored corners of the Solar System. The New Horizons spacecraft obtained the first images of the astonishingly complex worlds of Pluto, its moons, and 2014 MU₆₉ Ultima Thule (Stern et al. 2015, 2019). It collected information about the imprints of processes that shaped the outer Solar System over the course of its history (4.56 Gyr). The Cassini-Huygens mission explored Saturn and its moons, discovered a subsurface ocean of liquid water on Enceladus and landed on the surface of Titan (Niemann et al. 2005; Tomasko et al. 2005; Spencer & Nimmo 2013; Spilker 2019). It witnesses formation of moonlets within the rings of Saturn and dived into Saturn’s envelope during the spectacular finale of its journey (Beurle et al. 2010; Tiscareno et al. 2019). The Rosetta-Philae mission attempted to land on the surface of the comet 67P/Churyumov–Gerasimenko and succeeded, although it had quite a rough landing (Biele et al. 2015; Filacchione et al. 2016). The comet served as yet another relict of planet formation, providing a window into the past.

Observations of extrasolar planetary systems are at least equally important. Since the discovery of the first exoplanet orbiting a main-sequence star in 1995 (Mayor & Queloz 1995), the long-standing question ‘Are there planets similar to Earth somewhere in the Universe?’ is even more pressing. The hunt for exoplanets, with a huge contribution of the Kepler telescope (Borucki et al. 2010), resulted in a discovery of thousands of planetary bodies orbiting distant stars (Rowe et al. 2014). Although some of these exoplanets do exhibit Earth-like features (e.g. Quintana et al. 2014), it is perhaps even more striking that exoplanets are generally very diverse (see Fig. 1; Buchhave et al. 2012; Kane et al. 2012; Mann et al. 2012; Rogers 2015). Some of them are referred to as super-Earths, bodies of the terrestrial type but more massive compared to Earth. Others are classified as mini-Neptunes, little brothers of ice giants. And some gas giants are not only more massive than Jupiter, but they exhibit either very short orbital periods (hot Jupiters) or eccentric orbits.

With the advancement of observing techniques, both in terms of sensitivity and resolution, it is now possible to acquire incredibly detailed images of protoplanetary disks—birthplaces of planets (e.g. Andrews et al. 2018). These images provide an unprecedented insight into processes which consecutively agglomerate tiny dust grains into bigger and bigger objects. They also unveil footprints of hydrodynamic phenomena such as turbulence (essential to understand disk accretion) or dust substructures (essential to understand planet accretion).

All the aforementioned advancements were made possible thanks to a tremendous effort of researchers and engineers all over the world. People who forgot about their different opinions and different beliefs and joined their forces with one goal—to push the frontiers of human knowledge one step further. I think that their determination is a wonderful example of what the mankind is capable of when it follows a shared (and reasonable) purpose.

This thesis represents a tiny theoretical footprint on a huge field of planetary science. My only hope is that it is going to be useful.

Aims

The aim of this thesis is to study orbital evolution of multiple low-mass ($M_p \simeq 10^0 M_\oplus$) protoplanets while they are still embedded in a protoplanetary disk. The disk is assumed to consist mostly of gas, with a small fraction ($\sim 1\%$) of solid particles that determine the optical properties of the environment and also serve as a building material for planets. During this early evolutionary stage, the evolution of planets is dictated by the gravitational influence of the gas disk. The variations in the gas distribution caused by density waves (Goldreich & Tremaine 1979), horseshoe dynamics (Ward 1991; Masset 2001) and thermodynamic processes (Paardekooper & Mellema 2006; Lega et al. 2014; Benítez-Llambay et al. 2015) result in gravitational torques exerted on the planets. The torques trigger planetary migration.

At the same time, accretion of protoplanets is still ongoing. Motivated by recent results (Johansen et al. 2007; Ormel & Klahr 2010; Lambrechts & Johansen 2012), we assume that the major planet-forming process is accretion of pebbles, i.e. mm-dm solid particles that radially drift through the disk due to aerodynamic drag. The efficiency of pebble accretion is also provided by gas drag which enhances the effective cross-section of capture by massive bodies.

When protoplanets are accreting, they become heated by the release of the kinetic energy of the infalling material. The heat excess makes the protoplanets luminous so that they may heat up gas in their vicinity. Under such conditions, additional asymmetric perturbations arise in gas distribution, altering the torque exerted on the planets and thus modifying their migration rate.

Our goal is to explore the interplay between the aforementioned phenomena, i.e. to investigate feedback between planet migration, pebble accretion, and accretion heating. We incorporate these phenomena into state-of-the-art 2D and 3D radiation hydrodynamic (RHD) models.

The thesis is organised in two chapters. Chapter 1 is essentially an overview of planet formation and migration. It briefly summarises current knowledge about protoplanetary disks, presents theoretical foundations for RHD modelling, outlines the long-standing issues of accretion processes, provides a motivation for including pebble accretion, and describes the physics of Type I migration relevant for low-mass planets.

Chapter 2 discusses the dissertation research and summarises the contents of our scientific papers Chrenko et al. (2017), Brož et al. (2018), Chrenko et al. (2018),

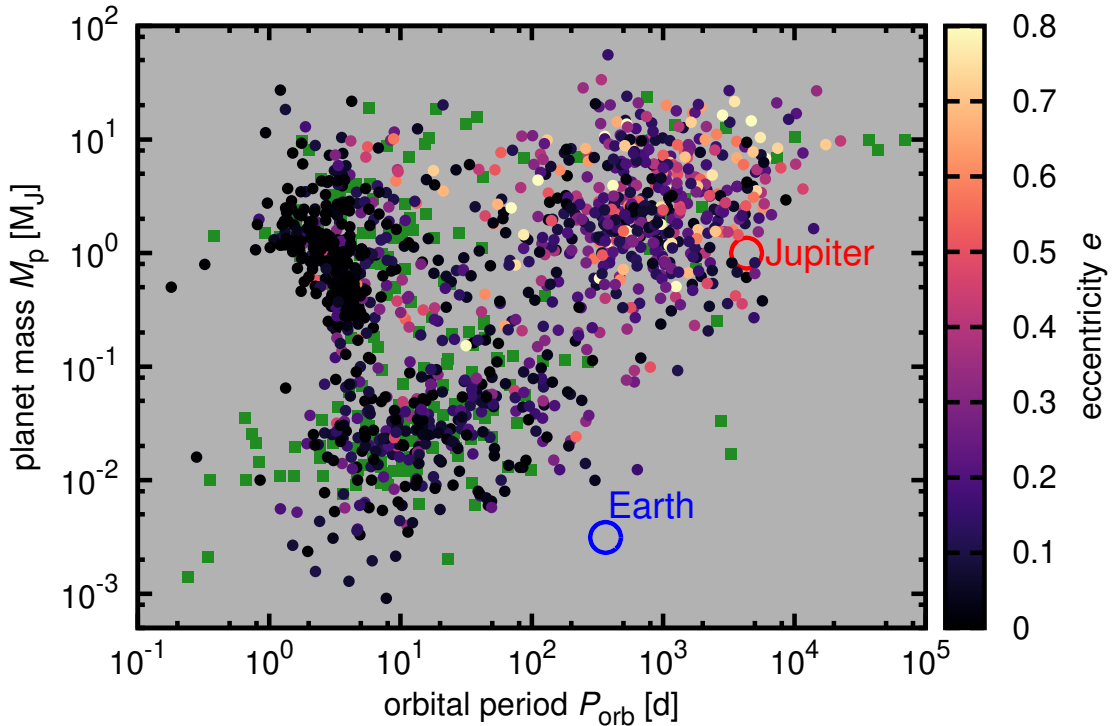


Figure 1: Planet mass M_p (in Jupiter masses) as a function of the orbital period P_{orb} (in days) for confirmed exoplanets. Approximately 1400 exoplanets, for which the displayed quantities are available, are contained in the plot. Filled circles are coloured according to the orbital eccentricity e , green squares are exoplanets with unconstrained e . Earth (blue circle) and Jupiter (red circle) are displayed for reference. Three clusters can be identified in the diagram, corresponding to exoplanet types that do not have solar-system analogues: close-in super-Earths and mini-Neptunes (lower left quadrant), hot Jupiters (upper left quadrant), and eccentric Jupiters (upper right quadrant). Data adapted from the NASA Exoplanet Archive, <https://exoplanetarchive.ipac.caltech.edu/>, as of June 2019.

and Chrenko & Lambrechts (2019) (in the following, we use abbreviations Paper I; Paper II; Paper III; Paper IV). Reprints are provided for Papers I, III and IV. The papers represent the main output of this thesis and readers who are proficient in planet-disk interactions should read them first (Chapter 2). For readers who are new to the field, it is suggested to start with Chapter 1.

1. Overview of planet formation and gas-driven migration

The goal of Chapter 1 is to provide a brief review of the current understanding of planet formation and migration during an early phase when a gas disk is still around. We focus on physical processes which play a key role in numerical models that are presented later in Chapter 2. Specifically, in Sect. 1.1 we discuss major observational constraints of protoplanetary disks and we provide a summary of radiation hydrodynamic equations which are often used to describe planet-disk interactions. Sect. 1.2 highlights the importance of hydrodynamic processes for the accretion of planets. Namely, it demonstrates that pebble accretion is an efficient process by which the planets can be assembled. In remaining Sects. 1.3 and 1.4, we discuss the complexity of gas-driven migration, especially for low-mass planets (i.e. those which are not massive enough to open a gap in the gas disk).

1.1 Protoplanetary disks

The environment of protoplanetary disks sets general conditions for planet formation and also determines the overall dynamics of planetary systems in early phases of their evolution. We thus start with a review of protoplanetary disks from both observational and theoretical points of view.

1.1.1 Observational constraints and relevant physics

Formation

Star-forming regions in our Galaxy are observed to encompass a filamentary network of the accumulating cold interstellar matter (ISM) from which dense pre-stellar cores form by the gravitational collapse (for a review see André et al. 2014). As the collapse proceeds, a ‘prototype’ core diversifies into three interacting parts (e.g. Adams et al. 1987; Robitaille et al. 2006): (i) a massive compact centre from which a pre-main-sequence star is formed; (ii) a low-mass circumstellar disk which is flattened and spun up as a result of the angular momentum conservation of infalling material; (iii) a leftover envelope.

The mass contained in individual components (i)–(iii) at a given time affects the observed slope of the spectral energy distribution (SED) in the mid-infrared (IR; typically between 2 and 25 μm). This very slope is a foundation for the basic classification of young stellar objects (YSOs; Lada & Wilking 1984; Lada 1987; André et al. 1993; André & Montmerle 1994; Greene et al. 1994; Williams & Cieza 2011). They are grouped as Class 0, I, II, and III YSOs (e.g. Dauphas & Chaussidon 2011). Classes 0 and I correspond to the protostellar phase and they contain the envelope which obscures the embedded disk and the protostar. Class II YSOs are no longer

embedded in envelopes and their circumstellar disk is considered protoplanetary rather than protostellar. Class III YSOs no longer contain a massive gas disk but the dust can still be present in a form of a debris disk. In this thesis, we are mainly concerned with Class II YSOs.

Accretion

Each protoplanetary disk is accreting onto the central star. The mass transfer at the rate \dot{M} is thought to be facilitated by the stellar magnetic field (Camenzind 1990; Königl 1991). The disk is truncated at the radius R_m equal to several stellar radii by the magnetospheric cavity and ionised gas is channelled along magnetic field lines (see Fig. 1.1), eventually falling onto the stellar surface and releasing its free-fall energy in the form of shocks and an excess luminosity (e.g. Calvet & Gullbring 1998; Bouvier et al. 2007). Using a primitive spherical accretion model, the accretion luminosity can be estimated as (Armitage 2015)

$$L_{\text{acc},\star} \simeq GM_{\star}\dot{M} \left(\frac{1}{R_{\star}} - \frac{1}{R_m} \right) \sim 0.2 \left(\frac{M_{\star}}{M_{\odot}} \right) \left(\frac{R_{\star}}{1.5R_{\odot}} \right)^{-1} \left(\frac{\dot{M}}{10^{-8}M_{\odot}\text{yr}^{-1}} \right) L_{\odot}. \quad (1.1)$$

The determination of \dot{M} therefore relies on our ability to measure L_{acc} and the respective stellar parameters. Measurements of L_{acc} need to carefully distinguish between the standard stellar atmospheric emission and the excess caused by the accretion.

This is usually done in the blue/UV wavelengths range, typically from 320 to 520 nm, where the continuum excess (‘veiling’) and Balmer emission lines of hydrogen recombination can be associated to the infalling material (Valenti et al. 1993; Hartigan et al. 1995; Gullbring et al. 1998; Herczeg & Hillenbrand 2008). Additionally, a correlation exists between the accretion luminosity and luminosity of several emission lines (such as H α or CaII triplet) because the gas infall leads to a substantial line broadening. Scaling relations can be derived which allow for the determination of L_{acc} from L_{line} (Muzerolle et al. 1998; Natta et al. 2002; Muzerolle et al. 2000, 2005; Fang et al. 2009). The applicability of the method has improved with modern instruments such as the VLT/X-Shooter with a broad spectral coverage (Rigliaco et al. 2012; Manara et al. 2016).

The distribution of inferred accretion rates depends on the disk age (which is discussed later). T Tauri ~ 1 Myr old stars in the Taurus and Chamaeleon I cloud complexes exhibit the median value of $\dot{M} \simeq 10^{-8} M_{\odot} \text{yr}^{-1}$ (Hartmann et al. 1998). A typical spread of accretion rates in a population of protoplanetary disks in the Lupus clouds is shown in Fig. 1.2.

Composition and types of emission

Protoplanetary disks adopt the chemical composition of the progenitor pre-stellar cores and they consist of both gas and dust (e.g. Pollack et al. 1994). The spatial distribution of gas and dust within the disk does not necessarily overlap (see

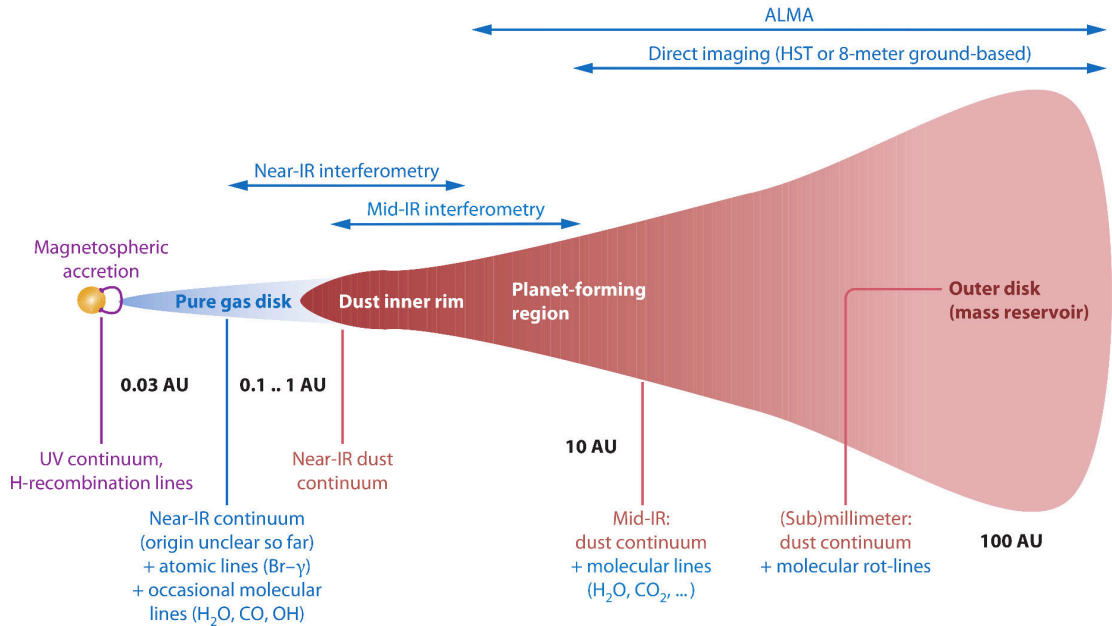


Figure 1.1: Schematic representation of a vertical slice of a protoplanetary disk around a pre-main-sequence star. The temperature and density generally decrease from left to right. Labels indicate which type of radiation is emitted from different disk regions and also which process or material generates it. The region containing a mixture of gas and dust is highlighted in red, the region of pure gas (where temperatures do not allow the dust to exist) is coloured in blue. The horizontal arrows show which disk region is scanned by selected observational techniques. The distances (given by labels in astronomical units) are not linear. Adapted from Dullemond & Monnier (2010).

Fig. 1.1). This is because dust grains become subjects to evaporation (e.g. Lin & Papaloizou 1985), radial drift towards the star (e.g. Adachi et al. 1976; Weidenschilling 1977), accumulation in local pressure maxima or turbulent vortices (e.g. Fromang & Nelson 2005), vertical settling (e.g. Weidenschilling 1980), turbulent stirring (e.g. Dubrulle et al. 1995), and eventually to gravitational perturbations from protoplanets (e.g. Paardekooper & Mellema 2004). Typically, the dusty part of the disk is less extended in both the radial and vertical directions compared to the gaseous component.

Although the gas is usually more abundant (by a factor of 100), the presence of dust is important because it serves as an agent for thermal regulation of the disk. When thermalised with the surrounding gas, the dust emits thermal radiation which can escape the disk and cool it down. When exposed to the irradiation from the central star, the dust can absorb it and contribute to the heating of gas. The optical properties of the dust are such that it dominates the material opacity of the disk wherever it is present, despite its marginal abundance. Several important observation techniques are based on the detection of either scattered light or thermal emission produced by dust grains.

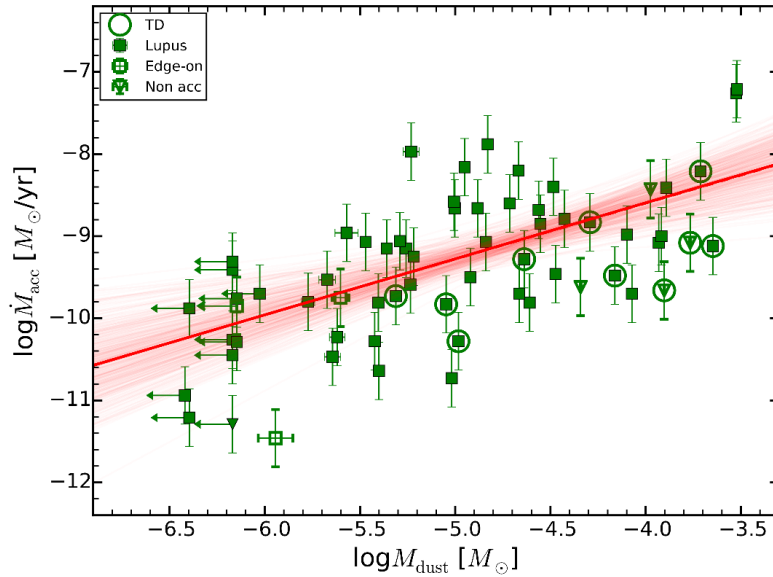


Figure 1.2: Logarithm of the accretion rate \dot{M}_{acc} versus logarithm of the dust mass M_{dust} . The span of values provides an insight into a typical range of disk masses (which are a factor of ~ 100 larger than the depicted dust mass) and accretion rates. The thick red line shows the best result of a Bayesian fit; there are, however, many outliers with respect to the fit. Open squares indicate edge-on objects, triangles show objects with an accretion undistinguishable from chromospheric noise, and circles are used for transition disks, i.e. disks with a large central hole. The disks belong to the Lupus star-forming region. Adapted from Manara et al. (2016)

The disk can be either optically thick or optically thin with respect to its own thermal emission. The former is typically true in inner regions because both the density and temperature profiles increase towards the centre (roughly as power laws, as we shall see in the following). Vice versa, the optically thin emission originates in outer regions which are colder and less dense, with the vertically integrated optical thickness $\tau < 1$. The radial decrease of the disk temperature implies that radiation originating at different disk regions has different characteristic wavelengths. The wavelength of an observation thus determines which disk region the observation probes (see Fig. 1.1):

- The blue and UV emission of gas detects the magnetospheric accretion signatures as discussed above.
- A bump in NIR of the spectral energy distribution (see Dullemond & Monnier 2010), observed for disk-bearing Herbig Ae/Be stars, is often interpreted as an evaporation front of dust which behaves as an optically thick hot wall, puffed up by a strong absorption of stellar radiation (Dullemond et al. 2001; Muzerolle et al. 2004; Isella & Natta 2005; Kama et al. 2009; Flock et al. 2016). This corresponds to the transition between the innermost dust-free disk and the

adjacent inner disk with both dust and gas. The dust rim¹ is located between ~ 0.1 and 1 au, depending on stellar luminosity.

- In the inner disk (below ~ 10 au), the dust emits in the optically thick regime and is responsible for the overall NIR and MIR excess of the SED.
- The outer disk produces optically thin (sub)millimetre thermal continuum emission of dust and it is also the source of numerous gas molecular lines.

Lifetime

The very presence (or absence) of the IR excess for YSOs serves as an indicator whether the protoplanetary disk exists (or not). It is then possible to determine the fraction of disk-bearing stars in the stellar population and infer the disk ages. A typical approach to such measurements is to perform a survey of a cluster or an association within a star-forming region, determine the fraction of sources with the IR excess and relate it to the age of the cluster (e.g. Hartmann et al. 1998; Haisch et al. 2001; Hernández et al. 2007). The reason for using the cluster age is that the ages of individual stars are biased and thus their mean value is statistically more reliable (Haisch et al. 2001). It turns out that the fraction of disk-bearing stars as a function of the cluster age is decreasing and can be well fitted by an exponential decay law. Generally, the results indicate that half of the stars lose their disks within $\simeq 3$ Myr and the upper limit on the disk age seems to be $\simeq 10$ Myr. For a selection of clusters, Fedele et al. (2010) compared the fraction f_{IRAC} of stars having the disk-related infrared excess (as found by Spitzer/IRAC; Lada et al. 2006) with the fraction f_{acc} of stars exhibiting the accretion-driven H α broadening (measured at VLT/VIMOS; see Fig. 1.3). Their fit of the dependence $f(t_{\text{age}}) \propto \exp(-t_{\text{age}}/\tau)$ revealed $\tau_{\text{IRAC}} = 3$ Myr and $\tau_{\text{acc}} = 2.3$ Myr. In other words, although the accretion and disk dissipation tend to follow the same trend with the increasing disk age, the accretion ceases even before the disk is dissipated. Finally, let us point out that the radiometric dating of primitive solar-system materials (such as calcium-aluminium-rich inclusions, iron meteorites, chondritic meteorites; e.g. Connolly & Jones 2016) can provide independent constraints on the age of the protosolar disk.

Thermal emission and dust mass

As the inner disk is optically thick, the respective thermal emission is sensitive to the temperature but not to the density. SED measurements compared with theoretical models can therefore constrain the temperature profile.

For optically thin (sub)mm emission of the outer parts, we can use the Kirchhoff's law and express the radiation flux (e.g. Hildebrand 1983; Andrews & Williams 2005; Armitage 2010)

$$F_{\nu} = \frac{M_{\text{dust}}}{d^2} \kappa_{\nu} B_{\nu}(T) \simeq \frac{M_{\text{disk}}}{d^2} \kappa_{\nu} \frac{2k_{\text{B}}T\nu^2}{c^2}, \quad (1.2)$$

¹It is important to distinguish whether the 'disk inner edge' refers to the dust rim or to the edge of the magnetospheric cavity which are two physically different structures.

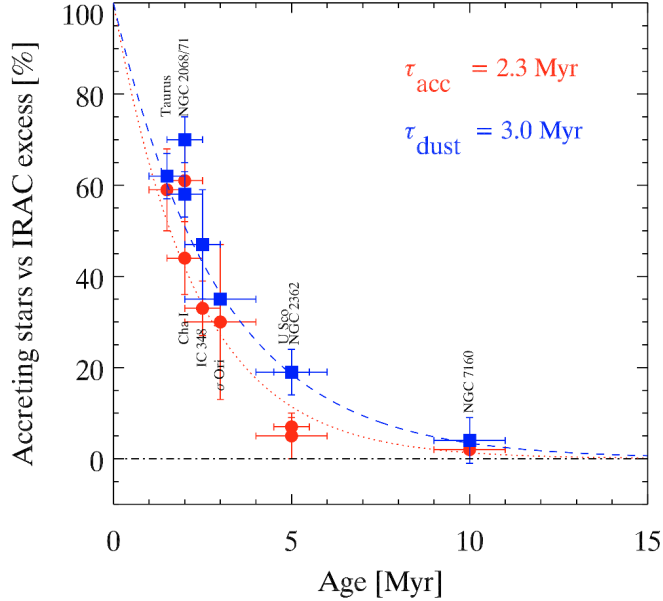


Figure 1.3: Measured fraction of accreting (f_{acc}) and disk-bearing (f_{IRAC}) stars in selected clusters (see labels) of various ages (horizontal axis). Red circles indicate f_{acc} and blue squares correspond to f_{IRAC} . The dependences are fitted with an exponential decay law (dotted and dashed line, respectively). The respective e-folding times are given inside the plot. Adapted from Fedele et al. (2010).

where M_{dust} is the disk mass, d is the distance, κ_ν is the monochromatic opacity and we approximated the Planck function $B_\nu(T)$ with the Rayleigh-Jeans limit suitable for the given wavelengths. If d is known, the relation directly constrains M_{dust} and κ_ν via observations. To disentangle the two unknowns, it is usual to assume $\kappa_\nu \propto \nu^\beta$ (Beckwith et al. 1990). Assuming that M_{dust} is constant and ν -independent, measurements at various wavelengths allow to determine β . For example, Pérez et al. (2012) and Pérez et al. (2015) found $\beta \sim 0.5$ below 50 au and $\beta > \beta_{\text{ISM}} = 1.7$ in the outer disk (in systems AS 209, CY Tau and DoAr 25). The variations in β are usually interpreted as a radius-dependent size distribution of dust grains created by dust coagulation (Stognienko et al. 1995; Draine 2006). Instead of fitting observations at different wavelengths separately, it is also possible to apply a multiwavelength fitting to simultaneously obtain the surface density, temperature and grain size profile. Using this method, Tazzari et al. (2016) found the maximum grain size $a_{\text{max}} \sim 1$ cm between 15 and 30 au, and $a_{\text{max}} \sim 1$ mm beyond 80 au (for systems AS 209, FT Tau, DR Tau).

Known M_{dust} enables to estimate M_{disk} (as $M_{\text{dust}} + M_{\text{gas}}$ where M_{gas} is inferred from M_{dust} using some dust-to-gas ratio). The results for Ophiuchus, Taurus and Orion star-forming regions reveal the median disk mass $5 M_J$, the upper mass limit $\approx 50 M_J$ and the median disk-to-star mass ratio 0.9% (Beckwith et al. 1990; André & Montmerle 1994; Andrews & Williams 2005, 2007; Mann & Williams 2010). Fig-

ure 1.2 provides an insight into a typical range of disk masses in Lupus and shows that protoplanetary disks are much less massive than their host stars. There are however several important caveats in their mass determination: a number of works make assumptions about the grain size and opacity by relating them directly to the interstellar medium (e.g. Mathis et al. 1977) rather than deriving them self-consistently. Furthermore, another assumption has to be made about the dust-to-gas ratio when inferring M_{gas} . Finally, larger solids (such as planetesimals or planets) may remain invisible to observations.

Molecular emission and gas mass

Is it possible to measure the gas mass itself? It turns out that such measurements are rather problematic since bulk of the gas in H_2 molecules cannot be observed due to the absence of the electric dipole moment. However, there are other less frequent molecules that are traceable through line emission, such as CO, CS or HCN at (sub)mm wavelengths (e.g. Henning & Semenov 2013; Dutrey et al. 2014). Far-IR measurements also detect cold water vapour (Hogerheijde et al. 2011; Podio et al. 2013) and ammonia (Salinas et al. 2016), both of which are essential from the astrobiological point of view.

CO molecules can be used to determine the disk mass independently of dust observations (Williams & Best 2014; Ansdell et al. 2016; Molyarova et al. 2017; Zhang et al. 2017). Yet there are some uncertainties: CO tends to freeze-out on dust grains if $T < 20$ K, it can become photodissociated by stellar irradiation in the disk atmosphere, and the exact CO-to- H_2 ratio is unknown (Henning & Semenov 2013; Williams & Best 2014). Moreover, the emission of CO itself is usually optically thick. To avoid these problems, rare isotopologues of CO, which have lower optical depths, are studied instead. Ansdell et al. (2016) performed an ALMA survey of protoplanetary disks in the Lupus complex and inferred their masses from both the dust continuum (near $890 \mu\text{m}$) and CO isotopologues measurements (^{13}CO and C^{18}O). The results show that M_{gas} is typically below the value of the minimum-mass solar nebula (MMSN; Weidenschilling 1977) and the dust-to-gas ratio exceeds that of ISM. Such a gas depletion is thought to be indicative of giant-planet formation.

Finally, let us point out that molecular lines can exhibit thermal or turbulent broadening. The latter could be of great importance since it might help to constrain our theoretical understanding of the disk turbulence. The first attempts to provide such constraints were undertaken using ALMA data (Flaherty et al. 2015; Teague et al. 2016; Flaherty et al. 2017) and imply relatively small vertical scales of turbulent layers. Observations of dust scale heights by Pinte et al. (2016), on the other hand, seem to be sufficiently explained by magnetic turbulent models (Flock et al. 2017).

Basic correlations

Once the disk mass M_{disk} is determined, it is important to point out that it exhibits correlations with some other characteristic quantities of protoplanetary systems.

First, it correlates with the mass of the host star. An ALMA survey of Chamaeleon I star-forming region (Pascucci et al. 2016) revealed a steeper-than-linear dependence $M_{\text{dust}} \propto M_{\star}^{1.3-1.9}$. Ansdell et al. (2016) reported that both M_{dust} and M_{gas} scale with the stellar mass. This should imply that more massive disks give birth to more massive planets since the population of giant exoplanets scales with the stellar mass as well (Johnson et al. 2010; Howard et al. 2012).

The disk mass also scales with the accretion rate \dot{M} . The study of Manara et al. (2016) based on ALMA and VLT/X-Shooter data implies a linear or slightly shallower dependence, as shown in Fig. 1.2 (but note that there are many outliers with respect to the fitted dependence). This is in accordance with the theory of viscous evolution which predicts $\dot{M} \propto M_{\text{disk}}/t_{\nu}(r_{\text{out}})$ where t_{ν} is the viscous timescale (Jones et al. 2012). Manara et al. (2016) also point out that masses M_{gas} inferred from CO may be underestimated, perhaps because the chemical balance of carbon-based molecules is not fully understood (Kama et al. 2016).

Geometrical constraints

The extent of protoplanetary disks is relatively difficult to determine since they exhibit very low temperatures and densities at their outer boundaries. One possibility is to use HST observations in the optical to image protoplanetary disks that block some source of bright background emission. Such measurements of disk shadows were indeed conducted for several objects in the Orion complex which are positioned against bright HII regions (McCaughrean & O’dell 1996; Vicente & Alves 2005). Another possibility is to use interferometric (sub)mm techniques to obtain resolved images. A general conclusion is that protoplanetary disks cover a large range of sizes and their intensity profiles are in accord with the self-similar surface density profiles of viscous accretion disks (Lynden-Bell & Pringle 1974)

$$\Sigma(r) = (2 - n) \frac{M_{\text{disk}}}{2\pi r_c^2} \left(\frac{r}{r_c}\right)^{-n} \exp\left[-\left(\frac{r}{r_c}\right)^{2-n}\right], \quad (1.3)$$

where M_{disk} is the disk mass, n is the slope of the viscosity profile ($\nu \propto r^n$) and r_c is the cut-off radius where the power-law surface density profile exhibits a sharp truncation. Values inferred from observations are $r_c \sim 10\text{--}200$ au and there appears to be a correlation $M_{\text{disk}} \propto r_c^{1.6 \pm 0.3}$ (Andrews et al. 2009; Isella et al. 2009; Andrews et al. 2010; Williams & Cieza 2011). Note however that disks are not perfectly confined within r_c but extend beyond it, albeit with a very low surface density. Additionally, disk density profiles tend to be shallower (Andrews et al. 2009) than the MMSN which has $\Sigma_{\text{MMSN}} \propto r^{-1.5}$.

Perhaps the most important finding related to the recent advancement of high-resolution radiointerferometry (especially ALMA) and adaptive optics (especially VLT/SPHERE) is a frequent occurrence of substructures and azimuthal asymmetries within imaged protoplanetary disks. The detection of such substructures is very important because they indirectly reveal physical processes operating within planet-forming environments.

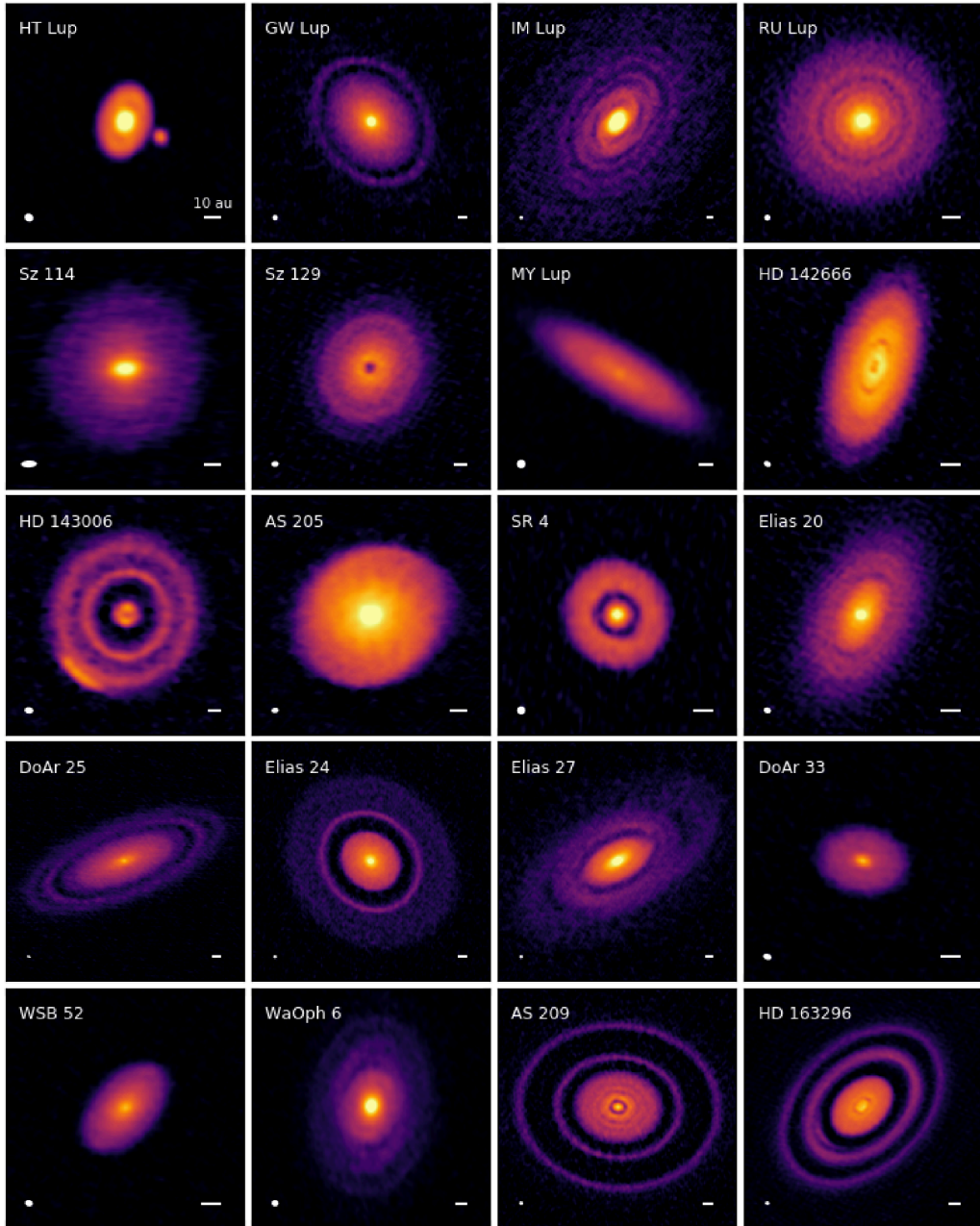


Figure 1.4: Overview of 20 targets of the DSHARP ALMA survey. The colormap represents the dust continuum emission at 1.25 mm (240 GHz). The names of objects are given by labels. Beam sizes and 10 au scalebars are indicated in the lower left and right corners of each panel. Resolved substructures include rings and gaps (Dullemond et al. 2018; Zhang et al. 2018), spirals (in case of IM Lup, Elias 27 and WaOph 6; Huang et al. 2018), azimuthal asymmetries (HD 143996 and HD 163296; Isella et al. 2018; Pérez et al. 2018), and perturbations from stellar companions (HT Lup and AS205; Kurtovic et al. 2018). Adapted from Andrews et al. (2018).

Recently, *The Disk Substructures at High Angular Resolution Project* (abbreviated as DSHARP; Andrews et al. 2018) provided a comprehensive study of patterns appearing in protoplanetary disks. This ALMA survey targeted 20 disks and their overview is provided in Fig. 1.4. Astonishingly, disk substructures are ubiquitous. They are found at various radial distances (from 5 to 150 au) and they map the distribution of dust. In the following, we review what the individual substructures tell us about underlying physical processes:

- *Rings/gaps*. Brightened rings and darkened gaps are the most frequent. Their very presence confirms that protoplanetary disks can efficiently pile up dust grains at certain locations, thus halting their loss via spiraling onto the central star (Adachi et al. 1976). The pile-up also improves local conditions for the accretion of solids. Quite often, dusty rings can be narrower than the local pressure scale height, which favours dust trapping (Dullemond et al. 2018). The trapped mass can be of the order of $\sim 10 M_{\oplus}$. The trapping in a ring is facilitated by a pressure bump (local reversal of the pressure gradient). This can be caused either by turbulence or by perturbations from (unseen) planetary bodies embedded in the disk. The former would constrain the upper limit of the respective α parameter (Shakura & Sunyaev 1973, see also Sect. 1.1.2), $\alpha \leq 10^{-4}$ (Dullemond et al. 2018). The latter would predict the existence of Neptune- to Jupiter-mass planets beyond 10 au, sometimes even at extreme separations such as $\simeq 100$ au (Zhang et al. 2018).
- *Spirals*. Spirals appear in three of the DSHARP targets. They are actually present in the largest and coldest disks and they are likely a result of gravitational instability (Huang et al. 2018), although other explanations are also possible.
- *Azimuthal asymmetries*. Two disks of the sample exhibit arc-shaped asymmetries. These can be assigned to dust-trapping vortices that can be either of a hydrodynamic origin or excited by an unseen planet (Isella et al. 2018; Pérez et al. 2018).

The observability of gaps at various viewing angles implies that protoplanetary disks are usually thin (since we can see through the gaps; e.g. ALMA Partnership et al. 2015). In addition to that, disks often exhibit a flaring geometry which can be deduced from the spectral energy distribution (Kenyon & Hartmann 1987), HST imaging (Padgett et al. 1999), or VLT/SPHERE imaging (Avenhaus et al. 2018). An example of the latter is shown in Fig. 1.5.

Physical processes relevant in disks

Although protoplanetary disks are relatively quiescent objects, there is a clear evidence that they are in fact slowly evolving all the time². First, since the matter

²In cases of episodic outbursts and thermal waves (e.g. Bell & Lin 1994; Bae et al. 2014; Schneider et al. 2018), the evolution can be rather abrupt.

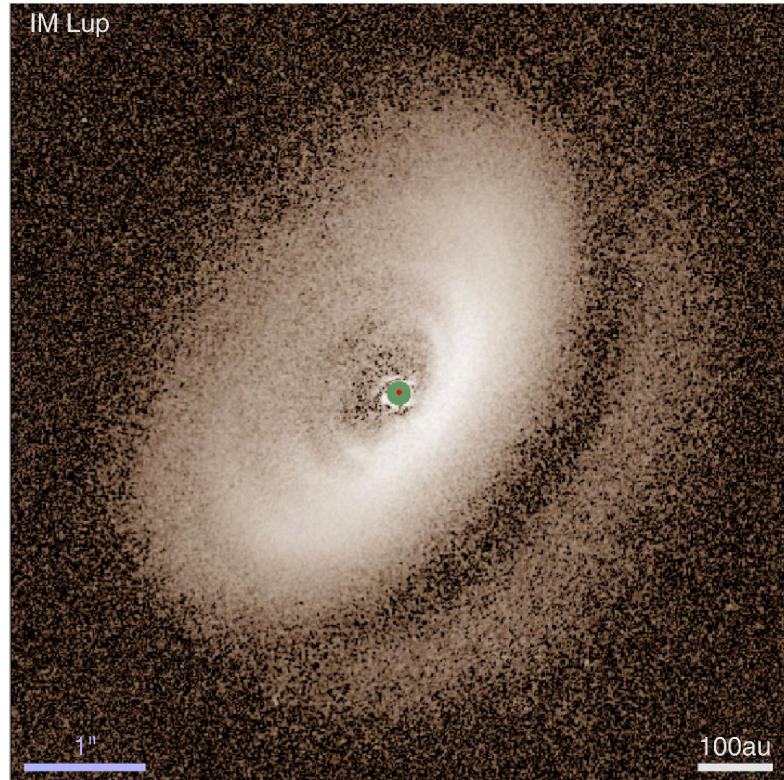


Figure 1.5: *H*-band image of surface layers of IM Lup disk reconstructed from light scattered off μm -sized grains. Polarimetric differential imaging was conducted using the adaptive-optics SPHERE/IRDIS instrument mounted on the VLT. The green circle marks the area obscured by the coronagraph. The “saucer-like” flared shape of the disk is apparent, as well as its large extent (which, however, is rather exceptional). Comparing this image to Fig. 1.4 (top row, third panel), one can see substantial differences between observations in scattered light and interferometry of thermal emission. Adapted from Avenhaus et al. (2018).

accretes onto the star, the mass conservation dictates that the accretion must be ongoing within the disk itself. Without it, there would be no permanent supply of the material towards the magnetospheric cavity and the excess accretion luminosity would vanish. Therefore the disk matter should, on average, flow towards the star, at least in a certain portion of the disk. At the same time, the angular momentum conservation must be fulfilled. Since disks have nearly Keplerian rotation curves, the angular momentum is an increasing function of the radius, $L \propto \sqrt{r}$. An inward displacement of a gas parcel is therefore only possible if it loses its angular momentum. The mechanism of angular momentum redistribution in disks is a long-standing issue (e.g. Pringle 1981; Blandford & Payne 1982; Balbus & Hawley 1998).

Second, since the lifetimes of disks are firmly constrained to be relatively short, there must be processes at play which eventually lead to a dispersal of disks. Although a part of the disk mass is transferred onto the star or incorporated in form-

ing planets, it is not enough to explain why disks vanish within several millions of years. Indeed, there are observations of transitional disks with large inner cavities that might be undergoing dispersal (e.g. Ercolano & Pascucci 2017).

Third, since disks emit radiation, it might contribute to their structure which is determined by the rotational force balance between the stellar gravity, the pressure gradient, and the centrifugal force. The pressure is dictated by the energy balance and this is where the radiation comes into play. Thermal emission of dust grains inevitably leads to a redistribution of energy and also to cooling by escaping photons. At the same time, surface layers and the inner edge are exposed to the stellar irradiation which can be absorbed and boost the local heat deposition.

Physical processes that have been studied over the past decades as possible drivers of the disk evolution are summarised as follows³ (for a review see Armitage 2011, 2015):

- The angular momentum transport is often attributed to the *eddy viscosity*. Since the molecular viscosity of disks is too low ($\sim 10^7 \text{ cm}^2 \text{ s}^{-1}$) to explain the observed accretion rates, the momentum redistribution can be caused by internal stresses induced by a *turbulence*. On a global scale, the disk then behaves as if it was viscous. Possible pathways to turbulent instabilities include (e.g. Balbus 2011; Klahr et al. 2018; Pfeil & Klahr 2019):
 - *magnetorotational instability* (MRI),
 - the effects of non-ideal magnetohydrodynamics (MHD), such as *Hall*, *ambipolar* and *Ohmic* terms,
 - *vertical shear instability* (VSI),
 - *subcritical baroclinic instability* (SBI),
 - *convective overstability* (COS),
 - *gravitational instability* (GI).
- The angular momentum can be also subtracted from the disk by external torques exerted by an *MHD wind* (e.g. Spruit 1996; Königl & Salmeron 2011). The wind can be, for example, of the Blandford-Payne type (Blandford & Payne 1982), but other possibilities exist as well. The viscosity of wind-driven accretion disks can be very low compared to turbulent disks.
- The disk dispersal can be caused by
 - *photoevaporation* when UV and X-ray photons cause *photodissociation* or *ionisation* of surface layers and trigger a *thermal wind* (e.g. Hollenbach et al. 2000),
 - *MHD wind* when the mass loss prevails over the angular momentum subtraction (e.g. Suzuki et al. 2010).

³The list is not complete; for example, we omit the evolution of solids which is covered in detail in Sect. 1.2.

- The structural aspects of disks (e.g. the flared geometry, the inner dust rim, pressure bumps, etc) can be explained by *radiative processes*, including *stellar irradiation* (e.g. Chiang & Goldreich 1997) and *radiation transfer* as they affect the local thermal balance. Alternatively, disks can be sculpted by the gravity of embedded protoplanets. Most importantly, giant planets can open substantial gaps (Crida et al. 2006).

1.1.2 Radiation hydrodynamic (RHD) disk model

Since the goal of this thesis is to understand the evolution of low-mass protoplanets as they (possibly) grow towards bigger sizes, it is necessary to construct a physical model describing the environment in which they evolve and with which they interact. Specifically, the distribution of gas and its response to the perturbations from planets has to be determined accurately because its gravity determines how planetary orbits evolve. At the same time, the model complexity cannot exceed current computational capabilities to allow for a reasonable balance between computational time, necessary resolution ($\gtrsim 1.5 \times 10^6$ cells in 2D, $\gtrsim 45 \times 10^6$ in 3D), and desired simulation timespan (at least 10^5 yr in 2D). In this section, we elaborate RHD equations which serve as the basis for Papers I–IV presented in Chapter 2. We also discuss several closure relations and approximations which are useful in the context of planet-disk interactions (Sect. 1.4).

First, let us mention our basic assumptions. We assume that the disk has a certain level of the turbulent eddy viscosity. However, it is not the aim of this work to study the very nature of turbulence and we therefore refrain from full MHD turbulence-oriented simulations. Instead, we model the disk as a laminar viscous fluid, with a parametrised viscosity. We also neglect the self-gravity and processes of disk dispersal because we aim to study stable disks and we focus on early phases during which the gas is still present in large amounts. A possible influence of neglected phenomena on planet migration is discussed later in Sect. 1.4.

Equations of hydrodynamics

Following the studies by Stone & Norman (1992), Masset (2000), D’Angelo et al. (2003), Kley & Crida (2008), Kley et al. (2009), Bitsch et al. (2013), Lega et al. (2014) and others, a suitable set of first-order differential equations to be used when studying planet-disk interactions reads

$$\boxed{\frac{\partial \rho}{\partial t} + (\vec{v} \cdot \nabla) \rho = -\rho \nabla \cdot \vec{v},} \quad (1.4)$$

$$\boxed{\frac{\partial \vec{v}}{\partial t} + (\vec{v} \cdot \nabla) \vec{v} = -\frac{\nabla P}{\rho} + \frac{\nabla \cdot \mathbb{T}}{\rho} + \vec{a}_{\text{ext}},} \quad (1.5)$$

$$\boxed{\frac{\partial \epsilon}{\partial t} + (\vec{v} \cdot \nabla) \epsilon = -P \nabla \cdot \vec{v} + Q_{\text{heat}}.} \quad (1.6)$$

The equations describe the temporal evolution of the volume gas density ρ , the flow velocity vector \vec{v} and the internal energy density ϵ . The remaining variables are the pressure P , the viscous stress tensor \mathbb{T} , the sum of accelerations acting on the continuum due to external forces \vec{a}_{ext} and the power density Q_{heat} supplied by (positive) heating sources and drained by (negative) cooling sources. The advective operator on the left-hand side, applied to an arbitrary vector field \vec{A} , evaluates as

$$[(\vec{v} \cdot \nabla) \vec{A}]_i = \sum_{j=1}^3 \left[\frac{v_j}{h_j} \frac{\partial A_i}{\partial q_j} + \frac{A_j}{h_i h_j} \left(v_i \frac{\partial h_i}{\partial q_j} - v_j \frac{\partial h_j}{\partial q_i} \right) \right], \quad (1.7)$$

where the coefficients $h_i = \sqrt{g_{ii}}$ are related to the components of the metric tensor of a given coordinate system q_i .

Eq. (1.4) is referred to as the *continuity equation*. It represents the mass conservation law and implies that the material density within a fixed volume can only change via advection (material inflow/outflow across the borders of the volume) or by compression/expansion (characterised by the right-hand side term $\propto \nabla \cdot \vec{v}$).

Eq. (1.5) is the *Navier-Stokes equation* which represents the momentum conservation under the action of perturbing forces arising within the continuum due to the pressure gradient (first term on the right-hand side), viscous stresses (second term on the right-hand side) and external forces (last term on the right-hand side), such as the gravity of the central star and protoplanets.

Eq. (1.6) is simply called the *energy equation* and represents the first law of thermodynamics (the energy conservation). It states that the internal energy of gas can only change by the energy transport due to the advection, work needed for compression/expansion (first term on the right-hand side) or heat production/removal (second term on the right-hand side).

To solve Eqs. (1.4–1.6) as 5 independent equations for 5 unknowns ρ , \vec{v} , and ϵ , several closure relations are needed. One needs to specify \mathbb{T} , \vec{a}_{ext} , Q_{heat} , and also the state equation $P(\rho, T)$ as a thermodynamic closure relation.

Viscous stress tensor

The need for the viscous stress tensor arises from the necessity to model the angular momentum transport which operates in realistic protoplanetary disks. A commonly used form is (Mihalas & Weibel Mihalas 1984)

$$\mathbb{T} = \rho\nu \left[\nabla \vec{v} + (\nabla \vec{v})^\top - \frac{2}{3} (\nabla \cdot \vec{v}) \mathbf{1} \right], \quad (1.8)$$

with the kinematic viscosity ν . In our models, the viscosity is always a *free parameter* and we treat it as a constant.

For many disk models, it is customary to express the viscosity ν in terms of the turbulent parameter α (Shakura & Sunyaev 1973) such that

$$\nu = \alpha c_s H, \quad (1.9)$$

where $H = c_s/\Omega_K$ is the pressure scale height. The prescription simply assumes that the largest dimension of turbulent vortices cannot exceed H and that they naturally propagate at the sound speed c_s since supersonic flows with shocks would dissipate.

In advanced models which model the turbulence directly, an effective α may be introduced as the combined level of the Reynolds fluid stress and the Maxwell magnetic stress:

$$\alpha = \left\langle \frac{\delta v_r \delta v_\theta}{c_s^2} - \frac{B_r B_\theta}{4\pi \rho c_s^2} \right\rangle, \quad (1.10)$$

where δv_r and δv_θ are radial and azimuthal velocity fluctuations, respectively, B_r and B_θ are magnetic field components, and the brackets represent a density-weighted average.

External forces

There are two external forces which we take into account. First, the disk evolves in the gravity field of the central protostar and also of other massive embedded objects which in our case correspond to n planet-sized bodies (planetary embryos or protoplanets). Second, since it is sometimes advantageous to study planet-disk interactions in a reference frame corotating with one of the planets, one has to take into account the non-inertial accelerations arising due to the frame rotation. The respective accelerations combine as

$$\vec{a}_{\text{ext}} = -\nabla \left(\Phi_\star + \sum_n \Phi_p^{(n)} \right) - \left[2\vec{\Omega} \times \vec{v} + \vec{\Omega} \times (\vec{\Omega} \times \vec{r}) + \partial_t \vec{\Omega} \times \vec{r} \right]. \quad (1.11)$$

where the accelerations in the square brackets are all non-inertial (they vanish for $\vec{\Omega} = \vec{0}$) and represent (left to right) the Coriolis acceleration, centrifugal acceleration and the correction in case of a non-uniform rotation ($\partial_t \Omega \neq 0$).

The gravitational potential of the protostar is

$$\Phi_\star = -\frac{GM_\star}{r}, \quad (1.12)$$

where M_\star is the mass of the protostar and r is the distance to the protostar. Similarly, the gravitational potential of a n -th protoplanet is

$$\Phi_p^{(n)} = -\frac{GM_p}{d} f_{\text{sm}} \Big|^{(n)}, \quad (1.13)$$

where M_p is the protoplanet's mass and d is the distance between the protoplanet and a point within the gas continuum. Unlike in Eq. (1.12), the protoplanets are directly embedded in the disk and thus the potential might diverge for $d \rightarrow 0$. In order to avoid this, a smoothing function f_{sm} is introduced which is often defined as

$$f_{\text{sm}} = \frac{d}{\sqrt{d^2 + r_{\text{sm}}^2}}, \quad (1.14)$$

and leads to a Plummer-type potential. Depending on the setup of a studied problem and also on the spatial discretisation, the smoothing length r_{sm} is either a fraction of the local pressure scale height H , or of the respective Hill sphere radius R_{H} , or rather a small multiple of the shortest cell dimension. An alternative approach in 3D is to use a cubic-spline tapering function (Klahr & Kley 2006)

$$f_{\text{sm}} = \begin{cases} 1, & \text{for } d > r_{\text{sm}}, \\ \left(\frac{d}{r_{\text{sm}}}\right)^4 - 2\left(\frac{d}{r_{\text{sm}}}\right)^3 + 2\frac{d}{r_{\text{sm}}}, & \text{for } d \leq r_{\text{sm}}, \end{cases} \quad (1.15)$$

which creates a deeper potential well and leads to a more realistic gas distribution close to the protoplanet (Kley et al. 2009).

Locally isothermal equation of state

The most simple equation of state assumes

$$P = c_s^2 \rho, \quad (1.16)$$

where P depends on ρ and r through the prescribed sound speed profile $c_s(r)$ which does not evolve in time and has to be given along with the initial state of the disk. In practice, it is usually supplied by means of a fixed aspect ratio $h(r) = h_0 r^{-f_0}$, where f_0 is the flaring index, which translates to $c_s = H\Omega = h(r)r\Omega$.

The approximation is called *locally isothermal* because although the disk temperature does not have to be radially uniform, it remains fixed at the individual radii. From the physical point of view, this approximation represents a system with an infinitely short radiative cooling timescale. As an illustration, one can imagine that in order to keep the temperature constant during an instantaneous increase of ρ , the compression work must be instantaneously dissipated, which is only possible by perfect radiative cooling.

Owing to the fixed temperature profile, Eq. (1.6) does not have to be solved which greatly simplifies the governing system of fluid equations. But such an approach is rather simplistic from a physical point of view.

Non-isothermal equation of state

Since the nebular gas in a protoplanetary disk has low density, it can be characterised by the ideal gas law

$$P = (\gamma - 1) \rho c_V T = \rho \frac{\mathcal{R}}{\mu} T, \quad (1.17)$$

where c_V is the specific heat at constant volume, \mathcal{R} is the universal gas constant, and γ is the adiabatic index (the ratio of specific heats at constant pressure and volume).

As the pressure now also becomes T -dependent (and vice versa), the energy equation can no longer be ignored and has to be solved as well. Since $\epsilon = \rho c_V T$, the pressure-energy coupling reads

$$P = (\gamma - 1) \epsilon. \quad (1.18)$$

Finally, the sound speed is calculated in its adiabatic rather than isothermal form, yielding

$$c_s = \sqrt{\gamma \frac{P}{\rho}} = \sqrt{\gamma \frac{\mathcal{R}}{\mu} T}. \quad (1.19)$$

When a non-isothermal equation of state is used, Eq. (1.6) needs to be solved and thus its exact form has to be specified. In the following, we provide approximations corresponding to the adiabatic energy equation and also radiative energy equation(s) (in 2-temperature and 1-temperature frameworks).

Adiabatic energy equation

The simplest approximation is the adiabatic one which assumes there is no heat transfer in the system and the internal energy of the gas can only change by compression or expansion. Therefore $Q_{\text{heat}} \equiv 0$ and the energy equation reads

$$\frac{D\epsilon}{Dt} = -P \nabla \cdot \vec{v}. \quad (1.20)$$

Radiative 2-temperature approximation

Compared to the approximations discussed above, one can expect the behaviour of radiative disks to be amidst the isothermal limit (when the radiative cooling is instantaneous) and the adiabatic non-isothermal limit (when there is no heat transfer by radiation). Since planet-forming regions are usually optically thick, the radiative solution in such regions often exhibits similarities to the adiabatic one.

Treating radiation in a numerical model is one of the most challenging astrophysical disciplines because:

- Although the propagation of photons is driven mostly by processes of quantum physics, it affects objects of vast astronomical sizes and moreover, the problem extends over a number of spatial scales.
- There is a plethora of processes related to photon-matter interactions, in particular:
 - Spontaneous emission, stimulated emission and absorption.
 - Photoionisation and recombination.
 - Bremsstrahlung and free-free absorption.
 - Scattering (with Thomson, Compton, Rayleigh and Mie regimes).

- The probabilistic nature of photon-matter interactions ranges from a random-walk behaviour of the photon field (in optically thick environments) to free streaming (in optically thin environments).
- The nature of the radiation transport may exhibit strong dependence on its wavelength (\dots , FIR, NIR, V, UV, X, \dots).

To maintain the fluid nature of the model, let us extend the set of equations to account for the energy contained in (and transferred by) a field of photons interacting with the disk. Our methodology closely follows that of Howell & Greenough (2003), Dobbs-Dixon et al. (2010), or Bitsch et al. (2013) (see e.g. Kuiper et al. 2010; Flock et al. 2013; Kolb et al. 2013; Kuiper & Klessen 2013; Ramsey & Dullemond 2015, for alternative approaches). We start by considering a relatively general case of a disk heated from inside by the viscous friction and from outside by the irradiation of the protostar. The disk cooling, as well as the energy transport in its interior, is ensured by its thermal radiation.

RADIATION TRANSFER EQUATION. We start by defining the specific monochromatic intensity I_ν of radiation as the rate of energy dE carried by photons in the unit frequency interval $d\nu$ through a surface element dA in the direction \vec{n} into the unit solid angle $d\Omega$ per unit time dt

$$dE = I_\nu(\vec{r}, t; \vec{n}, \nu) dA \cos \Theta d\Omega d\nu dt, \quad (1.21)$$

where Θ is the angle between \vec{n} and the normal direction to the surface dA . The dimension of the specific intensity is $[I_\nu] = \text{W m}^{-2} \text{sr}^{-1} \text{Hz}^{-1}$. A basic property of I_ν is its conservation along a ray in the vacuum, leading to the *intensity invariance*

$$\frac{dI_\nu}{dt} = \partial_t I_\nu + c\vec{n} \cdot \nabla I_\nu = 0. \quad (1.22)$$

However, the invariance is modified by radiation-matter interactions and leads to the radiation transfer equation (Dobbs-Dixon et al. 2010)

$$\frac{1}{c} \frac{\partial I_\nu}{\partial t} + \vec{n} \cdot \nabla I_\nu = \text{sources} - \text{sinks} \simeq \rho \left(j_\nu + \frac{\kappa_\nu^{\text{sca}} \Phi_\nu^{\text{sca}}}{4\pi} \right) - \rho \kappa_\nu I_\nu, \quad (1.23)$$

where we assumed that photon-matter interactions can be characterised by macroscopic quantities. Specifically, we introduced the monochromatic emissivity j_ν and the opacity $\kappa_\nu = \kappa_\nu^{\text{abs}} + \kappa_\nu^{\text{sca}}$ which is the sum of absorption and scattering opacities. The function $\Phi_\nu^{\text{sca}} = \int \chi_\nu(\vec{n}, \vec{n}') I_\nu(\vec{n}') d\Omega'$ describes the intensity scattered into the direction \vec{n} where $\chi_\nu(\vec{n}, \vec{n}')$ is the scattering probability.

To simplify the ν -dependence, we assume that the system contains only two groups of photons (Dobbs-Dixon et al. 2010):

- *Photon group 1* represents photons radiated by the central protostar which are impinging the protoplanetary disk, bring their energy into the system and act as a heat source (in case they become absorbed). The maximum of the spectral energy distribution of this group is in the optical range for a solar-type protostar.

- *Photon group 2* consists of photons originating from the disk itself. As the disk has a non-zero thermodynamic temperature, thermalised dust grains emit photons that contribute to: (i) energy redistribution within the disk; (ii) cooling of the disk whenever they become liberated from it, thus carrying their energy away. The spectral energy distribution of this group peaks in the infrared.

GROUP 1 SOLUTION. The photons of group 1 can only change the energy balance of the disk when they become absorbed. One can approximate the star with a point source and assume that photons propagate along the rays directed radially from the star. To capture such a geometry in a natural way, we will describe the disk on a spherical mesh of grid cells where the rays propagate solely along the radial dimension. After integration over all frequencies, Eq. (1.23) in a pure absorption limit reads

$$\frac{dI_\star}{dr} = -\rho\kappa_\star I_\star, \quad (1.24)$$

where the subscript ‘ \star ’ denotes quantities related to the photon group 1 and the opacity is averaged over the spectral intensity function of the protostar $S_\nu(T_\star)$, which can generally differ from the black-body radiation, as

$$\kappa_\star = \frac{\int \kappa_\nu S_\nu(T_\star) d\nu}{\int S_\nu(T_\star) d\nu}. \quad (1.25)$$

Formal solution of Eq. (1.24) leads to a simple exponential attenuation of the intensity

$$I_\star = I_{\star,0} \exp(-\rho\kappa_\star r) = I_{\star,0} \exp(-\tau_\star), \quad (1.26)$$

where we introduced the optical depth $\tau_\star = \int_0^r \rho\kappa_\star dr'$. Motivated by this solution, we can assemble the heating term related to the absorption of stellar radiation in a single grid cell with the optical depth $d\tau_\star$ (Dobbs-Dixon et al. 2010; Kolb et al. 2013)

$$Q_{\text{irr}} = \frac{L_\star}{4\pi r^2} \left(e^{-\tau_\star} - e^{-(\tau_\star+d\tau_\star)} \right) \frac{S_{\text{cell}}}{V_{\text{cell}}}. \quad (1.27)$$

The first right-hand-side fraction determines the flux [W m^{-2}] of irradiating photons at the distance r using the stellar luminosity $L = 4\pi R_\star^2 \sigma T_\star^4$ [W]. The difference of exponentials accounts for the difference between the flux arriving to and exiting from the cell. Multiplying by the cell cross-section S_{cell} interfacing the irradiating flux, one obtains the rate of energy production within one grid cell. Finally, dividing by the cell volume V_{cell} provides the energy density production rate [W m^{-3}] which can be directly included as a positive contribution to Q_{heat} of Eq. (1.6).

GROUP 2 SOLUTION. Regarding the photons of group 2, we need to solve the transfer equation for locally re-processed infrared radiation. To reduce the dimensionality of Eq. (1.23) for $I_\nu(\vec{r}, t; \vec{n}, \nu)$, the standard way is to take its integral over the solid angle, introducing the moments of the specific intensity. The zeroth and first moments are defined

$$\left(cE_\nu, \vec{F}_\nu \right) \equiv \int (I_\nu, \vec{n}I_\nu) d\Omega, \quad (1.28)$$

where E_ν is the monochromatic radiative energy density [$\text{J m}^{-3} \text{Hz}^{-1}$] and \vec{F}_ν is the monochromatic radiative flux [$\text{W m}^{-2} \text{Hz}^{-1}$]. In performing the integration, we assume that the *locally emitted* thermal radiation of the disk is isotropic and is in the local thermodynamic equilibrium (LTE) with matter, thus the disk emissivity follows the Kirchhoff law

$$j_\nu = B_\nu \kappa_\nu, \quad (1.29)$$

with the Planck function of black-body radiation

$$B_\nu(T) = \frac{2h\nu^3}{c^2} \frac{1}{\exp\left(\frac{h\nu}{k_B T}\right) - 1}, \quad (1.30)$$

where T is the *gas temperature*. Furthermore, we also integrate Eq. (1.23) over frequencies, noting that the integral of Eq. (1.30) is

$$\int B_\nu(T) d\nu = \frac{\sigma}{\pi} T^4. \quad (1.31)$$

RADIATIVE ENERGY EQUATION. Using the outlined approximations and integrations over Ω and ν leads to (Howell & Greenough 2003; Dobbs-Dixon et al. 2010)

$$\boxed{\frac{\partial E_R}{\partial t} + \nabla \cdot \vec{F} = \rho \kappa_P (4\sigma T^4 - cE_R)}, \quad (1.32)$$

where E_R is the frequency-averaged energy density of the *thermal radiation* of the disk, \vec{F} is the corresponding frequency-averaged radiation flux and κ_P is the Planck opacity

$$\kappa_P = \frac{\int \kappa_\nu B_\nu(T) d\nu}{\int B_\nu(T) d\nu}. \quad (1.33)$$

FLUX-LIMITED DIFFUSION. Adding E_R to the system of fluid equation as another unknown, Eq. (1.32) requires additional closure relations for \vec{F} and κ_P . Let us now focus on the former. One might be tempted to take yet another integral moment of Eq. (1.23) by performing $\int \vec{n} d\Omega$ but such an approach would only lead to an appearance of the radiation pressure in the model and a closure relation would still be needed.

To avoid introducing additional momenta of the intensity, we adopt the *flux-limited diffusion* (FLD; Levermore & Pomraning 1981). The FLD approximates the radiative flux with the diffusion equation

$$\vec{F} = -\lambda_{\text{lim}} \frac{c}{\rho \kappa_R} \nabla E_R \equiv -D \nabla E_R, \quad (1.34)$$

which has the form of the Fick's law and where κ_R is the Rosseland opacity

$$\kappa_R^{-1} = \frac{\int \kappa_\nu^{-1} \frac{\partial B_\nu(T)}{\partial T} d\nu}{\int \frac{\partial B_\nu(T)}{\partial T} d\nu}. \quad (1.35)$$

which is a harmonic mean that gives the greatest weight to the most transparent frequency bands and guarantees the correct radiative flux in the diffusion limit (Mihalas & Weibel Mihalas 1984).

The function λ_{lim} is called the *flux limiter* and it is designed to connect two limiting regimes of the radiation transfer and also to prevent unphysical propagation of photons at velocities exceeding the speed of light. The limiting regimes can be distinguished considering the mean free path of a photon $l = 1/(\kappa_{\text{R}}\rho)$ or alternatively the optical depth $\tau = \kappa_{\text{R}}\rho L$, where L is a characteristic spatial scale.

- If $l \gg L$ or $\tau \ll 1$, the environment is optically thin and photons undergo free streaming over distances $>L$. Then

$$|\vec{F}| \xrightarrow{\tau \ll 1} cE_{\text{R}}, \quad (1.36)$$

thus requiring

$$\lambda_{\text{lim}} \xrightarrow{\tau \ll 1} \frac{\rho\kappa_{\text{R}}E_{\text{R}}}{|\nabla E_{\text{R}}|} \equiv \frac{1}{R}. \quad (1.37)$$

- If, on the other hand, $l \ll L$ or $\tau \gg 1$, the environment is optically thick and photons behave according to the true diffusion limit. Then

$$|\vec{F}| \xrightarrow{\tau \gg 1} \frac{c}{3\rho\kappa_{\text{R}}} |\nabla E_{\text{R}}|, \quad (1.38)$$

and the limiter must converge to

$$\lambda_{\text{lim}} \xrightarrow{\tau \gg 1} \frac{1}{3}. \quad (1.39)$$

In our numerical models, we usually use the flux limiter of Kley (1989) which is specifically tailored for protoplanetary disks

$$\lambda_{\text{lim}} = \begin{cases} \frac{2}{3 + \sqrt{9 + 10R^2}}, & \text{for } 0 \leq R \leq 2, \\ \frac{10}{10R + 9 + \sqrt{81 + 180R}}, & \text{for } 2 < R. \end{cases} \quad (1.40)$$

The FLD is a useful approximation, although it has its drawbacks. For example, the transition between the optically thin and thick limit may not be accurately described by the flux limiter. In practice, however, this usually makes the solution unreliable only in relatively small regions because optically thin-to-thick transitions tend to be abrupt in protoplanetary disks (e.g. the condensation front of dust particles at the inner disk rim acts as an ‘instantaneous’ absorption barrier for stellar irradiation; Isella & Natta 2005).

COUPLED GAS ENERGY EQUATION. The introduction of radiation into the model also affects the final form of Eq. (1.6). The photon group 1 (irradiating photons) contributes via the term Q_{irr} (see 1.27). To account for the photon group 2 (thermal re-radiation), we can make use of the right-hand side of Eq. (1.32) which describes the sources and sinks of E_{R} . To ensure the energy conservation, a sink/source of E_{R} must be a source/sink of ϵ , leading to $[-\rho\kappa_{\text{P}}(4\sigma T^4 - cE_{\text{R}})]$.

Finally, the energy conservation dictates that the viscous friction generates heat as well, yielding the respective heat source (Mihalas & Weibel Mihalas 1984)

$$Q_{\text{visc}} = 2\rho\nu \left(\tau_{rr}^2 + \tau_{\theta\theta}^2 + \tau_{\phi\phi}^2 + 2\tau_{r\theta}^2 + 2\tau_{r\phi}^2 + 2\tau_{\theta\phi}^2 - \frac{1}{3}(\nabla \cdot \vec{v})^2 \right), \quad (1.41)$$

where τ_{ij} are the components of \mathbb{T} in spherical coordinates.

Eq. (1.6) therefore becomes

$$\boxed{\frac{\partial \epsilon}{\partial t} + (\vec{v} \cdot \nabla) \epsilon = -P\nabla \cdot \vec{v} - \rho\kappa_{\text{P}}(4\sigma T^4 - cE_{\text{R}}) + Q_{\text{visc}} + Q_{\text{irr}} + Q_+}, \quad (1.42)$$

where Q_+ symbolically denotes any additional problem-specific heat sources (such as the accretion heating from luminous protoplanets) or implementation-specific heat sources (such as the heating due to the shock-spreading artificial viscosity; Stone & Norman 1992).

OPACITY So far, we have defined 3 different opacity types (κ_* , κ_{P} and κ_{R}) entering the system of equations without providing any specifics on their calculations. In fact, the disk opacities represent one of the most significant unknowns and are usually subject to specialised studies, ‘decoupled’ from hydrodynamic modelling (e.g. Draine & Lee 1984; Lin & Papaloizou 1985; Bell & Lin 1994; Helling et al. 2000; Semenov et al. 2003; Zhu et al. 2009; Malygin et al. 2014; Woitke et al. 2016; Birnstiel et al. 2018).

Since we are interested in planet formation, we focus on disk regions with low enough temperatures to allow for the existence of dust grains. For a self-consistent determination of the dust opacities, one would have to (e.g. Cuzzi et al. 2014):

- Determine the chemical composition of grains at various conditions (since the temperature and density vary throughout the disk) and the fractional mass of each constituent. Typically, the materials that need to be considered, ordered from lowest evaporation temperatures, are: water ice, organics, graphite, silicates (e.g. troilite, pyroxene, olivine), and iron (Pollack et al. 1994; Zhu et al. 2012).
- From laboratory measurements, extract the refractive indices (Bohren & Huffman 1983; Voshchinnikov 2004) for each constituent. For this purpose, it is possible to utilise the database of dust optical properties from JENA laboratory⁴ (Jäger et al. 2003). Subsequently, effective refractive indices of grains, which are usually mixtures of multiple constituents, need to be calculated, e.g. using the effective medium theory (Ossenkopf 1991).

⁴<https://www.astro.uni-jena.de/Laboratory/Database/databases.html>

- Calculate the absorption and scattering cross-sections as functions of the wavelength and grain size using the Mie theory. Correct for the forward scattering. This step can be performed with some publicly available numerical code, e.g. `bhmie`⁵.
- Assemble monochromatic opacities by integrating over the size distribution of dust grains. For a precise treatment of the size distribution, a standalone fragmentation/coagulation model would be necessary (e.g Birnstiel et al. 2012).
- Calculate the frequency-averaged opacities.

To avoid the steps above, it is customary to use pre-calculated opacity tables which set the material opacity as a function of the local temperature and density. Following Bitsch et al. (2013), we use the opacity table of Bell & Lin (1994) and we set $\kappa_{\text{R}} = \kappa_{\text{P}} = \kappa_{\star}$ which is a valid approximation in optically thick and relatively cold planet-forming regions. However, we emphasise that this approach, including the averaging over frequencies, is rather simplistic and we refer the interested reader to Kuiper & Klessen (2013) for a broader discussion of the approximations used in the radiation physics of disks.

Radiative 1-temperature approximation

In the previous, we assumed the LTE between the matter and its *local* thermal emission, but generally we allowed the radiation field to decouple from gas. Sometimes it is convenient to assume such a coupling which can reduce Eqs. 1.32 and 1.42 into a single equation that might be easier to solve. According to the 1-temperature approximation, it is possible to relate the radiation energy to the thermodynamic temperature of gas and dust at any time

$$E_{\text{R}} = \frac{4\sigma}{c}T^4 \equiv a_{\text{R}}T^4, \quad (1.43)$$

where we defined the radiation constant a_{R} . Further assuming that $\partial E_{\text{R}}/\partial t \ll \partial \epsilon/\partial t$ (e.g. Kley et al. 2009), a direct sum of Eqs. (1.32) and (1.42) leads to

$$\frac{\text{D}\epsilon}{\text{D}t} = -P\nabla \cdot v - \nabla \cdot \vec{F} + Q_{\text{visc}} + Q_{\text{irr}} + Q_{+}, \quad (1.44)$$

and the radiation flux becomes

$$\vec{F} = -\lambda_{\text{lim}} \frac{c}{\rho\kappa_{\text{R}}} 4a_{\text{R}}T^3 \nabla T. \quad (1.45)$$

We point out that a special care is needed when combining the stellar irradiation term Q_{irr} with the 1-temperature approximation because of the imposed coupling between radiation and matter (Kuiper et al. 2010).

⁵See <https://www.astro.princeton.edu/~draine/scattering.html> for a version written by B.T. Draine.

2D description

The 3D RHD model can be further simplified to 2D which can significantly reduce its computational cost. This is highly desirable for global-scale long-term simulations of planet-disk interactions. The transformation from 3D to 2D is generally allowed because the dominant motion in disks is their in-plane sub-Keplerian rotation and their structure in the vertical direction can decouple from the radial one. The governing equations of a 2D model can be obtained from the 3D model by a vertical integration and they formally look very similar:

$$\frac{\partial \Sigma}{\partial t} + (\vec{v} \cdot \nabla) \Sigma = -\Sigma \nabla \cdot \vec{v}, \quad (1.46)$$

$$\frac{\partial \vec{v}}{\partial t} + (\vec{v} \cdot \nabla) \vec{v} = -\frac{\nabla P}{\Sigma} + \frac{\nabla \cdot \mathbb{T}}{\Sigma} + \vec{a}_{\text{ext}}, \quad (1.47)$$

$$\frac{\partial \epsilon}{\partial t} + (\vec{v} \cdot \nabla) \epsilon = -P \nabla \cdot \vec{v} + Q_{\text{heat}}. \quad (1.48)$$

but one has to keep in mind that the resulting quantities now represent vertically-integrated ones (e.g. Σ is the surface density), and that the dimensionality of vectors and tensors is reduced. Moreover, there is a trade-off between this reduction and model complexity. Most importantly, the stellar irradiation can no longer be treated by ray tracing, radiative diffusion in the vertical direction can be modelled only approximately, and the gravity of a thin disk acting on planets becomes notably different compared to that of a 3D disk. A viable workaround to these difficulties is to use vertically independent 1D models for radiation reprocessing (e.g. Hubeny 1990; Calvet et al. 1991; Chiang & Goldreich 1997; Isella & Natta 2005) and also gas distribution (Müller et al. 2012).

Model variants used in Papers I–IV

For completeness, we briefly discuss the variants and modifications of the RHD model outlined above which are used in Papers I–IV (Chapter 2). Papers I–III utilise a 2D 1-temperature approach with the vertical cooling and stellar irradiation based on a 1D model (Hubeny 1990; Menou & Goodman 2004). Additionally, a two-fluid approximation is used with one fluid representing the gas (as in this section) and the second one representing pebbles that can be accreted by embedded planets. Planetary luminosities (e.g. Benítez-Llambay et al. 2015) resulting from pebble accretion are included as another source term in the energy equation. The approach of Müller et al. (2012) is used to treat the gravity in planet-disk interactions. Systems of multiple embryos are studied and their mutual interactions are resolved using the *Ias15* integrator (Rein & Spiegel 2015).

Paper IV is based on a 3D 2-temperature model where the irradiation is neglected (although our implementation contains it). The accretion onto planets and accretion luminosity are parametrised (pebbles are not incorporated in the model). Only a single protoplanet is studied and we again account for its accretion luminosity.

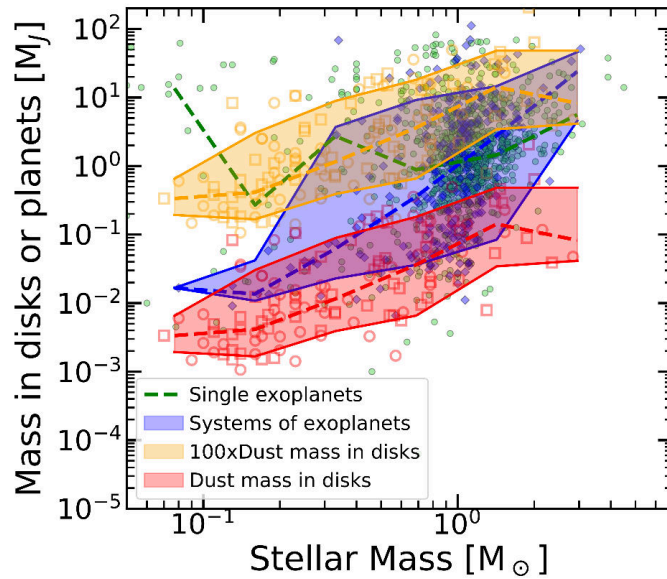


Figure 1.6: Mass distribution of single exoplanets (green), systems of exoplanets (blue) and protoplanetary disks (red for M_{dust} and yellow for M_{disk}) as a function of the mass of the host star. Displayed disks belong to the Lupus (empty circles) and Chamaeleon I (empty squares) regions. Dashed lines are used for medians, coloured regions are bordered by the 10th and 90th percentiles. It is obvious that the mass incorporated in many planetary systems exceeds the currently observed dust mass in protoplanetary disks. Adapted from Manara et al. (2018).

1.2 From dust to planets

With the observational and theoretical properties of protoplanetary disks in mind, we can now proceed to the discussion of planet formation. Solid bodies within disks are thought to grow by *accretion*, which is a sequence of processes that lead to a constructive agglomeration of smaller objects into larger objects. In terms of astrophysical scales, planetary accretion is a very puzzling phenomenon because it appears to be extremely efficient and extremely fast.

As a manifestation of the speed of accretion, giant planets regularly occur in extrasolar systems while the ages of gas disks are clearly limited to several Myr. But for a giant planet to come into existence, it is fundamental that its solid core ($\sim 10 M_{\oplus}$) is formed before the disk dispersal, otherwise the planet would never be able to accrete a massive gaseous envelope ($\sim 10^3 M_{\oplus}$) (Pollack et al. 1996). In other words, it is required that μm -sized dust grains are converted into bodies with diameters of $\sim 10^3$ – 10^5 km during several millions of years, within the lifetime of the disk. For smaller planets of the terrestrial type, the formation might take longer (in fact, formation of the solar-system terrestrial planets is considered to finish *after* the gas dispersal), but at least planetary embryos precluding terrestrial planets must already be assembled while the gas is still around (e.g. Kleine & Walker 2017).

Concerning the efficiency of accretion, recent observations revealed that the mass

of solids incorporated in planetary systems appears to be comparable to the dust mass observed in disks (Greaves & Rice 2010; Williams 2012; Najita & Kenyon 2014; Mulders et al. 2015; Manara et al. 2018). In fact, our current understanding of accretion processes cannot yet sufficiently explain such an efficient conversion of dust into planets (Manara et al. 2018), as demonstrated in Fig. 1.6. The discrepancy probably arises because a substantial fraction of small solids in disks remains hidden from observations, or because small solids possibly undergo efficient recycling and replenishment from the surrounding environment. But even then, the growth of planets has to be very efficient.

Finally, any planet formation theory should be able to answer why the planetary systems are so diverse (see Fig. 1). By this diversity we mean a surprisingly frequent occurrence of extrasolar systems that contain types of planets unknown from the Solar System, e.g. close-in super-Earths, mini-Neptunes, or hot Jupiters.

1.2.1 Coagulation of dust to pebbles

The first step of the accretion sequence leads from dust grains to pebbles (mm-cm particles). The process is known as *coagulation* and it is expected to proceed by means of random pairwise collisions of dust grains which may end up being stuck together via Van der Waals forces. However, both theoretical and experimental investigations of the process discovered that its efficiency is limited by rather strict mechanical and dynamical barriers. Let us now discuss the most important ones.

First, it is important to clarify what is the dynamical behaviour of solids orbiting within the gas (see Fig. 1.7). A solid particle would orbit the star at the Keplerian velocity $v_s = v_K = \sqrt{GM_\star/r}$. However, the orbital velocity of the gas disk is slightly different. Since a gas parcel of the disk is in a force equilibrium between the gravitational pull of the star, pressure support of the nearby gas and centrifugal force, the characteristic orbital velocity of the gas is then slightly sub-Keplerian, typically $v_g \simeq (1 - \eta)v_K$ where $\eta = \partial \log P / \partial \log r \sim 0.001$ represents the influence of the (unperturbed) pressure gradient on the rotation of gas. Solid particles therefore feel a headwind with the magnitude ηv_K . This headwind results in a *gas drag* (Adachi et al. 1976), i.e. in a force which tries to cancel the relative velocity v_{rel} between the gas and dust. The characteristic time for the drag to erase the relative velocity is known as the *stopping time* t_s , which is an important quantity that characterises the dynamical response of the solid particle with respect to gas.

The stopping time acquires various functional forms, depending on the drag regime relevant for a solid body of a given size a . If $a < 9\lambda/4$ where λ is the mean free path of gas molecules, the drag is primarily produced by collisions of individual molecules with the particle. This is known as the Epstein regime. If $a > 9\lambda/4$, the collective fluid nature of molecules prevails and the drag operates in the Stokes regime. The Stokes regime has its own sub-regimes, depending on whether the flow around the solid body remains laminar or turbulent, as characterised by the Reynolds number (e.g. Whipple 1972; Weidenschilling 1977). Usually, dust grains and pebbles remain mostly in the Epstein regime, apart from the innermost disk

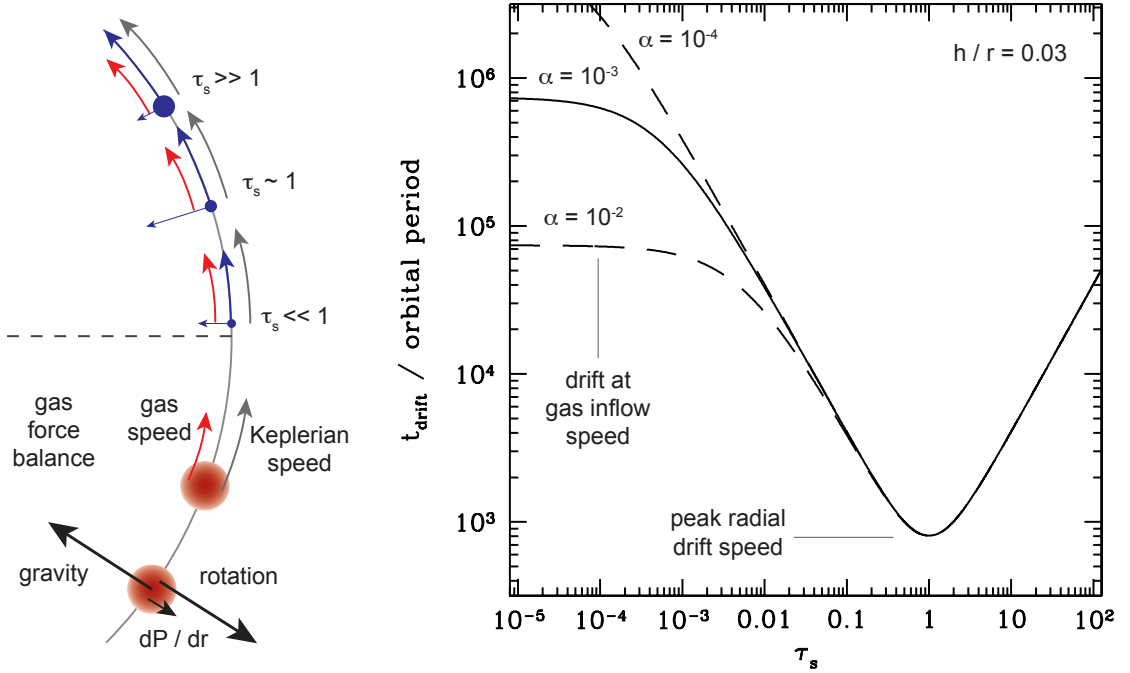


Figure 1.7: *Left:* Cartoon of the gas drag mechanism. In the lower half of the cartoon, the equilibrium of forces (black arrows) acting on a gas blob (red circle) is depicted. The force balance renders the gas rotation sub-Keplerian (red arrow versus grey arrow). In the upper half, various regimes of the aerodynamic coupling between the gas and a solid particle (blue circle) are shown. Three cases are distinguished by the size of the particle and its Stokes number. When $\tau \ll 1$, the particle synchronises with the gas. When $\tau \sim 1$, the particle is still substantially decelerated (its velocity is not exactly Keplerian), yet it does not synchronise with the gas. When $\tau \gg 1$, the particle orbits at the unperturbed Keplerian velocity. *Right:* Drift timescale t_{drift} from 1 au towards the disk centre as a function of the Stokes number of the drifting particle. The figure is constructed for disk models with $\Sigma \propto r^{-1}$, $T \propto r^{-1/2}$, $h/r = 0.03$, and three turbulent parameters $\alpha = 10^{-2}$, 10^{-3} and 10^{-4} that set the accretion timescale of the gas. The fastest drift occurs for $\tau \sim 1$. Adapted from Armitage (2015).

regions where the increase in gas density leads to a decrease in λ . On the other hand, planetesimals are influenced by the Stokes regime.

Focusing on the Epstein regime, the stopping time can be expressed as

$$t_s = \frac{\rho_s a}{\rho_g v_{\text{th}}}, \quad (1.49)$$

where ρ_s and ρ_g are volume densities of the solids and gas, respectively. The mean thermal velocity of gas v_{th} is comparable to c_s . The deceleration acting on solids is simply

$$\vec{a}_d = -\frac{\vec{v}_{\text{rel}}}{t_s}, \quad (1.50)$$

while the back-reaction of gas has a reversed sign and scales with the ratio Σ_s/Σ_g . Under normal circumstances the dust-to-gas ratio is ~ 0.01 and the dust is not abundant enough to affect the gas.

Aerodynamic response of solids is often characterised by the dimensionless stopping time known as the Stokes number

$$\tau = t_s \Omega_K. \quad (1.51)$$

It defines three classes of behaviour, as also highlighted in Fig. 1.7. If $\tau \ll 1$, any velocity difference between the dust and gas is damped within a single Keplerian orbit. The particle is tightly coupled to the gas flow. This coupling is characteristic for the smallest dust grains. If $\tau \gg 1$, the particle feels almost no influence of the gas drag and it becomes decoupled from gas motions. If τ acquires intermediate values, the particle feels a significant deceleration, yet it does not have enough time to synchronise its orbital velocity with that of gas. As a result, the deceleration forces the particle to lose its orbital momentum and follow a spiral trajectory leading towards the star. Particles with intermediate τ collectively *drift* through the gas disk and the most significant drift appears when $\tau \sim 1$. The radial drift velocity is (e.g. Nakagawa et al. 1986)

$$v_r \simeq -\frac{2\tau}{1+\tau^2}\eta v_K, \quad (1.52)$$

from which we see that the only way to stop the radial drift is by a reversal of the pressure gradient ($\eta < 0$ makes the rotation of gas super-Keplerian so that it traps solids drifting from outside).

Apart from the radial drift, the drag also leads to vertical *settling* of small particles towards the midplane of the disk. Equating the drag force to the vertical component of the stellar gravity ($F_{g,z} = m\Omega_K^2 z$) leads to the terminal settling velocity (e.g. Armitage 2010)

$$v_z = \frac{\rho_s a}{\rho_g v_{\text{th}}} \Omega_K^2 z, \quad (1.53)$$

and the settling timescale $t_{\text{set}} = z/v_z$. A natural question arises whether the dust settling can create a strong overdensity of solids in the midplane or not. The answer is negative (Weidenschilling 1980): such an overdensity would eventually spun up the gas in the midplane into Keplerian rotation due to the drag back-reaction. This would create a layer prone to Kelvin-Helmholtz turbulence between the Keplerian gas in the midplane and the slowly rotating unperturbed gas at larger $|z|$. The turbulence would therefore prevent ‘infinite’ sedimentation. Moreover, if the disk is turbulent due to other hydrodynamic instabilities, dust settling is opposed by *turbulent mixing*.

Coming back to the radial drift, Weidenschilling (1977) demonstrated that its velocities can be substantial, reaching $\sim 10^4 \text{ cm s}^{-1}$ for $\tau \sim 1$ near 1 au of the MMSN. Therefore the drift has important implications for coagulation because once grains grow to mm- and cm-sizes, their τ inevitably approaches ~ 1 and they eventually

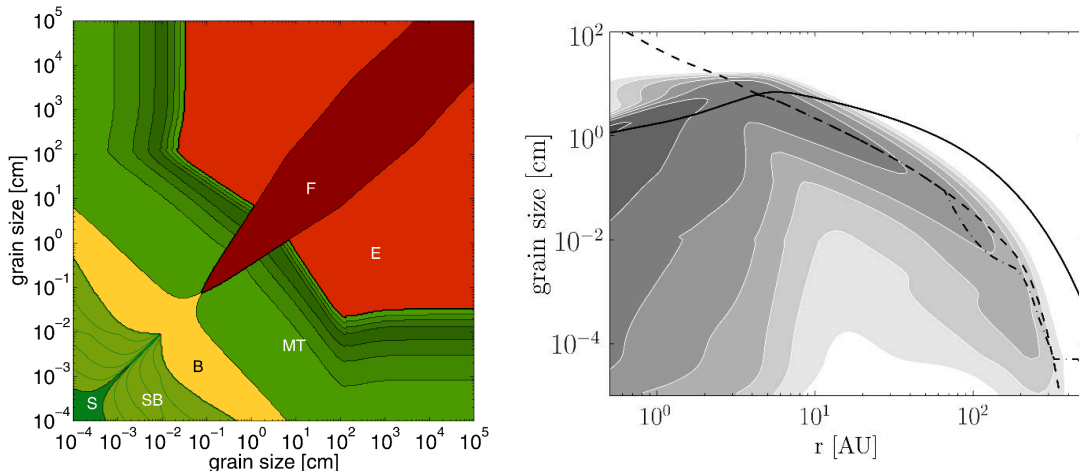


Figure 1.8: *Left:* Diagram of outcomes of pairwise collisions between dust grains. The individual regions represent fragmentation (F), erosion (E), mass transfer (MT), bouncing (B), the transition from sticking to bouncing (SB) and sticking (S). Only the cases from green regions lead to a net mass growth of the larger grain. It is evident that for an initial population occupying the lower left corner of the diagram, it would be difficult to grow beyond the bouncing barrier. The displayed result of a dust-size evolution model was obtained at 3 au for parameters $\Sigma_g = 330 \text{ g cm}^{-2}$ (MMSN), $T = 115 \text{ K}$, dust-to-gas ratio 0.01, $\alpha = 10^{-3}$, $\rho_s = 1.6 \text{ g cm}^{-3}$. Adapted from Windmark et al. (2012). *Right:* Surface density of dust grains (grey scale) as a function of the grain size and radial distance. The dark-grey isosurface corresponds to $\sim 10^{-1} \text{ g cm}^{-2}$, the white isosurface to $\sim 10^{-7} \text{ g cm}^{-2}$. The fragmentation-limited size (Eq. 1.55) is depicted by the solid line, the drift-limited size (Eq. 1.54) by the dashed line. The dash-dotted line corrects the drift-limited size for a delayed drift of small grains from outer regions. The disk model accounts for the viscous evolution (Birnstiel et al. 2010) with $\alpha = 10^{-3}$ and the displayed snapshot is taken at 1 Myr. Adapted from Birnstiel et al. (2012).

start to drift towards the star. If the drift timescale t_d at the given location becomes shorter than the timescale t_g of the growth by coagulation, the size distribution of solids becomes truncated and the pebble sizes cannot be exceeded. Using the growth rate of monodisperse coagulation (Brauer et al. 2008), Birnstiel et al. (2012) derived the maximum size that can be reached before the drift prevents further growth as

$$a_d \simeq \frac{2 \Sigma_d v_K^2}{\pi \rho_s c_s^2} \left(\frac{\partial \log P}{\partial \log r} \right)^{-1}, \quad (1.54)$$

where Σ_d is the surface density of dust.

Yet another barrier for the growth of dust beyond pebble sizes is related to fragmentation. As two grains collide, they do not always stick together. If their relative velocity is large enough, the collision might be disruptive, leading to a mass loss or a complete destruction of the participating grains. The increase of the relative velocity can be facilitated by turbulence, or by the differential drift speed of grains with various sizes and Stokes numbers. Birnstiel et al. (2012) provides the

fragmentation-limited maximum size as

$$a_f \simeq \frac{2}{3\pi} \frac{\Sigma_g}{\rho_s \alpha} \frac{v_f^2}{c_s^2}, \quad (1.55)$$

where v_f is the fragmentation velocity which is thought to range from ~ 1 to 10 m s^{-1} (Blum & Wurm 2000, 2008; Wada et al. 2009; Güttler et al. 2010; Gundlach & Blum 2015). The upper limit is required in the outer cold regions of protoplanetary disks to disrupt water-ice coated grains that have larger surface energies (Gundlach & Blum 2015). Lower impact velocities are sufficient for silicate grains.

The remaining obstacle is known as the bouncing barrier. If dust grains undergo compactification during their collisional history, the filling factor of their aggregate-like structure increases. Subsequently, colliding compactified grains have a tendency to bounce rather than stick together (Blum & Münch 1993; Weidling et al. 2009; Zsom et al. 2010).

In Fig. 1.8, we show a typical outcome of a local coagulation/fragmentation model (left panel; Windmark et al. 2012) and a global model with viscous evolution (right panel; Birnstiel et al. 2010, 2012). The figure demonstrates that owing to the bouncing barrier, it is difficult for dust grains to grow beyond mm-sizes in the inner disk. Even if the bouncing barrier is exceeded, the fragmentation barrier halts the growth at cm-sizes. In regions outside $\sim 10 \text{ au}$, the grain sizes are drift-limited and peak at $\sim 10 \text{ cm}$. Finally, it is clear that most of the dust surface density tends to reside in the largest available pebbles.

1.2.2 Planetesimal formation induced by turbulence

Since the nature of the aforementioned size barriers is physically simple, robust and hard to overcome, it seems that the accretion sequence has to continue beyond pebbles by directly building km-sized planetesimals. Such an abrupt increase in the size of solids can be indeed facilitated by gravitational collapse.

A first insight into the stability of a dust layer can be provided by a perturbation analysis for a planar, self-gravitating dust slab. Using linearised fluid equations (Safronov 1969) of continuity and momentum (e.g. Chiang & Youdin 2010), neglecting the influence of gas and working within the WKB approximation (e.g. Binney & Tremaine 2008), a dispersion relation for the angular frequency ω of perturbations can be found (Goldreich & Lynden-Bell 1965):

$$\omega^2 = c_s^2 k_r^2 - 2\pi G \Sigma_d |k_r| + \kappa^2, \quad (1.56)$$

where k_r is the radial wavenumber (the approximation focuses on axisymmetric modes) and κ is the epicyclic frequency. The relation implies that wave-like perturbations with short wavelengths are stabilised by pressure, long wavelengths are stabilised due to rotation, and self-gravity can lead to an instability if (Toomre 1964)

$$Q \equiv \frac{c_s \kappa}{\pi G \Sigma_d} < 1, \quad (1.57)$$

which is the well-known Toomre’s criterion. Knowing that $\kappa \simeq \Omega_K$, we can estimate the critical midplane volume density ρ_{crit} by plugging $\rho_{\text{crit}} \simeq \Sigma_d/(\sqrt{2\pi}H)$ and $H \simeq c_s/\Omega_K$ into the criterion. One finds that for densities of the solid layer (Chiang & Youdin 2010)

$$\rho_0 \gtrsim \rho_{\text{crit}} = \frac{M_\star}{\pi\sqrt{2\pi}r^3} \approx 10^{-7} \left(\frac{r}{\text{au}}\right)^{-3} \text{ g cm}^{-3}, \quad (1.58)$$

a collapse is triggered. However, such a particle concentration is not easily established in protoplanetary disks; the density of the solid layer predicted by the MMSN is typically three or four orders of magnitude below the critical threshold (assuming the dust-to-gas ratio 0.01).

Over the past two decades, however, several processes have been suggested which can *locally* boost the solid-to-gas ratio and create a particle concentration which is prone to gravitational collapse. The processes include:

- small-scale vortices in turbulent disks (Cuzzi et al. 2001, 2008; Pan et al. 2011);
- pressure bumps which can be created, e.g., by dust evaporation at a snow line (Ida & Guillot 2016; Drazkowska et al. 2016; Schoonenberg & Ormel 2017);
- large-scale vortices which can arise by means of the baroclinic instability (Klahr & Bodenheimer 2003) or the Rossby wave instability at the edge of the dead and active zone (Lyra et al. 2009);
- zonal flows which are launched in MRI-active disks with large-scale variations of the turbulent parameter α (Johansen et al. 2006, 2009; Simon et al. 2012; Dittrich et al. 2013);
- streaming instability, discussed in the following.

STREAMING INSTABILITY. Solid particles can start accumulating even if the disk is initially laminar and without pressure bumps. Youdin & Goodman (2005) demonstrated that if the two-way coupling via the linear drag term is included in the set of two-fluid equations describing the mixture of gas and dust, the inevitable radial drift triggers linearly unstable modes (see also Jacquet et al. 2011). The minimal set of equations which lead to the instability reads (e.g. Chiang & Youdin 2010)

$$\frac{D_g \rho_g}{Dt} = 0, \quad (1.59)$$

$$\frac{D_g \vec{v}_g}{Dt} = -\Omega_K^2 \vec{r} + \frac{\tilde{\rho}_s}{\rho_g} \frac{\vec{v}_s - \vec{v}_g}{t_s} - \frac{\nabla P}{\rho_g}, \quad (1.60)$$

$$\frac{D_s \tilde{\rho}_s}{Dt} = -\tilde{\rho}_s \nabla \cdot \vec{v}_s, \quad (1.61)$$

$$\frac{D_s \vec{v}_s}{Dt} = -\Omega_K^2 \vec{r} - \frac{\vec{v}_s - \vec{v}_g}{t_s}, \quad (1.62)$$

where the subscripts ‘s’ and ‘g’ are used for solid particles and gas, respectively. The notation $\tilde{\rho}_s$ is used to distinguish the density of the ‘fluid of particles’ from the

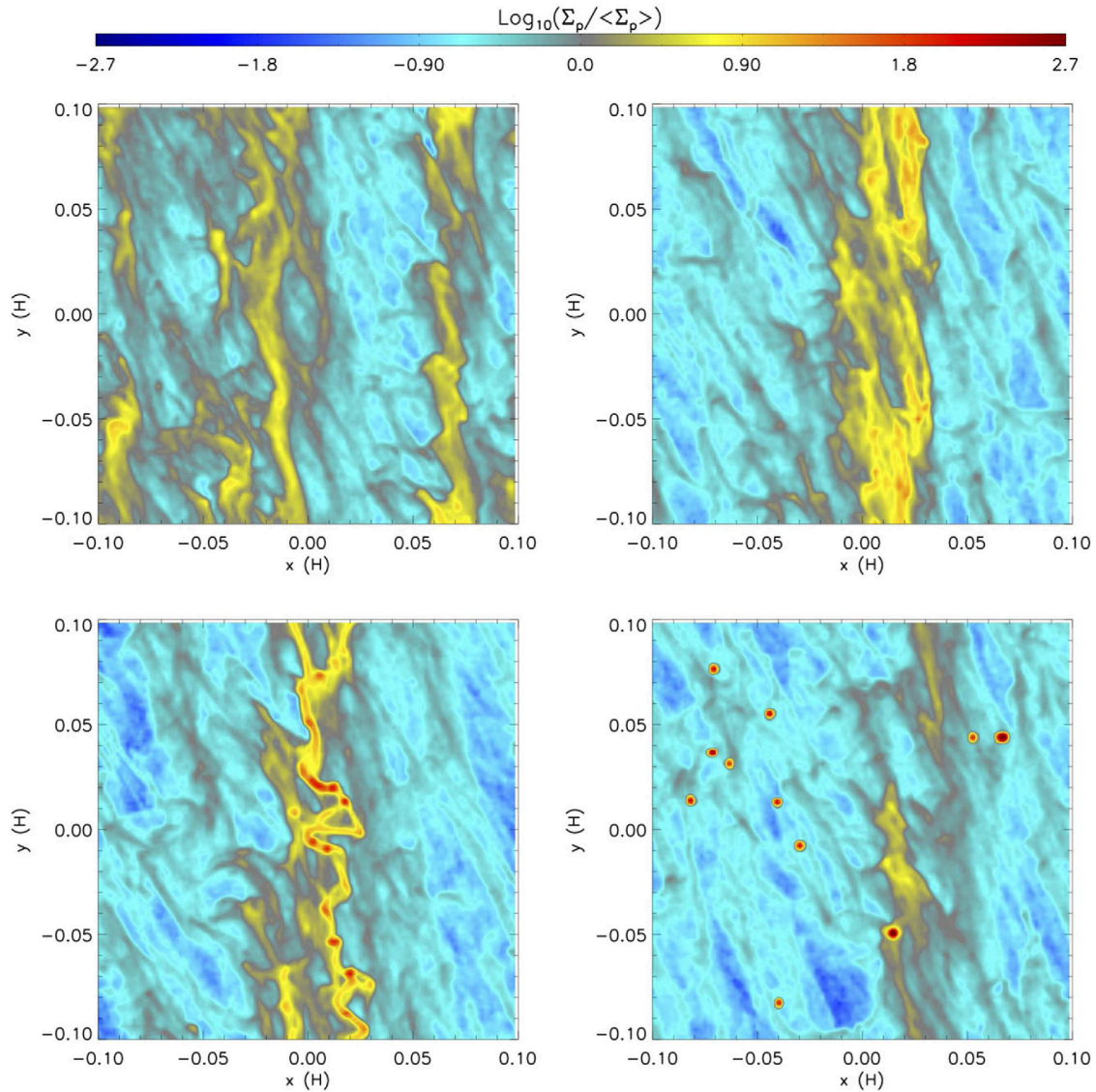


Figure 1.9: Example of a numerical simulation of the streaming instability. The logarithmic colour scale represents the relative density of a layer of solids (with respect to the mean density). The simulation time increases from top left to bottom right. The simulation treats the gas using isothermal hydrodynamics and solids as individual particles with self-gravity (Simon et al. 2016). A 3D shearing box with the edge length $0.2H$ is resolved by 128^3 cells. In total, 2.4×10^6 particles with $\tau = 0.3$ and the solid-to-gas ratio 0.02 are initially included. The streaming instability develops into non-linear perturbations which concentrate the particles into filaments. Self-gravitational clumping of the densest filaments is triggered and forms several planetesimals (red dots) with the maximum mass corresponding to $\simeq 0.2 M_{\text{Ceres}}$. Adapted from Simon et al. (2016).

previously used material density of solids ρ_s . The respective Lagrangian derivatives

are defined as

$$\frac{D_{s/g} \bullet}{Dt} = \frac{\partial \bullet}{\partial t} + (\vec{v}_{s/g} \cdot \nabla) \bullet. \quad (1.63)$$

The model neglects self-gravity, vertical component of the gravity (vertical stratification), and t_s is assumed constant as well as ρ_g , which implies the gas is treated in the incompressible limit (Eq. 1.59; $\nabla \cdot \vec{v}_g = 0$). Despite the absence of self-gravity, the dispersion relation obtained by Youdin & Goodman (2005) uncovers unstable modes driven by the relative drift of the two fluids. The instability leads to clumping of solid particles.

From the mathematical point of view, the particle clumping occurs due to the back-reaction term in Eq. (1.60). Since ρ_g and t_s are treated as constants, only variations of $\tilde{\rho}_s$ can compensate for the streaming term $\vec{v}_s - \vec{v}_g$. The energy of the relative (streaming) motion can only be extracted by particle clumping (Goodman & Pindor 2000; Youdin & Goodman 2005) and thus the process was named the *streaming instability*. Heuristically, the instability can be understood from the collective behaviour of drifting particles⁶.

The instability tends to create a filamentary network of concentrated particles (Johansen & Youdin 2007; Bai & Stone 2010), as shown in Fig. 1.9. The filaments can become subject to gravitational collapse and directly form planetesimals (Johansen et al. 2007) with characteristic sizes of the order of ~ 100 km (Johansen et al. 2015; Simon et al. 2016). This channel of planetesimal formation is therefore in accordance with primordial populations inferred from collisional models of the main asteroid belt (Morbidelli et al. 2009) and the Kuiper belt (Lambrechts & Morbidelli 2016).

Additionally, Kuiper belt objects are often observed to exist in binary configurations (Noll et al. 2008) and the primordial fraction of binaries might have been as large as 100% (Parker & Kavelaars 2010; Nesvorný et al. 2011; Fraser et al. 2017). Nesvorný et al. (2010) demonstrated that the gravitational collapse, such as the one triggered by the streaming instability, naturally produces a binary planetesimal. The streaming instability and gravitational collapse therefore represent a promising explanation of the origin of binaries in the Kuiper belt. It was also proposed that the properties of comet 67P/Churyumov–Gerasimenko can be naturally explained if the comet was formed by the streaming instability and a gentle collapse of participating solids (Blum et al. 2017).

However, the streaming instability is still limited by several drawbacks. The particles which trigger the unstable modes with the fastest growth rate are found to be dm-sized. But these sizes can scarcely be reached given the coagulation size

⁶Imagine a small clump of solids moving through the gas. The particles at the front of the clump feel a stronger headwind than particles deeper within the clump. The front particles are therefore decelerated more efficiently and the clump becomes more compact. The positive feedback then occurs because the compact clump accelerates the gas and then the radial drift velocity of the clump becomes smaller compared to isolated particles. If such isolated particles exist outside the orbit of the clump, they eventually catch up with the clump due to their larger radial drift velocities. This way the local concentration of solids increases.

limits discussed in Sect. 1.2.1. For small mm-sized chondrules, which are found in primitive meteorites, the streaming instability can only be triggered if the initial dust-to-gas ratio exceeds 4% (Yang et al. 2017). Further work is therefore needed to fully assess the importance of the streaming instability.

1.2.3 Growth of planets by pebble accretion

Why not planetesimal accretion?

Once a population of planetesimals is formed, pairwise low-velocity collisions (such that they do not shatter the bodies; e.g. Stewart & Leinhardt 2009) can eventually lead to formation of protoplanets. The process is known as *planetesimal accretion*. A collision occurs if one planetesimal approaches another with an impact parameter

$$b \leq \pi R_p^2 \left(1 + \frac{v_{\text{esc}}^2}{v_{\text{rel}}^2} \right), \quad (1.64)$$

where $v_{\text{esc}} = (2GM_p/R_p)^{1/2}$ is the mutual escape velocity and we assumed that the masses and radii of colliding planetesimal are the same (M_p , R_p). In Eq. (1.64), the geometrical cross-section is enhanced by the gravitational attraction of approaching bodies (the bracketed term is known as the gravitational focusing factor f_g).

The gravitational focusing can lead to two very distinct regimes of planetesimal accretion known as the *runaway* and *oligarchic* growth. The former appears if the population of planetesimals is dynamically cold, such that $v_{\text{rel}} \ll v_{\text{esc}}$ and $f_g \simeq (v_{\text{esc}}/v_{\text{rel}})^2$. If this is the case, even small initial differences in the mass distribution will start to increase exponentially, leading to a swift growth of the initially most massive bodies into larger ones (Greenberg et al. 1978; Wetherill & Stewart 1989). The oligarchic growth, on the other hand, operates when $v_{\text{rel}} \gtrsim v_{\text{esc}}$ and $f_g \sim 1$. Such a limit halts the increase of relative mass ratios within the population and the largest bodies continue to grow almost in an orderly fashion (Kokubo & Ida 1998, 2000).

The nature of planetesimal accretion is such that the aforementioned regimes lead to a low diversity of possible outcomes. The following caveats arise which make the importance of planetesimal accretion rather questionable:

- If the planetesimal population is initially in the runaway growth mode, largest bodies increase the relative velocities of planetesimals that miss them during close encounters. This dynamical stirring of the population leads to $v_{\text{rel}} \sim v_{\text{esc}}$ and prevents further runaway growth (Ida & Makino 1993).
- The previous caveat might be circumvented if the majority of planetesimals is at most km-sized. Then the Stokes gas drag would circularise their orbits and keep v_{rel} sufficiently low. However, as we discussed in the previous section, planetesimals were probably born large. For 100-km bodies, the Stokes drag is no longer important and the runaway growth cannot be maintained.

- Sooner or later, planetesimal accretion switches into the oligarchic regime. Its typical outcome comprises of several (or several tens of) protoplanets with relatively similar masses. These final masses are usually not large; the isolation mass for planetesimal accretion in the inner disk is comparable to Mars ($\sim 0.1 M_{\oplus}$ Lissauer 1987; Kokubo & Ida 2000). The isolation mass can become larger in the outer disk but at the same time, the longer orbital timescales lead to too long accretion timescales (since two planetesimals have a chance to collide only once per orbit). This poses a great difficulty for a successful explanation of the Solar System which exhibits a clear dichotomy between the inner terrestrial bodies and outer gas/ice giants.
- Adding to the previous issue, Levison et al. (2010) demonstrated with a robust set of models that the planetesimal accretion fails to produce giant planet cores in 90% of cases. The reason is that planetary embryos efficiently repel planetesimals away from their orbit rather than accrete them. Once the region around an embryo's orbit is devoid of any building material, planetesimals cannot repopulate it because their migration is not sufficient. The growth of embryos is then inevitably stalled.

Accretion from a swarm of pebbles

When first planetesimals form from collapsing clumps of pebbles (Sect. 1.2.2), they remain embedded in a sea of leftover pebbles which did not participate in the collapse. Additionally, pebbles from outer disk regions drift past the planetesimals. What happens to this leftover material? It turns out that it can be efficiently accreted by the planetesimals by the process known as *pebble accretion* (Ormel & Klahr 2010; Lambrechts & Johansen 2012). This way, the growth can proceed all the way to protoplanets.

Pebble accretion is yet another phenomenon which is facilitated by gas drag. Imagine a pebble passing a substantially larger body of mass M_p . Since pebbles are understood as efficient drifters, with their Stokes numbers close to unity, they are strongly influenced by the drag. If the pebble becomes deflected from an unperturbed trajectory by the massive body, its velocity vector becomes tilted with respect to the flow of rotating gas and the influence of gas drag is amplified and the orbital energy of the pebble is dissipated. As a result, the pebble can become captured and accreted by the gravitating body since the effective cross-section for the capture is enhanced by the gas drag.

To review the basic regimes of pebble accretion, we follow Ormel (2017). We define the *encounter time*

$$t_{\text{enc}} = \frac{2b}{v_{\text{rel}}}, \quad (1.65)$$

as the interval over which the pebble experiences the strongest deflection. The time it takes for a particle to descend onto the planet is referred to as the *settling time*

and it reads

$$t_{\text{set}} = \frac{b}{v_{\text{set}}} = \frac{b^3}{GM_{\text{p}}t_{\text{s}}}, \quad (1.66)$$

where the settling velocity is derived from the gravitational acceleration GM_{p}/b^2 acting at the separation b over the stopping time t_{s} (Eq. 1.49). The necessary conditions for the pebble to become accreted are $t_{\text{s}} < t_{\text{enc}}$ and $t_{\text{set}} < t_{\text{enc}}$. It is important to realise that although very small particles with small t_{s} easily fulfil the first condition, it is difficult for them to meet the second condition (due to the strong aerodynamic coupling, they are carried away by the gas flow before they can settle onto the accreting body). Conversely, large particles with large t_{s} can quickly settle onto the accreting body but the gas drag is not important for them and thus the cross-section of the interaction remains too small. Usually, an optimal size of pebbles exists for which the accretion is the most efficient.

Although several regimes of pebble accretion exist (Ormel & Klahr 2010; Ormel & Kobayashi 2012), we emphasise the two which become the most important for the planetary growth: the *Bondi* regime (headwind-dominated) and the *Hill* regime (shear-dominated; Lambrechts & Johansen 2012). They differ in the size of the gravitational deflection radius which is either the Bondi radius

$$R_{\text{B}} = \frac{GM_{\text{p}}}{v_{\text{rel}}^2}, \quad (1.67)$$

or the Hill radius

$$R_{\text{H}} = \left(\frac{GM_{\text{p}}}{3\Omega_{\text{K}}^2} \right)^{1/3}, \quad (1.68)$$

whichever is smaller.

The accretion cross-section is then determined by the relative velocity of the incoming pebble

$$v_{\text{rel}} = v_{\text{hw}} + v_{\text{shear}} \simeq \eta v_{\text{K}} + \frac{3}{2}\Omega_{\text{K}}b, \quad (1.69)$$

which consists of two components related to the local headwind and Keplerian shear. If the gravitational deflection radius is R_{B} , the pebbles which can possibly become accreted are those with relatively small impact parameters ($b \leq R_{\text{B}} < R_{\text{H}}$). For these small orbital separations, the shear component of the relative velocity is negligible and v_{rel} is set by the local disk headwind v_{hw} . Equating $t_{\text{enc}} \simeq 2b/v_{\text{hw}}$ to t_{set} leads to

$$b \simeq \sqrt{\frac{2GM_{\text{p}}t_{\text{s}}}{v_{\text{hw}}}} \simeq R_{\text{B}} \sqrt{\frac{\tau}{t_{\text{B}}\Omega_{\text{K}}}} \equiv R_{\text{eff,Bondi}}, \quad (1.70)$$

where τ is the Stokes number and we defined the crossing time of the Bondi radius $t_{\text{B}} = R_{\text{B}}/v_{\text{hw}}$.

If the deflection radius is R_{H} , v_{rel} is dominated by its shear component v_{shear} . The encounter timescale can now be estimated as the dynamical orbital timescale $t_{\text{enc}} = \Omega_{\text{K}}^{-1}$ and equating it again to t_{set} implies

$$b \simeq \left(\frac{GM_{\text{p}}t_{\text{s}}}{\Omega_{\text{K}}} \right)^{1/3} \simeq \tau^{1/3} R_{\text{H}} \equiv R_{\text{eff,Hill}}. \quad (1.71)$$

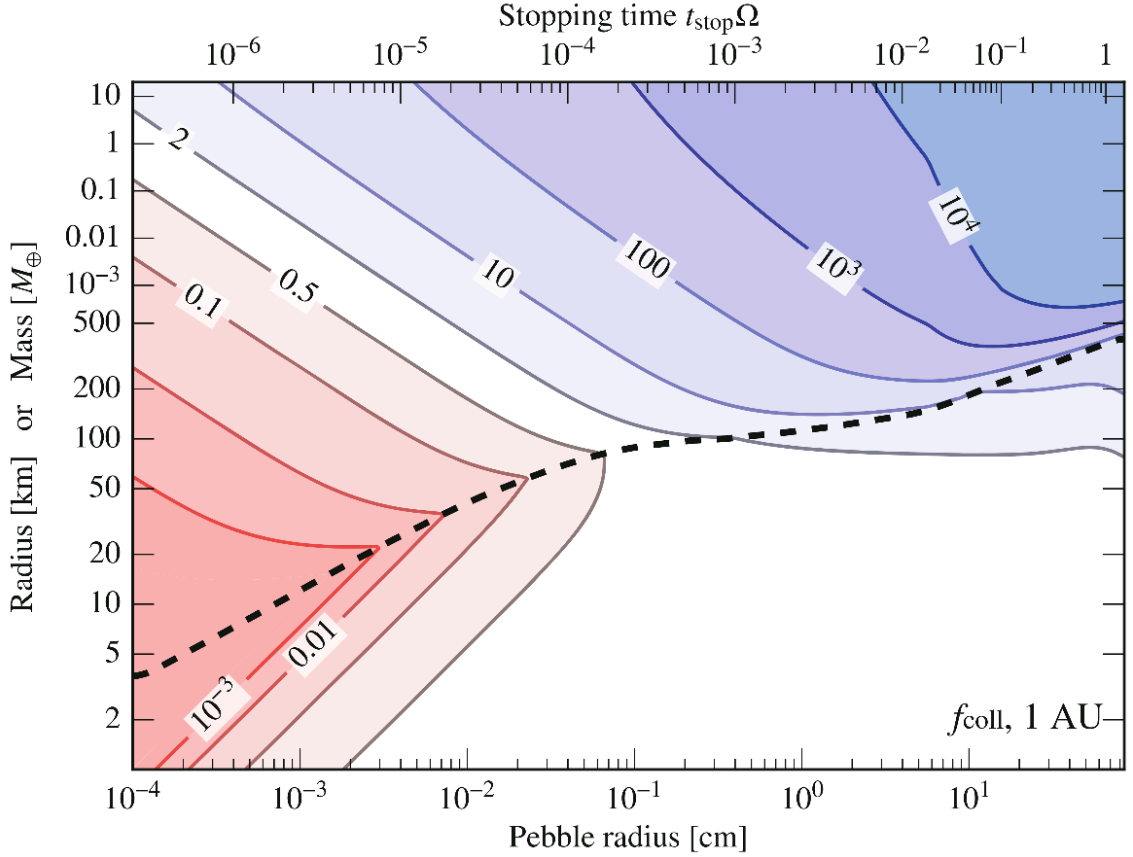


Figure 1.10: Map of the collision factor (given by coloured isocontours and isolevels), i.e. the ratio of the pebble accretion cross-section to the geometric cross-section. The pebble properties (radius and Stokes number) are given by the horizontal axes, the size or mass of the accreting body is displayed on the vertical axis. The dashed line delimits the gravitational focusing (lower half) from the Bondi and Hill regimes (upper half). Adapted from Ormel (2017).

The obtained cross-sections of pebble accretion imply that in the most favourable case, all pebbles which enter the Hill sphere radius of the growing body become accreted. This demonstrates why pebble accretion can be so efficient compared to planetesimal accretion: the Hill sphere radius is much larger than both the geometrical and gravitationally-focused cross-sections. Fig. 1.10 demonstrates the increase of the accretion radius for a wide range of masses and pebble properties. Fig. 1.11 shows trajectories of pebbles which are being accreted in the Hill regime.

The accretion rate further depends on the level of sedimentation of pebbles towards the midplane. If their characteristic scale height $H_{\text{peb}} = H\sqrt{\alpha/\tau}$ (Youdin & Lithwick 2007) is smaller than R_{eff} , they are being accreted in a 2D regime from a thin layer (e.g. Morbidelli et al. 2015; Johansen & Lambrechts 2017)

$$\dot{M}_{\text{peb},2\text{D}} = 2R_{\text{eff}}v_{\text{rel}}\Sigma_{\text{peb}}. \quad (1.72)$$

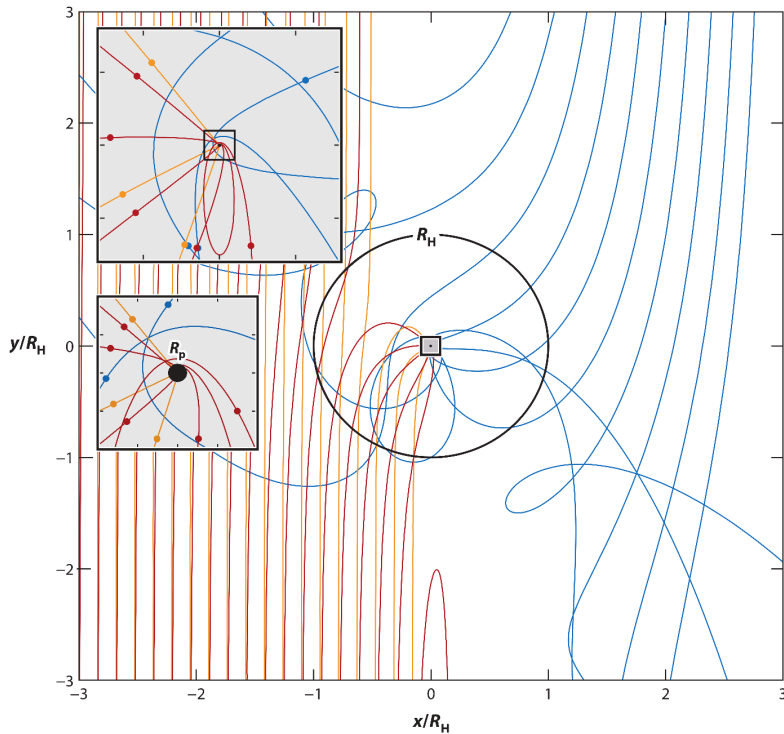


Figure 1.11: Trajectories of pebbles accreted in the Hill regime. The black circle shows the Hill sphere radius R_H of the accreting body. Three types of pebbles are shown: loosely coupled ($\tau \gg 1$) incoming from $x > 0$, $y > 0$ (blue curves); optimally coupled ($\tau = 1$) arriving from $x < 0$, $y < 0$ (red curves); strongly coupled ($\tau = 0.1$) arriving from $x < 0$, $y < 0$ (orange curves). We see that loosely coupled pebbles are mostly scattered, but optimally and strongly coupled pebbles are accreted from a substantial fraction of the Hill sphere. Adapted from Johansen & Lambrechts (2017).

If, on the other hand, the pebbles become strongly vertically stirred, their accretion rate becomes

$$\dot{M}_{\text{peb},3\text{D}} = \pi R_{\text{eff}}^2 v_{\text{rel}} \rho_{\text{peb}}. \quad (1.73)$$

Next, it is important to discuss whether pebble accretion suffers from a reservoir depletion or not. It turns out that if there is an ongoing coagulation in the disk which converts the dust grains into pebbles, the radial drift of pebbles produces a pebble flux through the disk. According to Lambrechts & Johansen (2014), the peak mass flux in pebbles can be of the order of $\sim 10^{-4} M_{\oplus} \text{yr}^{-1}$. However, only some of the pebbles from this flux can be accreted because their drift is sometimes so fast that they do not have an opportunity to encounter the accreting body during the orbital crossing (Morbidelli & Nesvorný 2012; Ormel & Kobayashi 2012; Guillot et al. 2014). The fraction of captured pebbles is referred to as the *filtering factor* and it can be estimated as (Lambrechts & Johansen 2014)

$$f_{\text{filt}} \simeq 0.034 \left(\frac{\tau}{0.1} \right)^{-1/3} \left(\frac{M_p}{M_{\oplus}} \right)^{2/3} \left(\frac{r}{10 \text{ au}} \right)^{-1/2}. \quad (1.74)$$

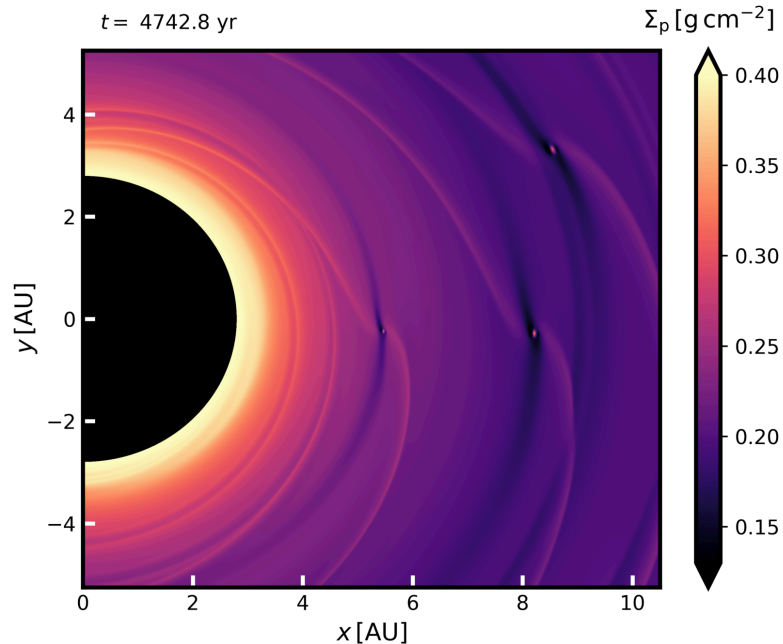


Figure 1.12: Surface density of pebbles in a disk region containing three accreting super-Earths. With the exception of shallow gaps created by pebble accretion, the radial flux of pebbles ($2 \times 10^{-4} M_{\oplus} \text{yr}^{-1}$) maintains a relatively smooth profile of the pebble disk and brings new material towards protoplanets. From Paper I.

This implies that the growth of a system of multiple protoplanets by pebble accretion can be non-trivial if, for example, the outer protoplanets start to drain the pebble flux too efficiently. Additionally, if the eccentricities and inclinations of protoplanets become excited, the relative velocities between the pebbles and protoplanets inevitably undergo variations which can affect the accretion efficiency (e.g. Johansen & Lambrechts 2017; Liu & Ormel 2018; Lambrechts et al. 2019). Despite these complexities, it is much easier to refill the surroundings of accreting bodies with a new building material in the framework of pebble accretion compared to planetesimal accretion. This is shown in Fig. 1.12 where three accreting super-Earths create shallow gaps in the surface density of pebbles, but the radial flux of pebbles maintains the mean surface density in a steady state.

Knowing that the efficiency of pebble accretion can be substantial, it is natural to ask what limits the final masses of planets that can be assembled this way. It turns out that the growth of planets by pebble accretion is self-limiting. When the planetary mass reaches a certain critical value, slightly exceeding the mass of a giant planet core, it starts to perturb the surrounding gas disk in a way that a pressure bump is formed outside its orbit. Within the pressure bump, the gas disk rotates at a super-Keplerian velocity and it therefore blocks the radial flux of pebbles which pile up there. When it happens, the planet is said to reach the *pebble isolation mass*,

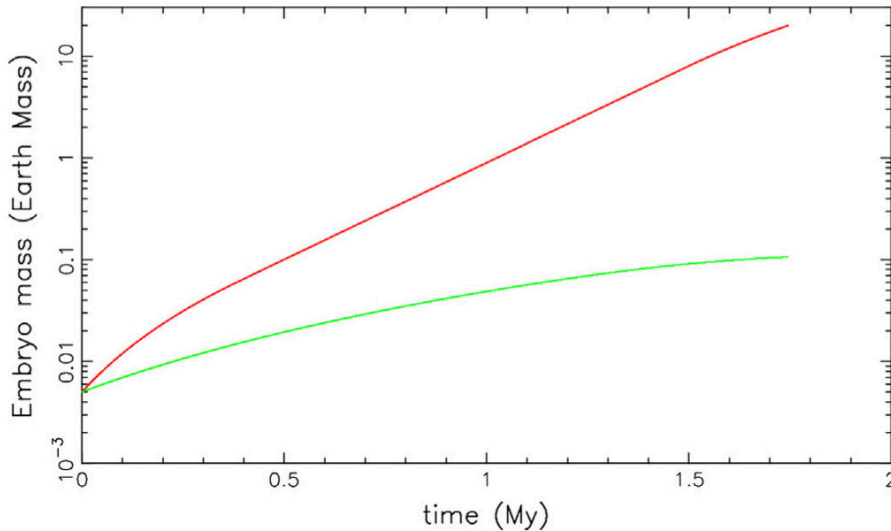


Figure 1.13: Growth of two planetary embryos located inside (green) and outside (red) the water-ice line, according to the model of Morbidelli et al. (2015). Near the outer embryo, there is a radial flux of icy pebbles ($\tau \simeq 0.03$) with $2 \times 10^{-4} M_{\oplus} \text{ yr}^{-1}$. Near the inner embryo, the mass flux and Stokes numbers are reduced. Consequently, the growth of the outer embryo is faster. The outer embryo reaches the pebble isolation mass $\simeq 20 M_{\oplus}$ at $\simeq 1.75 \text{ Myr}$. Adapted from Morbidelli et al. (2015).

which is approximately (Lambrechts et al. 2014)

$$M_{\text{iso}} \approx 20 \left(\frac{a}{5 \text{ au}} \right)^{3/4} M_{\oplus}. \quad (1.75)$$

The formula was further improved by 3D simulations of Bitsch et al. (2018) and Picogna et al. (2018).

Pebble accretion was successfully applied to explain the short growth timescale of giant planet cores (Lambrechts & Johansen 2014), the assembly of the outer solar-system planets (Levison et al. 2015) as well as of the pre-terrestrial embryos (Levison et al. 2015; Morbidelli et al. 2015). It naturally reproduces the dichotomy between the embryos born in the inner and outer Solar System if one takes into account that the water-ice snowline decreases the flux of pebbles by a factor of ~ 2 and the size of pebbles by a factor of ~ 10 (Morbidelli et al. 2015). Pebble accretion rates are then much larger in the outer Solar System and produce more massive objects, as shown in Fig. 1.13. Additionally, pebble accretion became a key component of many models oriented on explanation of exoplanetary systems (e.g. Chambers 2016; Matsumura et al. 2017; Bitsch et al. 2019; Ida et al. 2019; Schoonenberg et al. 2019).

1.3 Types of planetary migration

So far, we have discussed how to create planets in terms of mass accumulation. But the properties of newborn planets are determined by more than just their ability

to grow. Their orbital evolution is equally important because it determines the configuration and stability of the entire planetary system.

A process during which the semimajor axis of a planetary orbit changes in time is called *planetary migration*. Since several such processes seem to be plausible, the theoretical consensus is that planets are almost never born at the location of their present-day orbits. However, there is much less agreement on which types of migration are the most important and how exactly they relate to one another. This is simply because we only see the result of migration, not the initial conditions. Let us briefly summarise the main migration mechanisms:

- *Migration in a gas disk* is driven by gravitational interactions between the disk and the planet. More specifically, it is the angular momentum exchange which drives the evolution of the planetary semimajor axis. Depending on the planet mass, several regimes can be recognised.
 - *Type I* migration occurs for low-mass planets which do not change the structure of the disk on a global scale (they are incapable of gap opening; see Crida et al. 2006). It is typically dominant for sub-Saturn masses. It can be both inward or outward, depending on conditions within the disk and also on an interplay of viscous and radiative processes.
 - *Type II* migration replaces Type I migration if (i) the Hill sphere of the planet becomes comparable to the disk thickness, and (ii) the tidal torques exerted by the planet onto the disk operate on a timescale which is shorter than the viscous evolution timescale. The planet then opens a gap in the gas disk along its orbit. Type II migration tends to be directed inward (but see e.g. Hallam & Paardekooper 2018).
 - *Type III* refers to a mechanism which can lead to a runaway migration. Under specific conditions, the migrating planet can trap a part of the disk material within its horseshoe region and generate a coorbital mass deficit. Type III migration usually occurs for Saturn-mass planets capable of partial gap opening. It is directed inwards (under normal disk conditions) and it can halve the semimajor axis within several tens of orbits.

Migration in gas disks serves as a possible explanation for the origin of several classes of extrasolar planets, e.g. hot Jupiters (Lin et al. 1996) or close-in super-Earths (Cossou et al. 2014; Coleman & Nelson 2016). It might have also occurred for solar-system giant planets (Walsh et al. 2011).

- *Planet-planet interactions* in the protoplanetary disk can lead to locking of migrating planets in mutual mean-motion resonances. The migration of such a resonant convoy then becomes modified because of the resonant eccentricity pumping (e.g. Cossou et al. 2013; Pierens et al. 2013). Also after the disk dispersal, planet-planet interactions can lead to mutual scattering during close encounters (e.g. Lega et al. 2013). This process can abruptly modify the semimajor axes of the involved planets and also their eccentricities or inclinations.

It is possible that the eccentric giant exoplanets are the remnants of such encounters (Rasio & Ford 1996; Weidenschilling & Marzari 1996; Lin & Ida 1997).

- *Migration in a pebble disk* may arise due to strong azimuthal asymmetries within a flow of pebbles scattered by a planet (Benítez-Llambay & Pessah 2018). However, the importance of this migration regime strongly depends on the, a priori unknown, pebble-to-gas mass ratio.
- *Migration in a planetesimal disk* can operate after the dispersal of the gas disk. If a significant number of leftover planetesimals, which failed to accumulate into larger objects, remain in the system, their gravitational interactions with planets might cause a migration. There seems to be a convincing evidence in the orbital structure and collisional history of the Solar System that giant planets underwent the migration driven by a disk of trans-Neptunian planetesimals (e.g. Malhotra 1993; Tsiganis et al. 2005; Levison et al. 2007; Nesvorný & Morbidelli 2012).

This thesis is focused on early migration of low-mass protoplanets which are still embedded in a substantially massive gas disk. Such a setup promotes the importance of Type I migration and also planet-planet interactions (provided that the planetary system becomes closely packed). Since the outcome of Type I migration is determined by a complicated interplay of several hydrodynamic phenomena, we discuss them in detail in the following Sect. 1.4 to provide a background for our results presented in Chapter 2.

1.4 Type I migration

Torque and migration rate

A planet is said to be migrating when its orbital semimajor axis evolves as a consequence of gravitational interaction with a protoplanetary disk (e.g. Masset 2008; Lubow & Ida 2010; Kley & Nelson 2012; Baruteau & Masset 2013; Baruteau et al. 2014). This is not surprising; after all, the disk masses are of the order of $\sim 10^{-2} M_{\odot}$ and their gravitational influence on the embedded protoplanets is considerable.

The key quantity determining the outcome of migration is the *torque* Γ of the gravitational forces exerted by the disk on the protoplanet. To show that, let us consider that the protoplanet is formed on a circular orbit (a reasonable assumption since the planet-forming disk undergoes, on average, circular rotation). Its orbital angular momentum is

$$L = M_p a_p^2 \Omega_p = M_p \sqrt{GM_{\star} a_p}, \quad (1.76)$$

where a_p denotes the semimajor axis, M_p is the planet mass, and Ω_p is the Keplerian frequency of the planet. A temporal change of L implies a reconfiguration of the

semimajor axis. The change of the angular momentum can only be caused by a disturbing force with a non-zero torque

$$\frac{dL}{dt} = \Gamma. \quad (1.77)$$

When the gravitational pull of the disk acts on the planet with $\Gamma \neq 0$, the corresponding rate of change of the semimajor axis, referred to as the *migration rate*, is

$$\frac{da_p}{dt} = \frac{2\Gamma}{M_p a_p \Omega_p} \stackrel{\text{circ.}}{=} \frac{2\mathcal{T}}{\Omega_p}. \quad (1.78)$$

where the equality on the right-hand side corresponds to the Gauss perturbation equation and \mathcal{T} is the transversal acceleration (parallel or antiparallel with the orbital velocity). From Eq. 1.78, we see that a negative torque leads to shrinking of a_p , which is called the *inward migration*, and a positive torque leads to the opposite *outward migration* for which a_p grows.

The migration timescale τ_{mig} is defined as a time interval Δt after which $\Delta a_p = -a_p$, leading to

$$\tau_{\text{mig}} = -\frac{L}{2\Gamma}. \quad (1.79)$$

The negative sign is chosen so that $\Gamma < 0$ leads to $\tau_{\text{mig}} > 0$, implying a finite migration timescale (Papaloizou & Larwood 2000).

The torque (in a 2D disk) can be generally computed as (e.g. Kley & Nelson 2012)

$$\Gamma = \int_{\text{disk}} \Sigma (\vec{r}_p \times \vec{a}_g) dS = \int_{\text{disk}} \Sigma (\vec{r}_p \times \nabla \Phi_p) dS = \int_{\text{disk}} \Sigma \frac{\partial \Phi_p}{\partial \theta} dS, \quad (1.80)$$

where \vec{r}_p is the planet's position vector, \vec{a}_g is the specific gravitational acceleration arising from a disk element and Φ_p is the planet's potential. In a homogeneous disk with only radially varying $\Sigma = \Sigma(r)$, Γ would vanish because the contribution of each two gas parcels at $\theta_p + \Delta\theta$ and $\theta_p - \Delta\theta$ would cancel out. Clearly, for a disk to exert a non-zero torque, there has to exist some *azimuthal asymmetry* in the gas density distribution with respect to the planet.

In (1.80), the contribution of different gas parcels to the total torque is additive. One can thus determine the total torque (and thus the planet's migration rate) by identifying all processes capable of perturbing the azimuthal symmetry of the disk and then combining their independent torque contributions to a simple sum. The rich environment of protoplanetary disks can sustain several asymmetries that can possibly contribute to Type I migration. We summarise them below before diving into details.

Contributing effects

RESONANT TORQUES. First and foremost, the basic interaction of a rotating gas disk with an embedded planet is the angular momentum exchange at the or-

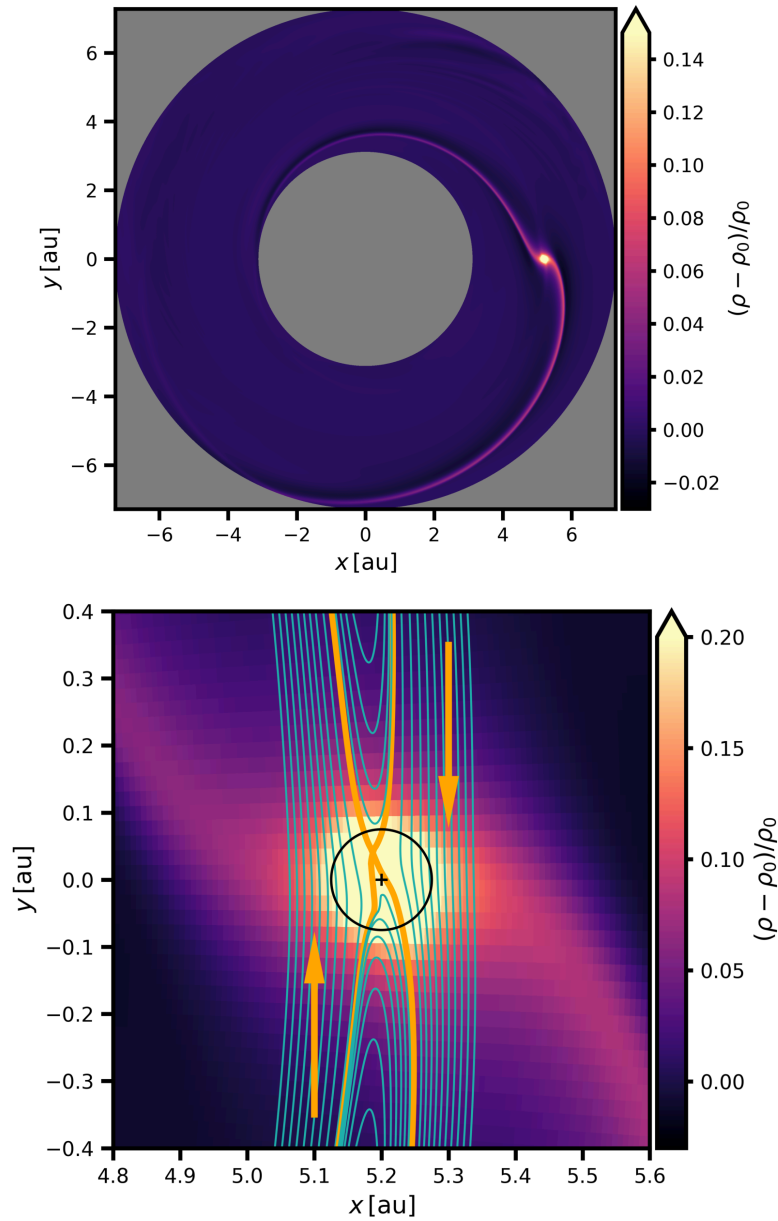


Figure 1.14: Basic features of planet-disk interactions. The colour scale shows the perturbed gas density in the midplane of a 3D RHD simulation. The planet $M_p = 3 M_\oplus$ is positioned at $x = 5.2$ au, $y = 0$ au. *Top:* View of the entire modelled disk annulus. Spiral arms propagating through the disk are apparent. *Bottom:* Close-up of the planetary surroundings. The black circle corresponds to the Hill sphere. By calculating the gas streamlines (green curves), it is possible to identify the horseshoe (corotation) region of the planet. It is delimited from the inner and outer circulating streamlines by the separatrixes (orange curves). The orange arrows indicate the flow direction relative to the planet (in an inertial frame, the planet would orbit counter-clockwise). Simulation taken from Paper IV.

bital resonances. It is *always* present as a natural consequence of the planet-disk gravitational coupling.

Similarly to the motion of a test particle in the 3-body (star-planet-particle) problem, the trajectory of a gas parcel is dominated by the primary mass. The gravity of the secondary represents a perturbation which is only important at small separations (roughly within the planet’s Hill sphere) or at resonant locations that can exist even at larger separations. As first realised by Goldreich & Tremaine (1979), the major angular momentum exchange occurs at the Lindblad and the corotation resonances (see Fig. 1.14), producing two basic components of the Type I torque (e.g. Baruteau & Masset 2013):

- *Differential Lindblad torque* arises when a gas parcel on a circulating trajectory (with respect to the planet) crosses the Lindblad resonance (usually at a supersonic velocity), becomes deflected, and exchanges its angular momentum and orbital energy with the planet during the interaction.
- *Corotation torque* is exerted by low-velocity gas on librating trajectories near the corotation with the planet. The gas responsible for the corotation torque usually moves along U-turn streamlines and occupies the horseshoe region of the planet.

The corotation can be characterised by the condition

$$[\Omega(r) - \Omega_p] = 0, \quad (1.81)$$

where $\Omega(r)$ is the angular frequency of gas at the radius r . The Lindblad resonant condition reads

$$m[\Omega(r) - \Omega_p] = \pm\kappa(r), \quad (1.82)$$

with m being a positive integer and κ denoting the epicyclic frequency of oscillations of linearly perturbed circular orbits. Taking $\kappa \simeq \Omega_K$ as an estimate (which would be exact only in a disk with the Keplerian rotation curve), Eq. (1.82) gives the radial location of the Lindblad resonances

$$r_L = \left(1 \pm \frac{1}{m}\right)^{\frac{2}{3}} a_p, \quad (1.83)$$

suggesting $r_L \rightarrow a_p$ for $m \rightarrow \infty$. Such an overlap of high-order resonant modes with the planet location is, however, unrealistic as we will show later.

THERMAL TORQUES. Thermal torques arise when the planet changes the heating/cooling balance of the gas in its vicinity.

- *The cold-finger effect* appears as a result of compressional heating and subsequent radiative cooling of gas which performs U-turns deep within the planetary Hill sphere (Lega et al. 2014). It results in an azimuthally asymmetric cold and overdense perturbation.
- *The heating torque* is facilitated by accretion heating of the planet which is radiatively transferred to the surrounding gas (Benítez-Llambay et al. 2015). The arising perturbation is hot and underdense.

REMAINING TORQUE CONTRIBUTIONS. The azimuthal asymmetry of the gas distribution can be further affected by the presence of magnetic fields or self-gravity, both of which modify the propagation of density waves. Additionally, turbulent disks that contain numerous vortices may exert stochastic forces on migrating planets.

1.4.1 Lindblad torque

At the Lindblad resonances, the Doppler-shifted frequency of the planetary gravitational forcing matches the natural oscillation frequency κ of the disk (Ward 1997). The generated sound waves constructively interfere and form a single spiral density wave (also called the wake) stretching outwards/inwards from the planetary orbit and trailing/leading the orbital motion of the planet. The gravitational planet-wake attraction (or alternatively the angular momentum exchange between the planet and the spirals) forces the planet to migrate.

To quantify the Lindblad torque, several approaches were applied in the past. First, it is possible to capture the basic dependencies of the Lindblad torque using the impulse approximation (e.g. Lin & Papaloizou 1979; Lubow & Ida 2010). Second, since low-mass planets are assumed to induce small perturbations in the disk, one can analyse the fluid equations in the framework of the linear perturbation theory (e.g. Goldreich & Tremaine 1979, 1980; Ward 1986; Meyer-Vernet & Sicardy 1987; Artymowicz 1993; Ward 1997). Third, the linearised equations can be investigated numerically (e.g. Korycansky & Pollack 1993; Tanaka et al. 2002; Paardekooper & Papaloizou 2008; Paardekooper et al. 2010). In the following, we summarise several important results obtained with the latter two approaches.

Analytic perturbation theory

The approach of the linear perturbation theory (Goldreich & Tremaine 1979) is to linearise the fluid equations by decomposing the fluid quantities as $q \rightarrow q_0 + q_1$. Here q_0 is the trivial solution of the unperturbed state of the system and q_1 is a small perturbation, such that the terms which are non-linear in q_1 (usually including its derivatives) can be neglected. The perturbation variables are then decomposed into Fourier m -harmonics. For example, the perturbing potential of the protoplanet on a circular orbit is azimuthally periodic and can be written without a loss of generality as (Meyer-Vernet & Sicardy 1987)

$$\Phi_p = \sum_m \Phi_m(r) \exp [im (\Omega - \Omega_p) t] , \quad (1.84)$$

where the amplitude for $m > 1$ is (Ward 1986)

$$\Phi_m = -\frac{GM_p}{a_p} b_{1/2}^{(m)}(r/a_p) , \quad (1.85)$$

and $b_{1/2}^{(m)}(x)$ denotes the respective Laplace coefficient with the argument x (Brouwer & Clemence 1961; Hagihara 1972; Ward 1989, 1997).

The linearisation and Fourier expansion allow to derive the expression for the torque Γ_m induced by an individual m -th order Lindblad resonance. The net differential Lindblad torque is then given by the sum of the discrete contributions. The derivation can be found e.g. in Goldreich & Tremaine (1979) or Meyer-Vernet & Sicardy (1987) with several improvements introduced in the follow-up works (Ward 1986; Artymowicz 1993; Ward 1997) which account for the influence of the structural gradients or the pressure, and also relax the use of the WKB approximation. One obtains

$$\Gamma_m = -\frac{\pi^2 m \Sigma}{r \frac{dD_\star}{dr}} \Psi_m^2, \quad (1.86)$$

with the forcing function

$$\Psi_m = \left(r \frac{d\Phi_m}{dr} + 2mf\Phi_m \right) (1 + 4\xi^2)^{-1/2}, \quad (1.87)$$

where $f = m(\Omega - \Omega_p)/\Omega$, $\xi = mc_s/(r\kappa)$ and

$$D_\star = \kappa^2 - m^2(\Omega - \Omega_p)^2 + \xi^2\kappa^2. \quad (1.88)$$

The first two terms in Eq. (1.88) measure the difference between the local natural oscillation frequency (κ) and the frequency of the m -th potential component as seen by a gas parcel ($m(\Omega - \Omega_p)$; Ward 1997; Kley & Nelson 2012).

The resonant condition can be characterised by $D_\star = 0$, leading to

$$m(\Omega - \Omega_p) = \pm\kappa\sqrt{1 + \xi^2} \simeq \Omega\sqrt{1 + \frac{m^2 H^2}{r^2}}, \quad (1.89)$$

where we used $\kappa \simeq \Omega$ and $H = c_s/\Omega$. Note that for $m \rightarrow \infty$, the Lindblad resonances are offset⁷ with respect to (1.83) and pile up at

$$r_L = r_p \pm \frac{2H}{3}. \quad (1.90)$$

This is an important result demonstrating that the waves with high-order wave-numbers are launched at a finite separation from the planet which is related to the local pressure scale height H . The effect is known as the *Lindblad torque cut-off* (Artymowicz 1993,) and appears at the distance from the planet where the relative velocity of the flow changes from subsonic to supersonic (because the planet is unable to excite sound waves in a subsonic flow; see Goodman & Rafikov 2001).

Finally, the gradient of the frequency difference at the resonant locations reads (see Ward 1997, Appendix A)

$$r \frac{dD_\star}{dr} \simeq -3\text{sgn}(\Omega - \Omega_p)m\Omega\Omega_p\sqrt{1 + \xi^2}, \quad (1.91)$$

⁷The offset can be further affected by the slope of the radial density and temperature profile, as also demonstrated by Ward (1997) (in Appendix A).

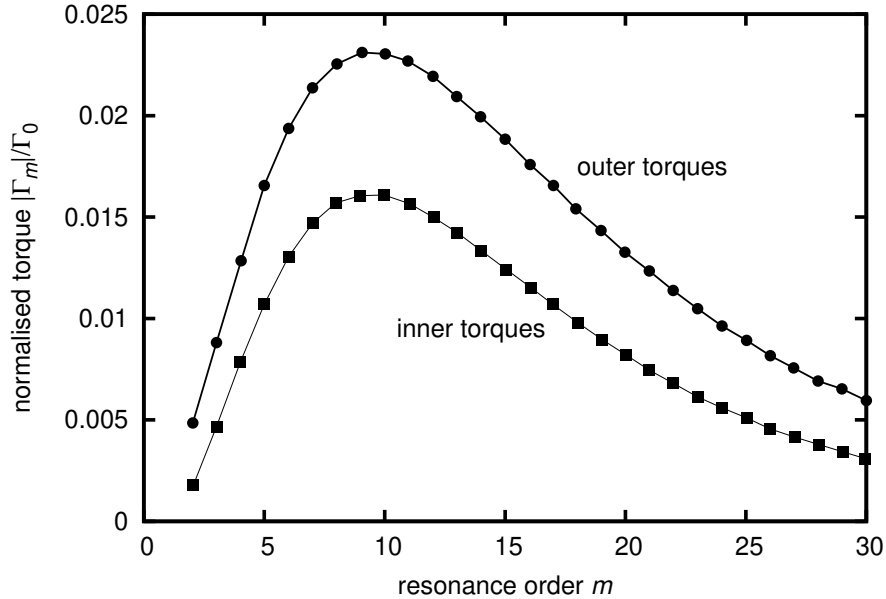


Figure 1.15: Absolute value of the Lindblad torque normalised to Γ_0 (Eq. 1.94) at the inner (squares) and outer (circles) resonances of the order m . The torque is evaluated in a disk with the surface density slope $\alpha = 1.5$ (assuming $\Sigma \propto r^{-\alpha}$) and the temperature slope $\beta = 1$ (assuming $T \propto r^{-\beta}$). It is apparent that the outer resonances, where $\Gamma_m < 0$, exert stronger torques than the inner ones, where $\Gamma_m > 0$. The total Lindblad torque is therefore negative and leads to inward migration. Data adopted from Ward (1997).

where we assumed a constant aspect ratio $h = H/r$ for simplicity and again set $\kappa \simeq \Omega$. The expression for the m -th Lindblad torque is then (e.g. Ward 1997; Kley & Nelson 2012)

$$\Gamma_m = \text{sgn}(\Omega - \Omega_p) \frac{\pi^2 \Sigma}{3\Omega\Omega_p} \left[r \frac{d\Phi_m}{dr} + \frac{2m^2(\Omega - \Omega_p)}{\Omega} \Phi_m \right]^2 (1 + 4\xi^2)^{-1} (1 + \xi^2)^{-1/2}. \quad (1.92)$$

Knowing the functional form of the discrete Lindblad torque, we can now estimate the properties of the net Lindblad torque, $\Gamma_L = \sum \Gamma_m$. Some of these properties can also be inferred from Fig. 1.15 which compares the values of Γ_m for inner and outer Lindblad resonances:

- For $r < a_p$, $\Omega(r) > \Omega_p$ which leads to $\Gamma_m > 0$ and the inner Lindblad resonances thus exert a positive torque on the planet. This corresponds to the fact that the inner spiral arm leads the orbital motion of the planet which therefore feels an acceleration in the direction of its instantaneous orbital velocity. The inner spiral arm thus forces the planet to migrate outwards.
- The situation is the opposite for the outer Lindblad resonances. For $r > a_p$, the outer trailing spiral arm causes $\Gamma_m < 0$ which results in inward migration.
- The torque exerted by the *outer spiral arm dominates* because the gradient

of the frequency separation $rdD_\star/dr \propto \kappa \simeq \Omega$ (see Eq. 1.91) and therefore becomes smaller for outer resonances. Since it appears in the denominator of Eq. (1.92), it tends to boost the torque at outer resonances. Moreover, outer resonances are located closer to the planet than their inner counterparts, at a separation where the forcing function (1.87) attains a larger value.

- The dominance of the outer spiral arm cannot be avoided by assuming a strong radial decline of the disk surface density, even though $\Gamma_m \propto \Sigma$. Steeper density gradient would indeed enhance the amount of gas near the inner resonances but at the same time, it would increase the inward-directed pressure gradient and the disk rotation would become more sub-Keplerian. As a result, the inner Lindblad resonances would recede from the planet while the outer ones would move closer to it. These two opposing effects often tend to cancel out and the differential Lindblad torque consequently exhibits a very weak dependence on the disk density gradient. This behaviour is known as the *pressure buffer* (Ward 1986; Korycansky & Pollack 1993).
- A strong radial decline of the temperature enhances the pressure gradient and shifts the resonances as in the previous case. However, a steeper temperature gradient does not provide any extra material near the inner resonances and thus the shift of the resonances prevails and makes the torque more negative.

All these properties imply that the Lindblad torque on its own causes *inward* migration of protoplanets which cannot be reverted by suitably steep (or flat) density or temperature profiles (assuming that these profiles can be approximated by smooth outward-decreasing power laws, which does not have to be always true e.g. at the opacity transitions).

The differential Lindblad torque obtained by the summation over all orders of the resonance exhibits a scaling (e.g. Ward 1986)

$$\Gamma_L \propto \Gamma_0, \quad (1.93)$$

where

$$\Gamma_0 = \left[\left(\frac{q}{h} \right)^2 \Sigma r^4 \Omega^2 \right]_p, \quad (1.94)$$

and it therefore scales with the square of the planet mass (hidden in the planet-to-star mass ratio $q = M_p/M_\star$), with the inverse square of the aspect ratio h and linearly with the disk mass (related to Σ). The migration due to the Lindblad torque therefore becomes rapid for massive planets, or in thin disks where the gas is strongly concentrated to the midplane, or alternatively in massive disks. Interestingly, there is no dependence on the disk viscosity ν .

Numerical perturbation theory

The dependence of the Lindblad torque indicated by (1.93) motivated several works to compute the constant of proportionality and its relation to disk properties more

precisely. Important studies in this regard were done by Tanaka et al. (2002) and Paardekooper et al. (2010). The former employed a semi-analytic perturbation theory in a 3D isothermal disk while the latter numerically solved linearised fluid equations in a 2D disk with arbitrary temperature and density profiles. Despite the 2D limitation and the unavoidable potential smoothing, we focus on the key results of Paardekooper et al. (2010) to demonstrate that the dependence of Γ_L on the temperature gradient is stronger than on the density gradient.

Following Paardekooper & Papaloizou (2008), the 2D Navier-Stokes equation can be converted into a pair of first-order ordinary differential equations. The necessary approximations include:

- The inviscid limit, $\nu \rightarrow 0$, which neglects all viscous terms. This approximation conveniently utilises the fact that the Lindblad torque is decoupled from the disk viscosity.
- The adiabatic limit

$$\frac{DS}{Dt} = 0, \quad (1.95)$$

where $S = c_V \log(P/\rho^\gamma)$ is the specific entropy. In the framework of Paardekooper & Mellema (2008), the adiabatic limit corresponds to a system with zero thermal diffusivity.

- The linear perturbation theory and the Fourier decomposition.

The resulting differential equations can be written as

$$\frac{dQ}{dr} = C_1 v_r + C_2 Q + S_1, \quad (1.96)$$

$$\frac{dU}{dr} = D_1 Q + D_2 v_r + S_2, \quad (1.97)$$

where $Q = P'/P^{1/\gamma}$ (with P' being the perturbed pressure), $U = rP^{1/\gamma}v_r$, and the functional form of the remaining coefficients can be found in Paardekooper & Papaloizou (2008).

Paardekooper et al. (2010) numerically solved these linear equations while exploring the parametric space of surface density profiles $\Sigma \propto r^{-\alpha}$ and temperature profiles $T \propto r^{-\beta}$ and derived

$$\gamma_{\text{eff}} \frac{\Gamma_L}{\Gamma_0} = (-2.5 - 1.7\beta + 0.1\alpha) \left(\frac{0.4}{b_{\text{sm}}/h} \right)^{0.71}, \quad (1.98)$$

where b_{sm} is a dimensionless scaling of the potential smoothing length, $r_{\text{sm}} = b_{\text{sm}} h r_p$. The effective adiabatic index γ_{eff} was introduced later by Paardekooper et al. (2011) to account not only for the adiabatic limit (for which the right-hand side of Eq. (1.98) was originally derived), but also to connect the formula to the isothermal limit and to intermediate regimes. When the thermal diffusivity vanishes, $\gamma_{\text{eff}} \rightarrow \gamma$ and the acoustic waves propagate at the adiabatic sound speed. When the thermal diffusivity becomes infinite, $\gamma_{\text{eff}} \rightarrow 1$ and the phase speed of the waves starts to match the isothermal sound speed. In radiative disks, regimes with non-zero finite thermal diffusivity are recovered using γ_{eff} (see Paardekooper et al. 2011).

Migration rate

An interesting point about the Lindblad torque can now be demonstrated by plugging Eq. (1.98) into (1.79) and evaluating the migration timescale. Setting $\alpha = 3/2$, $\beta = 1$, $r_{\text{sm}} = 0.4H$, $\gamma_{\text{eff}} = 1.4$, $M_{\text{p}} = 1 M_{\oplus}$, $M_{\star} = 1 M_{\odot}$, $h = H/r = 0.05$, $\Sigma = 1700 \text{ g cm}^{-2}$, and $a_{\text{p}} = 1 \text{ au}$ leads to the migration timescale of only $\tau_{\text{mig}} \simeq 0.25 \text{ Myr}$. The choice of the parameters corresponds to the MMSN (Weidenschilling 1977; Hayashi 1981) and the result indicates that if Earth-mass planets migrated solely under the influence of the Lindblad torque, they would be destroyed by falling onto the central star well before the dissipation of the protoplanetary disk. Such a rapid and overly efficient inward migration was discussed already by in Goldreich & Tremaine (1980) (see also Korycansky & Pollack 1993; Ward 1997; Tanaka et al. 2002).

For the giant-planet formation zone ($a_{\text{p}} \simeq 5 \text{ au}$), one may argue that once the protoplanets acquire significant masses due to gas accretion, their migration slows down because it switches to the Type II mode, potentially saving them from the inward drift. However, it turns out that the respective Lindblad migration timescale is even shorter than the gas accretion timescale of the classical giant-planet formation model (Pollack et al. 1996). Consequently, if protoplanets migrated due to the Lindblad torque alone, there would not be enough time for envelopes of giant planets to form before the disk dissipation and gas giants would be lost as well.

To overcome this issue, several explanations have been proposed. Generally, one can either rely on other torque contributions that might be positive and stronger than Γ_{L} (see the next sections), or one can explore possible modifications of Γ_{L} due to physical processes that were ignored so far:

- The inclusion of self-gravity tends to boost Γ_{L} by a factor $(1 + 1/Q)$ (Baruteau & Masset 2008) with Q being the Toomre's parameter (Eq. 1.57). Since $Q > 1$ in gravitationally stable disks, self-gravity enhances inward migration related to the Lindblad torque and thus cannot help preventing it.
- The inclusion of magnetic fields changes the nature of fluid waves from acoustic to the magneto-sonic ones, propagating at velocities $\sqrt{c_s^2 + v_A^2}$ (Terquem 2003) where v_A is the Alfvén velocity. A new set of magnetic resonances appears, located closer to the protoplanet than the classical Lindblad resonances. Owing to the radially outward decline of the ratio $\beta_{\text{m}} = c_s^2/v_A^2$, the magnetic resonance can cause outward migration if the magnetic field is strong enough (at least $\beta_{\text{m}} \sim 100$).
- Realistic disks contain opacity transitions (e.g. near the evaporation fronts of solids) where the density and temperature profiles cannot be described by simple power laws. The Lindblad torque at these transitions exhibits more complex behaviour and can also become positive (Menou & Goodman 2004). An alternative form of Eq. (1.98) which accounts for the opacity transitions can be found in Masset (2011).

- In inviscid laminar disks, the damping of density waves is low so they can diffuse into their surroundings, reducing the negative Lindblad torque (Rafikov 2002; Li et al. 2009; Fung & Chiang 2017).

1.4.2 Corotation torque

Let us now focus on the planet-disk interaction involving the gas which on average corotates with the planet. In the following, we demonstrate that the corotation torque consists of terms which scale with the vortensity, temperature, and entropy gradients over the corotation region. More specifically, the temperature and entropy gradients lead to the vorticity production within the corotation region and therefore the total corotation torque can be inferred from the vortensity distribution at any time.

For several decades since the paper by Goldreich & Tremaine (1979), it was unclear how to properly tackle the analytic theory of the corotation torque. Generally, two approaches are possible:

- The *linear perturbation theory* which uses a similar framework as the studies of the Lindblad torque discussed above. This approach leads to the *linear corotation torque*. As it exists under the same conditions as the Lindblad torque, one might expect the linear corotation torque to always influence the planet. However, the downside is that horseshoe orbits, which apparently exist in realistic coorbital regions, do *not* exist in the linear perturbation theory (only perturbed circular trajectories are considered).
- The approach of *horseshoe drag* introduced by Ward (1991). The respective torque is also called the *non-linear corotation torque*. In this case, the analysis is based on the *assumption* of horseshoe orbits and infers the torque by studying the angular momentum exchange during U-turns. The issue with the horseshoe drag is its *saturation*—it has been observed in several studies that the respective torque can vanish in time if the disk is inviscid, $\nu \rightarrow 0$, or not diffusive, $\chi \rightarrow 0$.

Another confusing fact is that the linear corotation torque is usually weaker than the Lindblad torque (Tanaka et al. 2002), whereas the horseshoe drag can suppress the Lindblad torque and revert the inward migration to outward, provided that the disk has suitable thermal/viscous properties (Paardekooper & Mellema 2006).

Since both approaches describe the same phenomenon, a question arises which one is correct. An accepted connection (Masset & Casoli 2010; Paardekooper et al. 2011; Jiménez & Masset 2017) can be summarised as follows:

- The linear corotation torque is only important if disk conditions, typically a high ν , suppress planet-induced perturbations in the corotation region. The influence of the linear corotation torque can also be seen at the beginning of hydrodynamic simulations when the planet is first introduced into the system.

- If disk conditions allow the horseshoe drag to remain unsaturated, it becomes fully responsible for the corotation torque (Paardekooper & Papaloizou 2009). The horseshoe drag exhibits a dependence on the entropy gradient $\nabla\mathcal{S}$ which can make it positive and stronger than the Lindblad torque.
- If the horseshoe drag saturates ($\nu \rightarrow 0$, $\chi \rightarrow 0$), the corotation torque vanishes.

Linear corotation torque

The linear perturbation theory (Goldreich & Tremaine 1979), improved for 3D isothermal disks by Tanaka et al. (2002), leads to the torque components

$$\Gamma_m = \frac{\pi^2 m}{2} \left[\frac{|\Phi_m + \eta'_m|^2}{d\Omega/dr} \frac{d}{dr} \left(\frac{2\Sigma}{\omega_z} \right) \right]_{r_c}, \quad (1.99)$$

that are evaluated at the corotation radius r_c , η'_m is the m -th component of the perturbed gas enthalpy (discussed later), and ω_z is the vertical component of the vorticity $\vec{\omega} = \nabla \times \vec{v}$. In cylindrical coordinates, we can write

$$\omega_z = (\nabla \times \vec{v})_z = \frac{1}{r} \left(\frac{\partial(rv_\theta)}{\partial r} - \frac{\partial v_r}{\partial \theta} \right) = \frac{1}{r} \frac{d(r^2\Omega)}{dr} = 2B, \quad (1.100)$$

where we assumed $(v_r, v_\theta) = (0, v_K)$, and we related ω_z to the Oort constant

$$B = \frac{1}{2r} \frac{d(r^2\Omega)}{dr}, \quad (1.101)$$

which characterises the angular momentum of the disk and also relates to the epicyclic frequency as $B = \kappa^2/(4\Omega) \simeq \Omega/4 \propto r^{-3/2}$.

Defining the ratio ω_z/Σ as the vertically integrated *vortensity*, Eq. 1.99 implies that the corotation torque is proportional to the gradient of the inverse vortensity across the corotation. If the surface density can be approximated by a power law $\Sigma \propto r^{-\alpha}$, we can deduce from the radial dependence of B (or ω_z) that the gradient of inverse vortensity is proportional to $\propto r^{3/2-\alpha}$. In fact, the factor $(3/2 - \alpha)$ often appears in the formulae for the corotation torque.

A numerical approach to the linear perturbation theory (Eqs. 1.96, 1.97; Paardekooper et al. 2010) leads to the torque expression

$$\gamma_{\text{eff}} \frac{\Gamma_{c,\text{lin}}}{\Gamma_0} = 0.7 \left(\frac{3}{2} - \alpha - \frac{2\xi}{\gamma_{\text{eff}}} \right) \left(\frac{0.4}{b_{\text{sm}}/h} \right)^{1.26} + 2.2\xi \left(\frac{0.4}{b_{\text{sm}}/h} \right)^{0.71}, \quad (1.102)$$

which again exhibits a scaling with Γ_0 (Eq. 1.94), and γ_{eff} generalises the formula for transitions between isothermal and adiabatic disks (Paardekooper et al. 2011).

The quantity ξ is the negative of the power-law slope of the entropy⁸

$$\mathcal{S} = \frac{P}{\Sigma\gamma} \propto \frac{\Sigma T}{\Sigma\gamma} \propto \frac{r^{-\alpha} r^{-\beta}}{r^{-\gamma\alpha}} \propto r^{-(\beta-(\gamma-1)\alpha)}, \quad (1.103)$$

⁸Strictly speaking, \mathcal{S} is a *measure of entropy* while the true entropy is defined otherwise; see e.g. Eq. (1.95) and the adjoining discussion.

thus

$$\xi = \beta - (\gamma - 1) \alpha. \quad (1.104)$$

The case when $\xi = 0$ is called *barotropic* and the linear corotation torque is often split into the barotropic part

$$\gamma_{\text{eff}} \frac{\Gamma_{\text{c,lin,baro}}}{\Gamma_0} = 0.7 \left(\frac{3}{2} - \alpha \right) \left(\frac{0.4}{b_{\text{sm}}/h} \right)^{1.26}, \quad (1.105)$$

and the entropy-related part

$$\gamma_{\text{eff}} \frac{\Gamma_{\text{c,lin,ent}}}{\Gamma_0} = -\frac{1.4\xi}{\gamma_{\text{eff}}} \left(\frac{0.4}{b_{\text{sm}}/h} \right)^{1.26} + 2.2\xi \left(\frac{0.4}{b_{\text{sm}}/h} \right)^{0.71}. \quad (1.106)$$

Particle horseshoe drag

Let us review the concept of the horseshoe drag according to Ward (1991). Consider a planet M_p on a circular orbit r_p around the primary, embedded in a ring of test particles filling out its horseshoe region. Focusing on test particles sharing a single horseshoe orbit, let us assume that they jump from $r_{\text{in}} < r_p$ to $r_{\text{out}} > r_p$ when crossing the rear⁹ U-turn and from r_{out} to r_{in} during the front U-turn.

The jump when performing the rear (front) U-turn has to be associated with the gain (loss) of the angular momentum by individual test particles which, in order to remain conserved, is subtracted from (transferred to) the planet. An elementary gain *of a test particle* when moving from r_{in} to r_{out} is

$$\delta l = r_{\text{out}}^2 \Omega_{\text{out}} - r_{\text{in}}^2 \Omega_{\text{in}} \simeq 2rB (r_{\text{out}} - r_{\text{in}}), \quad (1.107)$$

where $2rB \simeq \Delta(r^2\Omega)/\Delta r$ results from Eq. (1.101). The loss of a particle moving from r_{out} to r_{in} is $(-\delta l)$.

Let us imagine that during a time interval δt , a multitude of test particles undergoes an exchange of angular momentum. Denoting δm_{in} and δm_{out} the total mass of particles originating before the exchange at r_{in} and r_{out} , respectively, the angular momentum change *felt by the planet* is

$$\Delta L = (\delta m_{\text{out}} - \delta m_{\text{in}}) \delta l = [(\Sigma r \delta \theta \delta r)_{\text{out}} - (\Sigma r \delta \theta \delta r)_{\text{in}}] \delta l \quad (1.108)$$

where Σ is the surface density of test particles at a given radial distance and $r \delta \theta \delta r$ represents the differential area. Our next task is to compare the inner and outer differential areas.

Regarding the azimuthal distances, a test particle travels (over δt)

$$\delta \theta = |\Omega - \Omega_p| \delta t, \quad (1.109)$$

which implies

$$\frac{(r \delta \theta)_{\text{in}}}{(r \delta \theta)_{\text{out}}} = \frac{r_{\text{in}} |\Omega_{\text{in}} - \Omega_p|}{r_{\text{out}} |\Omega_{\text{out}} - \Omega_p|}, \quad (1.110)$$

⁹By ‘rear’ we understand the region ‘behind’ the orbital motion of the planet.

To compare the radial distances, we recall the Jacobi constant of the restricted 3-body problem (RTBP) in the reference frame corotating with the planet (to avoid the temporal dependence of the perturbing potential). We can ignore the U-turn itself and simply assume that when a particle on the horseshoe orbit is far from the planet, having the radial distance r , its Jacobi constant is

$$J = \Omega_p \left(r^2 \Omega \right) - \frac{1}{2} (r \Omega)^2 - \Phi. \quad (1.111)$$

Then $(\delta r |dJ/dr|)_{\text{in}}$ has to be equal to $(\delta r |dJ/dr|)_{\text{out}}$. Since $dJ/dr = 2rB(\Omega_p - \Omega)$, it follows that

$$\frac{\delta r_{\text{in}}}{\delta r_{\text{out}}} = \frac{(rB|\Omega - \Omega_p|)_{\text{out}}}{(rB|\Omega - \Omega_p|)_{\text{in}}}. \quad (1.112)$$

Plugging Eqs. (1.110) and (1.112) into (1.108) leads to

$$\Delta L = (Br\delta\theta\delta r)_{\text{out}} \left[\left(\frac{\Sigma}{B} \right)_{\text{out}} - \left(\frac{\Sigma}{B} \right)_{\text{in}} \right] \Delta l. \quad (1.113)$$

The torque arising from a single horseshoe orbit can be acquired from Eq. (1.77) as

$$\delta\Gamma = \frac{\Delta L}{\delta t} = 16|A|B^2 (r_{\text{out}} - r_p)^3 r \delta r \frac{d}{dr} \left(\frac{\Sigma}{B} \right), \quad (1.114)$$

where we used Eq. (1.107) and $\delta\theta_{\text{out}}/\delta t = |\Omega_{\text{out}} - \Omega_p|$, along with lowest-order approximations $(\Sigma/B)_{\text{out}} - (\Sigma/B)_{\text{in}} \simeq (r_{\text{out}} - r_{\text{in}})d(\Sigma/B)/dr$, $|\Omega_{\text{out}} - \Omega_p| \simeq 2|A|(r_{\text{out}} - r_p)/r$, $(r_{\text{out}} - r_{\text{in}}) \simeq 2(r_{\text{out}} - r_p)$, and the first Oort constant $A = (r/2)d\Omega/dr$.

Integrating over all orbits within one halfwidth of the horseshoe region, $x_s = r_{\text{out}} - r_p$, yields the total torque of the horseshoe drag (Ward 1991)

$$\Gamma_{\text{hs,W91}} = 4\Sigma|A|Bx_s^4 \frac{d\log(\Sigma/B)}{d\log r} \stackrel{\text{Kepl.}}{\simeq} \frac{3}{4} \left(\frac{3}{2} - \alpha \right) \Sigma x_s^4 \Omega^2, \quad (1.115)$$

where the final evaluation is done for a Keplerian disk with a power-law radial density profile, $\Sigma \propto r^{-\alpha}$. Similarly to the linear corotation torque, we see that the horseshoe drag depends on the gradient of the inverse vortensity, $\Sigma/B = 2\Sigma/\omega_z$.

Horseshoe dynamics of gas disks

The concept of the particle horseshoe drag can be extended for the horseshoe drag in gas disks in order to describe the corotation torque outside the limits of the linear perturbation theory. Masset (2001) demonstrated in a model with a uniform density and constant aspect ratio that the angular exchange of gas parcels when performing U-turns in the horseshoe region follows the same functional dependence as Eq. (1.115).

However, fluid parcels do not behave the same way as test particles because they are pressure-supported and also subject to the laws of thermodynamics. Two major

issues have to be tackled: First, the strong scaling of Eq. (1.115) with x_s^4 implies that the width of the horseshoe region has to be determined accurately. Second, all thermodynamic processes that can alter the vorticity gradient across the corotation zone need to be identified and evaluated. In this section, we focus on the description of horseshoe dynamics of *fluid* parcels and provide expressions for x_s , as well as for the characteristic timescale of the horseshoe motion τ_{hs} .

Let us review the differences between horseshoe trajectories of gas parcels (GPs) and those followed by test particles (TPs) in the RTBP (see Baruteau & Masset 2013). Focusing on low-mass planets in the Type I migration regime, it turns out that:

- In the absence of shocks, the trajectories of GPs cannot overlap, nor exhibit epicyclic motion in addition to the horseshoe motion. For TPs, on the other hand, epicyclic perturbations are common.
- GPs do not follow Roche-lobe trajectories. Therefore low-mass planets are not surrounded by circumplanetary disks.
- Stagnation points (i.e. intersections of zero-velocity curves which delimit the horseshoe region) of GPs are radially located near the exact corotation with the planet, whereas stagnation points of TPs correspond to the Lagrange points L_1 and L_2 .
- The horseshoe region of GPs is substantially narrower compared to that of TPs. This influences the characteristic dynamical timescales within the gaseous horseshoe region.

Following Masset et al. (2006), the width of the horseshoe region can be described by assuming the conservation of the Bernoulli invariant (Masset & Papaloizou 2003; Casoli & Masset 2009)

$$\mathcal{B} = \frac{v^2}{2} + \eta + \Phi - \frac{1}{2}r^2\Omega_p^2. \quad (1.116)$$

Its first term represents the specific kinetic energy, the second term is the enthalpy, and the remaining two terms together represent the effective potential. In order to characterise a horseshoe separatrix, one can utilise the invariance of \mathcal{B} and assume that it is the same at a stagnation point (where $v = 0$) and also far from the planet (at the separation x_s which is to be determined); $\mathcal{B}_{\text{stag}} = \mathcal{B}_{\text{sep}}$. Φ and η can be decomposed into the background state and planet-induced perturbations, and the second-order expansion in x_s/r_p leads to (Masset et al. 2006)

$$x_s \propto r_p \sqrt{\frac{q}{h}}. \quad (1.117)$$

Thus x_s scales with the square root of the planet mass, $q = M_p/M_*$. Moreover, using this functional dependence in the Ward's formula (1.115) reveals $\Gamma_{\text{hs}} \propto \Gamma_0$. In other words, the horseshoe drag exhibits the same scaling (Eq. 1.94) as the Lindblad or the linear corotation torque.

A generally valid expression for x_s is difficult to obtain as it depends on several aspects of the underlying physical model. For example, Paardekooper & Papaloizou (2009) found that x_s also scales with the adiabatic index as $\gamma^{-1/4}$. Moreover, the shape of the horseshoe region depends on the exact location of the stagnation point(s) which can be affected by interactions with the spiral wake. These interactions, however, are difficult to account for analytically. A commonly used expression found by Paardekooper et al. (2010), with an extension for non-isothermal disks (Paardekooper et al. 2011), reads¹⁰

$$x_s = r_p \frac{1.1}{\gamma_{\text{eff}}^{1/4}} \left(\frac{0.4}{b_{\text{sm}}/h} \right)^{1/4} \sqrt{\frac{q}{h}}. \quad (1.118)$$

Nevertheless, it is important to keep in mind that a characterisation of the horseshoe region by a single width parameter is already a simplification as realistic horseshoe regions often exhibit a front-rear asymmetry (Casoli & Masset 2009).

The width of the horseshoe region enables to determine the horseshoe timescale on which the corotating gas parcels perform their libration cycles (e.g. Masset 2001). The timescale can be estimated by dividing the length of one libration cycle $\sim 4\pi r_p$ by the shear velocity $\sim 3\Omega x_s/2$ of gas parcels at the separation x_s with respect to the planet

$$\tau_{\text{hs}} = \frac{8\pi r_p}{3\Omega x_s}. \quad (1.119)$$

Choosing the parameters $M_p = 5 M_\oplus$, $M_\star = 1 M_\odot$, $r_p = 5.2 \text{ au}$, $h = 0.05$, $\gamma_{\text{eff}} = 1.4$ and $b_{\text{sm}} = 0.4h$, one obtains $x_s \simeq 0.13 \text{ au}$ and $\tau_{\text{hs}} \simeq 52 P_{\text{orb}}$. Clearly, the time for a gas parcel to complete its horseshoe orbit is considerably larger than the orbital period P_{orb} of the planet.

Horseshoe drag (non-linear corotation torque)

Detailed investigations of the horseshoe drag in gas disks confirmed that it can be described within the same framework as used by Ward (1991) for test particles. Specifically, the torque becomes (Masset & Papaloizou 2003)

$$\Gamma_{\text{hs}} = 8|A|B^2 r_p \left[\int_{-x_s}^{x_s} \left(\frac{\Sigma}{\omega_z} \Big|_{\text{F}} - \frac{\Sigma}{\omega_z} \Big|_{\text{R}} \right) x^2 dx \right], \quad (1.120)$$

where the subscripts F and R indicate the evaluation in the front and rear horseshoe region with respect to the planet. The integral implies that the horseshoe drag is given by the vortensity distribution within the horseshoe region.

The dependence on Σ/ω_z shows that the horseshoe drag always has a non-zero component associated to the inherent radial gradient of vortensity in the protoplanetary disk. This component is called *barotropic* since in a very special case of a

¹⁰We point out that the formulation of Paardekooper et al. (2010) assumes $r_p \equiv 1$, unlike our Eq. (1.118).

barotropic disk (i.e. a disk where the pressure depends only on the gas density), Eq. (1.120) yields a result similar to Eq. (1.115) (Casoli & Masset 2009; Paardekooper et al. 2010; Masset & Benítez-Llambay 2016).

However, realistic disks cannot be regarded as barotropic and it was discovered that the vortensity distribution within the horseshoe region can be further affected by both temperature and entropy gradients, as we discuss in the following. Consequently, we may expect the final expression for the horseshoe drag to be more complicated than Eq. (1.115). We shall discuss two flavours of vortensity-producing processes which arise in two thermodynamic limits – locally isothermal and adiabatic.

LOCALLY ISOTHERMAL LIMIT. Stating with a locally isothermal disk (see Casoli & Masset 2009), it is important to realise that the disk cannot remain barotropic (as the pressure becomes the function of both position and density; see Eq. 1.16). Moreover, it can become *baroclinic* at certain locations owing to the interactions with the planet. Taking the curl of the Navier-Stokes Eq. 1.47 and dividing by Σ leads to¹¹

$$\frac{D}{Dt} \left(\frac{\omega_z}{\Sigma} \right) \simeq \frac{\nabla \Sigma \times \nabla P}{\Sigma^3} \propto \frac{\nabla \Sigma \times \nabla T}{\Sigma^2}. \quad (1.121)$$

Therefore, the vortensity of the flow can be altered wherever there is a misalignment of the density and temperature gradients. A fluid is said to be baroclinic in such a case. Although the temperature gradient in a locally isothermal disk is strictly radial, the density is perturbed by the planet and its gradient inevitably acquires a non-zero azimuthal component at certain locations. For example, the horseshoe streamlines which perform U-turns close to the planet cross a region of increased density which surrounds the planet, the vortensity is produced at that location and it is then advected downstream the separatrix. This vortensity production would operate even in a disk with a zero background vortensity gradient, therefore it indeed represents an independent component of the horseshoe drag.

ADIABATIC LIMIT. In the case of an adiabatic disk, another form of the vortensity production is facilitated when there is a non-zero radial entropy gradient in the disk (Paardekooper & Mellema 2006; Baruteau & Masset 2008; Masset & Casoli 2009). Let us imagine that a gas parcel is transported along the outward-directed separatrix of the horseshoe region. It comes from inside the planetary orbit, carrying a certain amount of the entropy. When it moves outside the planetary orbit, it suddenly becomes located at the edge of a disk region where the entropy is different and an entropy discontinuity is produced along the downstream separatrix. Since the pressure balance of the disk has to be maintained, the entropy difference is compensated for by the change in the gas density (see Eq. 1.103). The sheet of the entropy discontinuity then also represents a sheet of vortensity production¹².

¹¹The given form neglects the viscous term, as well as the twisting and stretching of vortex tubes (e.g. Paper IV).

¹²The outlined reasoning is not entirely physically accurate. As pointed out by Masset & Casoli (2009), the pressure balance is never instantaneous, instead, evanescent pressure waves are excited. This is also true for the locally isothermal case discussed above.

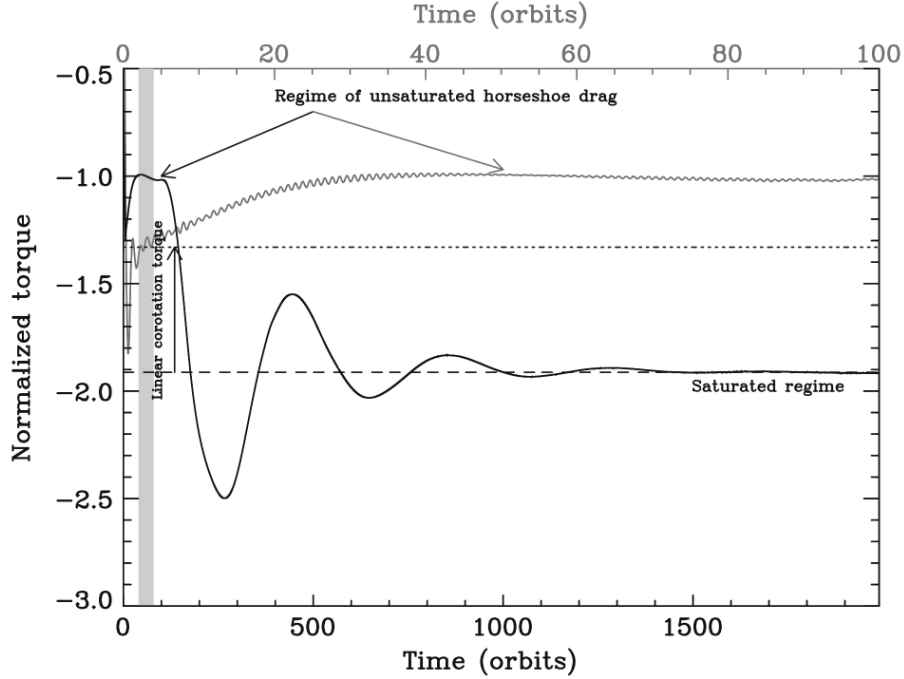


Figure 1.16: Comparison of the torque evolution in the regime of unsaturated horseshoe drag (grey curve; upper horizontal axis) with the regime of saturated horseshoe drag (black curve; lower horizontal axis). The vertical dotted line represents the linear corotation torque determined by averaging over the grey rectangle. Adapted from Masset (2011).

To provide a ready-to-use prescription for the horseshoe drag, we once again follow the studies Paardekooper et al. (2010) and Paardekooper et al. (2011) that lead to

$$\gamma_{\text{eff}} \frac{\Gamma_{\text{c,hs}}}{\Gamma_0} = 1.1 \left(\frac{0.4}{b/h} \right) \left(\frac{3}{2} - \alpha \right) + \frac{\xi}{\gamma_{\text{eff}}} \left(\frac{0.4}{b/h} \right) \left[10.1 \sqrt{\frac{0.4}{b/h}} - 2.2 \right], \quad (1.122)$$

where the first term is the vortensity-related (barotropic) part of the horseshoe drag ($\Gamma_{\text{c,hs,baro}}$) and the second term is entropy-related ($\Gamma_{\text{c,hs,ent}}$). The temperature-related horseshoe drag is not explicitly considered by this model. We refer an interested reader to a recent alternative model of Jiménez & Masset (2017) for a full description of the horseshoe drag.

Saturation versus desaturation

In numerical experiments of planet-disk interactions, a standard procedure is to insert the planet as a point-mass gravitating source into a relaxed state of the disk. Subsequently, the temporal evolution of the torque acting on the planet is recorded. During the first several tens of planetary orbits, the disk adjusts to the presence of the planet: the spiral waves are launched and the gas within the coorbital region becomes deflected along U-turns close to the planet, forming the horseshoe region

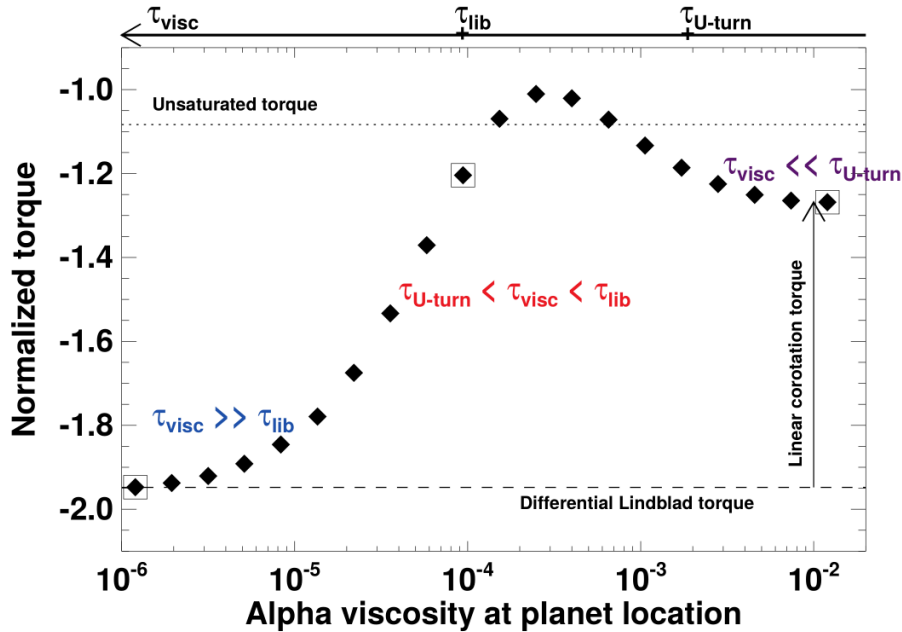


Figure 1.17: Torque as a function of the α -viscosity at the planet location. For large viscosities, the torque is the sum of the differential Lindblad torque and the linear corotation torque. For moderate viscosities, the torque peaks and it is given by the sum of the differential Lindblad torque and the unsaturated horseshoe drag. For low viscosities, the corotation torque becomes saturated and the differential Lindblad torque remains. For each of these regimes, the inequalities are given which describe the relations between the U-turn timescale $\tau_{U\text{-turn}}$, viscous timescale τ_{visc} and libration timescale τ_{hs} (here denoted τ_{lib}). Adapted from Baruteau & Masset (2013).

in the frame corotating with the planet. The torque converges to a stationary value when a new equilibrium state is reached. This equilibrium has been found to depend strongly on the evolution of the horseshoe drag.

As shown in Fig. 1.16, the disk torque starts to operate at the value determined by the combined influence of the Lindblad and the linear corotation torque. The latter is active because soon after the planet insertion, the orbits of gas parcels did not yet have enough time to deviate from their initial stellarcentric circulation. Afterwards, the horseshoe drag is established, contributes to the torque and reaches its maximum *unsaturated* value. Subsequently, there are two possibilities. Either the unsaturated horseshoe drag can be maintained or it *saturates* and vanishes. The saturation depends on the stability of gradients responsible for the individual components of the horseshoe drag.

SATURATION. In the absence of diffusion processes (if the disk is inviscid, $\nu \rightarrow 0$, and there is no thermal diffusion, $\chi \rightarrow 0$), the horseshoe region represents a thermodynamically isolated system. Although the very first horseshoe cycle of the gas after the planet insertion takes place in the presence of unperturbed disk gradients, any subsequent horseshoe cycles diminish these gradients. This is because the

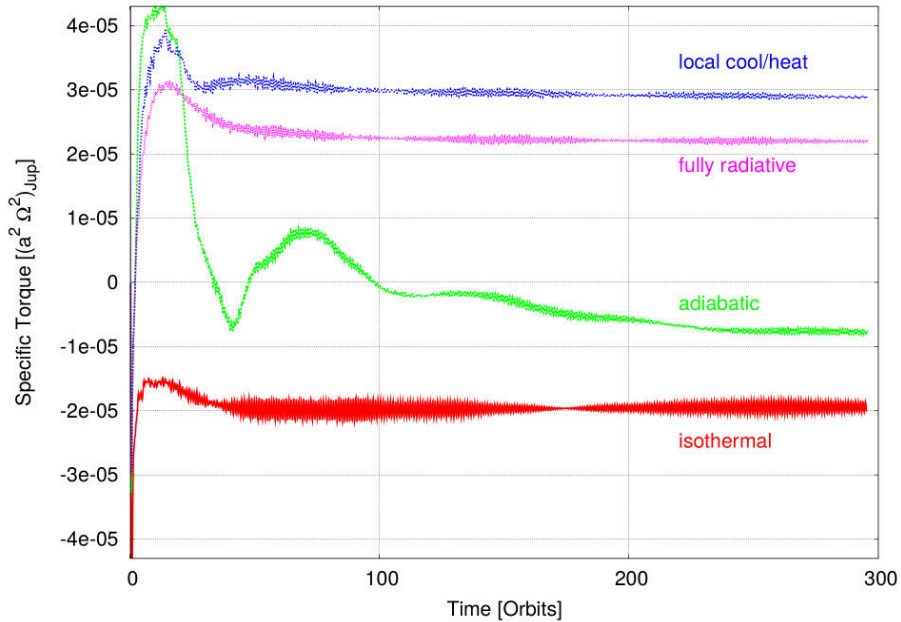


Figure 1.18: Torque evolution acting on a $20 M_{\oplus}$ planet in 2D disk models with various energy/diffusion treatments. The differences between the curves demonstrate how the disk physics affects the corotation torque. When switching from the isothermal limit (red) to the adiabatic one (green), the horseshoe drag receives a strong positive boost. However, it quickly becomes saturated because there is no heat diffusion. When local cooling/heating (blue) or radiative diffusion (purple) are considered, the horseshoe drag can remain unsaturated and the planet can migrate outwards, if the local entropy gradient is steep enough (see Fig. 1.19). Adapted from Kley & Crida (2008).

material advection spans the entire width of the horseshoe region, ‘stirs it up’ and cancels out any vortensity or entropy gradients. In such a situation, the horseshoe drag starts to oscillate with a decreasing amplitude until it becomes negligible.

DESATURATION. The restoration of the vortensity gradient can be provided by means of a viscous coupling¹³. If the viscosity is too small, it cannot prevent the phase mixing and the horseshoe drag saturates. If the viscosity is too large, it breaks the horseshoe drag mechanism and the corotation torque converges to its linear regime. If the viscosity is moderate, the horseshoe drag can operate. Usually, the drag peaks for a certain value of the viscosity which is large enough to maintain the initial value of the vortensity at the downstream separatrices, yet small enough not to destroy the vortensity contrast developed at the U-turns (Baruteau & Masset 2013). This can be expressed by the inequality of the characteristic timescales

$$\tau_{\text{U-turn}} \leq \tau_{\text{visc}} \leq \tau_{\text{hs}}/2, \quad (1.123)$$

¹³It can be shown when deriving the vortensity equation that it inherits the viscous term from the Navier-Stokes equation.

where $\tau_{\text{U-turn}} \simeq h\tau_{\text{hs}}$ is the time it takes a gas parcel to perform a U-turn (Baruteau & Masset 2008) and $\tau_{\text{visc}} \simeq x_s^2/\nu(r_p)$ is the timescale of the viscous transport over the width of the horseshoe region. The torque evolution for various ratios between the characteristic times is shown in Fig. 1.17.

Similarly to the influence of the viscosity on the desaturation of the vortensity-related component of the horseshoe drag, the desaturation of the other components can be provided by a suitable thermal diffusivity (Paardekooper et al. 2011). In realistic disks, thermal diffusion is believed to be provided by the radiation transport (Paardekooper & Mellema 2006). An example of such a radiation-driven desaturation is provided in Fig. 1.18.

The torque formulae of Masset & Casoli (2010), Paardekooper et al. (2011) or Jiménez & Masset (2017) are complemented with blending functions which describe the transitions of the corotation torque between the linear, unsaturated non-linear and fully saturated regimes of the corotation torque. This complicated behaviour of the corotation torque represents one of the reasons for the large diversity of possible outcomes of planetary migration. Depending on the disk conditions (see e.g. Figs. 1.18 and 1.19), the corotation torque can be negative or positive (as controlled by the disk gradients), and it can dominate over the Lindblad torque or vanish completely (as controlled by the viscosity and thermal diffusion).

1.4.3 Migration maps

The analytic formulae for the Lindblad and corotation torques can be used in two ways. First, they can be included as artificial forces in N-body integrators in order to mimic Type I migration without the need to use a hydrodynamic description. Second, they can be applied as a diagnostic tool to estimate possible outcomes of planet migration for a variety of disk models.

The torque formulae allow to construct *migration maps*, i.e. diagrams where the torque acting on planets is displayed as the function of the orbital distance and planet mass (see Fig. 1.19). The studies of migration maps (e.g. Kretke & Lin 2012; Bitsch et al. 2013; Coleman & Nelson 2014; Baillié et al. 2016) revealed that:

- Type I migration is mostly inward.
- Based on the disk model and local conditions, islands of outward migration can arise for a limited range of radii and planet masses. They appear:
 - in regions with a steep entropy gradient which boosts the positive entropy-related corotation torque (see Fig. 1.19). These regions can be usually identified from an outward decline of the aspect ratio $h = H/r$ which indicates a steep gradient of temperature ∇T and therefore also entropy $\nabla \mathcal{S}$. This occurs for example at the opacity transitions where the local cooling rate abruptly changes.
 - in regions with the reversal of the density profile. If the density profile exhibits a local bump (i.e. a steep outward-directed gradient), the local

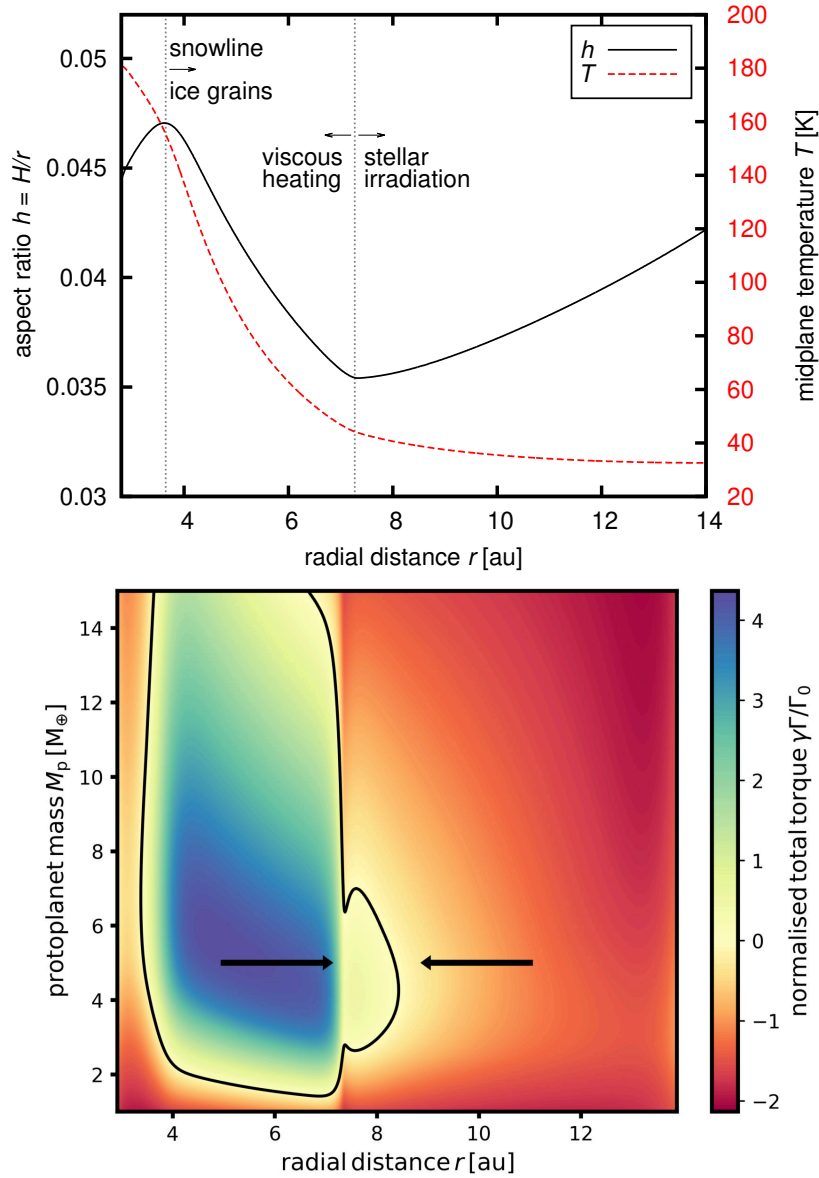


Figure 1.19: *Top:* radial profiles of the aspect ratio h (black solid curve; left vertical axis) and temperature T (red dashed curve; right vertical axis) in a disk model from Paper I. The slope of the aspect ratio changes at locations where the local heating/cooling balance is modified, namely at the opacity transition related to evaporation of water ice, and also at the transition to the outer efficiently irradiated region. *Bottom:* Type I migration map constructed for the same disk model. The coloured scale represents the normalised value of the torque predicted by the formulae of Paardekooper et al. (2011), including the Lindblad and corotation torques. The black curve shows the isocountour of $\Gamma = 0$. Migration is convergent near ≈ 7 au, as indicated by the arrows. The blue region of outward migration can clearly be related to the radially decreasing aspect ratio h . Adapted from Paper I.

jump in the vortensity ω_z/Σ makes the corotation torque positive. This is the principle of the planet trap (Masset et al. 2006) and such a configuration can naturally occur due to viscosity transitions in layered disks (Kretke & Lin 2012), near the inner disk rim (Flock et al. 2016) or in the inner disk dominated by a magnetically-driven wind (Ogihara et al. 2015).

- If the islands of outward migration are present, they create *zero-torque radii* or *convergent zones*. Inwards from these radii, planets migrate outwards, and outwards from these radii, planets migrate inwards. Planets therefore tend to concentrate near these sweetspots. Conversely, regions with the opposite behaviour have to exist where migration is divergent. Such regions become devoid of planets and are sometimes dubbed *planet deserts*.
- In evolving disks, the shapes and sizes of the islands of outward migration evolve as well.

LIMITATIONS. At first glance, it might seem that the torque formulae and migration maps easily solve the problem of planet migration. So why do we bother with RHD simulations in Chapter 2? It is because the torque formulae cannot self-consistently account for several important phenomena. First, since the torque formulae are derived for single planets, they do not account for perturbations from multiple planets, such as overlaps of spiral arms and their influence on close encounters (e.g. Paper II; Paper III). Second, the torque formulae are derived for fixed orbits, therefore they cannot recover dynamical torques (e.g. Pierens & Raymond 2016). Third, they do not consider the influence of accretion heating¹⁴ that generates the heating torque (Benítez-Llambay et al. 2015, see also Sect. 1.4.5) and the hot-trail effect (Paper I), both of which substantially change the orbital evolution.

1.4.4 Orbital eccentricity and inclination

Up to this point, we omitted the fact that the migrating planet may acquire non-zero eccentricity e or inclination i , e.g. due to gravitational interactions with other planets, or perhaps with a binary stellar companion. The deviations with respect to a planar circular orbit inevitably modify the Type I torque as the planet makes vertical or epicyclic excursions with respect to the mean gas distribution.

If e or i increases, the corotation torque becomes reduced because the width of the horseshoe region narrows (Bitsch & Kley 2010). The reduction factor is (Fendyke & Nelson 2014; Coleman & Nelson 2014)

$$\Delta_{\text{C}} = \exp\left(-\frac{e}{e_{\text{f}}}\right) \left[1 - \tanh\left(\frac{i}{h}\right)\right], \quad (1.124)$$

¹⁴There are several studies focusing on an analytic description of the heating torque and the hot-trail effect (Masset 2017; Fromenteau & Masset 2019; Guilera et al. 2019) and we discuss them in Chapter 2. However, they are not yet widely used at the time of writing of this thesis and they were not available back in 2017 when our first Paper I was published.

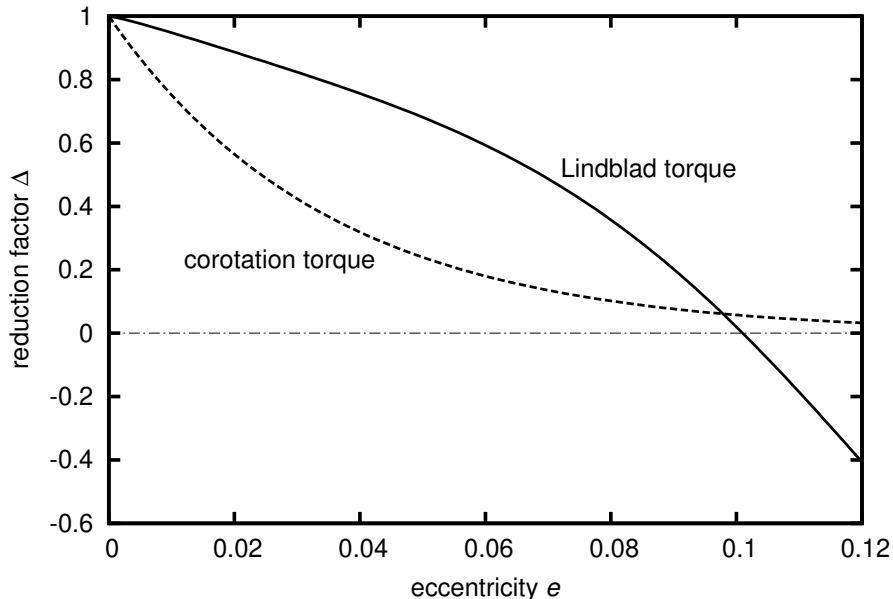


Figure 1.20: Reduction factors of the Lindblad torque (solid line; Eq. 1.125) and the corotation torque (dashed line; Eq. 1.124) as functions of the orbital eccentricity. Inclination $i = 0$ and aspect ratio $h = 0.05$ are used in this example. The corotation torque is being damped to zero with increasing e , while the Lindblad torque evolves towards a sign reversal. For low values of e , the corotation torque is reduced more prominently compared to the Lindblad torque.

where $e_f = 0.5h + 0.01$.

The Lindblad torque is modified by the shift of the planet with respect to the spiral wakes it launches. The respective reduction factor is (Cresswell & Nelson 2008)

$$\Delta_L = \left[P_e + \frac{P_e}{|P_e|} \left\{ 0.07 \frac{i}{h} + 0.085 \left(\frac{i}{h} \right)^4 - 0.08 \frac{e}{h} \left(\frac{i}{h} \right)^2 \right\} \right]^{-1}, \quad (1.125)$$

where

$$P_e = \frac{1 + \left(\frac{e}{2.25h} \right)^{1.2} + \left(\frac{e}{2.84h} \right)^6}{1 - \left(\frac{e}{2.02h} \right)^4}. \quad (1.126)$$

The eccentricity dependence of the reduction formulae is plotted in Fig. 1.20. For a low eccentricity excitation, we see that the negative Lindblad torque usually dominates over the corotation torque because the latter is reduced more significantly. Therefore, if regions of outward migration exist in a migration map for circular orbits, there is no guarantee that they will persist for eccentric orbits because the reduction of the corotation torque can shrink or destroy them.

Another interesting fact is that while the corotation torque decays with increasing e , the Lindblad torque proceeds towards its *reversal*, i.e. it changes from negative to

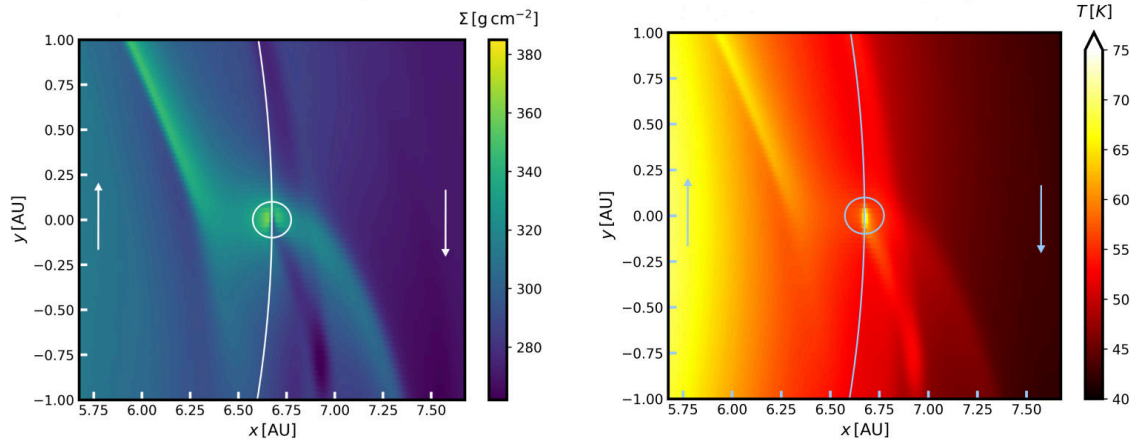


Figure 1.21: An example of the hot-trail effect (discussed in detail in Chapter 2). The figure shows the surface density Σ (*left*) and temperature T (*right*) near an accreting $3 M_{\oplus}$ protoplanet. The Hill sphere of the protoplanet is indicated by the white circle, the white curve shows the osculating orbit. The arrows show the direction of the gas flow relative to the protoplanet. In addition to the spiral arms, there is an underdense hot trail directed from the location of the protoplanet towards the lower right quadrant. The hot trail accelerates the protoplanet in its epicyclic motion, thus exciting its eccentricity and counteracting eccentricity damping. Adapted from Paper I.

positive. Such a situation occurs for $e \gtrsim 2h$ (Papaloizou & Larwood 2000) when the planet starts to cross resonances that normally do not overlap its orbit. Moreover, it spends more time interacting with the gas in the apocentre where the relative velocities boost the outward migration.

In addition to torque reductions, *damping* of eccentricities and inclinations operates in disks (Artymowicz 1993; Ward & Hahn 1994; Papaloizou & Larwood 2000; Tanaka & Ward 2004; Cresswell et al. 2007; Bitsch & Kley 2010). It is caused by eccentricity/bending waves excited by radial/vertical excursions of a planet with non-zero e/i (Tanaka & Ward 2004). When $e < h$, the eccentricity damping exhibits $de/dt \propto -e$ on timescales $\approx h^2 \tau_{\text{mig}}$. If $e \gtrsim h$, the damping becomes amplified as $de/dt \propto -e^2$. Similar scaling is followed by the inclination damping (with i swapped for e , of course). Cresswell & Nelson (2008) fitted the results of their hydrodynamic damping experiments and found the damping timescales for the eccentricity

$$t_e = \frac{t_{\text{wave}}}{0.78} \left[1 - 0.14 \left(\frac{e}{h} \right)^2 + 0.06 \left(\frac{e}{h} \right)^3 + 0.18 \left(\frac{e}{h} \right) \left(\frac{i}{h} \right)^2 \right], \quad (1.127)$$

and inclination

$$t_i = \frac{t_{\text{wave}}}{0.544} \left[1 - 0.3 \left(\frac{i}{h} \right)^2 + 0.24 \left(\frac{i}{h} \right)^3 + 0.14 \left(\frac{e}{h} \right)^2 \left(\frac{i}{h} \right) \right], \quad (1.128)$$

with

$$t_{\text{wave}} = \frac{1}{q\Omega_K} \frac{M_{\star}}{\Sigma a^2} h^4. \quad (1.129)$$

LIMITATIONS. Similarly to the case of migration maps (Sect. 1.4.3), the formulae for eccentricity and inclination damping cannot be regarded as generally valid, as we show in Chapter 2. Moreover, it is not generally true that orbital eccentricities and inclinations of protoplanets embedded in gas disks asymptotically converge to zero. Without going into details, we point out that there are processes that can counteract the damping, such as resonant perturbations in systems of protoplanets (e.g. Cossou et al. 2013) or the hot-trail effect related to accretion heating (e.g. Paper I). An example of the latter is shown in Fig. 1.21.

1.4.5 Thermal torques

In addition to the Lindblad and corotation torques, a special class of torques arises due to thermal effects in the vicinity of a protoplanet. These torques are related to the heating/cooling interplay between the protoplanet and gas which enters and leaves the Hill sphere¹⁵. For this reason, they are collectively referred to as the *thermal torques* (Masset 2017) and they only appear in radiative disks.

Essentially, there are two types of thermal torques corresponding to two limiting behaviours of the planet in terms of its energy output. If the planet is cold and does not directly radiate any energy into its surroundings, the gas which performs U-turns deep within the Hill sphere becomes heated by compression. The energy excess is radiated away (in a radiative disk) so when the gas becomes decompressed, it has a deficit of the internal energy. Consequently, two lobes of cold and therefore overdense gas appear along the outflow of front and rear horseshoe streamlines from the Hill sphere (Lega et al. 2014). The situation is shown in Fig. 1.22 (top).

Due to the sub-Keplerian rotation of the disk, the horseshoe region is not centred around the planetary orbit, it is rather shifted inwards. For this reason, the outer (rear) lobe tends to be slightly larger than the inner (front) one. In other words, there is a mass excess behind the planet which pulls the planet against the orbital motion. The lobes therefore exert a negative torque and force the planet to migrate inwards. This negative torque was named the *cold-finger effect* (Lega et al. 2014) and it represents an extra component which stacks on top of the Lindblad and corotation torques.

An opposite situation arises if the planet is accreting because it may become hot and luminous. Focusing again on the gas that flows close to the planet (see Fig. 1.22, bottom), it now becomes overheated by the accretion luminosity. The lobes which form along the streamlines leaving the Hill sphere are therefore hot and underdense (Benítez-Llambay et al. 2015), contrary to the cold-planet situation. The arising torque then becomes positive, using a similar reasoning as above (in this situation, there is a paucity of gas behind the planet). Benítez-Llambay et al. (2015) named the additional positive contribution the *heating torque* and demonstrated that it can lead to outward migration of $\lesssim 10 M_{\oplus}$ planets for accretion rates characterised by the mass doubling time $\tau_{\text{acc}} \simeq 100$ kyr or shorter.

¹⁵The described effects are *not* necessarily bound by the extent of the Hill sphere, we simply use it as a zero-order proxy of the region where the effects are the most prominent.

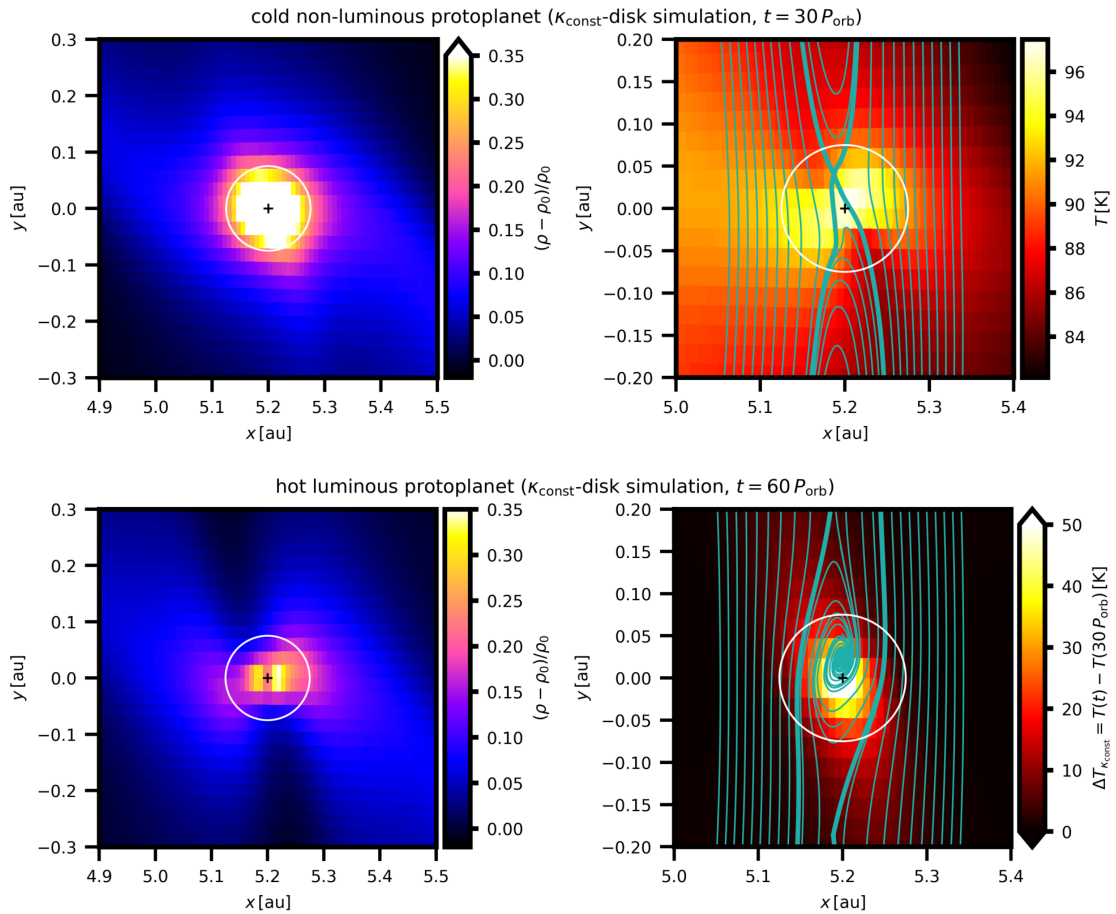


Figure 1.22: Two flavours of thermal torques acting on low-mass planets in radiative disks. *Top:* The cold-finger effect arises for a non-luminous planet as a result of the compressional heating and radiative cooling near U-turns within the Hill sphere. Two cold lobes are formed (dark regions along the downstream separatrices; *top right*) which are overdense (*top left*). *Bottom:* The heating torque arises when the planet accretes solids and becomes luminous. Two underdense lobes appear (*bottom left*) corresponding to the overheated gas. This is shown in the *bottom right* panel where we plot the temperature excess with respect to the non-luminous planet. The green curves in *right* panels represent streamlines. From Paper IV.

The heating torque is one of the key processes investigated throughout Papers I–IV. We studied its implications for the dynamics of systems of protoplanets (using 2D RHD models in Papers I–III) and whether or not the above-mentioned heuristic explanation for the formation of hot lobes agrees with complex 3D flows around hot protoplanets (using a 3D RHD model in Paper IV). Papers I–IV are discussed in the upcoming Chapter 2, therefore it is time to conclude the overview of planet migration and move on to the results of our numerical modelling.

2. Migration of accreting low-mass protoplanets

Chapter 2 deals with scientific outputs of the dissertation thesis. We focus on our four papers that were published between years 2017 and 2019 in peer-reviewed astrophysical journals. For each of these papers, we provide an introduction where we outline our motivation, methodology, and we summarise both expected and unexpected results. We also put our conclusions into a broader context of planetary sciences at the time of writing of each paper. The introductory commentary is followed by a reprint of the respective paper (with the exception of Paper II). The papers are ordered chronologically as they map the progress that the author has made during the doctoral studies. The unifying topic of these papers is the *migration of accreting low-mass protoplanets*.

2.1 Paper I: Eccentricity excitation and merging of planetary embryos heated by pebble accretion

State of the art before 2017

Before 2017, convincing evidence was assembled demonstrating that:

- Pebble accretion is likely the most efficient accretion process that can turn planetesimals into protoplanets (Ormel & Klahr 2010; Lambrechts & Johansen 2012).
- Dynamical evolution of low-mass protoplanets in disks is dominated by Type I migration (e.g. Kley & Crida 2008; Paardekooper et al. 2011; Lega et al. 2014, 2015). In this regard, however, the sensitive dependence of Type I migration on disk conditions and physical modelling makes it very difficult to establish migration pathways that would be generally applicable. Type I migration is rather problem-dependent.

With the physical background provided throughout Chapter 1, it seems inevitable that pebble accretion and planet migration has to influence one another. One can think of at least the following interplays:

- The torque acting on a planet changes as a result of the growth of the planet mass (see Eq. 1.94).
- Planets undergoing rapid pebble accretion become substantially luminous and therefore subject to the heating torque. In 2017, however, the heating torque was only known from the pioneering study by Benítez-Llambay et al. (2015) but it was not clear how it affects the dynamics of multiplanet systems.

- Migration can lead planets into mutual encounters which can pump orbital eccentricities or inclinations. Eccentricity pumping can change the relative velocities between planets and pebbles, with important implications for accretion rates (e.g. Liu & Ormel 2018). Similarly, inclined planets might spend substantial orbital time vertically offset with respect to the pebble feeding zone (Levison et al. 2015).
- If two or more planets become closely packed, the disk is going to be threaded by multiple density waves that can overlap and exert stochastic forces back on the planets.
- Perturbations in gas distribution can directly affect pebble distribution due to the aerodynamic coupling of gas and pebbles.
- If planets collide and merge, the merger event instantaneously doubles the mass of the resulting body. From this point of view, mergers can outperform pebble accretion.

In 2017, there was no model available which would self-consistently take all these feedbacks into account. There were studies conducted with hydrodynamic codes (e.g. Pierens et al. 2013), but these neglected pebble accretion. Other studies were using N-body codes with prescribed migration (e.g. Izidoro et al. 2015), but the torque formulae suffer from a large amount of simplifications (they were derived for static circular orbits; they cannot account for combined perturbations from multiple planets; etc). Some N-body codes with advanced treatment of pebbles and collisional evolution ignored the gas-driven migration completely (e.g. Levison et al. 2015). Therefore we decided it was worthwhile to invest our initial effort in developing a new code.

Development of a new code

We developed an extension of the 2D `Fargo` code (Masset 2000) dubbed `Thorin` (which stands for `Fargo` with two-fluid hydrodynamics, a `Rebound` integrator interface and non-isothermal gas physics). It is a 2D RHD code which employs the Eulerian fluid description on a polar staggered mesh. The 2D nature of the code provides a good tradeoff between an accurate hydrodynamic description of disk-planet interactions and the computing time which has to allow for long-term simulations covering $\sim 10^5$ yr. The code is tailored to run on CPU clusters and can be parallelised using the MPI, OpenMP, or a combination of both. In the following, we summarise the important features of the code.

TWO-FLUID APPROXIMATION. We included an additional fluid which represents pebbles. The pebble fluid has no thermal pressure and it is inviscid. Its evolution is driven by the gravitational potential, aerodynamic drag and a diffusive term which mimics small-scale turbulence. A back-reaction drag term is also included in the Navier-Stokes equation for gas. The temporal update of pebble velocities is performed using the semi-implicit method of Rosotti et al. (2016). The

main purpose for the inclusion of the pebble disk is to precisely simulate the material delivery towards accreting protoplanets.

INITIAL STATE OF THE PEBBLE DISK. A simple coagulation/drift model (Lambrechts & Johansen 2014) is employed which assumes that the drift-limited size of pebbles (Eq. 1.54) represents the dominant size, in which most of the pebble surface density resides. Consequently, we use the drift-limited size to calculate the Stokes number (Eq. 1.51) of pebbles which determines their aerodynamic interaction with gas and also the efficiency of pebble accretion. The initial surface density of pebbles is scaled by the radial pebble mass flux which is one of the free parameters.

PEBBLE ACCRETION. Since the resolution of the computational domain is tailored to study planet-disk interactions on a global scale, it does not allow to sufficiently resolve pebble trajectories close to planets. Moreover, such trajectories would be inaccurate anyway, due to the smoothing of the gravitational potential. For these reasons, we employ an accretion recipe which is based on introducing sink cells (e.g. Kley 1999). First, the effective accretion radius is calculated (see Sect. 1.2.3). Second, we assume that pebbles have a non-zero vertical scale height H_{peb} and we determine the overlap of the pebble disk with the accretion radius. This way we determine the sink cells. Finally, we transfer part of the mass from these sink cells onto the planet to match the theoretically predicted pebble accretion rate. We distinguish between 2D and 3D regimes of pebble accretion. Furthermore, we self-consistently determine the relative velocities between the pebble fluid and planets to account for variations of pebble accretion rate with the orbital eccentricity of planets. For each accreting planet, the accretion rate can be converted into a planetary luminosity (Benítez-Llambay et al. 2015) which serves as an additional heat source for the gas and the heating torque can operate.

RADIATION PHYSICS. The 1-temperature equation for the internal energy of gas is implemented (see Sect. 1.1.2). The source terms account for the viscous heating, compressional heating, accretion heating, in-plane radiative diffusion, vertical cooling, and vertical reprocessing of the stellar irradiation. The latter two processes are treated approximately, using a decoupled vertical 1D model of Hubeny (1990) and Menou & Goodman (2004). Opacities of Bell & Lin (1994) are used. The radiative transfer is treated in the flux-limited diffusion (FLD; Levermore & Pomraning 1981) approximation. The energy evolution is treated in a linearised implicit form. The linear problem is solved by the successive over-relaxation (SOR) method.

GRAVITATIONAL INTERACTIONS. Although the disk is effectively modelled in 2D, planets are evolved in 3D. An artificial vertical acceleration is included to account for the inclination damping by bending waves which cannot be recovered by the model (Tanaka & Ward 2004). Planet-disk interactions are calculated using the method of Müller et al. (2012): in each cell, we replace the respective razor-thin patch of gas with a vertically isothermal distribution of the volume density ρ , scaled by the local pressure scale height H . Planets then interact with these columns of material so that the resulting acceleration resembles a full 3D simulation. Moreover, this approach allows to use much smaller smoothing length and thus deeper potential

wells compared to standard 2D simulations. The N-body problem (star-planet and planet-planet interactions) is integrated with the `Ias15` integrator (Rein & Spiegel 2015) from the `Rebound` package (Rein & Liu 2012). We track possible collisions and resolve them as merger events, assuming perfect merging for simplicity.

PERFORMANCE. To validate the code, we reproduced several published disk models and torque measurements obtained with advanced 3D RHD codes (Kley et al. 2009; Lega et al. 2014). We found a very good agreement between these works and the results of our validations, despite the 2D limitation of `Thorin` (see Appendix D of Paper I).

Simulation outline

The aim of simulations in Paper I was to investigate the evolution of multiple $3 M_{\oplus}$ planetary embryos, migrating towards a zero-torque radius located in the giant-planet formation zone. We compared three cases. Case I neglected the influence of pebbles and planet migration was driven solely by the classical (Lindblad and corotation) Type I torques. Case II included the pebble disk and pebble accretion, but neglected accretion luminosities of embryos. These were finally considered in Case III.

The motivation for focusing on the giant-planet formation zone was twofold: first, we wanted to see if the heating torque changes the expected migration of embryos near the convergent radius. Second, we aimed to check whether the formation of giant planet cores by embryo mergers is a common process or not.

Major results

ECCENTRICITY EXCITATION. In the presence of accretion heating, we identified a pumping of planetary eccentricities unrelated to gravitational interactions between planets. We concluded that the eccentricity excitation is of a hydrodynamic origin. We named this new phenomenon the *hot-trail effect*. It is important to point out that this effect was independently discovered in 3D by Eklund & Masset (2017), a short time before Paper I.

The hot-trail effect arises due to the relative motion between the planet and the surrounding gas which receives the accretion heat and creates an underdense disturbance. On a circular orbit, the disturbance exists in a form of two underdense lobes Benítez-Llambay et al. (2015). The outer lobe attached to the rear of the planet tends to be slightly more pronounced because the corotation between the planet and the sub-Keplerian gas disk is shifted inwards with respect to the orbit of the planet. When the planet starts to migrate, however, its orbit cannot remain perfectly circular. Once the planet is in the pericentre, it feels a headwind (because the inward shift of the corotation is enhanced). Then the underdense disturbance is represented by a single dominant lobe positioned behind the orbital motion of the planet. Once the planet is in the apocentre, the corotation shifts close to the planetary orbit (or even outwards for sufficiently large eccentricities). Then the

underdense disturbance is again two-lobed (or a dominant lobe is created ahead of the planet).

Alternatively, one can imagine the redistribution of hot underdense lobes as a result of the epicyclic motion of the accreting planet which inevitably leaves behind a hot trail (see also Eklund & Masset 2017).

We analysed variations of the gravitational acceleration imposed by the underdense gas onto the planet and we used the Gauss perturbation equations to demonstrate that the orbitally averaged change of eccentricity is positive. This drives a positive feedback: if the eccentricity increases, the relative motions between the heated gas and the planet start to vary even more prominently.

The growth of the eccentricity, however, is not unlimited. It is terminated when $e \simeq h$ which is when the Lindblad torque is close to its reversal and the eccentricity damping switches from $de/dt \propto -e$ to $de/dt \propto -e^2$ (see Sect. 1.4.4).

IMPLICATIONS OF EXCITED ECCENTRICITIES. In a regime of a convergent migration, it is difficult for planets to become locked in mutual mean-motion resonances if their eccentricities are sufficiently large prior to the resonance crossing. A Hamiltonian description of this phenomenon was worked out by Batygin (2015) who found that if eccentricities of migrating planets are excited at least to $\simeq 0.02$, the resulting fraction of planetary systems locked in resonant chains is low, in accordance with the observed exoplanetary systems. Surprisingly, the eccentricities excited by the hot-trail effect are $\simeq 0.03$ and could potentially explain the paucity of resonant configurations in the population of exoplanets. The inability of migrating planets to form a resonant chain once they become closely packed typically results in a violent phase of evolution during which close encounters occur frequently, possibly leading to mergers. Alternatively, planetary encounters occasionally lead to formation of coorbital planets (orbiting in a 1:1 resonance; see also Cresswell & Nelson 2008).

The very presence of excited eccentricities challenges the standard approach to the eccentricity damping which is applied in N-body models with prescribed migration (e.g. Sándor et al. 2011; Coleman & Nelson 2016). In these models, the eccentricity damping is usually implemented as described in Sect. 1.4.4. However, if planets experience substantial accretion heating, the efficiency of the eccentricity damping should be reduced and moreover, the asymptotic value of eccentricity should be non-zero.

MASS EVOLUTION. We found pebble filtering factors to range between 10 and 25%, in an agreement with the findings of Lambrechts & Johansen (2014). The resulting doubling time of planetary masses due to pebble accretion is then $\simeq 80$ kyr for the radial pebble mass flux $2 \times 10^{-4} M_{\oplus} \text{ yr}^{-1}$. However, we also saw that planetary mergers indeed occur. They directly form giant planet cores, break the oligarchic growth and reduce the multiplicity of the system at the same time.

2.1.1 Reprint

Here we include the reprint of Paper I.

Eccentricity excitation and merging of planetary embryos heated by pebble accretion[★]

O. Chrenko¹, M. Brož¹, and M. Lambrechts²¹ Institute of Astronomy, Charles University in Prague, V Holešovičkách 2, 18000 Prague 8, Czech Republic
e-mail: chrenko@sirrah.troja.mff.cuni.cz² Laboratoire Lagrange, UMR 7293, Université Côte d’Azur, CNRS, Observatoire de la Côte d’Azur, Boulevard de l’Observatoire, 06304 Nice Cedex 4, France

Received 24 April 2017 / Accepted 17 June 2017

ABSTRACT

Context. Planetary embryos can continue to grow by pebble accretion until they become giant planet cores. Simultaneously, these embryos mutually interact and also migrate due to torques arising from the protoplanetary disk.

Aims. Our aim is to study how pebble accretion alters the orbital evolution of embryos undergoing Type-I migration. In particular, we try to determine whether or not the embryos establish resonant chains, and if so, whether or not these chains are prone to instabilities. Further, we investigate the possibility that giant planet cores form through embryo merging which can be more rapid than pebble accretion alone.

Methods. For the first time, we perform self-consistent global-scale radiative hydrodynamic simulations of a two-fluid protoplanetary disk consisting of gas and pebbles, the latter being accreted by embedded embryos. Accretion heating, along with other radiative processes, is accounted for to correctly model the Type-I migration.

Results. We track the evolution of four super-Earth-like embryos, initially located in a region where the disk structure allows for a convergent migration. Generally, embryo merging is facilitated by rapidly increasing embryo masses and breaks the otherwise oligarchic growth. Moreover, we find that the orbital eccentricity of each embryo is considerably excited (≈ 0.03) due to the presence of an asymmetric under-dense lobe of gas – a so-called “hot trail” – produced by accretion heating of the embryo’s vicinity. Eccentric orbits lead the embryos to frequent close encounters and make resonant locking more difficult.

Conclusions. Embryo merging typically produces one massive core ($\geq 10 M_{\oplus}$) in our simulations, orbiting near 10 AU. Pebble accretion is naturally accompanied by the occurrence of eccentric orbits which should be considered in future efforts to explain the structure of exoplanetary systems.

Key words. hydrodynamics – planets and satellites: formation – planet-disk interactions – protoplanetary disks – planets and satellites: gaseous planets

1. Introduction

Interactions of gas and solids in protoplanetary disks are the basis for subsequent growth of all kinds of planets, whether they finally become terrestrial, super-Earths, ice giants or gas giants. These interactions have to be computed with an appropriate feedback, as there are a number of relatively complicated but inevitable phenomena. Setting the classical in-spiralling of solids due to gas drag aside, there are processes like streaming instability and local collapse (Johansen et al. 2007), pebble accretion assisted by aerodynamic drag (Lambrechts & Johansen 2012; Morbidelli & Nesvorný 2012), accretion heating of planetary embryos and surrounding gas (Benítez-Llambay et al. 2015), or embryo-disk interactions in general (e.g. Kley et al. 2009). Sufficiently complex hydrodynamic models with radiative transfer (RHD) are usually needed for realistic treatment of these processes.

The radiative properties of the protoplanetary disk are mostly determined by the opacity κ . As a flux-mean (Rosseland) value, κ is mostly caused by icy, silicate or carbonaceous dust grains (Mathis et al. 1977; Bell & Lin 1994) that have different wavelength-dependent optical constants (Jäger et al. 2003). The size-frequency distribution of dust grains is often assumed to be shallow, with a cumulative slope $q = -2.5$ (Mathis et al. 1977; Birnstiel et al. 2012). Any sudden transition in the composition of the dust component (e.g. grain evaporation or “rain out”) affects local heating and cooling properties of the gas disk. Consequently, variations of the scale height $H(r)$ might occur, and moreover, the pressure gradient might exhibit a reversal, $\nabla P > 0$, which leads to accumulation of solids (and even planetary embryos). Typical transitions are located, for example, at the inner rim of the disk due to UV photoionisation and corotation with stellar magnetic field, at the evaporation line of silicates (Flock et al. 2016), and at the snowline corresponding to water evaporation (Morbidelli et al. 2015). Important heating sources are provided by viscous dissipation, especially in the inner disk, and stellar irradiation of the inclined/flared disk atmosphere (Bitsch et al. 2014).

[★] The code is publicly available at <http://sirrah.troja.mff.cuni.cz/~chrenko/>, and also at the CDS via anonymous ftp to cdsarc.u-strasbg.fr (130.79.128.5) or via <http://cdsarc.u-strasbg.fr/viz-bin/qcat?J/A+A/606/A114>

While small (μm -sized) grains usually influence overall optical properties, large (mm-sized) dust particles or (cm-sized) pebbles – if already present – dominate the mass distribution. According to recent developments in the theory of planet formation, pebbles can be efficiently accreted by larger seed masses, for example planetesimals or embryos, with high enough accretion rate to finally produce giant planet cores (Lambrechts & Johansen 2012, 2014) with masses $\geq 10 M_E$, well within the protoplanetary disk lifetime, which is typically ≈ 10 Myr (Fedele et al. 2010). Global-scale N -body simulations demonstrated that the giant planets of the Solar System can be reproduced by pebble accretion (Levison et al. 2015), provided that dynamical stirring of orbital inclinations breaks the oligarchic growth of the seed masses (Kretke & Levison 2014).

A downside of the aforementioned global-scale simulations with pebble accretion is that they do not model the interactions between the protoplanets and the surrounding gaseous disk in a self-consistent way because no hydrodynamics is employed. However, during the evolutionary phase when multiple low-mass embryos are present, it is inevitable that these embryos interact gravitationally with the disk and undergo Type-I migration, when no gap is opened. There are many purely hydrodynamical effects contributing to the resulting torque acting on the planets: Spiral arms (launched at the Lindblad resonances and independent of viscosity ν), the corotation torque from the asymmetric gas structures formed in the corotation regions of embryos (Masset 2002) and additional forcing produced by asymmetries related to radiative effects operating in the vicinity of the embryos, for example the cold finger (Lega et al. 2014) or the heating torque (Benítez-Llambay et al. 2015).

The embryos – albeit having generally different migration rates – can accumulate near some of the pressure gradient reversals, mutually interact, and get locked in a resonant configuration and create a “convoy” (Pierens et al. 2013). Such a configuration naturally prevents any merging. It is possible that the stability of the resonant chain can be reduced by larger numbers of embryos present in the system (Pierens et al. 2013), when the disk is massive and exhibits large accretion rates, ($10^{-7} M_\odot \text{ yr}^{-1}$ according to Zhang et al. 2014), or when some of the embryos enter a fast migration regime due to strong corotation torque when the initially librating gaseous material is contracted into the tadpole region (Pierens 2015). According to current understanding, it is unclear how pebble accretion and accretion heating affect the convergent migration and resonant chain stability and we address these particular issues in this paper. We aim to determine whether the migrating embryos merge or remain in the chain while they continue to grow. The resonant chain (in)stability is important also with respect to the observed exoplanetary systems because these are often non-resonant (e.g. Winn & Fabrycky 2015).

The embryo growth and/or merging closely precede an evolutionary epoch which provides important observational evidence of the planet-forming processes. Once a giant planet core is formed it can clear a gap in the disk along its orbit and its further migration is driven by the viscous evolution of the disk (the Type-II migration, e.g. Lin & Papaloizou 1986; Crida & Bitsch 2017). Such a gap may become observable and the disk is then classified as pre-transitional (according to Espaillat et al. 2010, 2014).

To summarise, the protoplanetary system within the scope of this paper is assumed to consist of a gas disk with opacities dominated by fully coupled dust, a pebble disk (strongly but not fully coupled) and already formed low-mass embryos ($\sim 1 M_E$) that continue to grow by pebble accretion. Our hydrodynamic

simulations aim to investigate if different migration rates, evolving embryo masses, accretion heating and mutual perturbations between embryos can break the resonant chains and create a giant-planet core capable of opening a gap.

Our paper is organised as follows. In Sect. 2 we summarise all the equations and approximations of our two-dimensional (2D) RHD model. We also describe relevant initial and boundary conditions. Technical details of the model and useful explanatory derivations are given in Appendices A–C. A validation of our model is given later in Appendix D. In Sect. 3 we present results of our global-scale simulations focused on the migration of several pebble-accreting and heated embryos. Section 4 describes how the accretion heating affects the orbital eccentricities and disk torques acting on the embryos. We discuss possible future model improvements and also possibilities of relating our results with observations in Sect. 5. Section 6 is devoted to conclusions.

2. Protoplanetary system modelling

The model we present is based on the publicly available 2D hydrodynamic code FARGO (Masset 2000; Baruteau & Masset 2008) which we extensively modified in order to follow the evolution and mutual interactions between three components of protoplanetary systems: a differentially rotating disk of the nebular gas, a partially coupled disk of pebbles, and several embedded planetary embryos. The FARGO code is designed as an Eulerian solver on a polar staggered mesh. The numerical scheme relies on the operator-splitting technique according to Stone & Norman (1992), with a modified transport sub-step which utilises van Leer’s second-order upwind interpolation (van Leer 1977) for radial advection and the FARGO algorithm (Masset 2000) in the azimuthal direction. Let us briefly summarise new physical modules that were implemented in our modified version of the code.

Considering the gaseous disk, we relax the isothermal approximation and account for the evolution of temperature within the disk. The extended set of hydrodynamic equations thus contains the energy equation with multiple relevant source terms; in particular: compressional heating, viscous heating, stellar irradiation, vertical escape of radiation, radiative diffusion in the mid-plane and radiative feedback to accretion heating of embryos.

Regarding the pebble disk, we assume it consists of mm- to cm-sized pebbles (Lambrechts & Johansen 2012). Pebbles orbiting within the nebular gas are subject to the aerodynamic drag which changes their angular momentum. The characteristic time scale of the angular momentum change is usually described by the stopping time t_s (Adachi et al. 1976; Weidenschilling 1977). Its dimensionless form, the Stokes number, is defined as $\tau \equiv \Omega_K t_s$, where Ω_K denotes the Keplerian angular frequency. The Stokes number is an important quantity encapsulating the particle size and coupling to the nebular gas. In this study, we follow Lambrechts & Johansen (2014) and consider particles smaller than the mean free path in the nebular gas, typically with $\tau \lesssim 0.1$. The friction then arises due to anisotropic collisions between individual gas molecules and pebbles and the drag operates in the Epstein regime. Due to parametrisation by τ , we practically neglect drag regimes relative to the local Reynolds number. Because of their aerodynamic properties, pebbles are strongly coupled with the gas flow and thus we study their evolution using a two-fluid model in which the pebble disk is modelled as another Eulerian fluid which is, unlike the gas, pressureless and inviscid (e.g. Youdin & Goodman 2005).

The embedded embryos are evolved in three dimensions (3D) using a high-accuracy integration technique, accounting for

O. Chrenko et al.: Eccentricity excitation and merging of planetary embryos heated by pebble accretion

close encounters, possible collisions, and merging. An artificial vertical force acting on the embryos is applied to damp their inclinations as predicted for 3D disks (Tanaka & Ward 2004). The embryos are allowed to grow by drag-assisted pebble accretion, capturing pebbles from the circumplanetary flow. We also consider that the embryos can be heated by this vigorous material deposition and consequently radiate the excessive energy into the surrounding gas.

The mutual interactions accounted for in the model are as follows. Both the gas and pebbles evolve in the gravitational potential of the protostar and embryos. The potential is computed by an averaging procedure in a direction perpendicular to the midplane to avoid unrealistic potential smoothing and spreading (Müller et al. 2012). All the embryos participate in mutual N -body interactions and they also feel the gravitational pull of the gas disk, but the gravity of the pebble disk is ignored due to its relatively low mass. The gas disk and pebbles are only coupled through the linear drag term and no self-gravity is taken into account. The detailed aspects of the model implementation into FARGO are elaborated in the following individual subsections.

2.1. Two-fluid model of the gas-pebble disk

In our hydrodynamic model, we study the evolution of the gas surface density Σ , the vertically averaged gas flow velocity $\mathbf{v} = (v_r, v_\theta)$, the specific internal energy of the gas E , the surface density of the pebble disk Σ_p and its velocity field $\mathbf{V} = (V_r, V_\theta)$. The fundamental fluid equations to be solved can be written by means of the vertically integrated quantities as follows:

$$\frac{\partial \Sigma}{\partial t} + \nabla \cdot (\Sigma \mathbf{v}) = 0, \quad (1)$$

$$\frac{\partial \mathbf{v}}{\partial t} + \mathbf{v} \cdot \nabla \mathbf{v} = -\frac{1}{\Sigma} \nabla P + \frac{1}{\Sigma} \nabla \cdot \mathbb{T} - \frac{\int \rho \nabla \phi dz}{\Sigma} + \frac{\Sigma_p \Omega_K}{\Sigma \tau} (\mathbf{V} - \mathbf{v}), \quad (2)$$

$$\frac{\partial E}{\partial t} + \nabla \cdot (E \mathbf{v}) = -P \nabla \cdot \mathbf{v} + Q_{\text{visc}} + Q_{\text{irr}} + Q_{\text{acc}} - Q_{\text{rad}}, \quad (3)$$

$$\frac{\partial \Sigma_p}{\partial t} + \nabla \cdot (\Sigma_p \mathbf{V}) = -\left(\frac{\partial \Sigma_p}{\partial t}\right)_{\text{acc}}, \quad (4)$$

$$\frac{\partial \mathbf{V}}{\partial t} + \mathbf{V} \cdot \nabla \mathbf{V} = -\frac{\int \rho_p \nabla \phi dz}{\Sigma_p} - \frac{\Omega_K}{\tau} (\mathbf{V} - \mathbf{v}). \quad (5)$$

Here P denotes the vertically integrated pressure, \mathbb{T} is the viscous stress tensor (e.g. Masset 2002), ϕ is the gravitational potential arising from the protostar and planetary embryos, ρ and ρ_p are the volume densities of the gas and pebbles, respectively. The individual source terms on the right-hand side of the energy equation represent the compressional heating, the viscous heating Q_{visc} , the stellar irradiation Q_{irr} , the radiative diffusion Q_{rad} and the heating Q_{acc} arising from pebble accretion which is symbolically considered in the pebble mass continuity equation as the $-(\partial \Sigma_p / \partial t)_{\text{acc}}$ term. We emphasise that the gradient and divergence operators are always 2D in our model.

The following ideal gas equation of state is introduced as the thermodynamic closing relation

$$P = \Sigma \frac{RT}{\mu} = (\gamma - 1) E, \quad (6)$$

with R being the universal gas constant, $\mu = 2.4 \text{ g mol}^{-1}$ being the mean molecular weight and $\gamma = 1.4$ denoting the adiabatic index (specific heat ratio).

Before proceeding to the description of all the individual source terms, let us highlight that we assume a simple vertical stratification of the disk in order to approximate certain effects that are expected to operate in realistic 3D disks. The gas volume density $\rho(r, \theta, z)$ follows a Gaussian form

$$\rho(r, \theta, z) = \frac{\Sigma(r, \theta)}{\sqrt{2\pi}H(r, \theta)} \exp\left(-\frac{z^2}{2H(r, \theta)^2}\right), \quad (7)$$

where $H = c_{s, \text{iso}} / \Omega_K = c_s / (\sqrt{\gamma} \Omega_K)$ is the local pressure scale height and $c_s = \sqrt{\gamma P / \Sigma}$ is the adiabatic sound speed which differs from the isothermal sound speed $c_{s, \text{iso}}$ by a factor $\sqrt{\gamma}$. The normalisation constant $\Sigma / (\sqrt{2\pi}H)$ actually represents the gas volume density ρ_0 in the midplane. In principle, Eq. (7) holds only for vertically isothermal disks, which is an assumption we do not impose when discussing the energy source terms in Sect. 2.2. But because recent 3D simulations demonstrated that the optically thick parts of protoplanetary disks have a flat vertical temperature distribution (Flock et al. 2013), we decided to use Eq. (7) as a viable first approximation of the vertical stratification.

2.2. Energy source terms

Let us first describe how the radiation transport is treated in our model. The corresponding term Q_{rad} is given by the vertically integrated divergence of the 3D radiative flux \mathbf{F}_{3D} :

$$\begin{aligned} Q_{\text{rad}} &= \int_{-\infty}^{\infty} \nabla_{3D} \cdot \mathbf{F}_{3D} dz \approx \int_{-H}^H \frac{\partial F_z}{\partial z} dz + 2H \nabla \cdot \mathbf{F} \\ &\equiv Q_{\text{vert}} + 2H \nabla \cdot \mathbf{F}, \end{aligned} \quad (8)$$

where we assumed that the vertical outward radiation is liberated at H which is expected to be much smaller than the radial extent of the disk. The amount of energy transported by radiation is therefore dominant in the vertical direction (D'Angelo et al. 2003). We estimate these radiative losses caused by the vertical escape of radiation from both sides of the disk as

$$Q_{\text{vert}} \approx 2\sigma_R T_{\text{eff}}^4 = \frac{2\sigma_R T^4}{\tau_{\text{eff}}}, \quad (9)$$

where σ_R is the Stefan-Boltzmann constant, T stands for the midplane temperature and τ_{eff} is the effective optical depth. Hubeny (1990) generalized the gray model of stellar atmospheres in LTE for the case of accretion disks and found

$$\tau_{\text{eff}} = \frac{3}{8} \tau_{\text{opt}} + \frac{1}{2} + \frac{1}{4\tau_{\text{opt}}}, \quad (10)$$

where we implicitly assumed that the disk is stellar irradiated (otherwise $1/2$ term should be replaced with $\sqrt{3}/4$; D'Angelo & Marzari 2012) and that the mean Rosseland opacity and the Planck opacity are identical which is a viable approximation as discussed, for example, by Bitsch et al. (2013). The relation (10) is highly convenient in the case of a protoplanetary disk because it can characterise both optically thin and thick environment.

The optical depth τ_{opt} is measured from the midplane to the disk surface and we estimate it as

$$\begin{aligned} \tau_{\text{opt}} &= \int_0^{\infty} \kappa(r, \theta, z) \rho(r, \theta, z) dz \simeq c_\kappa \kappa(r, \theta) \int_0^{\infty} \rho(r, \theta, z) dz \\ &= c_\kappa \frac{\kappa(r, \theta) \Sigma(r, \theta)}{2}, \end{aligned} \quad (11)$$

where $c_\kappa = 0.6$ is a correction factor that accounts for the opacity drop in the layers above the midplane (we refer to Müller & Kley 2012 for a similar approach). This parametric factor in fact sets the local efficiency of vertical cooling and can be tuned so that the resulting disk structure resembles the one obtained in 3D models.

We adopt the power-law mean Rosseland opacity $\kappa = \kappa_0 \rho^a T^b$ with the coefficients a and b derived by Lin & Papaloizou (1985) and further refined by Bell & Lin (1994) for various temperature intervals and corresponding opacity regimes. The transitions between individual opacity regimes are smoothed out as in (Lin & Papaloizou 1985; we also refer to Keith & Wardle 2014).

Coming back to the midplane radiative flux (see Eq. (8)), we use the flux-limited diffusion approximation (Levermore & Pomraning 1981; Klahr & Kley 2006) to express

$$F = -\lambda_{\text{lim}} \frac{16\sigma_{\text{R}}}{\rho_0 \kappa} T^3 \nabla T. \quad (12)$$

In this approximation, scattering effects are neglected and λ_{lim} denotes the flux limiter, which is calculated according to Kley (1989). The radiative transport is treated by means of the one-temperature approach (Kley et al. 2009). This means that the internal energy of the gas is presumed to be dominated by the thermal energy whereas the radiative energy is relatively small. The radiation field is thermalised to the same temperature T as the gas.

The stellar irradiation is governed by Q_{irr} term which is complementary to Q_{vert} and reads

$$Q_{\text{irr}} = \frac{2\sigma_{\text{R}} T_{\text{irr}}^4}{\tau_{\text{eff}}}. \quad (13)$$

The irradiation temperature T_{irr} can be obtained from the projection of the stellar radiation flux onto the disk surface (Chiang & Goldreich 1997; Menou & Goodman 2004; Pierens 2015)

$$T_{\text{irr}}^4 = (1 - A) \left(\frac{R_\star}{r} \right)^2 T_\star^4 \sin \alpha. \quad (14)$$

Here $A = 0.5$ is the disk albedo, assumed to be a mean value implicitly averaged over the stellar flux, and $T_\star = 4370$ K is the effective temperature of the protostar with the stellar radius $R_\star = 1.5 R_\odot$. Together with the stellar mass $M_\star = 1.0 M_\odot$, the given parameters represent a protostar similar to T Tauri type (Paxton et al. 2015). Finally, α is the grazing angle at which the starlight strikes the disk. The grazing angle can be approximated by reconstructing the disk surface from the local pressure scale height H . Adopting the geometric formulation of Baillié & Charnoz (2014), we use

$$\alpha = \arctan\left(\frac{dH}{dr}\right) - \arctan\left(\frac{H - 0.4R_\star}{r}\right). \quad (15)$$

If $\alpha < 0$, the corresponding surface facet is not oriented towards the incident irradiating flux thus we set $Q_{\text{irr}} = 0$ in this case.

Unlike in an isothermal model, the aspect ratio $h(r) = H(r)/r$ is not time independent but it evolves instead. Therefore the disk can flare in its outer parts where the stellar irradiation dominates the energy budget (D'Alessio et al. 1998; Dullemond 2002; Bitsch et al. 2013).

The viscous dissipation heating Q_{visc} is calculated according to Mihalas & Weibel Mihalas (1984)

$$Q_{\text{visc}} = \frac{1}{2\nu\Sigma} \left(\tau_{rr}^2 + 2\tau_{r\theta}^2 + \tau_{\theta\theta}^2 \right) + \frac{2\nu\Sigma}{9} (\nabla \cdot \mathbf{v})^2. \quad (16)$$

Here $\nu = 5 \times 10^{14} \text{ cm}^2 \text{ s}^{-1}$ is the kinematic viscosity and τ_{ij} corresponds to the individual components of the viscous stress tensor T . We emphasise that the viscosity is fixed and not solved explicitly in the model.

The accretion heating term Q_{acc} is non-zero only in the nearest vicinity of embedded planetary embryos and it depends on their accretion rate. The luminosity of an accreting embryo with the mass M_{em} and the radius R_{em} is given by

$$L = \frac{GM_{\text{em}}}{R_{\text{em}}} \frac{dM_{\text{em}}}{dt}. \quad (17)$$

The resulting heating of the surrounding gas is provided by placing an inner heat source into the grid cell which contains the respective embryo. The specific power of this source reads

$$Q_{\text{acc}} = \frac{L}{S}, \quad (18)$$

where S is the cell area. In this work, we assume that the mass growth of embryos is driven solely by pebble accretion. The accretion rate dM_{em}/dt is computed self-consistently as described in Sect. 2.5. We emphasise that the accretion heating term Q_{acc} is not always switched on in our simulations and we remind the reader in such cases.

The numerical solution of the energy equation (Eq. (3)) is described in Appendix A.

2.3. Initial state of the gas disk

The thermal equilibrium of any gaseous disk studied in our model is achieved by a rather complicated interplay between the heating and cooling sources introduced above. Therefore it would be difficult to search for an analytic formula describing the initial state of an isolated disk in equilibrium. In order to initialise the hydrodynamic fields over the computational domain, we use either simple power-law functions or equilibrium solutions known from less sophisticated models. The resulting gas disk, which lacks the pebble component and embedded objects at this point, is then numerically relaxed towards its stationary state. This serves as a preparation stage for the following complete simulations.

The non-relaxed hydrodynamic profiles are assumed to be symmetric in θ . The surface density is described by the power-law profile $\Sigma = 750 (r/(1 \text{ AU}))^{-0.5} \text{ g cm}^{-2}$. We start with an initially non-flaring disk, having the aspect ratio $h = H/r = 0.05$. In accordance with this setup, we can subsequently initialise c_s , P and T . We verified that the choice of initially non-flaring disk does not prevent flaring during the relaxation. The radial velocity v_r is initially set to zero, while v_θ is set by imposing the equilibrium between the central gravity, pressure gradient, and centrifugal acceleration. The disk is fully extended in azimuth and radially bordered by the inner boundary $r_{\text{min}} = 2.8 \text{ AU}$ and the outer boundary $r_{\text{max}} = 14 \text{ AU}$. The polar computational domain is divided into 1536 azimuthal sectors and 1024 evenly spaced

O. Chrenko et al.: Eccentricity excitation and merging of planetary embryos heated by pebble accretion

radial rings. The grid sampling should be sufficient to reasonably resolve the corotation region of low-mass embryos and properly reproduce the related torques (e.g. Lega et al. 2014).

2.4. Initial state of the pebble disk

We use the hydrodynamic polar grid to insert a sea of pebbles within the gaseous disk which has already been relaxed towards its equilibrium state in the absence of planetary embryos. Using solely the hydrodynamic quantities together with several parameters introduced in this section, we initialise Σ_p , V_r and V_θ over the computational domain and evolve the fluid of pebbles over the course of the simulation.

The aerodynamic properties of pebbles which interact with the gas in the Epstein regime are characterised by the Stokes number

$$\tau = \frac{\rho_b R_p}{\rho_0 c_s} \Omega_K, \quad (19)$$

where $\rho_b = 1 \text{ g cm}^{-3}$ is the pebble bulk density, R_p is the pebble size and ρ_0 is the midplane volume density of the nebular gas. Then the initial velocity field can be described by an analytic estimate for a pebble drifting in a steady-state gaseous disk while neglecting the presence of any massive perturbers besides the protostar (e.g. Nakagawa et al. 1986; Guillot et al. 2014, and also Appendix B)

$$V_r = -\frac{2\tau}{1+\tau^2} \left(\eta v_K - \frac{1}{2\tau} v_r \right), \quad (20)$$

$$V_\theta = v_K - \frac{1}{1+\tau^2} \left(\eta v_K - \frac{\tau}{2} v_r \right), \quad (21)$$

where v_K is the local Keplerian velocity and η measures how much the gas departs from local Keplerian rotation

$$v_\theta = (1-\eta)v_K. \quad (22)$$

In simple stationary disks, η is a monotonic function reflecting the sub-Keplerian rotation of the pressure-supported nebular gas. In realistic disks, however, the situation is more complicated; the η profile is affected, for example, by the pressure dips and bumps, which can occur at the opacity transitions (Bitsch et al. 2014), and also by viscous shear.

As mentioned above, we aim to describe the pebble disk by a single fluid while in reality, protoplanetary systems are certainly populated by pebbles of various sizes. Despite our simplification, we would like the material delivery towards the accreting embryos to be realistic. It is thus important to discuss the choice of the particle size and Stokes number. As argued by Birnstiel et al. (2012), most of the pebble mass is concentrated towards the upper end of the size spectrum and, at the same time, the largest pebbles are the fastest drifters. At a given radial distance, it is reasonable to assume that the pebble size distribution has a steep upper cutoff and all the particles larger than this cutoff are swiftly removed by the drift, while particles smaller than this cutoff do not significantly contribute to the total mass of solids. In this work we presume that such a dominant size is also the best choice for characterising the pebble disk by a single fluid so that its resulting hydrodynamic behaviour is the most similar to a real pebble disk, which is a mixture of many particle species. In other words, the dominant pebble size can be viewed as an effective workaround to avoid using a numerically demanding multi-fluid model and obtain a reasonably evolving disk of solids

at the same time. We highlight that R_p is always understood as the dominant drift-limited size in what follows and that we also neglect other size-limiting processes such as fragmentation.

The Stokes number τ_d of the dominant pebble size can be found by balancing the characteristic time scale for the particle growth $t_{\text{grow}} = R_p/\dot{R}_p$ and the time scale of the particle removal by the drift $t_{\text{drift}} = r/V_r$. Following Garaud (2007) and staying within the limits of the Epstein regime, the growth time scale is

$$t_{\text{grow}} = \frac{4}{\sqrt{3}\epsilon_p (\Sigma_p/\Sigma) \Omega_K}, \quad (23)$$

and depends only on the local solid-to-gas ratio, orbital frequency and the pebble coagulation efficiency, assumed $\epsilon_p = 0.5$. Because $\tau < 1$, we approximate $V_r \approx -2\tau\eta r\Omega_K$ and, by equating the characteristic time scales, we write

$$\tau_d = \frac{\sqrt{3}\epsilon_p \Sigma_p}{8\eta\Sigma}. \quad (24)$$

Up to this point, the pebble surface density Σ_p was unconstrained. When studying pebble accretion, it is useful to keep track of the total radial mass flux \dot{M}_F of solids through the system. In the following, we set the initial $\dot{M}_F = 2 \times 10^{-4} M_E \text{ yr}^{-1}$ (Lambrechts & Johansen 2014) as an input parameter and assuming an equilibrium situation, we impose the following continuity requirement (Lambrechts & Johansen 2014)

$$\Sigma_p = \frac{\dot{M}_F}{2\pi r V_r}. \quad (25)$$

Plugging Eq. (25) in (24) and using the approximate expression for V_r again, one finds

$$\tau_d = \frac{1}{r\eta} \sqrt{\frac{\sqrt{3}\epsilon_p \dot{M}_F}{32\pi\Omega_K\Sigma}}. \quad (26)$$

The corresponding dominant particle size can be easily obtained when using the inverse of Eq. (19). In the last expression, τ_d depends only on two model parameters (ϵ_p and \dot{M}_F) and the hydrodynamic state of the gaseous background. Therefore it is a convenient starting point for the pebble disk initialisation.

To summarise the initial conditions, we first use the combination of Eqs. (19) and (26) to find $R_p(r)$. Because the relaxed gaseous disk is very close to axial symmetry (within discretisation errors and numerical artefacts) when we incorporate the pebble disk, it is reasonable to consider that the pebble size changes only radially. We further assume that once the planetary embryos are present, they do not cause global-scale changes of η , thus the initial $R_p(r)$ profile is kept fixed during our simulations. Subsequently, we calculate the initial (V_r, V_θ) field (Eqs. (20) and (21)) which sets Σ_p from the mass flux conservation law (25). We emphasise that unlike $R_p(r)$, the Stokes number $\tau(r, \theta)$ is considered a cell-dependent quantity during the simulations and it is recalculated each time step to obtain proper aerodynamics for a given particle size moving in the evolving gaseous background. This is to account for situations when pebbles suddenly enter gas clumps or underdense regions.

2.5. Pebble accretion

Pebble accretion enters our model through Eq. (4) in which it acts like a mass sink. At the same time, the mass removed from the pebble component is accreted by the growing embryos.

According to [Lambrechts & Johansen \(2012\)](#), two fundamental regimes of pebble accretion have to be considered, namely the Bondi¹ and the Hill regimes, while the transition between the two occurs when the pebble accretion Bondi radius R_B becomes comparable to the Hill sphere radius R_H of the accreting body. The former radius corresponds to the distance whereby a pebble with impact parameter $b \leq R_B$ will suffer a ≥ 1 rad deflection, while the latter radius defines the region in which the gravitational pull of the accreting body dominates over the primary field. The defining equations are

$$R_B = \frac{GM_{\text{em}}}{v_{\text{rel}}^2}, \quad (27)$$

and

$$R_H = \left(\frac{GM_{\text{em}}}{3\Omega_K^2} \right)^{1/3}, \quad (28)$$

where v_{rel} denotes the relative velocity between the pebble and the accreting body with mass M_{em} .

In the Bondi regime, if $R_B \lesssim R_H$, the only pebbles that experience a significant deflection arrive through a small fraction of the Hill sphere thus they enter the encounter region with the relative velocity which is set by the local headwind experienced by the embryo, therefore $v_{\text{rel}} \simeq v_{\text{head}}$.

On the other hand, if $R_B \gtrsim R_H$, the relative encounter velocity for most of the pebbles is dominated by the Keplerian shear which becomes more important than headwind on orbital separations comparable to R_H . In such a case, the Hill regime is triggered. It is obvious that the equality of R_B and R_H is reached for a specific value of M_{em} called the transition mass

$$M_t = \sqrt[3]{\frac{1}{3} \frac{v_{\text{head}}^3}{G\Omega_K}}. \quad (29)$$

Super-Earth-like embryos which we investigate in this paper usually grow in the Hill regime.

[Lambrechts & Johansen \(2012\)](#) also found that there is a well-defined maximum distance at which the pebbles must approach the embryo in order to be accreted. This effective accretion radius for both regimes is given by

$$R_{\text{eff}} = \begin{cases} R_B \sqrt{\frac{\tau}{t_B \Omega_K}}, & \text{Bondi regime } (M_{\text{em}} < M_t) \\ \min \left[R_H \left(\frac{\tau}{0.1} \right)^{1/3}, R_H \right], & \text{Hill regime } (M_{\text{em}} \geq M_t) \end{cases} \quad (30)$$

where $t_B = R_B/v_{\text{rel}}$ is the crossing time of the Bondi radius.

Because our simulations cover a relatively large portion of the protoplanetary disk, the grid resolution near embryos is not detailed enough to capture the final stage of the in-spiraling motion of pebbles. Thus the fluid model does not allow for fully self-consistent pebble accretion calculation because we are not able to resolve the flow of pebbles falling on the embryo's surface. We instead rely on the knowledge of the effective accretion radius R_{eff} and we employ a recipe which is somewhat similar to the usual gas accretion treatment in 2D hydrodynamic models ([Kley 1999](#)).

First, we identify all the grid cells which have a midplane distance from the embryo smaller than R_{eff} . Second, we compute the following mass-related quantities:

¹ In the original work of [Lambrechts & Johansen \(2012\)](#), the Bondi regime is referred to as the drift regime.

- The expected embryo mass increase ΔM_{expec} : here we use the analytic accretion rates derived from detailed pebble accretion models ([Lambrechts & Johansen 2012](#)). Following [Morbidelli et al. \(2015\)](#), we set

$$v_{\text{rel}} = \begin{cases} v_{\text{head}}, & \text{Bondi regime } (M_{\text{em}} < M_t) \\ v_{\text{shear}}, & \text{Hill regime } (M_{\text{em}} \geq M_t), \end{cases} \quad (31)$$

where v_{shear} is the relative velocity due to Keplerian shear at the orbital separation R_{eff} , and

$$\Delta M_{\text{expec}} = \begin{cases} 2R_{\text{eff}} v_{\text{rel}} \bar{\Sigma}_p \times \Delta t, & (\bar{H}_p < R_{\text{eff}}) \\ \pi R_{\text{eff}}^2 v_{\text{rel}} \frac{\bar{\Sigma}_p}{\sqrt{2\pi} \bar{H}_p} \times \Delta t, & (\bar{H}_p \geq R_{\text{eff}}), \end{cases} \quad (32)$$

where the overbar indicates the mean value taken over the respective cells and Δt is the time step. Because v_{rel} is calculated self-consistently, the pebble accretion rate is approximately corrected for eccentric orbits (v_{rel} increases with the eccentricity, M_t increases as well and the embryo can experience a transition to the Bondi accretion regime which is less effective).

- The total available mass ΔM_{avail} : assuming that pebbles have non-zero scale height H_p and that their vertical z -distribution is Gaussian (like for the gas; cf. Eq. (7)), we calculate ΔM_{avail} by numerically integrating the pebble fluid mass inside the overlap between the vertically spread disk of pebbles and the accretion sphere of radius R_{eff} , located around the embryo which can generally be shifted in z direction. The purpose of ΔM_{avail} is mainly to account for 3D effects, for example inclined orbits, which can lead the accreting bodies away from their feeding zones.

The pebble disk scale height is ([Youdin & Lithwick 2007](#))

$$H_p \simeq H \sqrt{\frac{\alpha_p}{\tau}}, \quad (33)$$

where $\alpha_p = 1 \times 10^{-4}$ parametrises the turbulent stirring of the solids in the protoplanetary disk.

Finally, the mass transferred on the embryo in one time step is

$$\Delta M_{\text{em}} = \min(\Delta M_{\text{expec}}, \Delta M_{\text{avail}}). \quad (34)$$

The pebble surface density in the cells below R_{eff} is reduced accordingly. This instantaneous accretion rate $\Delta M_{\text{em}}/\Delta t$ is also used to calculate the accretion heating Q_{acc} (Eq. (18)). The change in Σ_p due to accretion can propagate to radial distances interior to the embryo, thus affecting the pebble mass flux.

2.6. Numerical solution of the pebble fluid motion equation

After the accretion step, the hydrodynamic quantities describing the pebble disk are evolved as follows. First, the Stokes number $\tau(r, \theta)$ is recalculated for each cell from Eq. (19) using the known dominant pebble size R_d and the quantities ρ_0 and c_s reflecting the state of the gaseous background. Second, the velocity field V_r, V_θ is updated under the action of the source terms standing on the right-hand side of the pebble fluid motion Eq. (5). Third, all the quantities are advected using the same transport FARGO algorithm as for the gas.

Regarding the source step, it is necessary to take into consideration that pebbles are usually well coupled to the gas and they have stopping times t_s much smaller than the typical time

O. Chrenko et al.: Eccentricity excitation and merging of planetary embryos heated by pebble accretion

step Δt adopted for the explicit update of the gas dynamics. Applying the same explicit integration for the pebble fluid might require significant limitations of Δt . In order to avoid this, we adopt a semi-implicit solution as in (Rosotti et al. 2016; we refer to Appendix C for a brief overview of this method), also including a particle diffusion term related to turbulent mixing. This is accounted for by adding the diffusive velocity (Clarke & Pringle 1988),

$$\mathbf{V}_D = -\frac{\nu}{Sc} \frac{\Sigma}{\Sigma_p} \nabla \frac{\Sigma_p}{\Sigma}, \quad (35)$$

to the pebble fluid velocity. The Schmidt number $Sc = 1$ is considered, representing the ratio of the gas diffusivity to the pebble diffusivity (e.g. Cuzzi et al. 1993; Youdin & Lithwick 2007).

2.7. Boundary conditions

The radial boundaries r_{\min} and r_{\max} are closed for all hydrodynamic quantities. In addition, we set wave-killing zones in the annuli adjacent to the inner and outer boundary. These zones cover the intervals of $r \in [r_{\min}, 1.2r_{\min}]$ and $r \in [0.9r_{\max}, r_{\max}]$. Inside these zones, the following equation is solved each time the boundary condition is applied (Kley & Dirksen 2006; de Val-Borro et al. 2006)

$$\frac{dq}{dt} = -\frac{q - q_0}{t_{\text{damp}}} f(r), \quad (36)$$

where q represents any hydrodynamic quantity and q_0 is its reference value that is about to be reached by the damping. The characteristic time scale is $t_{\text{damp}} = 0.1T_{\text{orb}}$ (Müller & Kley 2013) with T_{orb} being the Keplerian orbital period at the corresponding (inner or outer) boundary. By $f(r)$ we denote a dimensionless ramp function which decreases from 1 at the boundary to 0 at the end of the wave-killing zone (de Val-Borro et al. 2006).

The choice of q_0 for the gas disk is the following: The radial velocity v_r is damped to zero at the boundaries. The remaining hydrodynamic quantities characterising the gas (Σ , E , v_θ) are damped towards the values they attain at the end of the relaxation stage. Owing to these conditions, any spiral wake that is invoked by an embedded planet cannot reflect at the boundary.

The boundary conditions for pebbles are also imposed within the wave-killing zones by damping Σ_p , V_r and V_θ towards the initial steady-state solutions. Owing to these conditions, the outer wave-killing zone behaves like a pebble reservoir and the pebble disk does not decay in time due to its inward drift.

2.8. Embryo-disk interaction

In 2D simulations, a standard procedure when simulating the planet-disk gravitational interactions is to replace the real planetary potential with a Plummer-type smoothed potential of a point mass (Morbidelli et al. 2008) $\phi_{\text{em}} = -GM_{\text{em}} / \sqrt{s^2 + z_{\text{em}}^2 + \epsilon^2}$, where $s = \sqrt{(x - x_{\text{em}})^2 + (y - y_{\text{em}})^2}$ is the midplane separation between a cell center and an embryo with 3D coordinates $(x_{\text{em}}, y_{\text{em}}, z_{\text{em}})$ and ϵ is the smoothing length, typically taken as a fraction of the pressure scale height H_{em} at the embryo's orbit. The reason for the smoothing is twofold. First, it is to keep the otherwise diverging potential regular for the gas parcels located close to the planet and second, it is to mimic the interaction with columns of gas instead of razor-thin midplane distribution.

However, we decided not to use the ϵ -smoothed potential in our case because of the following inconveniences. As the embryo masses are typically $M_{\text{em}} \approx 1 M_{\text{E}}$, one can expect that the

Hill sphere of the embryo will be smaller than the vertical extent of the disk most of the time. This means that the ϵ -smoothing based on the thickness would cause a significant underestimation of the embryo's gravitational influence already outside the Hill sphere (Kley et al. 2009). This could have at least two negative impacts on the reliability of our model: the torques arising from the regions close to the planet would be poorly reproduced and too many pebbles might be able to cross the Hill sphere without being accreted as they would drift in a shallower potential well.

To avoid these difficulties, we follow Klahr & Kley (2006) and use the following deeper potential

$$\phi_{\text{em}} = \begin{cases} -\frac{GM_{\text{em}}}{d}, & (d > r_{\text{sm}}) \\ -\frac{GM_{\text{em}}}{d} \left[\left(\frac{d}{r_{\text{sm}}}\right)^4 - 2\left(\frac{d}{r_{\text{sm}}}\right)^3 + 2\frac{d}{r_{\text{sm}}} \right], & (d \leq r_{\text{sm}}) \end{cases} \quad (37)$$

where $r_{\text{sm}} = 0.5R_{\text{H}}$ is the actually used (sufficiently small) smoothing length. For the purpose of the embryo-disk interaction modelling, we assume that the gas is stratified symmetrically above and beneath the midplane, according to the distribution function (7). Hereinafter, d is the 3D separation between a point in the space (located above or below a cell center) and the embryo.

Because the gas cells in our model are 2D, we employ a method to vertically average the 3D potential given by Eq. (37) in the calculations. Adopting the approach outlined by (Müller et al. 2012; we also refer to their Appendix A), the acceleration of 2D gas cells in the gravitational field of the embryo can be obtained by calculating the specific density of the force projected on the midplane

$$F_{\text{em}}(s) = - \int \rho \frac{\partial \phi_{\text{em}}}{\partial s} dz, \quad (38)$$

where ϕ_{em} follows from Eq. (37) and $\rho(r, \theta, z)$ from Eq. (7). As demonstrated in Müller et al. (2012), replacing the integral with a coarse sum over at least ten vertical grid points per side of the disk leads to an accurate yet numerically feasible reproduction of the realistic 3D interaction.

Equation (7) in principle neglects the influence of embryos on the vertical gas distribution in their vicinity. Although this effect can (and should) be easily incorporated in fully isothermal models (as in Müller et al. 2012), it is not straightforward in our non-isothermal disk because we only use an approximate treatment of the vertical radiation transport, the model is convection-free, and so on. Nevertheless, we found, by means of numerical experiments, that even the simple $\rho(z)$ dependence leads to results which agree with some of the advanced 3D simulations very well (Appendix D). This justification is possible due to the local nature of the pressure scale height H in our model and also owing to the mass range of embryos which we study; they are not massive enough to perturb the disk scale height significantly, nor do they form circumplanetary disks. Absence of large gaseous structures gravitationally bound to the embryos is also a motivation for including all parts of the Hill sphere in the disk-embryo torque computation.

In general, the orbits of embryos can become inclined or eccentric during mutual close encounters, it is thus necessary to ensure the inclination damping and the circularisation of the orbit as it would operate in 3D disks. Unfortunately, our 2D disk cannot support vertical waves and moreover, Eq. (7) always leads to a symmetric density distribution with respect to the midplane which is certainly not true if inclined perturbers are present. An

artificial vertical force is thus imposed on the embryos in order to damp their orbital inclinations in a fashion similar to realistic 3D disks (Tanaka & Ward 2004):

$$F_z = \beta \frac{M_{\text{em}} \Sigma \Omega_K}{c_s^4} (2A_z^c v_z^{\text{em}} + A_z^s z_{\text{em}} \Omega_K), \quad (39)$$

where v_z^{em} is the vertical component of the planet's velocity, $A_z^c = -1.088$ and $A_z^s = -0.871$ are the coefficients given by Tanaka & Ward (2004). The parameter β is problem-dependent and has to be tuned so that the eccentricity damping, provided naturally by the potential (Eq. (37)), and the inclination damping operate both on comparable time scales.

Finally, let us point out that the stellar potential is also modelled in terms of the acceleration obtained by the vertical averaging procedure. The evolution of pebbles in the gravitational field follows the same recipe as for the gas (cf. Eqs. (37) and (38)) but their scale height H_p is of course different (Eq. (33)).

2.9. Embryo-embryo interaction

The mutual gravitational interaction among the massive bodies is solved using the IAS15 integrator (Rein & Spiegel 2015) from the REBOUND package (Rein & Liu 2012) which we interfaced with FARGO. The integration follows a 15th order non-symplectic Runge-Kutta scheme improved with the Gauss-Radau quadrature (we refer also to Everhart 1985). There are several fundamental reasons for choosing this integrator over more common symplectic integrators:

- The time step Δt in FARGO is controlled by the hydrodynamic Courant-Friedrichs-Lewy (CFL) condition and the original code adopts the same time step to ensure that the planets and gas evolve synchronously. Some symplectic integration schemes can produce numerical errors if the time step is not fixed.
- The N -body integrator must be capable of dealing with close encounters which are expected to occur in our simulations. IAS15 is convenient for this purpose because of its high-order accuracy and adaptive time-step subdivision.
- Although IAS15 is not symplectic in nature, it is reported to preserve the energy error within the double floating-point machine precision (Rein & Spiegel 2015). Moreover, the energy error behaves like a random walk which we think is the best option for the rather short time spans (compared to long-term integrations in celestial mechanics) that our simulations cover.

Additionally, the REBOUND package contains several routines to detect and resolve collisions. In our runs, we use the direct collision search and the embryos are allowed to merge whenever they collide. Merging is treated in the most simple way, in which the mass and momentum are conserved but the released energy and possible mass loss are neglected. The embryo radii, which are used to detect collisions, are inferred from the embryo masses, assuming the spherical shape and the uniform material density 3 g cm^{-3} .

2.10. Code performance

The performance of our new RHD code of course depends on the given machine architecture and the simulations usually require parallel computation in order to be efficient. Following the original FARGO code, our version supports distributed memory parallelism using MPI-based domain decomposition, shared

Table 1. A summary of the hydrodynamic model parameters introduced in Sect. 2.

Parameter	Notation	Value/reference
Gas surface density	Σ	$750 \left(\frac{r}{1 \text{ AU}}\right)^{-0.5} \text{ g cm}^{-2}$
Kinematic viscosity	ν	$5 \times 10^{14} \text{ cm}^2 \text{ s}^{-1}$
Non-relaxed aspect ratio	h	$H/r = 0.05$
Adiabatic index	γ	1.4
Mean molecular weight	μ	2.4 g mol^{-1}
Mean Rosseland opacity	κ	Bell & Lin (1994)
Vertical opacity drop	c_κ	0.6
Stellar temperature	T_\star	4370 K
Stellar radius	R_\star	$1.5 R_\odot$
Disk albedo	A	0.5
Radial grid resolution	N_r	1024
Azimuthal grid resolution	N_θ	1536
Inner radial boundary	r_{min}	2.8 AU
Outer radial boundary	r_{max}	14 AU
Pebble radial mass flux	\dot{M}_F	$2 \times 10^{-4} M_E \text{ yr}^{-1}$
Pebble turbulent stirring	α_p	1×10^{-4}
Schmidt number	Sc	1.0
Coagulation efficiency	ϵ_p	0.5
Pebble bulk density	ρ_b	1 g cm^{-3}

memory parallelism using OpenMP, or a combination of both. The simulations in this paper were performed on clusters of Intel Xeon E5-2650 CPUs (v2 and v4; with comparable core performance ≈ 33 according to the SPECfp2006 benchmark) using MPI exclusively. To provide a typical computation time required for our simulations, here we present values measured for a test simulation with the full two-fluid disk, four embedded embryos and all implemented radiative processes. The simulation spanned 50 kyr of evolution and required ≈ 5.4 d on 32 cores and ≈ 3 d on 96 cores.

3. Protoplanetary system simulations

3.1. Equilibrium disk structure

In this section, we discuss global characteristics of the protoplanetary disk in thermal equilibrium, before we actually start simulations with embedded embryos. All the important hydrodynamic model parameters were introduced one by one throughout Sect. 2 and we summarise all of them in Table 1 for the reader's convenience.

Figure 1 (top panel) shows the aspect ratio $h(r) = H(r)/r$ and the temperature radial profile $T(r)$ of the modelled disk. We notice that h first increases with the radius, reaches a maximum at $r \approx 4$ AU, drops again when moving to $r > 4$ AU and has another turn-over point at $r \approx 7$ AU. The temperature T on the other hand steadily decreases outwards as a sequence of power-law functions with slopes that change at radii corresponding to the inflection points in h .

We can follow the reasoning of Bitsch et al. (2013) to explain the changes in h as well as in T . Looking at the opacity profile $\kappa(r)$ (bottom of Fig. 1), we notice that it has a maximum at $r \approx 4$ AU. This is related to the temperature rise up to $T \approx 170$ K

O. Chrenko et al.: Eccentricity excitation and merging of planetary embryos heated by pebble accretion

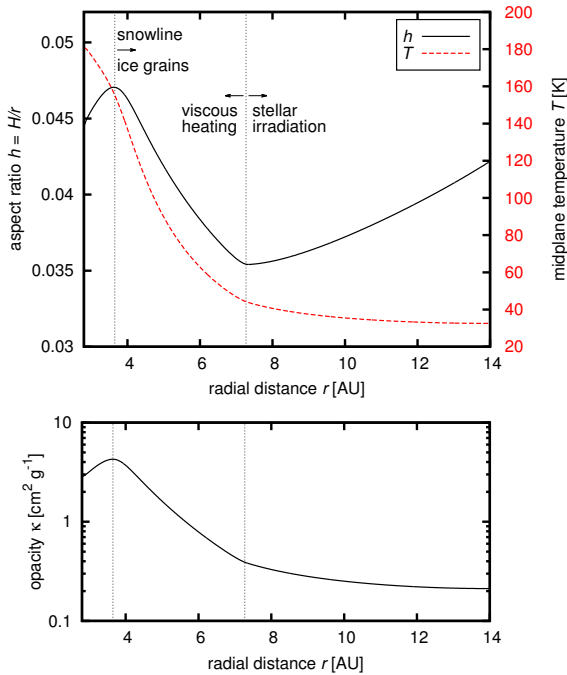


Fig. 1. *Top:* radial profile of the aspect ratio $h = H/r$ (black curve, left vertical axis) and midplane temperature T (red dashed curve, right vertical axis) in our disk model. *Bottom:* radial profile of the opacity κ . The plots show the state reached after a relaxation, with all the heating and cooling terms in balance. This is considered an equilibrium state prior to the follow-up simulations with embedded embryos. Vertical dotted lines indicate important changes in the disk structure, namely the snowline close to $r \approx 4$ AU and the transition to the flared stellar-irradiated outer region near $r \approx 7$ AU.

at which ice grains sublimate (Bell & Lin 1994), a snowline is formed and silicate grains become the main source of the opacity. The opacity maximum at $r \approx 4$ AU prolongs the radiative cooling time scale and viscous friction deposits more heat in the midplane and creates a thermal pressure gradient which puffs up the disk. Therefore the maximum of h corresponds to the maximum of κ .

The transition of h at $r \approx 7$ AU cannot be explained in the same way because κ is steadily decreasing in this region (there is no change of the opacity regime), albeit with a shallower slope. The transition is rather caused by the change of the dominant heating source. Unlike at $r < 7$ AU, where the viscous shear is the main source of heating, the stellar irradiation becomes more efficient and prevails at $r > 7$ AU. This is possible because both Σ and κ are decreasing in the outer disk and so is the vertical optical depth τ_{opt} . Therefore starlight can penetrate deeper into the disk, counteract the radiative cooling and slow down the temperature decrease in the outer disk which becomes flared.

3.2. Dominant pebble properties

The described transitions in the gas disk are of a great importance for the remaining components of the system – both pebbles and embryos. Let us turn our attention to pebbles first. Figure 2 shows the radial profile of the gas rotation parameter η (Eq. (22)). The profile implies that the rotation curve of the gas changes

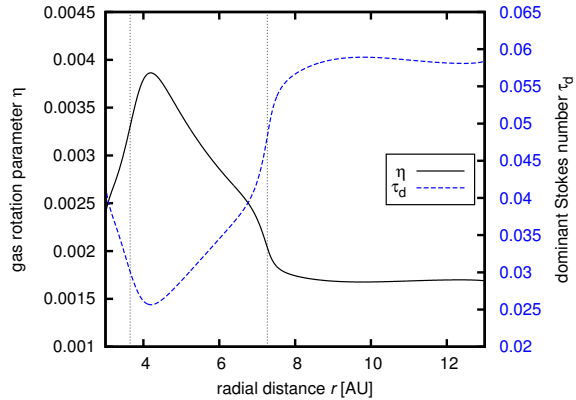


Fig. 2. Radial profile of the η parameter (black curve, left vertical axis) which expresses the difference between the sub-Keplerian gas velocity and the Keplerian velocity, $v_\theta = (1 - \eta)v_K$. Initial radial profile of the dominant Stokes number τ_d (blue dashed curve, right vertical axis) which characterises aerodynamic properties of pebbles prevalent in the size-frequency distribution of solid particles.

at the 4 and 7 AU transitions. For example, there is a rotation slowdown in the inner part of the disk due to stronger pressure support and viscous friction.

The rotation velocity of the gas is directly related to the headwind felt by drifting pebbles. Because the radial pebble mass flux through the disk is assumed to be at a steady state, the radial distribution of the dominant Stokes number τ_d (Eq. (26)) must adapt to the η profile in order to maintain the flux, as shown by the blue dashed curve in Fig. 2. We recall that in our model, the initial $\tau_d(r)$ profile sets the dominant pebble sizes $R_p(r)$ throughout the system for the rest of the simulation. Going from large r inwards, R_p first grows from 7.5 to 9 cm, when crossing $r \approx 7$ AU the sizes begin to decrease down to 5 cm and finally they increase at $r < 4$ AU up to 8 cm.

However, the described variations of particle sizes and Stokes numbers are rather small, within a factor ~ 2 in the region of interest. This is expected because the rotation curve transitions are smooth and the initial state of the pebble disk (Sect. 2.4) is based on the Lambrechts & Johansen (2014) model which predicts the properties of the drifting pebbles to depend weakly on η in smooth disks.

3.3. Migration map

Let us also discuss the influence of the gas disk structure on the orbital evolution of embedded planetary embryos. In particular, we can estimate the expected direction and rate of the Type-I migration of an embryo, depending on its mass and location in the disk. As in for example Kretke & Lin (2012) or Bitsch et al. (2013), we apply the analytical formulae from Paardekooper et al. (2011) on the azimuthally averaged profiles of the equilibrium disk and compute the torque acting on embryos. We do not list individual steps of the torque calculation here, as there are many, but note that the model of Paardekooper et al. (2011) is 2D and gives a prediction for low-mass planets on fixed circular orbits, while accounting for both Lindblad and corotation torques in the non-linear regime, saturated and unsaturated limits. The heating torque is not considered in their model. Moreover, they used the ϵ -smoothed

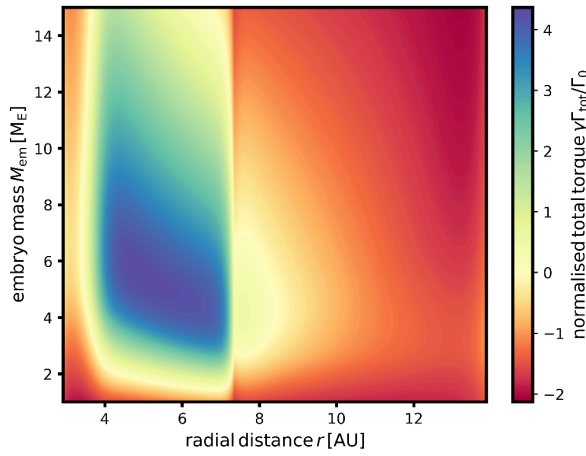


Fig. 3. Migration map based on the equilibrium state of the protoplanetary disk. The colour code shows the normalised value of the total torque $\gamma\Gamma_{\text{tot}}/\Gamma_0$ acting on an embryo with the mass M_{em} (vertical axis) placed on a circular orbit at the radial distance r (horizontal axis) in the disk. Calculated according to Paardekooper et al. (2011), using the constant kinematic viscosity $\nu = 5 \times 10^{14} \text{ cm}^2 \text{ s}^{-1}$ and the potential smoothing parameter $\epsilon = 0.4H_{\text{em}}$.

Plummer-type potential for planet-disk interactions and thus their torque formulae are parametric in the smoothing length ϵ .

The resulting migration map, calculated for rather small $\epsilon = 0.4H_{\text{em}}$, is shown in Fig. 3. The total torque Γ_{tot} felt by embryos of various masses M_{em} is normalised as $\gamma\Gamma_{\text{tot}}/\Gamma_0$, where

$$\Gamma_0 = \left(\frac{q}{h_{\text{em}}}\right)^2 \Sigma_{\text{em}} r_{\text{em}}^4 \Omega_{\text{em}}^2, \quad (40)$$

$q = M_{\text{em}}/M_{\star}$ is the embryo-to-protostar mass ratio and all of the remaining quantities are calculated at the respective orbital radius r_{em} . It is important to emphasise that Fig. 3 is only an auxiliary diagram which does not exactly represent the torque felt by embryos in our simulations (we refer to Appendix D for a comparison of torques with Paardekooper et al. 2011). Despite this, it is a useful tool for getting a general picture of the expected migration rates in different regions of the disk before actually performing self-consistent simulations.

We notice there are two borderlines between positive and negative torques in the disk. The first is located at the snowline ($r \approx 4 \text{ AU}$) and the second is located at (roughly) $r \approx 7 \text{ AU}$, that is, the transition between the viscously heated and stellar-irradiated region. The outer borderline represents a zero-torque radius where an accumulation (convergent migration) of embryos is expected to occur because positive torques Γ_{tot} drive the embryos outwards while negative torques inwards.

In the positive torque region, the negative Lindblad torque is suppressed by the corotation torque. The corotation torque generally arises as the gas parcels performing U-turns exchange angular momentum with the embryo and it is known to be determined by the vortensity distribution which can be modified by advection along the streamlines, or additional vorticity can be produced by the temperature and entropy gradients (Baruteau & Masset 2008; Paardekooper & Papaloizou 2008). The latter is responsible for the strong positive torque between the snowline and the stellar-irradiated region because a suitable (negative) entropy gradient is present due to the aspect ratio decrease.

The positive torque region should exist only for masses $1.5 M_{\text{E}} \lesssim M_{\text{em}} \lesssim 15 M_{\text{E}}$ for which the thermodynamic conditions in the surrounding disk can sustain the corotation torque. The corotation torque can be prevented from saturation when the viscous and heat diffusion time scales are shorter than the whole libration time scale (which decreases with increasing embryo mass) but longer than the single U-turn time scale (e.g. Pierens 2015).

3.4. Case I – migration of non-accreting embryos in the gas disk only

Hereinafter we present and compare three different simulation cases which start from the equilibrium disk and are numerically evolved for time spans covering $t_{\text{span}} \approx 50 \text{ kyr}$. In all these simulations, we placed four embryos with equal mass $M_{\text{em}} = 3 M_{\text{E}}$ on initially circular orbits with semimajor axes equal to $a_1 = 5 \text{ AU}$, $a_2 = 6.7 \text{ AU}$, $a_3 = 8.4 \text{ AU}$ and $a_4 = 10.1 \text{ AU}$; the embryos being numbered inside out. The initial inclinations were randomly chosen as small non-zero values ($\lesssim 0.1^\circ$). The mass of the embryos is always introduced into the system gradually in order to avoid shocks. The same holds for the cases in which the embryos act as the heat sources – the released heat is gradually amplified from zero towards the self-consistently calculated value during several initial orbits.

The simulation cases differ in the following manner. In Case I, we completely neglect the pebble disk, thus the embryos interact only with the gaseous disk and among themselves. Their masses remain fixed and they do not release any heat into their vicinity. In Case II, the pebble disk is included and the embryos are allowed to accrete from it, but the corresponding accretion heating is still switched *off*. Therefore the heating torque cannot operate. Finally, Case III is the same as Case II except the accretion heating is switched *on*. Case I represents a relatively standard scenario (comparable e.g. with Pierens 2015) in which one can study interactions of multiple embryos with the non-isothermal radiative disk. We already made some predictions of the embryo migration rates for this case in Sect. 3.3.

Figure 4 (top panel) shows the temporal evolution of the oscillating semimajor axis a , periastron distance $q_p = a(1 - e)$ and apoastron distance $Q_a = a(1 + e)$ of embryos. At the beginning, embryos 1 and 2 (purple and blue curves, respectively) migrate outwards while embryos 3 and 4 (orange and red curves) migrate inwards, in accordance with the preliminary migration map (Fig. 3). After $\approx 8 \text{ kyr}$ of convergent migration towards the zero-torque radius, the outermost three embryos become locked in mutual mean-motion resonances which start to excite their orbital eccentricities. The innermost embryo catches up with the resonant chain at $\approx 17 \text{ kyr}$ and shortly after its eccentricity excitation it undergoes a close encounter with the second embryo during which they switch positions in the disk. As embryo 1 is scattered outwards, it interacts with embryo 3 in a series of close encounters which, due to damping effects of the surrounding disk, end up in a formation of a coorbital pair (1:1 commensurability). The system remains stable for the rest of the simulation.

3.5. Case II – introducing pebble disk and embryo growth by pebble accretion

In Case II, the pebble disk is considered and the embryos grow by pebble accretion. The pebble accretion rate onto individual embryos, which sets their mass growth and eventually the amount of heat released to their surroundings (Sect. 3.6), is

O. Chrenko et al.: Eccentricity excitation and merging of planetary embryos heated by pebble accretion

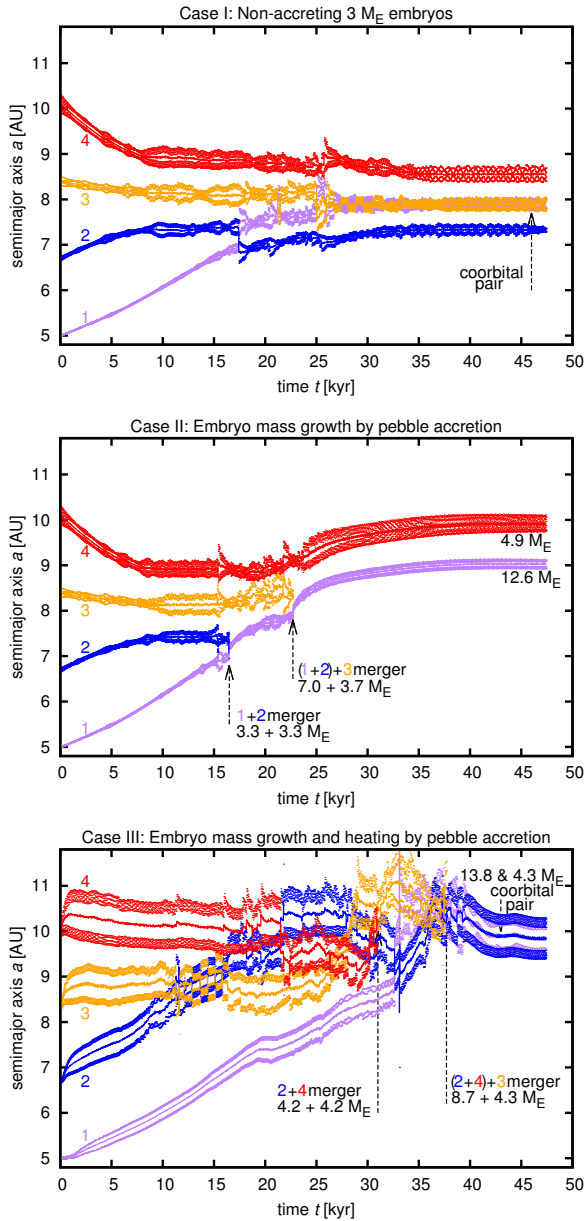


Fig. 4. Temporal evolution of semimajor axes $a(t)$, periastron distances q_p and apoastron distances Q_a of four embryos with the initial mass $3 M_E$ in three distinct simulation cases: Case I neglecting the pebble disk (*top*), Case II including the pebble disk but only allowing for the mass growth of embryos by pebble accretion (*middle*) and finally Case III, considering also the effect of accretion heating (*bottom*). Embryos are numbered from 1 to 4. Additional arrows and labels indicate mergers or coorbital pairs detected in the simulations, with corresponding embryo masses which can grow by pebble accretion (Cases II and III) or merging. Striking differences are observed in Case III as the migration rates are modified by the heating torque, orbits become moderately eccentric shortly after the simulation starts and the evolution is more violent compared to Cases I and II.

shown in Fig. 5 in terms of the filtering factor F , defined as

$$F \equiv \frac{\dot{M}_{em}}{\dot{M}_F}. \quad (41)$$

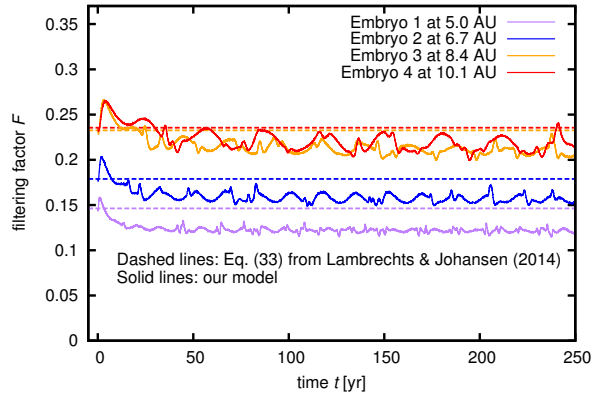


Fig. 5. Filtering factor F measured for the embryos at the beginning of Case II (solid curves); also applicable in Case III. As a comparison (dashed lines), we plot the filtering factors calculated at $t = 0$ according to formula (33) from Lambrechts & Johansen (2014). The analytical prediction is in good agreement with results of our model.

We plot its temporal dependence with respect to a fixed value of the radial pebble mass flux, $\dot{M}_F = 2 \times 10^{-4} M_E$. We compare the filtering factor measured at the beginning of Case II with the analytical formula from Lambrechts & Johansen (2014) which we applied on the equilibrium disk model. At $t = 0$, F is in an excellent agreement with the analytical prediction and at later times, the differences are not larger than 3%. Temporal oscillations of F are due to the nature of the accretion algorithm implementation. The expected embryo mass change ΔM_{expec} (Eq. (32)) depends on the instantaneous $\bar{\Sigma}_p$ within the accretion radius. The amount of removed pebbles per Δt is not precisely balanced by the inflow of new pebbles so the removal and inflow adapt to each other. If, for example, density waves are propagating near an accreting embryo, they can temporarily increase the concentration of pebbles ($\bar{\Sigma}_p$) and we observe an increase of F . Such variations cannot be reproduced by the Lambrechts & Johansen (2014) model because it is not hydrodynamic. We verified that the filtering factors measured in Case II are in agreement with those obtained later in Case III. Finally, we notice that the outermost embryo is the fastest grower which is because $F \sim 1/\eta$ (Lambrechts & Johansen 2014) and η is smaller in the outer part of the disk (Fig. 2). However, the differences in F between individual embryos are rather marginal and the mass growth by pebble accretion initially proceeds in the oligarchic fashion, as expected (Morbidelli & Nesvorný 2012).

The orbital evolution of embryos in Case II is shown in the middle panel of Fig. 4. At first, the embryos evolve similarly to Case I, but the interaction among embryos 1 and 2 results in a merger at $t \approx 16.5$ kyr. The resulting mass of the merger is $6.6 M_E$. As the system adapts to the loss of one of its members and to the suddenly increased mass of the merger, embryo 3 is pushed slightly outwards and encounters embryo 4. One of these events scatters embryo 3 inwards where it eventually collides with the previous merger. The collision takes place at $t \approx 22.7$ kyr and merges masses $3.7 M_E$ (embryo 3) and $7 M_E$ (previous merger). The remaining embryos are stabilised at somewhat distant orbits in comparison with Case I. The embryo masses at the end of the simulation are $12.6 M_E$ (the inner one) and $4.9 M_E$ (the outer one). The outer embryo 4 gained $1.9 M_E$ by pebble accretion during the simulation time span.

Let us emphasise that as the mergers naturally occur in the system of pebble-accreting embryos, they immediately break the oligarchic growth of the embryos by pebble accretion; instead of multiple similar-sized embryos, a dominant massive core is formed within the system. In the light of this statement, models that estimate the final planetary masses by tracking a single pebble-accreting protoplanet (e.g. Bitsch et al. 2015) probably underestimate how massive the planets can actually become, at least near the zero-torque radii.

Because of possible strong sensitivity to the initial conditions, the significance of the differences that we identified between Cases I and II is debatable. To partially answer this question, we ran two more simulations for each case. In the first additional set we increased the initial inclinations to about $\approx 1^\circ$ and in the second additional set we started from a more closely-packed system of embryos with orbital separations equal to 4.5 mutual Hill radius $R_{\text{mH}} = 0.5(a + a')[(q + q')/3]^{1/3}$. In these additional simulations, Case I always resulted in one merger before the system became stabilised, whereas in Case II, we always detected two mergers. The larger number of mergers in Case II occurs because the resonant chains are destabilised more often. The destabilisation is provided by the mass growth which changes the strength of the resonant forcing and the streamline topology near the embryos, thus modifying the acting torques. At the same time, more massive embryos have a larger encounter cross-section. Yet our simulation statistics are too poor to estimate corresponding probabilities or merging in Cases I and II.

3.6. Case III – introducing heating by pebble accretion

We now discuss Case III, presented in the bottom panel of Fig. 4. The system evolves differently after the beginning of the simulation compared to the previous cases. First of all, the dispersion of both q_p and Q_a with respect to a is much larger in the presence of accretion heating. In other words, the orbits of embryos are more eccentric. We find $e \approx 0.02$ for the innermost embryo 1 and $e \approx 0.04$ for the outermost embryo 4 after 5 kyr of evolution, while the corresponding values in Case II were $e \approx 0.004$ and $e \approx 0.01$, respectively. Moreover, the increased eccentricity is not produced by the resonant forcing; it is observable already before the embryos form a closely-packed configuration. Looking at the beginning of the simulation, we see a brief period during which both the semimajor axis and orbital eccentricity swiftly increase, especially for the three outer embryos. It seems that this period of evolution must represent a transitional state of the system during which the hydrodynamic background adjusts to the presence of the new heat source and the orbits react accordingly. The ability of the gas disk to circularise the orbits is clearly reduced in this case which is a new and unexpected phenomenon, explored in detail in Sect. 4.

Modified disk torques. Another surprising feature is that the inner embryos 1 and 2 are able to maintain outward migration despite having moderate eccentricity. We recall that the eccentricity growth leads to shrinking of the horseshoe region, and the corotation torque Γ_c in its unsaturated non-linear limit depends on the half-width of the horseshoe region x_{hs} (Paardekooper & Papaloizou 2009) as $\Gamma_c \sim x_{\text{hs}}^4$ (Fendyke & Nelson 2014). The positive contribution of Γ_c in the region of outward migration is thus expected to vanish with increasing eccentricity (Bitsch & Kley 2010). Yet, we observe that the migration of the inner embryos 1 and 2 is still directed outwards with a rate similar to Cases I and II and the torques even

allow the embryos to penetrate into the outer disk. As for the outer embryos 3 and 4, their migration first proceeds inwards (except for a short initial phase) but with significantly reduced migration rate.

It is worth noting that the zero-torque radius is somewhat ignored by embryos in Case III. As a result, we do not see the embryos to become closely-packed around ≈ 7.5 AU like in the previous cases. Instead, embryo 2 swiftly penetrates into the outer disk and interacts with embryo 3, and shortly after that with embryo 4. Meanwhile, embryo 1 reaches the expected location of the zero-torque radius and stays there for a while, being stopped by interactions with embryo 3. But ultimately, it continues outwards, migrating along with embryo 3 almost as a pair.

Examining the excited orbital eccentricities properly, we notice that $e \approx h$. Therefore one can expect significant modifications of the Lindblad torque (Papaloizou & Larwood 2000; Cresswell & Nelson 2006) as the eccentric embryos exhibit radial excursions in the disk and variations of the orbital velocity, thus periodically exciting density waves propagating inwards and outwards during the orbit. In such a case, the Lindblad torque, which is usually negative, can become reduced, or even reversed. Regarding the heating torque, its contribution is positive. But we emphasise that because of the increased eccentricity and due to narrowing of the horseshoe region, we can expect the heating torque to operate in a mode that was not described by Benítez-Llambay et al. (2015) who studied the heating torque for planets on fixed circular orbits. Here we summarise that the migration rate in Case III is driven by the modified Lindblad and heating torques acting on eccentric orbits. Detailed investigation of the torques accompanying the accretion heating is provided in Sect. 4.4.

Merging and resonant chain instabilities. Once the embryos become closely packed, they interact violently because their eccentric orbits drive one another into frequent close encounters. At $t \approx 12$ kyr, embryos 2 and 3 become temporarily locked in a coorbital resonance which is disrupted by convergent migration towards the outer embryo 4. The three outer embryos then strongly interact and swap positions several times before there is a first merger of two $4.2 M_E$ embryos (blue and red) at ≈ 31 kyr. Three-body interactions of the remaining embryos produce another merger at ≈ 37.7 kyr when $8.7 M_E$ embryo (blue) and $4.3 M_E$ embryo (orange) collide. The system is stabilised by formation of a coorbital pair, having final masses of $13.8 M_E$ and $4.3 M_E$.

Although the system evolves into a 1:1 orbital resonance at the end, it is not capable of establishing a global resonant chain during its evolution, apart from temporal resonant captures. This is different with respect to Cases I and II where the system becomes resonant once the embryos become closely packed and stays that way except for occasional instabilities during encounters, orbital swapping, and embryo merging. The decreased probability of resonant capture is again caused by excited eccentricities, as discussed, for example, by Batygin (2015).

Regarding the possibility of mergers, their number is the same as in Case II but they occur later during the evolution. This is slightly surprising because we already argued that close encounters are more frequent, and therefore a natural question arises – why do mergers not appear sooner? To provide a basic statistical check, as in Cases I and II, we performed two additional simulations, the first with initially smaller orbital separations ($4.5 R_{\text{mH}}$) and the second with slightly larger inclinations ($\approx 1^\circ$). The first simulation produced only one merger, the second

O. Chrenko et al.: Eccentricity excitation and merging of planetary embryos heated by pebble accretion

produced none. At the same time, we confirmed the strong eccentricity increase unrelated to mutual close encounters which became frequent as a consequence of the eccentricity growth.

The reduced merging efficiency compared to Case II is probably another consequence of larger eccentricities which lead to larger relative velocities during encounters and subsequently, merging is more difficult. Regarding the second additional simulation with zero mergers, we find that orbital inclinations are not reduced enough before the close encounters start to occur. Due to larger encounter velocities, vertical stirring is observed, maintaining the inclinations above zero. Such an inclined orbital configuration is not suitable for merging.

We remark that the influence of the accretion heating on the system’s evolution and stability may be even more evident if higher numbers of embryos are considered, which is what we intend to study in the future (as proposed in Sect. 5).

In both Cases II and III, we see that mergers produce embryos massive enough to potentially become giant planet cores. However, this subsequent evolution is not covered in our simulations as the gravitational attraction and subsequent collapse of a massive gaseous envelope is a delicate and not well understood process which is beyond the scope of this paper (e.g. [Ayliffe & Bate 2009](#); [Machida et al. 2010](#)).

Gas and pebble surface density. To begin the investigation of the unexpected eccentricity growth related to accretion heating, we first compare snapshots of the gas and pebble surface density in Cases II and III. Figure 6 shows Σ and Σ_p in Case II, after 4.7 kyr of evolution. The gas disk exhibits typical features – embryos launch spiral arms and produce minor density variations in their horseshoe regions. The pebble disk is affected by the ongoing pebble accretion. Accreting embryos carve partial gaps in the pebble component along their orbits. The gap has two parts; one of them is trailing and the other one is leading the orbital motion of an embryo (which is oriented counter-clockwise in all plots). The formation of these two parts can be explained simply by the trajectories of pebbles with respect to the embryo ([Morbidelli & Nesvorný 2012](#)) – those drifting from outside meet the embryo head-on, and those which have drifted across the embryo’s orbit catch up with it from behind. After a portion of the pebble flux is filtered out by the embryo, there is a paucity of pebbles behind it, slightly outside the embryo’s orbit, and another cavity is formed in the direction of orbital motion, slightly inside the embryo’s orbit.

Figure 7 shows Σ and Σ_p in Case III, again in simulation time 4.7 kyr. We see that the shape of spiral arms is somewhat modified, which is to be expected as the embryos already orbit with considerable eccentricities ([Cresswell et al. 2007](#); [Bitsch & Kley 2010](#)). The gaps in the pebble disk are slightly skewed and widened because the eccentric embryos perform radial excursions while carving the gaps. But looking at Σ , there is a strange feature; underdense structures trailing the embryos, starting at their locations and stretching slightly to $r > r_{em}$. An explanation of these underdensities, as well as investigation of the eccentricity growth, is given in the following section.

4. The “hot-trail” effect – the orbital eccentricity excitation due to accretion heating

In order to understand the process leading to the eccentricity excitation and also to the formation of underdense structures in the gas distribution adjacent to the embryos, we must first check whether we can recover these phenomena in simulations with a

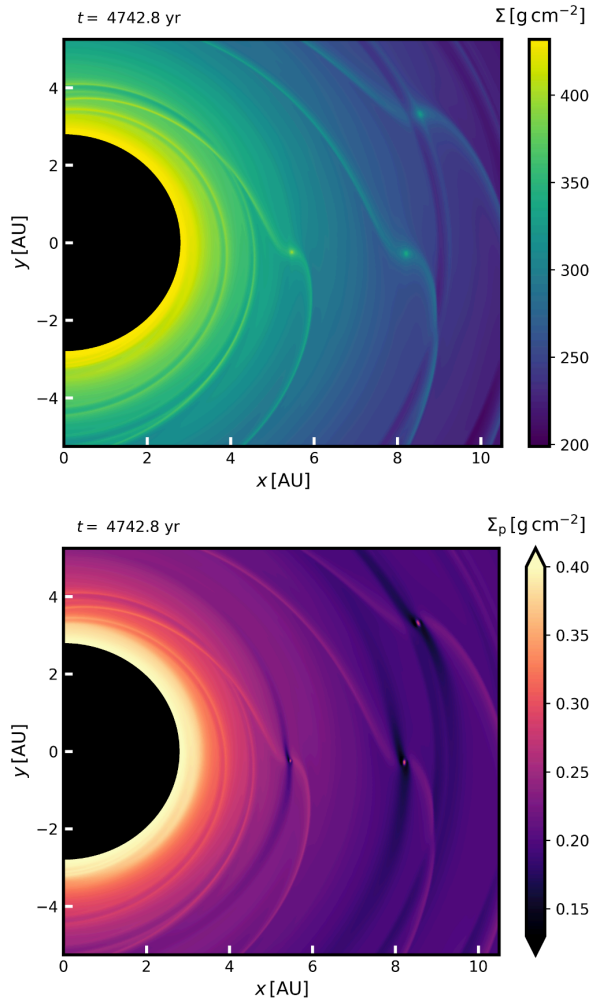


Fig. 6. A closeup of the gas surface density Σ (*top*) and pebble surface density Σ_p (*bottom*) after ≈ 5 kyr of evolution in the simulation with pebble accretion but *without* accretion heating, i.e. Case II. The gaps in the pebble disk are opened by accreting planetary embryos. A fourth embryo is also present in the system but it is located outside the range.

single embryo. This should verify whether the disk \leftrightarrow embryo interaction *alone* is sufficient to raise the eccentricity, without the help of any additional perturbers.

Starting again with the equilibrium fiducial disk, we placed a single $3 M_E$ embryo on an orbit with semimajor axis $a = 6.5$ AU. The orbit was initially circular in one case, and $e_0 = 0.05$ was assigned to the embryo in another case. Both the circular and the eccentric orbits were evolved for several hundred years; (i) in the gas disk only with fixed embryo mass, and (ii) with pebble accretion and respective heating considered. The embryo was allowed to fully interact with the disk, that is, the orbit was not held fixed.

Let us first examine the eccentricity evolution in these four simulation setups, as shown in Fig. 8. In simulations with fixed embryo mass, the initially circular orbit oscillates around small eccentricity values and the initially eccentric orbit is being damped and almost circularised ($e = 0.003$). On the other hand, e in simulations with accretion heating converges to moderate

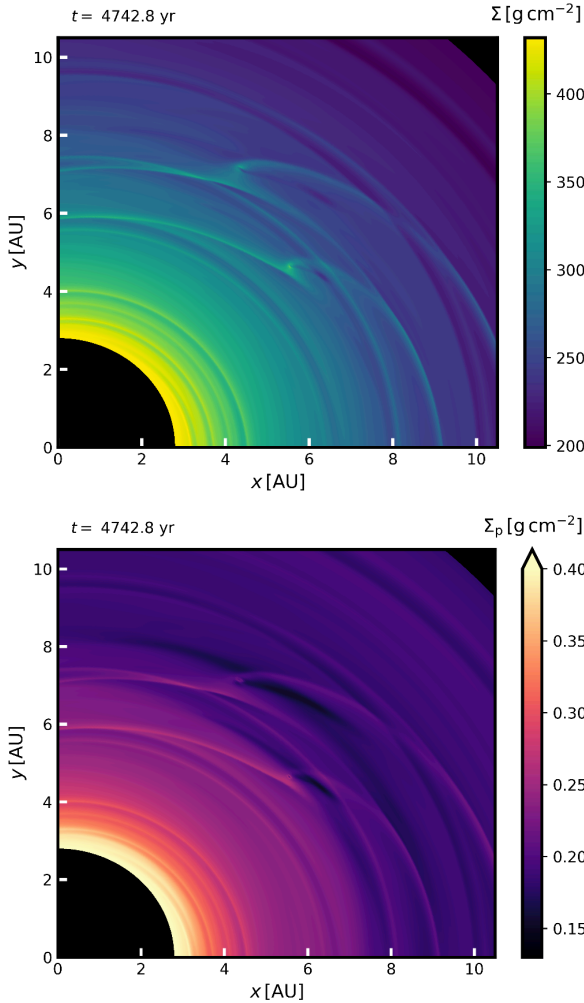


Fig. 7. Same as Fig. 6 but for the simulation *with* accretion heating (Case III). Two embryos are located at $x = 5.55, y = 4.65$ AU and $x = 4.35, y = 7.17$ AU; two other embryos are located outside the range. The Σ distribution shows that there are trails of underdense gas stretching outwards from the embryos, trailing their orbital motion. The shape of cavities in the pebble component is affected by the eccentric orbits of embryos. Unlike in Fig. 6, the concentration peak at the embryos' location is somewhat blurred in both gas and pebbles.

non-zero value ($e = 0.03$), even for the initially circular orbit. Therefore the eccentricity excitation and reduced eccentricity damping that we identified in Sect. 3.6 are indeed reproduced.

The simulation with $e_0 = 0$ and heating by pebble accretion is the most interesting one because it proves that the embryo can gain and sustain eccentricity solely due to forces arising from the disk. We therefore discuss this simulation in detail for the remainder of this section. Looking at the red curve in Fig. 8, it is obvious that there are several distinct stages during which the eccentricity excitation rate changes. We pick three characteristic times $t \approx 180, 360$, and 1130 yr at which we investigate the disk-embryo interaction during one orbital period. We refer to these three evolutionary stages as the *onset*, *growth*, and *saturation* phase for brevity.

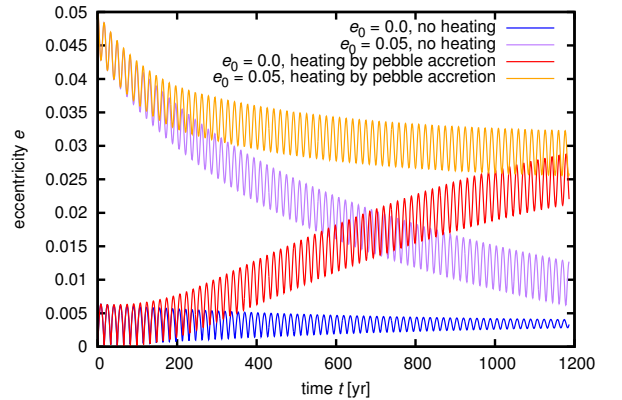


Fig. 8. Temporal evolution of the osculating eccentricity $e(t)$ for a single $3 M_E$ embryo in four distinct simulation setups. In the first two setups we neglect pebble accretion and the initial eccentricity is $e_0 = 0$ (blue curve) and $e_0 = 0.05$ (purple curve). In the other two setups, we consider pebble accretion and heating, the initial eccentricity being again $e_0 = 0$ (red curve) and $e_0 = 0.05$ (orange curve). Accretion heating reduces the eccentricity damping efficiency for the eccentric orbit and excites the eccentricity of the circular orbit.

In order to identify contributions from the disk responsible for de/dt variations, we employ the Gauss perturbation equation for the eccentricity

$$\frac{de}{dt} = \frac{\sqrt{1-e^2}}{na} [\mathcal{R} \sin f + \mathcal{T}(\cos f + \cos E)], \quad (42)$$

where n denotes the embryo's mean motion, \mathcal{R} and \mathcal{T} are the radial and tangential components of the perturbing acceleration arising from the disk, f is the true anomaly and E is the eccentric anomaly, for which one can write $\cos E = (e + \cos f)/(1 + e \cos f)$. Assuming that the variation of orbital elements during one orbital period is negligible, we can limit ourselves to an analysis of the Gauss factors inside the square brackets in Eq. (42). We shall denote $G_r \equiv \mathcal{R} \sin f$ and $G_\theta \equiv \mathcal{T}(\cos f + \cos E)$.

4.1. Radial perturbation

Figure 9 (top panel) shows the values of G_r acting on the embryo as it travels along its orbit during the onset, growth, and saturation phases. Because \mathcal{R} itself is always negative and almost identical in all the individual phases, G_r also does not change significantly. It is a f -periodic function and we find it to be typically an order of magnitude stronger than G_θ . Thus from the dynamical point of view, it is responsible for fast variations of the orbital eccentricity which occur on the orbital time scale. The varying $e(t)$ function corresponding to the onset phase is overplotted in Fig. 9 (dashed curve). As the embryo moves from the periastron towards the apoastron, $G_r < 0$ implies $de/dt < 0$ which decreases e , and vice versa. Because of G_r symmetry, the respective changes of the eccentricity average out and do *not* lead to secular variations.

The existence of non-zero radial acceleration \mathcal{R} is due to the gas surface density profile of the surrounding disk which is in general an outward-decreasing power-law function. Consequently, within an arbitrary radius around the embryo, one can expect overabundance of gas inwards from the orbit, while the mass of the gas outwards is smaller.

O. Chrenko et al.: Eccentricity excitation and merging of planetary embryos heated by pebble accretion

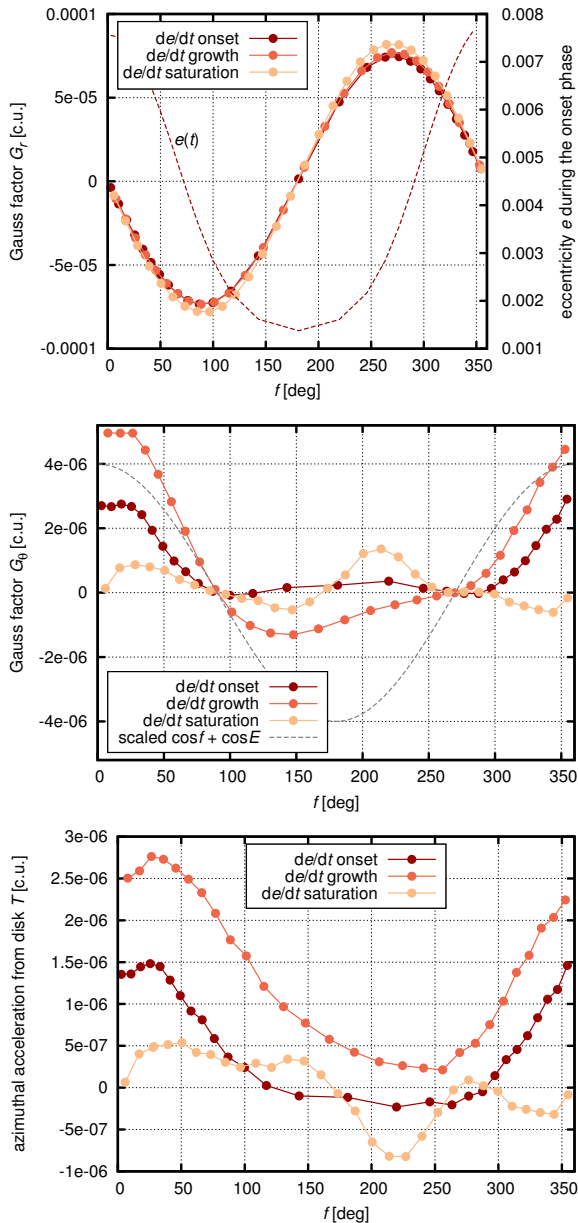


Fig. 9. Measures of the gravitational acceleration from the disk acting on the embryo, evolving from initially circular orbit in the presence of pebble accretion and the heating torque (i.e. red curve in Fig. 8). The values are recorded during one orbital period (represented by the true anomaly f), at around $t \approx 180, 360$ and 1130 yr of the simulation, that is, during the onset, growth, and saturation phase of the eccentricity excitation. *Top:* evolution of the Gauss factor $G_r \equiv \mathcal{R} \sin f$ (left vertical axis) and the osculating eccentricity e , which was recorded during the onset phase (right vertical axis). *Middle:* evolution of the Gauss factor $G_\theta \equiv \mathcal{T}(\cos f + \cos E)$. The function $(\cos f + \cos E)$ for $e = 0.005$ heated to the axis range is also given for reference (grey dashed curve). *Bottom:* the azimuthal acceleration \mathcal{T} from the disk.

4.2. Azimuthal perturbation

As argued above, G_r is related to the orbital frequency in the e -oscillations and cannot cause the runaway growth of the

eccentricity. Consequently, G_θ must be responsible for the secular changes and we plot it in the middle panel of Fig. 9. In order to guide the eye, we overplot the $(\cos f + \cos E)$ function for $e = 0.005$, scaled down to the figure range; it represents a dependence which G_θ would follow if \mathcal{T} was a constant positive acceleration. Examining the G_θ profile measured in our simulation, we notice there are some asymmetries during the orbital period which can accumulate in time and cause e to grow.

During the onset phase, G_θ is maximum when the embryo is at periastron and shortly afterwards. Then it decreases to zero as $f \rightarrow 90^\circ$, stays at low positive values through the apoastron passage and at $f \approx 290^\circ$ it finally starts to increase back to the maximum value. G_θ averaged over one orbital period is positive which implies $de/dt > 0$, in agreement with the onset of the eccentricity excitation in Fig. 8.

The azimuthal acceleration \mathcal{T} related to G_θ is plotted in the bottom panel of Fig. 9. We see that the embryo undergoes strong positive acceleration in the direction of its orbital motion around the periastron, with the peak slightly shifted to $f \approx 30^\circ$. From $f \approx 110^\circ$ to $f \approx 290^\circ$, \mathcal{T} has a flat profile and is negative. In terms of the expected gas distribution, there must be an accumulation of mass in front of the embryo around the periastron. For the rest of the orbit, this accumulation should become weaker and from $f \approx 110^\circ$ to $f \approx 290^\circ$, an excess of gas behind the embryo's orbital motion is expected.

In the growth phase, the azimuthal acceleration \mathcal{T} remains positive for the entire orbit, having a similar orbital evolution as in the onset phase, with an enhanced peak near the periastron, followed by decrease and plateau towards the apoastron. Consequently, G_θ has an increased amplitude but it also becomes negative from $f = 90^\circ$ to 270° . Despite that, the averaged G_θ is again positive and so is de/dt . The shape of $\mathcal{T}(f)$ tells us that we can expect the gas distribution around the embryo to be denser ahead of the embryo for the *entire* orbit.

During the saturation phase, the azimuthal acceleration \mathcal{T} has a somewhat complex dependence on f . Its overall amplitude is smaller compared to the previous phases by an order of magnitude. The acceleration \mathcal{T} remains positive from periastron to apoastron and it is negative through the remaining half of the orbit, apart from a short interval at around $f \approx 275^\circ$. Looking at the respective G_θ dependence, its shape is quite similar to a π -periodic function in f , oscillating around zero, having two maxima between the periastron and $f = 90^\circ$ and between the apoastron and $f = 270^\circ$ and vice versa.

4.3. Hydrodynamic explanation of the eccentricity excitation

In the following, we explain the eccentricity excitation from the hydrodynamic point of view. For this purpose, we present a series of figures capturing the gas density Σ and temperature T distribution in the embryo's vicinity, corresponding to the onset phase (Fig. 10) and the saturation phase (Fig. 11).

Let us first recall the advection-diffusion problem which causes the standard mode of the heating torque on fixed circular orbits according to Benítez-Llambay et al. (2015). The embryo heats the gas near its position and the gas becomes overdense², in order to maintain the pressure balance with the surroundings. The heated gas is being advected by the nearby flows and in the meantime, its internal energy changes by the radiative diffusion. For a circular orbit of the embryo, the gas from the outer part of the disk approaches the

² We remind the reader that our model can only produce an underdensity in terms of the surface density Σ .

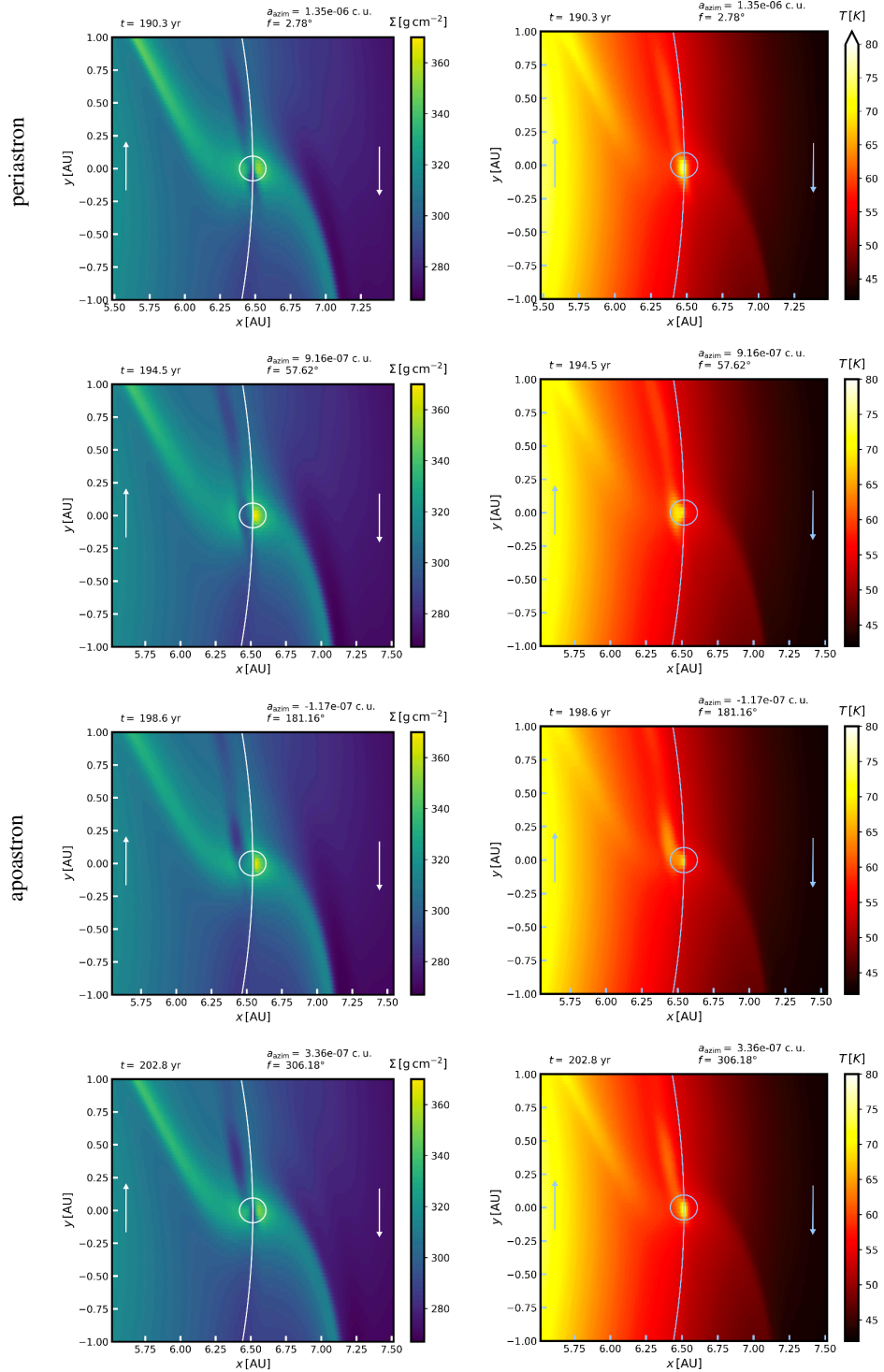


Fig. 10. Evolution of the gas surface density Σ (left column) and temperature T (right column) during one orbital period, recorded within the onset phase of the eccentricity growth. Individual snapshots are labelled with the respective simulation time t , embryo's true anomaly f and azimuthal acceleration imposed by the disk, labelled here a_{azim} . The figures are transformed to the corotating frame centered on the embryo. The Hill sphere and embryo's osculating orbit are plotted and we also indicate general directions of the gas flow with respect to the embryo by arrows. The orbital direction of the embryo is directed counterclockwise and the protostar is located at $(x = 0, y = 0)$. The *top row* depicts the situation in the periastron, while the *third row* corresponds to the apoastron. The *second row* is recorded approximately halfway from periastron to apoastron, and vice versa for the *bottom row*.

O. Chrenko et al.: Eccentricity excitation and merging of planetary embryos heated by pebble accretion

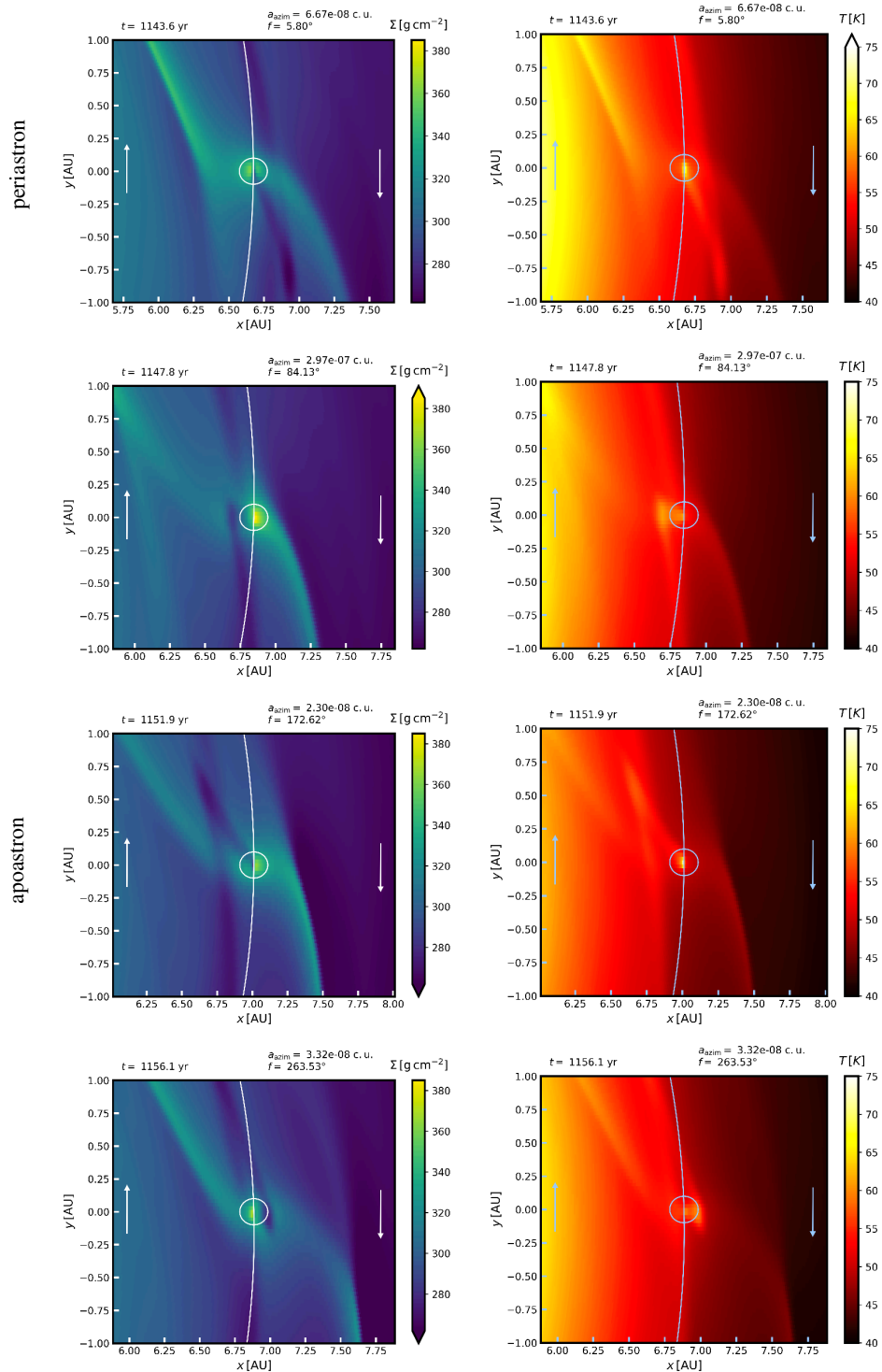


Fig. 11. Same as Fig. 10 but the hydrodynamic quantities are recorded within the saturation phase of the eccentricity excitation.

embryo head-on, is heated, and forms an underdense lobe behind the embryo. The gas from the inner disk, which is moving faster than the embryo, approaches from behind, forming an underdense lobe in front of the embryo. Because the gas velocity

is sub-Keplerian, the corotation between the embryo and the gas is shifted slightly inwards, and therefore there is a prevalence of gas approaching as the headwind, and the underdense lobe behind the embryo is dominant.

For an embryo that is allowed to move freely in the disk, we already saw that the orbit is never perfectly circular. It periodically gains a small eccentricity ($\sim 10^{-3}$) due to the G_r forcing (Fig. 9). Thus the embryo makes small radial excursions in the disk (see the changing range of the x -axis in Fig. 10) as it performs a small epicyclic motion. The heat source located at the embryo's position trails this epicyclic motion. In the temperature map, the epicyclic motion manifests itself as a "hot trail", attached to the temperature maximum, which wobbles around between the individual snapshots. We thus name this new phenomenon the hot-trail effect.

Looking at the Σ profiles in Fig. 10, we see that in the periastron, there are again two underdense lobes, similar to the circular case. The deep lobe attached behind the embryo represents the dominant paucity of material. The less pronounced and more stretched lobe in front of the embryo is rather a leftover of the dominant lobe which was displaced by the epicyclic motion during the previous orbit. This is proved by the sequence of Σ profiles; as the embryo travels towards the apoastron, its radial distance increases, thus the dominant lobe is left at $r < r_{em}$ and subsequently moves ahead of the embryo due to the transport by the interior flows, which move faster than the embryo. In the meantime, the less dominant leftover lobe is being lost by the Keplerian shear and diffusive effects.

Near the apoastron, the embryo has the lowest orbital velocity. If we, for example, consider the eccentricity $e = 0.003$ (typical value due to the G_r forcing), the orbital velocity in the apoastron with respect to the Keplerian velocity is $v_{apo} = (1 - 0.003)v_K$. At the corresponding orbital distance $r \simeq 6.5$ AU, the gas orbital velocity is $v_\theta = (1 - 0.0026)v_K$ (cf. Fig. 2). The headwind therefore significantly vanishes and no additional lobe can be formed behind the embryo. The embryo is left with the lobe formed at the periastron which has already been transported by the flows interior to the orbit.

The position of the dominant underdense lobe is the key factor determining the resulting azimuthal acceleration \mathcal{T} acting on the embryo. In the periastron, there is a paucity of mass behind the planet, so the acceleration is in the orbital direction. In the apoastron, the lobe is located ahead of the embryo, but it is also radially displaced ($r < r_{em}$) with respect to the embryo. As a consequence, \mathcal{T} is negative but its magnitude is much smaller compared to that at periastron, where the underdense lobe is adjacent to the embryo. This asymmetry between the periastron and apoastron causes the eccentricity excitation.

During the growth phase (not shown in figures), the situation is similar to the onset phase. But as e continuously grows, the lobe at the periastron becomes prolonged because the relative velocity of the embryo with respect to the gas increases. As a consequence, the azimuthal acceleration \mathcal{T} measured in the periastron of the growth phase is larger compared to the onset phase. The relative velocities become large enough for the embryo to start feeling tailwind near the apoastron, which delivers heat to the lobe positioned ahead of the embryo at that time. But because the gas is sub-Keplerian, the relative velocity is always larger in the periastron than in the apoastron thus the positive eccentricity pumping during the periastron passage still prevails and the runaway eccentricity growth continues.

The eccentricity cannot grow indefinitely, however, but its excitation saturates at a certain level. The hydrodynamic state at the saturation phase is given in Fig. 11 where we see that the hot trail spans a larger portion of the embryo's surroundings because the radial excursion (the epicycle) of the embryo has already increased significantly. As a consequence, the underdense structures are more distant from the embryo and the Hill sphere can

refill with gas which is yet-to-be heated and which blurs asymmetries in the embryo's vicinity, responsible for the eccentricity excitation. At the same time, the underdense structures are strongly affected by the Keplerian shear because their radial extension is considerable.

At the saturation phase, the eccentricity growth stops right before exceeding the local value of the aspect ratio $h \simeq 0.036$. For $e \gtrsim h$, the relative motions could lead to the reversal of normally negative Lindblad torque (Papaloizou & Larwood 2000). Cresswell & Nelson (2006) found that the Lindblad torque transition for $e \gtrsim h$ is accompanied by very efficient eccentricity damping leading to a strong energy loss which can outweigh the angular momentum gain. This efficient damping is finally able to prevent the hot trail from exciting the eccentricity even more. But for lower e , the hot-trail effect dominates – otherwise the eccentricity would not grow in the first place.

4.4. Torque distribution

The periodic changes of Σ and of the related \mathcal{T} are also reflected in the variations of the torque Γ_{tot} felt by the embryo during its orbit. Figure 12 shows the normalised radial torque distribution $\Gamma(r)/\Gamma_0$ which relates to the total torque Γ_{tot} as

$$\Gamma_{tot} = \int_{r_{min}}^{r_{max}} \Gamma(r) dr. \quad (43)$$

Figure 12 generally demonstrates which parts of the disk are responsible for positive and negative torques and how the magnitude of these torques changes with radial separation from the embryo.

During the onset phase (Fig. 12, top panel), the shape of $\Gamma(r)/\Gamma_0$ is similar to the calculations of (Benítez-Llambay et al. 2015; cf. their Fig. 1). In the periastron, it exhibits a negative peak at $r < r_{em}$ that is smaller than a positive peak at $r > r_{em}$. As the embryo travels along its orbit, the difference compared to Benítez-Llambay et al. (2015) is in the position of the profile with respect to the embryo (indicated with arrows) and in the asymmetry between the positive and negative peak. The asymmetry is pronounced in the periastron and disappears in the apoastron, in accordance with our previous findings.

During the saturation phase (Fig. 12, bottom panel), $\Gamma(r)/\Gamma_0$ becomes wavy and complex. It corresponds to the hot trail strongly distorted by the Keplerian shear, which is produced by a large epicycle. Compared to the onset phase, the torque contribution arising from the density waves is modified. Let us focus on the situation in periastron first. Looking at Fig. 11, we notice that the gas surface density exhibits a pronounced inner density wave. The underdense structure related to the hot-trail effect is located at $r > r_{em}$ thus the dominant contribution to $\Gamma(r)$ at $r < r_{em}$ must be related to the inner density wave.

The contribution from the inner density wave is labelled in Fig. 12 (bottom panel). Although the inner Lindblad torque is purely positive for circular orbits, we can see that it has both positive and negative contributions for the eccentric orbit during the saturation phase. In the apoastron, the situation is similar (but the outer density wave is more pronounced). This implies that the orbit is indeed close to the state of the Lindblad torque reversal and proves our aforementioned argument about what phenomenon finally stops the eccentricity growth.

O. Chrenko et al.: Eccentricity excitation and merging of planetary embryos heated by pebble accretion

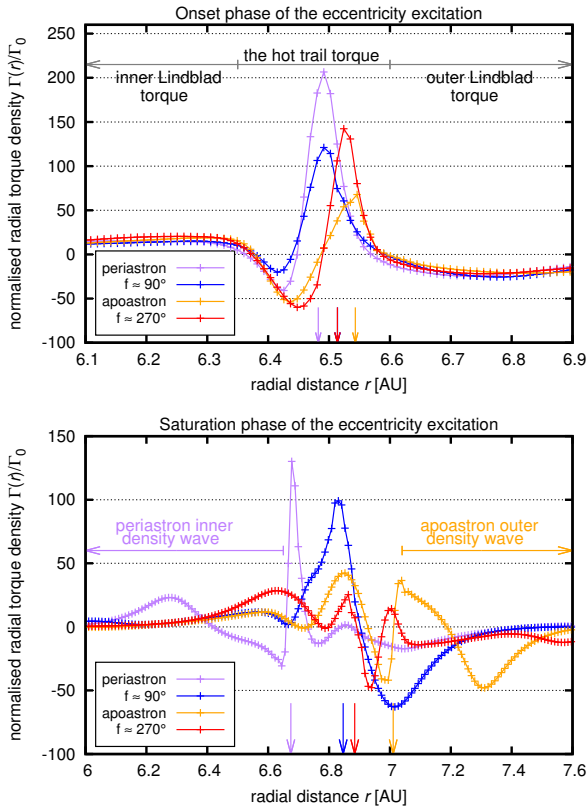


Fig. 12. Radial torque density $\Gamma(r)$ acting on the embryo during the onset (*top*) and saturation (*bottom*) phases, normalised to Γ_0 . The individual curves represent measurements in the periastron (purple), apostron (orange) and in-between. The vertical arrows indicate the instantaneous radial distance of the embryo corresponding to the individual curves. The horizontal arrows and labels approximately distinguish some of the important torque contributions discussed in the text. To avoid misinterpretation, we remark that the hot-trail torque is acting in the *bottom panel* as well but it spans different radial extent for each curve and thus cannot be marked unambiguously.

5. Future improvements and observational signatures

Additional free parameters. Regarding the discussion in this paper, we essentially restricted ourselves to switching pebble accretion and the accretion heating on and off, in order to understand the basic physics of the hot-trail effect and to simplify the discussion. It is clear, however, that our problem has a number of additional free parameters. In particular, the number of embryos (up to 10^1 , for example); initial embryo masses (of the order of $10^0 M_E$); initial spacing of embryos (multiples of R_{mH}); embryo positions in the disk and with respect to the zero-torque radius; the radial pebble flux \dot{M}_F ; gas surface density Σ_0 and its slope; viscosity ν (or α); turbulent stirring of solids α_p ; or stellar luminosity L_* ; and so on. Even if we have only two values per parameter, the resulting number of models is so high that we are unable to compute a full matrix. Nevertheless, it is certainly possible to compute differences (derivatives) with respect to the fiducial model; work postponed to the following paper, in fact.

Possible model improvements. We can outline a number of opportunities for the hydrodynamic model extensions, for example, full 3D treatment, implementation of gas accretion, deposition of pebbles in various layers of protoatmospheres, gas self-gravity, stochastic forcing by turbulent flows (Pierens et al. 2013), independently evolved dust component as the main opacity constituent, and so on.

Moreover, as we demonstrated that the hot-trail effect reduces the ability of the surrounding disk to damp the orbital eccentricity, it is also possible that the inclination damping is somehow modified if a full 3D disk is considered. In our 2D model, the inclination damping is provided by Eq. (39) which is not self-consistent but based on a model that neglects the accretion heating (Tanaka & Ward 2004). We also plan to refine this part of the model in the future.

Observational signatures. From an observational point of view, the imprints of various migration histories and orbital excitations should be recognisable in the observed exoplanetary systems, but they can be successfully understood only when the effects described in this paper are taken into account in future works dealing with this issue.

There could be observational signatures of, for example, mergers or multiple embryos on closely-packed orbits in the datasets of the campaigns involved in the direct protoplanetary disk imaging (e.g. by ALMA). We have already started to investigate this possibility and plan to publish the study in a separate paper.

In our case, most if not all observational circumstances should be determined by 3D radiative transfer in the dust continuum. The optical thickness for the typical Bell & Lin (1994) opacity $\kappa \approx 10^0 \text{ cm}^2 \text{ g}^{-1}$ and the surface density $\Sigma \approx 10^2 \text{ g cm}^{-2}$ is $\tau_{\text{opt}} \approx \kappa \Sigma \approx 10^2 \gg 1$. We thus definitely need a good enough description of the disk atmosphere, far from the midplane.

In order to become observable, it seems that protoplanets must open considerably large gaps in the gas disk (Rosotti et al. 2016). Partially opened gaps are probably not observable because these are still optically thick; the density contrast has to be at least 10^2 . The close encounters between embryos in our simulations lead to an asymmetry, but are only present for a short time interval. As argued in Rosotti et al. (2016), the threshold mass for detection is about $12 M_E$ in sub-mm. Moreover, for VLT/SPHERE or Gemini/GPI instruments, the protostar should be more massive ($M_* \approx 2 M_\odot$) to become at least a Herbig Ae star, because of current flux limitations.

6. Conclusions

In this paper, we studied the orbital evolution of four $3 M_E$ embryos embedded in a region of a protoplanetary disk where the convergent migration is expected to occur under the influence of the standard Type-I torques. In our simulations, however, we considered that the embryos rapidly accrete mass from the pebble disk (modelled hydrodynamically). Three classes of simulations were performed: Case I as a reference scenario in which pebble accretion is completely neglected, Case II in which pebble accretion leads to the mass growth of embryos and Case III in which embryos also become heated by the deposition of pebbles. We investigated the impact of the additional processes on the migration and mutual interactions of the embryos. The simulations were performed using a new state-of-the-art and rather self-consistent hydrodynamical model, which we extensively described and verified.

We found that in both Cases I and II, the system evolves through a sequence of resonant chains, the first of which is usually established around the zero-torque radius. As the embryos gain non-zero eccentricity (typically ranging from 0.004 to 0.01) due to perturbations from the mean-motion resonances, occasional close encounters are possible, leading to mutual scattering (sometimes accompanied by a swap of orbits) or embryo merging.

We reported that merging of embryos is more probable in Case II in which the mass growth by pebble accretion is accounted for. The reason for this is that the resonant chain is destabilised more often as the masses of embryos responsible for the resonant forcing (e.g. of eccentricities) evolve. Additional forcing is provided as the streamline topology around the embryos changes with the evolving masses, thus imposing a slightly different disk torque.

In Case III, the positive heating torque changes the expected migration rates. As a result, the embryos somewhat ignore the zero-torque radius and are driven into mutual interactions preferentially in the outer part of the disk, rather than being packed in a resonant chain around the zone of convergence.

Close encounters occur frequently in Case III and cover a longer period of the evolution. We realised that the encounters are facilitated by an eccentricity increase ($e \approx h$, typically ranging from 0.02 to 0.04) prior to resonant perturbations by means of a new ‘hot-trail’ effect. The effect is due to variable gravitational acceleration arising from the gas in the vicinity of each embryo, which is periodically modified by formation and advection of an overheated and thus underdense lobe trailing the epicyclic motion of the embryo. The effect was independently reported by Eklund & Masset (2017; we also refer to Masset & Velasco Romero 2017) while our research was ongoing (Chrenko & Brož 2016). The hot trail effect reduces the ability of the surrounding disk to damp the eccentricities and circularise the orbits. Despite the fact that more encounters pose more opportunities for merging, we actually found that merging is less frequent compared to Case II, probably because of larger encounter velocities on the eccentric orbits.

The eccentricity excitation by the hot-trail effect stalls when $e \approx h$ because the Lindblad torque acting on eccentric orbits is modified and can actually operate in a mode close to its reversal (from negative to positive, Papaloizou & Larwood 2000; Cresswell et al. 2007; Bitsch & Kley 2010). Because the transition to the reversed Lindblad torque would require the embryo to cross the orbital resonances at which it excites the density waves, strong eccentricity damping occurs and the eccentricity growth saturates. Nevertheless, the eccentricity does not decrease and is, in fact, maintained by the hot-trail effect. We note that many N -body models (e.g. Sándor et al. 2011; Izidoro et al. 2015; Coleman & Nelson 2016, and many others) usually employ a strong eccentricity damping prescription (e.g. Cresswell & Nelson 2006, 2008) derived from hydrodynamic models which neglect the accretion heating. We suggest that these analytic damping rates should be carefully refined for future applications because they could be inaccurate in cases when the protoplanets undergo any kind of strong accretion.

Orbital excitation of embryos heated by pebble accretion prevents formation of a global resonant chain, except for short transient periods. An interesting overlap of this result can be found with recent developments in the analytical theory. For example, Batygin (2015) used the Hamiltonian formalism to study the probability of the resonant capture for migrating low-mass planets and compared his predictions with the occurrence of the first-order mean-motion resonances in exoplanetary systems. He

found that the probability of the resonant capture is greatly diminished (and thus the observed non-resonant systems can be explained) if a pre-encounter orbital excitation $e \gtrsim 0.02$ is considered. Our model thus provides a natural way of exciting the eccentricity enough to prevent resonant locking and may have important implications for explaining the structure of exoplanetary systems.

Mergers large enough to possibly become giant planet cores with masses $\approx 13 M_E$ were found in both Cases II and III. We emphasise that merging caused by fast migration and accretion in convergence zones breaks the otherwise oligarchic nature of the embryo growth by pebble accretion.

We conclude that orbital instabilities, eccentricity excitations and (possibly) mergers naturally accompany evolution of pebble-accreting embryos and may have an important impact on shaping the final architecture of any planetary system. This is a major result compared to previous models which neglected self-consistent hydrodynamics, accretion or heating. But in order to find general implications, a larger statistical sample of simulations is required because we expect a strong dependence on the initial conditions (possibly on the initial number and masses of embryos, their position within the disk, accretion rate related to the pebble mass flux and heating efficiency influenced by the opacity).

Acknowledgements. We thank Alessandro Morbidelli, Steven N. Shore and David Nesvorný for helpful discussions during this project. We are very grateful to Bertram Bitsch who kindly provided his code for calculating the migration maps. We also thank an anonymous referee for valuable comments. The work of O.C. and M.B. has been supported by Charles University in Prague (project GA UK No. 128216; project SVV-260441). The work of M.B. was supported by the Grant Agency of the Czech Republic (grant No. 13-01308S). Access to computing and storage facilities owned by parties and projects contributing to the National Grid Infrastructure MetaCentrum, provided under the program “Projects of Large Research, Development, and Innovations Infrastructures” (CESNET LM2015042), is greatly appreciated.

References

- Adachi, I., Hayashi, C., & Nakazawa, K. 1976, *Prog. Theor. Phys.*, **56**, 1756
 Ayliffe, B. A., & Bate, M. R. 2009, *MNRAS*, **393**, 49
 Baillié, K., & Charnoz, S. 2014, *ApJ*, **786**, 35
 Baruteau, C., & Masset, F. 2008, *ApJ*, **672**, 1054
 Batygin, K. 2015, *MNRAS*, **451**, 2589
 Bell, K. R., & Lin, D. N. C. 1994, *ApJ*, **427**, 987
 Benítez-Llambay, P., Masset, F., Koenigsberger, G., & Szulágyi, J. 2015, *Nature*, **520**, 63
 Birnstiel, T., Klahr, H., & Ercolano, B. 2012, *A&A*, **539**, A148
 Bitsch, B., & Kley, W. 2010, *A&A*, **523**, A30
 Bitsch, B., & Kley, W. 2011, *A&A*, **536**, A77
 Bitsch, B., Crida, A., Morbidelli, A., Kley, W., & Dobbs-Dixon, I. 2013, *A&A*, **549**, A124
 Bitsch, B., Morbidelli, A., Lega, E., Kretke, K., & Crida, A. 2014, *A&A*, **570**, A75
 Bitsch, B., Lambrechts, M., & Johansen, A. 2015, *A&A*, **582**, A112
 Chiang, E. I., & Goldreich, P. 1997, *ApJ*, **490**, 368
 Chrenko, O., & Brož, M. 2016, in AAS/Division for Planetary Sciences Meeting Abstracts, **48**, 318.03
 Clarke, C. J., & Pringle, J. E. 1988, *MNRAS*, **235**, 365
 Coleman, G. A. L., & Nelson, R. P. 2016, *MNRAS*, **457**, 2480
 Commerçon, B., Teysier, R., Audit, E., Hennebelle, P., & Chabrier, G. 2011, *A&A*, **529**, A35
 Cresswell, P., & Nelson, R. P. 2006, *A&A*, **450**, 833
 Cresswell, P., & Nelson, R. P. 2008, *A&A*, **482**, 677
 Cresswell, P., Dirksen, G., Kley, W., & Nelson, R. P. 2007, *A&A*, **473**, 329
 Crida, A., & Bitsch, B. 2017, *Icarus*, **285**, 145
 Cuzzi, J. N., Dobrovolskis, A. R., & Champney, J. M. 1993, *Icarus*, **106**, 102
 D’Alessio, P., Cantó, J., Calvet, N., & Lizano, S. 1998, *ApJ*, **500**, 411
 D’Angelo, G., & Marzari, F. 2012, *ApJ*, **757**, 50
 D’Angelo, G., Henning, T., & Kley, W. 2003, *ApJ*, **599**, 548
 de Val-Borro, M., Edgar, R. G., Artymowicz, P., et al. 2006, *MNRAS*, **370**, 529

O. Chrenko et al.: Eccentricity excitation and merging of planetary embryos heated by pebble accretion

- Dullemond, C. P. 2002, *A&A*, 395, 853
- Eklund, H., & Masset, F. S. 2017, *MNRAS*, 469, 206
- Espaillet, C., D'Alessio, P., Hernández, J., et al. 2010, *ApJ*, 717, 441
- Espaillet, C., Muzerolle, J., Najita, J., et al. 2014, in *Protostars and Planets VI* (University of Arizona Press), 497
- Everhart, E. 1985, in *Dynamics of Comets: Their Origin and Evolution*, Proceedings of IAU Colloq., 83, held in Rome, Italy, June 11–15, 1984, eds. A. Carusi, G. B. Valsecchi (Dordrecht: Reidel), *Astrophys. Space Sci. Lib.*, 115, 185
- Fedele, D., van den Ancker, M. E., Henning, T., Jayawardhana, R., & Oliveira, J. M. 2010, *A&A*, 510, A72
- Fendyke, S. M., & Nelson, R. P. 2014, *MNRAS*, 437, 96
- Flock, M., Fromang, S., González, M., & Commerçon, B. 2013, *A&A*, 560, A43
- Flock, M., Fromang, S., Turner, N. J., & Benisty, M. 2016, *ApJ*, 827, 144
- Garaud, P. 2007, *ApJ*, 671, 2091
- Guillot, T., Ida, S., & Ormel, C. W. 2014, *A&A*, 572, A72
- Hubeny, I. 1990, *ApJ*, 351, 632
- Izidoro, A., Raymond, S. N., Morbidelli, A., Hersant, F., & Pierens, A. 2015, *ApJ*, 800, L22
- Jäger, C., Dorschner, J., Mutschke, H., Posch, T., & Henning, T. 2003, *A&A*, 408, 193
- Johansen, A., & Klahr, H. 2005, *ApJ*, 634, 1353
- Johansen, A., Oishi, J. S., Mac Low, M.-M., et al. 2007, *Nature*, 448, 1022
- Keith, S. L., & Wardle, M. 2014, *MNRAS*, 440, 89
- Klahr, H., & Kley, W. 2006, *A&A*, 445, 747
- Kley, W. 1989, *A&A*, 208, 98
- Kley, W. 1999, *MNRAS*, 303, 696
- Kley, W., & Dirksen, G. 2006, *A&A*, 447, 369
- Kley, W., Bitsch, B., & Klahr, H. 2009, *A&A*, 506, 971
- Kretke, K. A., & Levison, H. F. 2014, *AJ*, 148, 109
- Kretke, K. A., & Lin, D. N. C. 2012, *ApJ*, 755, 74
- Lambrechts, M., & Johansen, A. 2012, *A&A*, 544, A32
- Lambrechts, M., & Johansen, A. 2014, *A&A*, 572, A107
- Lega, E., Crida, A., Bitsch, B., & Morbidelli, A. 2014, *MNRAS*, 440, 683
- Levermore, C. D., & Pomraning, G. C. 1981, *ApJ*, 248, 321
- Levison, H. F., Kretke, K. A., & Duncan, M. J. 2015, *Nature*, 524, 322
- Lin, D. N. C., & Papaloizou, J. 1985, in *Protostars and Planets II*, eds. D. C. Black, & M. S. Matthews (University of Arizona Press), 981
- Lin, D. N. C., & Papaloizou, J. 1986, *ApJ*, 309, 846
- Machida, M. N., Kokubo, E., Inutsuka, S.-I., & Matsumoto, T. 2010, *MNRAS*, 405, 1227
- Masset, F. 2000, *A&AS*, 141, 165
- Masset, F. S. 2002, *A&A*, 387, 605
- Masset, F. S., & Velasco Romero, D. A. 2017, *MNRAS*, 465, 3175
- Mathis, J. S., Rumpl, W., & Nordsieck, K. H. 1977, *ApJ*, 217, 425
- Menou, K., & Goodman, J. 2004, *ApJ*, 606, 520
- Mihalas, D., & Weibel Mihalas, B. 1984, *Foundations of radiation hydrodynamics* (New York: Oxford University Press)
- Morbidelli, A., & Nesvorný, D. 2012, *A&A*, 546, A18
- Morbidelli, A., Crida, A., Masset, F., & Nelson, R. P. 2008, *A&A*, 478, 929
- Morbidelli, A., Lambrechts, M., Jacobson, S., & Bitsch, B. 2015, *Icarus*, 258, 418
- Müller, T. W. A., & Kley, W. 2012, *A&A*, 539, A18
- Müller, T. W. A., & Kley, W. 2013, *A&A*, 560, A40
- Müller, T. W. A., Kley, W., & Meru, F. 2012, *A&A*, 541, A123
- Nakagawa, Y., Sekiya, M., & Hayashi, C. 1986, *Icarus*, 67, 375
- Paardekooper, S.-J., & Papaloizou, J. C. B. 2008, *A&A*, 485, 877
- Paardekooper, S.-J., & Papaloizou, J. C. B. 2009, *MNRAS*, 394, 2297
- Paardekooper, S.-J., Baruteau, C., & Kley, W. 2011, *MNRAS*, 410, 293
- Papaloizou, J. C. B., & Larwood, J. D. 2000, *MNRAS*, 315, 823
- Paxton, B., Marchant, P., Schwab, J., et al. 2015, *ApJS*, 220, 15
- Pierens, A. 2015, *MNRAS*, 454, 2003
- Pierens, A., Cossou, C., & Raymond, S. N. 2013, *A&A*, 558, A105
- Rein, H., & Liu, S.-F. 2012, *A&A*, 537, A128
- Rein, H., & Spiegel, D. S. 2015, *MNRAS*, 446, 1424
- Rosotti, G. P., Juhasz, A., Booth, R. A., & Clarke, C. J. 2016, *MNRAS*, 459, 2790
- Sándor, Z., Lyra, W., & Dullemond, C. P. 2011, *ApJ*, 728, L9
- Stone, J. M., & Norman, M. L. 1992, *ApJS*, 80, 753
- Tanaka, H., & Ward, W. R. 2004, *ApJ*, 602, 388
- van Leer, B. 1977, *J. Comput. Phys.*, 23, 276
- Weidenschilling, S. J. 1977, *MNRAS*, 180, 57
- Winn, J. N., & Fabrycky, D. C. 2015, *ARA&A*, 53, 409
- Youdin, A. N., & Goodman, J. 2005, *ApJ*, 620, 459
- Youdin, A. N., & Lithwick, Y. 2007, *Icarus*, 192, 588
- Zhang, X., Liu, B., Lin, D. N. C., & Li, H. 2014, *ApJ*, 797, 20

Appendix A: Numerical scheme of the energy equation solver

This appendix summarises our approach to modelling non-isothermal disks, which undergo heating and cooling, within the framework of the original 2D FARGO code. Here we elaborate the numerical update of the internal energy due to the considered source terms (Sect. 2). Following the formalism of Stone & Norman (1992), the advection term is treated separately in the transport step.

Starting with the energy equation (Eq. (3)), our aim is to derive an implicit numerical scheme. The reason for this is to avoid a possible time-step restriction which could arise in the case of an explicit solution due to the Courant-Friedrichs-Lewy condition related to the radiative transport. As discussed in Sect. 2, we assume that the specific internal energy is entirely thermal thus we can write $E = \Sigma c_V T$, where c_V is the specific heat at constant volume. Within the one-temperature approach, the radiation field with the energy density $4\sigma_R T^4/c$ only contributes to the energy transport via the radiative diffusion term. In order to obtain the implicit scheme, we rewrite Eq. (3) for the temperature only and we drop the advection term, which is treated separately

$$\frac{\partial \Sigma c_V T}{\partial t} = -\Sigma \frac{R}{\mu} T \nabla \cdot \mathbf{v} + Q_{\text{visc}} + Q_{\text{irr}} + Q_{\text{acc}} - Q_{\text{vert}} + 2H \nabla \cdot D \nabla T, \quad (\text{A.1})$$

where $D = 16\lambda\sigma_R T^3 / (\rho_0 \kappa)$ is the diffusion coefficient.

For simplicity, let us first discretise the diffusion term and return to the other source terms later on. Because FARGO is designed as a staggered-mesh code, all scalar quantities are cell-centred whereas components of vector quantities are face-centred. In the following, the differential operators are written in polar coordinates, and integers i and j represent the indices of radial zones and azimuthal sectors, respectively:

$$\begin{aligned} \frac{T_{i,j}^{n+1} - T_{i,j}^n}{\Delta t} &= \left(\frac{2H}{\Sigma c_V} \right)_{i,j} \frac{1}{r_i^c} \\ &\times \left[\frac{1}{(\Delta r)_i^f} \left(r_{i+1}^f \bar{D}_{i+1,j}^r \frac{T_{i+1,j} - T_{i,j}}{(\Delta r)_{i+1}^c} - r_i^f \bar{D}_{i,j}^r \frac{T_{i,j} - T_{i-1,j}}{(\Delta r)_i^c} \right) \right. \\ &\left. + \frac{1}{\Delta \theta} \left(\bar{D}_{i,j+1}^\theta \frac{T_{i,j+1} - T_{i,j}}{r_i^c \Delta \theta} - \bar{D}_{i,j}^\theta \frac{T_{i,j} - T_{i,j-1}}{r_i^c \Delta \theta} \right) \right]. \quad (\text{A.2}) \end{aligned}$$

Here r_i^c denotes the radial coordinate of a cell centre, r_i^f is the radius of an inner radial cell interface and $\Delta \theta$ denotes the angular width of sectors, which is identical for all cells. The additional quantities naturally occur because of the staggered-grid formalism:

$$\bar{D}_{i,j}^r = \frac{1}{2} (D_{i,j} + D_{i-1,j}), \quad (\text{A.3})$$

$$\bar{D}_{i,j}^\theta = \frac{1}{2} (D_{i,j} + D_{i,j-1}), \quad (\text{A.4})$$

$$(\Delta r)_i^c = r_i^c - r_{i-1}^c, \quad (\text{A.5})$$

$$(\Delta r)_i^f = r_{i+1}^f - r_i^f. \quad (\text{A.6})$$

Obviously, $(\Delta r)_i^c = (\Delta r)_i^f$ in the case of an equidistant radial spacing.

The implicit form can now be obtained by putting $T_{i,j}^{n+1} \equiv T_{i,j}$ and by placing all $T_{i,j}$ -dependent terms on one side of the left-hand side, while moving the remaining terms to the right-hand side. Because any non-linear terms in temperature would make the problem difficult to invert, we shall linearise the equation. To do so, the diffusion coefficients are evaluated using the hydrodynamic quantities from the beginning of the sub-step.

Concerning the remaining source terms and their linearity, Q_{visc} , Q_{acc} and Q_{irr} terms are temperature independent. The compressional heating term is linear in temperature and thus can be easily incorporated in the left-hand side. The vertical radiative cooling term Q_{vert} is proportional to T^4 but it can be linearised, as, for example, in Commerçon et al. (2011) or Bitsch et al. (2013). If the temperature changes over Δt are sufficiently small, we can rewrite Eq. (9) as

$$\begin{aligned} (Q_{\text{vert}})_{i,j} &= \frac{2\sigma_R}{(\tau_{\text{eff}})_{i,j}} (T_{i,j}^n)^4 \left(1 + \frac{T - T^n}{T^n} \right)_{i,j}^4 \\ &\approx \frac{2\sigma_R}{(\tau_{\text{eff}})_{i,j}} \left[4(T^n)^3 T - 3(T^n)^4 \right]_{i,j} \equiv (Q'_{\text{vert}} T - Q''_{\text{vert}})_{i,j}. \quad (\text{A.7}) \end{aligned}$$

After some algebraic rearrangements, we can formally write

$$\begin{aligned} A_{i,j} T_{i,j} + B_{i,j} T_{i+1,j} + C_{i,j} T_{i-1,j} + D_{i,j} T_{i,j+1} + E_{i,j} T_{i,j-1} = \\ T_{i,j}^n + \Delta t \left(\frac{Q_{\text{visc}} + Q_{\text{irr}} + Q_{\text{acc}} + Q'_{\text{vert}}}{\Sigma c_V} \right)_{i,j}, \quad (\text{A.8}) \end{aligned}$$

which is a linear matrix equation. To solve this linear problem, we use the successive over-relaxation (SOR) method with odd-even ordering. Our implementation is parallelised by the domain splitting which is complementary to the radial grid decomposition of the original FARGO code. The optimisation of the over-relaxation parameter is done similarly to Kley (1989).

Appendix B: Steady-state motion equations of a pebble

Here we reproduce the derivation of Eqs. (20) and (21) which are used to initialise the velocity field of the pebble disk. The approach is well known and closely follows the derivation of Adachi et al. (1976), with one clarification.

Let us study a system consisting of a pebble with negligible mass which orbits a massive primary M_\star and experiences the aerodynamic friction acceleration F_D in the gaseous environment at the same time. We further assume that the motion is confined to one plane and no vertical perturbations are present.

The dynamical equation for the pebble takes the form

$$\frac{d^2 \mathbf{r}}{dt^2} = -\frac{GM_\star}{r^3} \mathbf{r} + \mathbf{F}_D. \quad (\text{B.1})$$

Transforming into polar coordinates, one obtains

$$\frac{\partial V_r}{\partial t} + V_r \frac{\partial V_r}{\partial r} - \frac{V_\theta^2}{r} = -\frac{GM_\star}{r^2} - \frac{F_D}{v_{\text{rel}}} (V_r - v_r), \quad (\text{B.2})$$

$$\frac{\partial V_\theta}{\partial t} + V_r \frac{\partial V_\theta}{\partial r} - \frac{V_r V_\theta}{r} = -\frac{F_D}{v_{\text{rel}}} (V_\theta - v_\theta), \quad (\text{B.3})$$

where we utilise the fact that the friction force is directed against the relative velocity vector, having the magnitude

O. Chrenko et al.: Eccentricity excitation and merging of planetary embryos heated by pebble accretion

$v_{\text{rel}} = \sqrt{(V_r - v_r)^2 + (V_\theta - v_\theta)^2}$. Unlike [Adachi et al. \(1976\)](#), we retain the v_r component of the flow and allow for the radial transport in the gaseous disk (we also refer to [Guillot et al. 2014](#)).

Let us simplify the equations above by assuming a steady-state situation, $\partial_t = 0$. Furthermore, we only allow the drag force to cause small perturbations in pebbles' azimuthal velocity, compared to the local Keplerian rotation. We thus decompose $V_\theta = v_K + V'_\theta$, using $|V'_\theta| \lesssim \delta \ll v_K$. Similarly, the radial velocity of the pebble itself is considered to be highly sub-Keplerian $|V_r| \lesssim \delta \ll v_K$. We assume that the spatial derivatives of V'_θ and V_r are also as small as δ .

In Eq. (B.2), the first and the second term on the left-hand side can be neglected in our approximation, while the third term can be rearranged using the V_θ decomposition. Consequently

$$v_K^2 + 2v_K V'_\theta + \mathcal{O}(\delta^2) = v_K^2 + \frac{F_D}{v_{\text{rel}}} r (V_r - v_r), \quad (\text{B.4})$$

which is obviously equivalent to

$$2\Omega_K V'_\theta = \frac{F_D}{v_{\text{rel}}} (V_r - v_r). \quad (\text{B.5})$$

Concerning Eq. (B.3), the first term on the left-hand side can again be discarded but the radial derivative has to be performed, leading to

$$V_r \frac{\partial v_K}{\partial r} + \frac{V_r v_K}{r} + \mathcal{O}(\delta^2) = -\frac{F_D}{v_{\text{rel}}} (v_K + V'_\theta - v_\theta). \quad (\text{B.6})$$

A useful simplification of the right-hand side can be made using the η parameter, describing sub-Keplerian rotation of the gas as $v_\theta = (1 - \eta) v_K$, yielding

$$\frac{1}{2} \Omega_K V_r = -\frac{F_D}{v_{\text{rel}}} (V'_\theta + \eta v_K). \quad (\text{B.7})$$

Recalling the Stokes number definition $\tau = t_s \Omega_K = v_{\text{rel}} \Omega_K / F_D$, one can rewrite the set of Eqs. (B.5) and (B.7) as

$$V_r = -\frac{2}{\tau} (V'_\theta + \eta v_K), \quad (\text{B.8})$$

$$V'_\theta = \frac{1}{2\tau} (V_r - v_r). \quad (\text{B.9})$$

Final arithmetic rearrangements are required to eliminate V'_θ from V_r and then plug them both back into the V_θ decomposition. The resulting set of equations directly describes steady-state velocities of the drifting pebble ([Guillot et al. 2014](#))

$$V_r = -\frac{2\tau}{1 + \tau^2} \left(\eta v_K - \frac{1}{2\tau} v_r \right), \quad (\text{B.10})$$

$$V_\theta = v_K - \frac{1}{1 + \tau^2} \left(\eta v_K - \frac{\tau}{2} v_r \right). \quad (\text{B.11})$$

Appendix C: Semi-implicit source-term update of the pebble fluid

In order to perform the source step ([Stone & Norman 1992](#)) for the fluid of pebbles and avoid severe time-step limitations due to small friction time scales, we do not use the explicit integration scheme for pebbles and use the semi-implicit approach of [Rosotti et al. \(2016\)](#) instead.

Let us rewrite the fluid motion Eqs. (2) and (5) in a symbolic notation and without advection, which is solved separately. We have

$$\frac{\partial \mathbf{v}}{\partial t} = \mathbf{a}_g, \quad (\text{C.1})$$

$$\frac{\partial \mathbf{V}}{\partial t} = \mathbf{a}_p - \frac{\Omega_K}{\tau} (\mathbf{V} - \mathbf{v}), \quad (\text{C.2})$$

where \mathbf{a}_p is the non-drag acceleration of the pebble fluid and \mathbf{a}_g is now understood as the total acceleration acting on the gas which is calculated explicitly at time t . We note that the drag back-reaction term is contained in \mathbf{a}_g and is also evaluated explicitly. This is justified if the solid-to-gas ratio remains low (which is what we expect in our simulations). Under these assumptions, an analytical solution for the pebble fluid velocity update can be found ([Rosotti et al. 2016](#)):

$$\begin{aligned} \mathbf{V}^{n+1} &= \mathbf{V}^n \exp\left(-\Delta t \frac{\Omega_K}{\tau}\right) + \mathbf{a}_g \Delta t \\ &+ \left[\mathbf{v}^n + (\mathbf{a}_p - \mathbf{a}_g) \frac{\tau}{\Omega_K} \right] \left[1 - \exp\left(-\Delta t \frac{\Omega_K}{\tau}\right) \right]. \end{aligned} \quad (\text{C.3})$$

The solution conveniently provides a smooth transition between two limiting cases: when $\Delta t \ll \tau/\Omega_K$, the solution is equivalent to the explicit integration. If on the other hand $\Delta t \gg \tau/\Omega_K$, the solution turns into a form known as the short friction time approximation (e.g. [Johansen & Klahr 2005](#)).

To ensure the numerical stability, a CFL condition, additional to the one that controls the gas evolution, must be imposed on the time step Δt . The condition is given by

$$\Delta t = C \frac{\Delta x_{r,\theta}}{\max(V, V - v)_{r,\theta}}, \quad (\text{C.4})$$

where Δx is the cell size in the radial (index r) or azimuthal (index θ) direction and $C = 0.5$ is the Courant number.

Appendix D: Verification of the code

Embryo-disk interaction in radiative disks. Here we try to reproduce several recent advanced simulations of the embryo-disk interactions using our new hydrodynamic code. These test runs are compared to the original results in order to provide a verification of our code and some benchmarks. We note that most of the comparison models are 3D whereas our code is essentially 2D. The results of the verification runs therefore prove that we are indeed able to capture many aspects of 3D models if the physics is treated carefully. In the following, the stellar irradiation is always neglected as well as the pebble disk, and the opacity drop factor $c_\kappa = 0.6$ is introduced into the simulation parameters. Comparison figures are always provided in the unit systems corresponding to the original works.

First, we present a reproduction of an equilibrium gas disk corresponding to the initial setup of [Kley et al. \(2009\)](#) who performed simulations using the 3D NIRVANA code. The comparison of the radial temperature profile $T(r)$ is given in Fig. D.1. The surface density profile $\Sigma(r)$ is also displayed for reference (without a comparison curve for clarity of the figure). We see that $T(r)$ is in a good agreement with the 3D model, apart from variations in the inner disk. These are missing mostly because our 2D model does not support vertical convection.

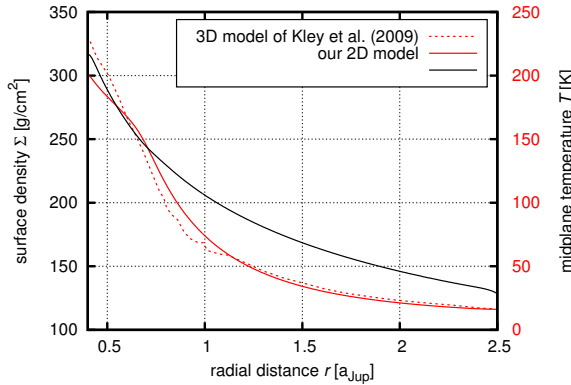


Fig. D.1. Equilibrium gas surface density $\Sigma(r)$ (black curve, left vertical axis) and temperature $T(r)$ profile (red curve, right vertical axis) in a radiative disk according to the setup from Kley et al. (2009), as it was reproduced by our code. Temperature profile obtained by the original 3D model of Kley et al. (2009) is given by the red dashed curve for comparison. The obtained disk is indeed in good agreement with the comparison simulation and serves as the hydrodynamic background for verification runs of the disk-embryo interaction.

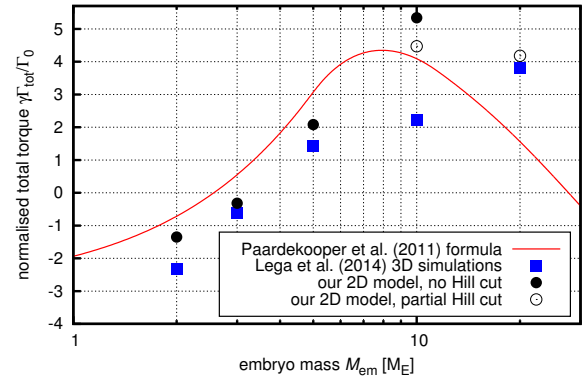


Fig. D.2. A comparison of the normalised total torque $\gamma\Gamma_{\text{tot}}/\Gamma_0$ acting on embryos of various masses M_{em} , moving on fixed circular orbits in the disk shown in Fig. D.1. The results achieved with our code are shown by black circles, or open circles if the Hill cut was applied. Values obtained by 3D calculations of Lega et al. (2014) are represented by blue squares. Formula from Paardekooper et al. (2011) applied to the equilibrium disk profile (with the potential smoothing parameter $\epsilon = 0.4$) is given by the red curve. We consider the differences between our model and the comparison simulations to be acceptable.

We use exactly this equilibrium disk to compare the embryo-disk interactions for various masses M_{em} . Since this work is focused on low-mass embryos, we perform tests with $M_{\text{em}} = 2, 3, 5, 10$ and $20 M_{\text{E}}$. This range of masses was studied by Lega et al. (2014) who used the 3D FARGO3 code and conveniently, the same equilibrium disk model was used in their work. The embryo mass $M_{\text{em}} = 20 M_{\text{E}}$ was also studied by Kley et al. (2009). It is customary to exclude part of the gas enclosed by the Hill sphere from the torque calculation (a so-called Hill cut) if the planet is massive enough to form a distinct circumplanetary disk. However, the determination of the threshold mass is not straightforward. Thus we always perform the Hill cut for $M_{\text{em}} = 20 M_{\text{E}}$ and for $M_{\text{em}} = 10 M_{\text{E}}$ we perform two simulations with and without the Hill cut. For lower masses, no gas is excluded from calculations.

After placing the embryos on fixed circular orbits with $a = a_{\text{Jup}} = 5.2 \text{ AU}$, we evolved the system for several tens of orbits until the torque converged to a stationary value. In Fig. D.2, we compare the measured normalised torques with results of Lega et al. (2014) as well as with the torque-mass dependence given by the formulae of Paardekooper et al. (2011), applied to the equilibrium disk. For low-mass embryos, the agreement seems good enough. The torque in our model is generally between the prediction of Paardekooper et al. (2011) and the result of the 3D model from Lega et al. (2014). The torque on the $M_{\text{em}} = 10 M_{\text{E}}$ embryo differs the most; nevertheless the result is improved when the Hill cut is applied. For the medium-mass embryo $M_{\text{em}} = 20 M_{\text{E}}$, we see that the value is in agreement with Lega et al. (2014) which is a desirable result as 3D models generally lead to torque that is larger than the prediction by Paardekooper et al. (2011) by a factor of 3 to 4 (Bitsch & Kley 2011) for the medium-mass embryos.

Lega et al. (2014) also discovered the so-called cold finger structure near low-mass embryos. These overdensity structures are responsible for a modification of the radial torque density profile, it is thus worth checking whether or not we can find these modifications using our code as well. In Fig. D.3, we plot the normalised radial torque density $\Gamma(r)/\Gamma_0$ (Eq. (43)) for $2 M_{\text{E}}$ and $3 M_{\text{E}}$ embryos, compared to corresponding results from

Lega et al. (2014). It is obvious that the strong positive and negative peaks are less pronounced in our case. As the cold finger is responsible for the enhancement of these peaks, the effect is not entirely recovered by our code. We conclude that this is due to the local nature of the cold-finger effect. In our model, the gas flow around an embryo follows the velocity field affected by the vertically averaged potential and the resulting compressional heating is not strong enough for the cold-finger effect to fully develop. Nevertheless, the overall torque magnitude obtained by our model is still viable (Fig. D.2) as the asymmetry of the positive versus negative contributions is preserved to a satisfactory level.

Finally, we compare the torque for the upper end of the tested embryo mass spectrum. Figure D.4 shows the radial specific torque density (not normalised) for $M_{\text{em}} = 20 M_{\text{E}}$ compared to the result of Kley et al. (2009). The agreement is very good in this case, with slight departures from the 3D model.

The heating torque. In order to assess how the heating torque is recovered by our code, we repeated the numerical experiment from Benítez-Llambay et al. (2015). Their setup is different from the verification runs above; namely the surface density profile is different and the opacity is assumed constant, $\kappa = 1 \text{ cm}^2 \text{ g}^{-1}$. Therefore, we prevented any vertical opacity drop ($\kappa = 1$) in our test. The stellar irradiation and pebble disk are again excluded. We use grid resolution $N_r = 738$ and $N_\theta = 1382$, unlike Benítez-Llambay et al. (2015) who used 512 cells in radius and 1024 cells in azimuth but also included colatitude.

An embryo with $M_{\text{em}} = 3 M_{\text{E}}$ is embedded in the disk at a_{Jup} after the relaxation phase and the static torque is measured. The source of the mass growth and accretion heating is simply parametrised using the embryo mass doubling time $\tau = M_{\text{em}}/\dot{M}_{\text{em}}$. We studied cases with fixed embryo mass and with $\tau = 30, 55, 92$ and 300 kyr . Shorter τ means higher accretion rate and should correspond to stronger heating torque.

The results of our test are shown in Fig. D.5 which can be directly compared with the original experiment in

O. Chrenko et al.: Eccentricity excitation and merging of planetary embryos heated by pebble accretion

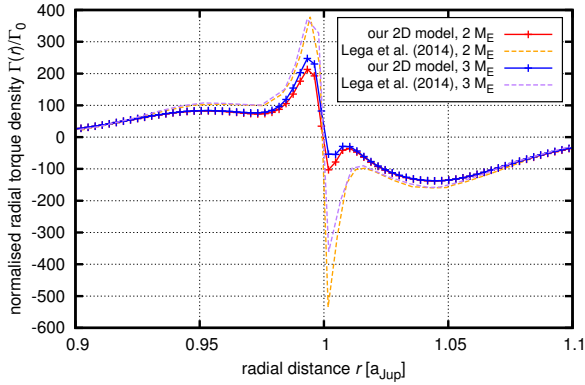


Fig. D.3. Normalised radial torque density $\Gamma(r)/\Gamma_0$ acting on $2 M_E$ and $3 M_E$ embryos as obtained by our code (red and blue curve, respectively). Results of the original 3D experiment from [Lega et al. \(2014\)](#) are given for comparison (orange dashed curve for $2 M_E$ and purple dashed curve for $3 M_E$). As the cold finger structure is not entirely reproduced by our code, the torque density peaks are less pronounced. However, the overall torque (i.e. the integral of $\Gamma(r)$ over r) is still in very good agreement with the 3D model (cf. [Fig. D.2](#)).

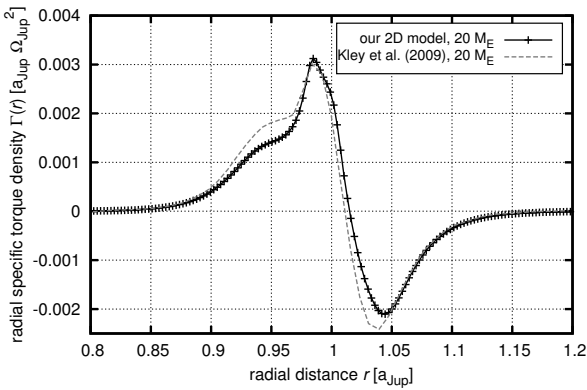


Fig. D.4. Radial density of the specific torque $\Gamma(r)$ acting on a $20 M_E$ embryo as calculated by our code (black curve). The comparative profile from the original 3D experiment of [Kley et al. \(2009\)](#) is represented by the grey dashed line. Again, the agreement is very good.

[Benítez-Llambay et al. \(2015\)](#); cf. their [Fig. 2](#). First, it is important to notice that the steady-state torque on the embryo in the absence of heating is less negative in our case. This

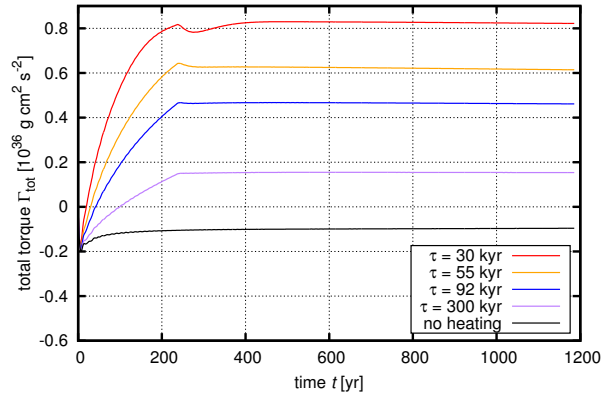


Fig. D.5. Total torque Γ_{tot} measurement in the experiment according to [Benítez-Llambay et al. \(2015\)](#), reproduced using our 2D code. The $3 M_E$ embryo is either non-accreting (black curve) or growing with the doubling time τ (we refer to the legend). The positive heating torque becomes stronger with high accretion rates corresponding to short doubling times.

essentially corresponds to [Fig. D.2](#), where we found that the torque acting on the low-mass embryos in our model is always more positive than in 3D models. Another reason might be related to the midplane resolution which is slightly better in our test, thus we cover the embryo's horseshoe region with more cells. According to [Lega et al. \(2014\)](#), increasing the resolution of the horseshoe region makes the torque more positive.

Because the torque in the absence of heating is less negative compared to [Benítez-Llambay et al. \(2015\)](#), it is easier for even the low accretion rates and respective luminosities to revert the migration because the heating torque does not have to compete with strong negative counteracting torques.

Finally, the torque scaling with increasing accretion rate is more efficient in our model than in the original 3D model. We notice that the total difference between the torque with $\tau = 30$ kyr and the torque without accretion is $\Delta\Gamma \approx 0.9 \times 10^{36} \text{ g cm}^2 \text{ s}^{-2}$, compared to $\Delta\Gamma \approx 0.6 \times 10^{36} \text{ g cm}^2 \text{ s}^{-2}$ found by the 3D modelling. The slight discrepancy is again caused by the vertically averaged flow field around the planet (as already discussed for the cold-finger effect) and also due to the simplified treatment of the radiative diffusion which in our case is acting only in the midplane and is replaced by an approximation of the radiation escape in the vertical direction. Yet, we consider the heating torque to be reproduced accurately enough and we shall strive in future works to achieve an improved agreement with the 3D model.

2.1.2 Corrigendum

In 2019, we found an error in the `Thorin` code. The hydrodynamic field of the sound speed c_s was not recalculated before the update of planet-disk accelerations¹. At a given time t , $c_s(t - \delta t)$ was entering the calculation rather than $c_s(t)$, with δt being the internal timestep of `Fargo` determined by the Courant-Friedrichs-Lewy (CFL) condition. In this section, we provide a reproduction of Cases I–III from Paper I performed with a corrected version of `Thorin`. Our aim is to investigate the error introduced in our original simulations. We plan to publish this corrigendum in near future.

Fig. 2.1 shows the orbital evolution in Cases I–III. Unlike in Paper I, the zero-torque radius is shifted *inwards* with respect to the location predicted by formulae of Paardekooper et al. (2011) ($r_{\Gamma=0} \simeq 7$ au; see also Fig. 1.19). It is established approximately at 5.5 au. This shift is actually more consistent with previous works and we explain it as follows: once the eccentricities of protoplanets become excited (by resonant perturbations in Cases I and II, and by the hot-trail effect in Case III), reduction of the corotation torque (Sect. 1.4.4) diminishes the contribution of the positive entropy-related horseshoe drag and outward migration is no longer possible. Such an inward shift of the zero-torque radius was already described, for example, by Cossou et al. (2013) and Pierens et al. (2013). In the corrected Case III, the heating torque does not seem to be able to shift the zero-torque radius outwards which is significantly different from Paper I. Nevertheless, major conclusions, in particular the hot-trail effect, remain the same.

In Paper I, Cases I and II led to formation of a resonant chain which, however, was prone to instabilities. Fig. 2.1 shows a different evolution. Protoplanets in corrected Cases I and II establish a resonant chain which is stable over the simulation timespan 120 kyr (the timespan was only $\simeq 50$ kyr in Paper I). In the corrected Case III, eccentricity excitation by the hot-trail effect prevents formation of a stable resonant chain. Consequently, protoplanets undergo close encounters and a merger occurs, directly forming a giant planet core. This is in accordance with Paper I, although the frequency of close encounters seems rather reduced. Orbital evolution in the corrected Case III is not finished during the simulation timespan. However, it would not be safe to prolong the simulation because our model from Paper I does not account for gas accretion and thus the transition from Type I to Type II migration would not be captured correctly.

It is natural to ask whether the incorrect treatment of c_s affected the verification tests of `Thorin` presented in Appendix D of Paper I. The answer is no (at least not substantially). Since majority of these tests was performed for a single protoplanet in a corotating frame, the frame rotation compensated for the lag of the c_s field. Finally, we point out that the lag would have zero impact on evolution of a disk without embedded protoplanets because c_s was correctly updated when solving RHD equations even in the old version of `Thorin`.

¹In the calculation, c_s is needed to derive correct scale heights H for vertical integrations of gas distribution using the method of Müller et al. (2012).

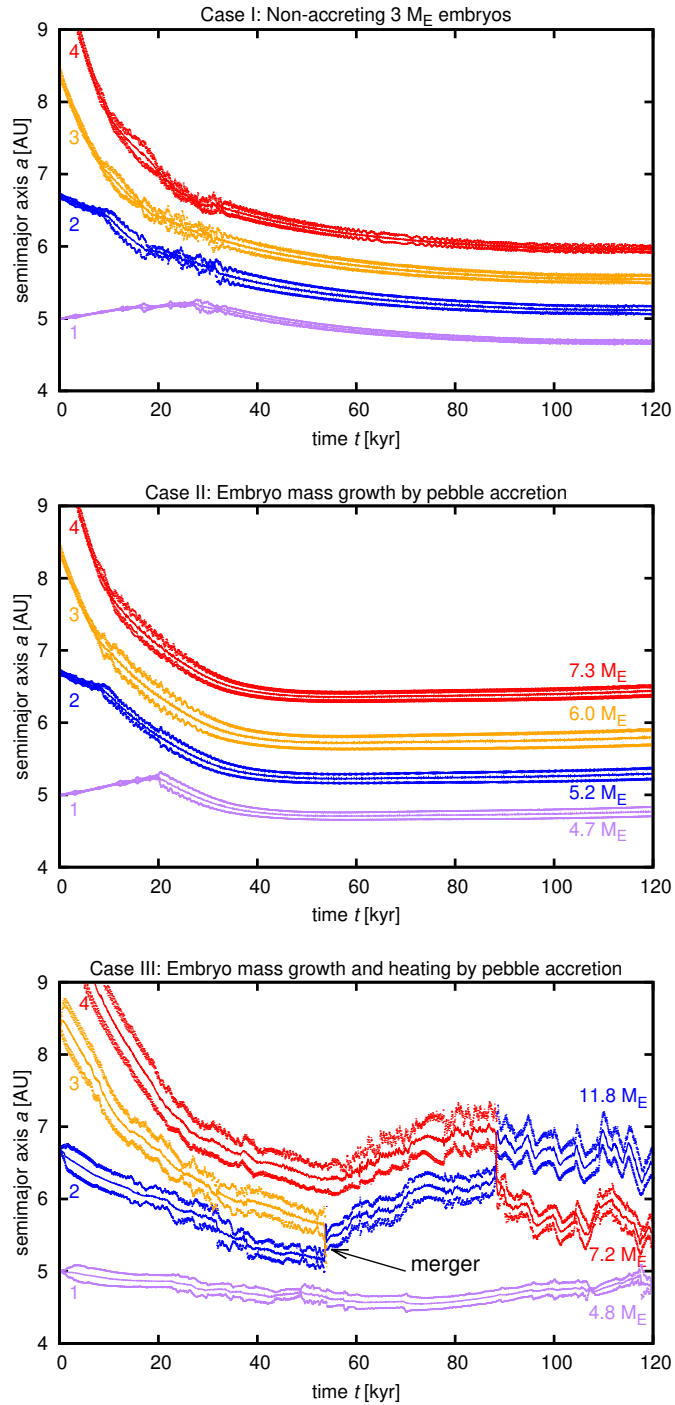


Figure 2.1: Cases I–III recalculated with a corrected version of Thorin. Overall, there is an inward shift of the zero-torque radius with respect to the original results of Paper I. Stable resonant chains are established in Cases I and II, while resonant locking is prevented in Case III due to eccentricity excitation by the hot-trail effect. Orbital instabilities lead to a merger and formation of a giant planet core ($M_p \gtrsim 10 M_\oplus$) in Case III.

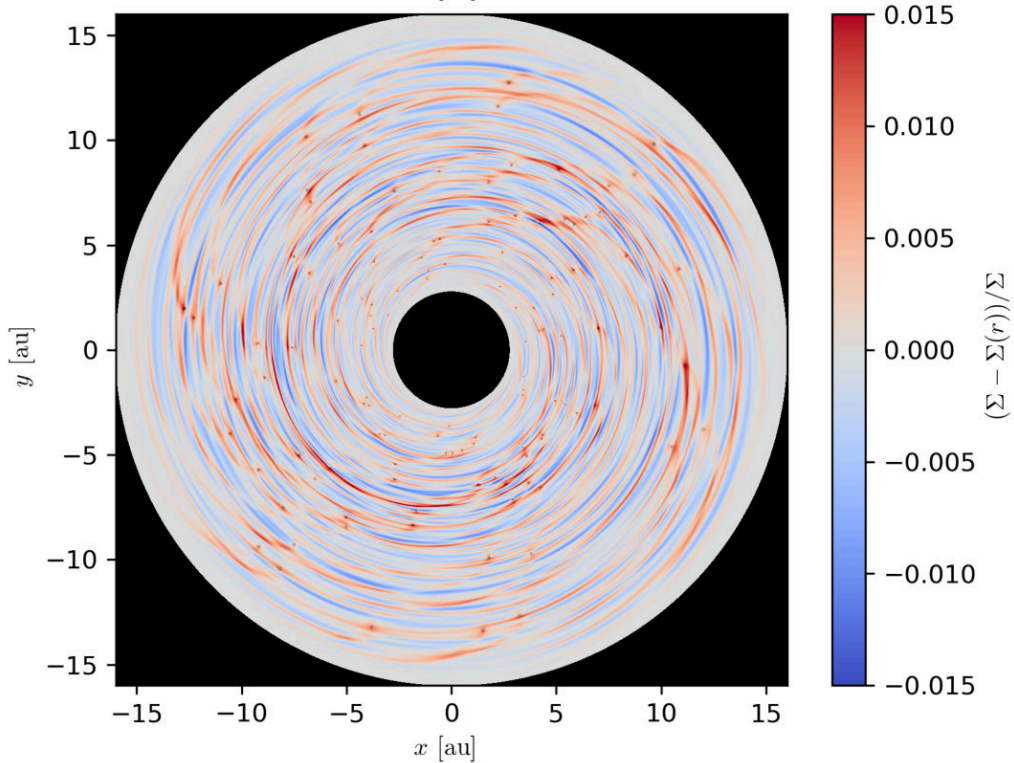


Figure 2.2: Perturbed surface density of a gas disk with 120 embryos, each with an initial mass $0.1 M_{\oplus}$. The overlapping spiral arms create a complex network of overdense and underdense disturbances. For a comparison, we refer back to Fig. 1.14 which shows a gas distribution perturbed by a single planet. From Paper II.

2.2 Paper II: Dynamics of multiple protoplanets embedded in gas and pebble disks and its dependence on Σ and ν parameters

Aims

Paper I described important implications of the heating torque but only a very limited part of the parametric space was explored. Paper II was designed as a follow-up parametric study, with an additional focus on the dynamics of close encounters in gas disks. We took Case III from Paper I as a nominal parametric set and then we varied one or two parameters to investigate the differences with respect to the nominal simulation.

Specifically, we varied the gas surface density Σ (using a three times larger or smaller initial value), radial mass flux of pebbles \dot{M}_F (decreasing it by an order of magnitude), viscosity ν (decreasing it by an order of magnitude), initial masses and multiplicity of planetary embryos (using 4 embryos with $5 M_{\oplus}$, 8 embryos with $1.5 M_{\oplus}$, and 120 embryos with $0.1 M_{\oplus}$). Since there are similarities between Paper I

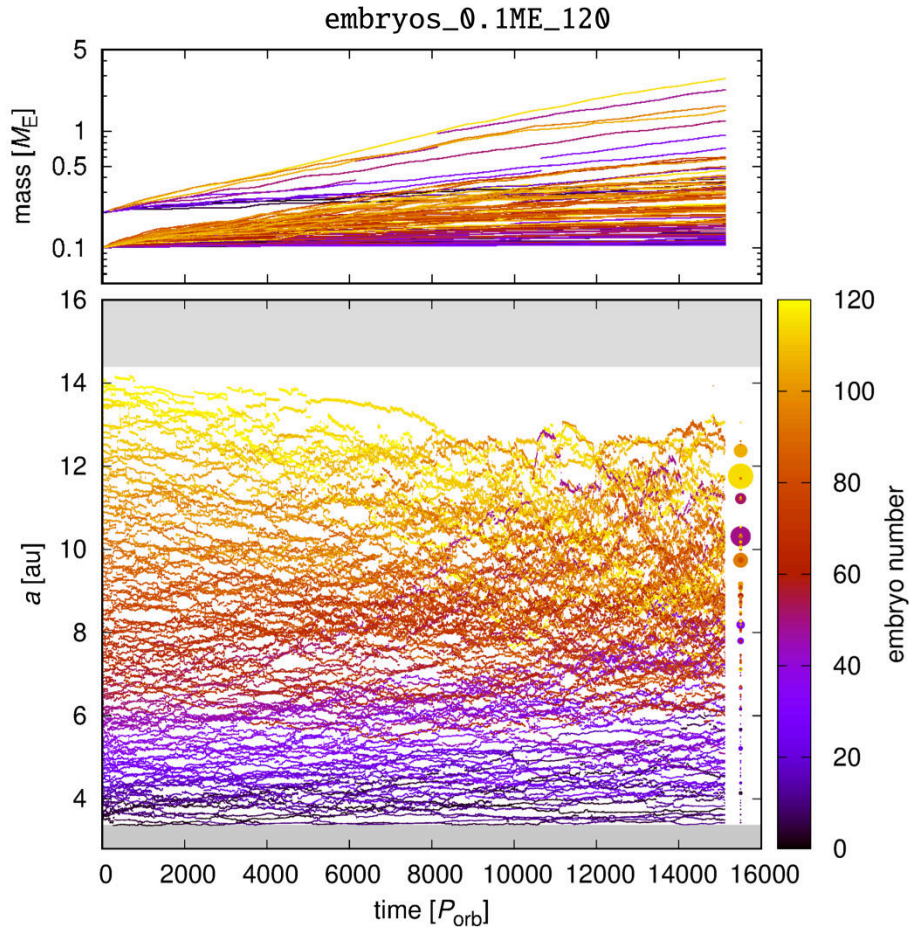


Figure 2.3: Temporal evolution of semimajor axes (*bottom*) and masses (*top*) of 120 embryos displayed in Fig. 2.2. The time is measured in orbital periods at 5.2 au. The individual evolutionary tracks are coloured according to the initial positions of embryos. The final masses in the *bottom* panel are also indicated by the size of the end-points. From Paper II.

and Paper II from the physical point of view, we do not provide a full reprint in this case. However, we discuss the most important and novel findings in the following.

Major results

HYDRODYNAMIC AND ORBITAL FEATURES. We found that when coorbital planets are formed, they can block the radial flux of pebbles if their combined masses exceed M_{iso} (see Eq. 1.75), although their individual masses can still be below M_{iso} . This mechanism provides another possibility for developing a pebble-isolating pressure bump in planet-forming disks.

Regarding merger events, we recognised that they are usually preceded by 3-body encounters of planetary embryos. Moreover, the encounters are perturbed by the gravity of overlapping or aligned spiral arms. Therefore the encounter geometry is at

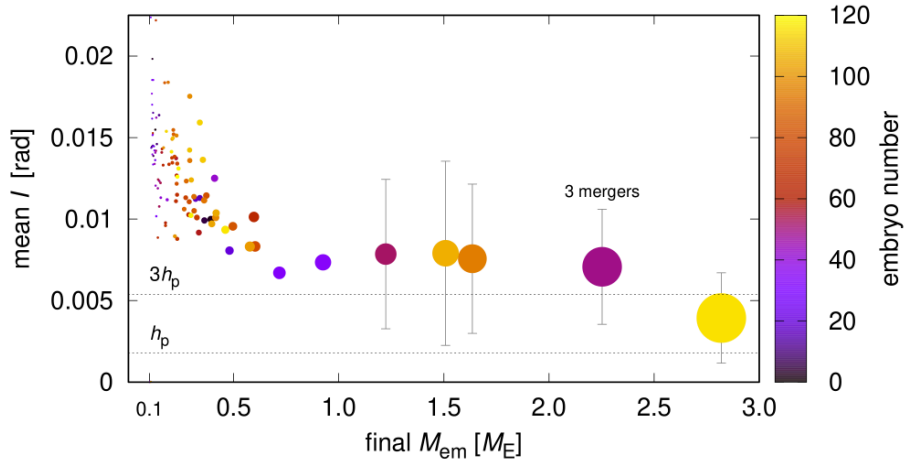


Figure 2.4: Mean inclination as a function of the final embryo mass. Sizes of circles are scaled by the embryo masses and their colours indicate initial positions in the disk. Dotted lines correspond to multiples of the aspect ratio of the pebble disk. The most massive embryos remain at low inclinations (variations of inclinations are indicated by error bars) so that they overlap with the pebble feeding zone and thus they continue to grow efficiently. The smallest embryos are excited to inclinations which lead them away from the pebble disk and thus their mass growth is not very efficient. From Paper II.

least partially controlled by hydrodynamics. This effect clearly cannot be accounted for in N-body models with prescribed torque formulae.

Finally, we found that embryos with $\simeq 6 M_{\oplus}$ can sometimes enter a mode of rapid outward migration driven by the dynamical torque, similarly to the mechanism described by Pierens & Raymond (2016).

A SIMULATION WITH 120 EMBRYOS. For the first time, we applied an RHD disk model to study the evolution of a swarm ($N = 120$) of low-mass embryos ($M_p = 0.1 M_{\oplus}$). Such swarms are usually studied with N-body models, it was therefore worthwhile to investigate whether our RHD approach leads to different conclusions or not. Because a simulation like this is numerically very demanding, it was ran on the NASA Pleiades CPU cluster. The simulations timespan was $\simeq 200$ kyr and the disk was resolved by 1024 and 1536 cells in radius and azimuth, respectively. Such a resolution is still not ideal for a precise recovery of disk torques, given the unusually low masses of the embryos, but an improved resolution would slow down the computation too much.

Fig. 2.2 shows the perturbed gas distribution under the influence of 120 small embryos. Clearly, the overlapping density waves create a complex pattern which leads to stochastic forcing acting on top of the standard torques. The evolution of semimajor axes and masses is shown in Fig. 2.3. It is surprisingly slow, with rather small orbital drifts. Eccentricities and inclinations are excited early (not shown in the figure), with average values being $e \simeq 0.02$ and $i \simeq 0.01$. The later occurs despite the inclination damping (Tanaka & Ward 2004) and it significantly decreases the frequency of mergers (there were only < 20 mergers during the course

of the simulation). The evolution of masses is thus dominated by pebble accretion. We notice that the largest bodies are formed in the outer part of the disk which is indicative of pebble filtering (i.e. the decrease of the pebble flux for inner embryos owing to the accretion of outer embryos).

In Fig. 2.4, we show the distribution of mean inclinations as a function of the final mass. Comparing this distribution with the thickness of the pebble disk, we find that the bodies which orbit closest to the midplane are also the largest. This is because the overlap of their accretion radii with the pebble disk covers a longer fraction of their orbital periods compared to inclined embryos which spend more time outside the feeding zone and thus remain less massive. This finding confirms the mechanism of *viscously-stirred pebble accretion* (VSPA) that was described by Levison et al. (2015). Our RHD model therefore provides an independent confirmation of the VSPA which was previously known only from N-body modelling.

2.3 Paper III: Binary planet formation by gas-assisted encounters of planetary embryos

Motivation and methods

Eklund & Masset (2017) described the eccentricity excitation of luminous planets in 3D and pointed out that the inclination can also become excited by the vertical component of the heating force. They found the growth rate of the inclination to be three times smaller than that of the eccentricity. Consequently, the eccentricity growth tend to quench the inclination growth and the asymptotic inclination value is then $\simeq 0.001$, although this value strongly depends on the initial e and i .

Paper I and Paper II did not recover the inclination excitation because of 2D limitations of the `Thorin` code. Since excited eccentricities can substantially influence the orbital dynamics of migrating interacting planets, it is natural to ask what happens if the inclination damping is opposed by the inclination growth, leading to misaligned orbital planes.

In order to explore the influence of excited inclinations in the framework of our 2D model, we introduced a simple modification to the Tanaka & Ward (2004) vertical damping force. We assumed that if i is below a certain asymptotic value, the damping force is inactive. If i is above the asymptotic value, the damping force operates in a usual way. The asymptotic value was treated as a free parameter and its value was motivated by the findings of Eklund & Masset (2017).

Major results

FORMATION OF BINARY PLANETS. Performing several simulations with the reduced efficiency of the inclination damping brought an unexpected result: binary planets² appeared in the evolving systems of embryos. Here we review the process of their formation.

When embryos undergo convergent migration, both their eccentricities and inclinations become excited by the combination of resonant perturbations and the hot-trail effect (both horizontal and vertical). This allows them to avoid collisions and therefore close encounters continue to stir e and i . The geometry of encounters eventually becomes such that two embryos can enter their mutual Hill sphere and form a transient binary planet. This capture is facilitated by the dissipative influence of the gas disk: approaching embryos create a shared density wave, they have to cross it, and this crossing is accompanied by a subtraction of the orbital energy from the embryos.

The transients, however, quickly dissolve, typically within a single orbital period. Their lifetime can only be prolonged if they undergo a 3-body encounter with a third embryo. In the process, the binary becomes bound more tightly and the third body

²By a binary planet we understand a gravitationally bound pair of planetary bodies orbiting their barycentre, which is located outside their physical radii.

receives a kick. The same process is known from star clusters as the *binary hardening* (e.g. Hills 1975). The described mechanism of binary planet formation is not entirely surprising, its hints were first recognised by Morbidelli et al. (2008). However, it was not studied in detail until Paper III.

DYNAMICS OF BINARY PLANETS. After the formation event, the separation of binary components predominantly decreases in time. The secular decrease of the separation is caused by pebble accretion. As the mass and linear momentum of pebbles is transferred onto the binary components, their orbital momentum inevitably changes and the binary semimajor axis shrinks.

Abrupt changes of the binary separation are caused by repeated 3-body encounters (hardening). We found that these encounters can sometimes proceed as exchange events during which one binary component is replaced by the third, initially unbound, embryo. These reconfigurations often lead to an abrupt change of the binary eccentricity and inclination, the latter of which can flip the binary orbit between prograde and retrograde orientations.

None of the binary planets found in our simulations survived longer than $\simeq 10^4$ yr. However, it is still viable that late-forming binary planets (i.e. forming shortly before the disk dispersal) might survive, provided they are not destroyed by subsequent orbital instabilities of the whole planetary system. We studied the latter using a set of follow-up N-body integrations of the gas-free phase.

IMPLICATIONS FOR OBSERVED PLANETARY SYSTEMS. From our calculations, we derived: the fraction of binary-producing protoplanetary disks, the fraction of disks which contain a binary at the end of their lifetime, and the fraction of planetary systems in which binaries remain stable after the disk dispersal. Multiplying these fractions, we made an order-of-magnitude estimate of the fraction of observable exoplanetary systems that could potentially host a binary planet. We found that one binary planet should be found within $\simeq (2-5) \times 10^4$ planetary systems.

Since it is expected that the sample of known exoplanetary systems will substantially increase with ongoing and future missions (e.g. TESS, PLATO), our estimate suggests that signatures of binary planets should be searched for in the datasets. The techniques for detection of binary planets should be identical to those developed for detection of exomoons (Simon et al. 2007; Kipping 2009; Kipping et al. 2012; Simon et al. 2012; Heller 2014; Bennett et al. 2014; Ben-Jaffel & Ballester 2014). Indeed, a binary planet has been recently discovered (Teachey & Kipping 2018), consisting of a massive gas giant Kepler-1625b and a Neptune-mass companion. However, we think that the origin of such a system cannot be explained by the mechanism of gas-assisted encounters of planetary embryos because gas accretion would probably disrupt the binary configuration.

Our estimate of binary-hosting systems is of course biased by several issues: we were not able to take into account the tidal evolution of binary planets, our numerical resolution was rather poor with respect to binary orbits with small separations, our treatment of 3D disk-planet interactions on inclined orbits was simplistic, and we did not account for other formation mechanisms proposed for binary planets (e.g.

Ochiai et al. 2014; Ryan et al. 2014). But even if binary planets eventually turn out to be scarcer than predicted by our estimate, the very possibility of their occurrence during planet formation is intriguing. Specifically, our simulations indicate that the existence of a binary planet is often terminated by a collision and merging of its components. Such a collision would have a different geometry compared to initially unbound orbits and thus could be of a potential interest e.g. for the scenarios of the Moon-forming impact (Canup 2012).

2.3.1 Reprint

Here we include the reprint of Paper III.



Binary Planet Formation by Gas-assisted Encounters of Planetary Embryos

Ondřej Chrenko¹, Miroslav Brož¹, and David Nesvorný²¹Institute of Astronomy, Charles University in Prague, V Holešovičkách 2, 18000 Prague 8, Czech Republic; chrenko@sirrah.troja.mff.cuni.cz²Southwest Research Institute, Department of Space Studies, 1050 Walnut Street, Suite 300, Boulder, CO 80302, USA

Received 2018 June 28; revised 2018 October 22; accepted 2018 October 22; published 2018 December 4

Abstract

We present radiation hydrodynamic simulations in which binary planets form by close encounters in a system of several super-Earth embryos. The embryos are embedded in a protoplanetary disk consisting of gas and pebbles and evolve in a region where the disk structure supports convergent migration due to Type I torques. As the embryos accrete pebbles, they become heated and thus affected by the thermal torque and the hot-trail effect, which excites orbital eccentricities. Motivated by findings of Eklund & Masset, we assume that the hot-trail effect also operates vertically and reduces the efficiency of inclination damping. Non-zero inclinations allow the embryos to become closely packed and also vertically stirred within the convergence zone. Subsequently, close encounters of two embryos assisted by the disk gravity can form transient binary planets that quickly dissolve. Binary planets with a longer lifetime of $\sim 10^4$ yr form in three-body interactions of a transient pair with one of the remaining embryos. The separation of binary components generally decreases in subsequent encounters and because of pebble accretion until the binary merges, forming a giant planet core. We provide an order-of-magnitude estimate of the expected occurrence rate of binary planets, yielding one binary planet per $\simeq (2-5) \times 10^4$ planetary systems. Therefore, although rare, binary planets may exist in exoplanetary systems and they should be systematically searched for.

Key words: planet–disk interactions – planets and satellites: detection – planets and satellites: dynamical evolution and stability – planets and satellites: formation – planets and satellites: general – protoplanetary disks

Supporting material: animations

1. Introduction

Several classes of celestial objects (e.g., minor solar system bodies, dwarf planets, stars, etc.) are known to exist in binary configurations, i.e., as two bodies orbiting their barycenter, which is located exterior to their physical radii. The existence of binaries is an important observational constraint because a successful population synthesis model for a given class of objects must be able to explain how binaries form, how frequent they are, and how they evolve dynamically and affect their neighborhood.

The richest sample of binary objects within the scope of planetary sciences is in the population of minor solar system bodies. Examples can be found among the near-Earth objects (NEOs; e.g., Margot et al. 2002; Pravec et al. 2006; Scheeres et al. 2006), main-belt asteroids (MBAs; e.g., Marchis et al. 2008; Pravec et al. 2012), Jovian Trojans (e.g., Marchis et al. 2006; Sonnett et al. 2015), and surprisingly frequently among the Kuiper-belt objects (KBOs; e.g., Veillet et al. 2002; Brown et al. 2006; Richardson & Walsh 2006; Noll et al. 2008). Formation of binary minor bodies took place during various epochs of the solar system. Some binary asteroids originated in recent breakup events (Walsh et al. 2008), whereas the binary KBOs were probably established early, during the formation of planetesimals (Goldreich et al. 2002; Nesvorný et al. 2010; Fraser et al. 2017) more than four billion years ago.

For large bodies, the number of binary configurations drops suddenly almost to zero. Of the known and confirmed objects, only Pluto and Charon can be considered as a binary (Christy & Harrington 1978; Walker 1980; Lee & Peale 2006; Brozović et al. 2015), likely of an impact origin (Canup 2011; McKinnon et al. 2017). Since Pluto and Charon were classified as *dwarf*

planets, the conclusion stands that no planets in binary configurations have yet been discovered.

Given that more than 3700 exoplanets have been confirmed to date,³ the paucity of binary planets is a well-established characteristic of the data set. However, its implications for our understanding of planet formation are unclear and maybe even underrated at present. Are binary planets scarce, and is it just that current methods preclude their discovery? Or is their non-existence a universal feature shared by all planetary systems throughout the Galaxy?

To start addressing these questions, this paper discusses the formation of binary planets by two- and three-body encounters of planetary embryos in protoplanetary disks, during the phase when the gas is still abundant and the embryos still grow by pebble accretion (Ormel & Klahr 2010; Lambrechts & Johansen 2012). We advocate that suitable conditions to form binary planets are achieved when orbital eccentricities and inclinations of embryos are excited by thermal torques related to accretion heating (Chrenko et al. 2017; Eklund & Masset 2017). Our model utilizes radiation hydrodynamics (RHD) to account for these effects.

Although the results of this paper are preliminary in many aspects, they demonstrate that binary planets can exist and it may be only a matter of time (or advancements in methods) before such an object is discovered in one of the exoplanet search campaigns. To motivate future observations and data mining, we emphasize that promising methods for detections of exomoons have been developed and applied in recent years. These include, for example, transit timing variations (TTVs; Simon et al. 2007) and transit duration variations (TDVs;

³ As of 2018 August, according to the NASA Exoplanet Archive: <https://exoplanetarchive.ipac.caltech.edu/>.

Kipping 2009), their Bayesian analysis in the framework of direct star–planet–moon modeling and fitting (Kipping et al. 2012), photometric analysis of phase-folded light curves using the scatter peak (SP) method (Simon et al. 2012) or the orbital sampling effect (OSE; Heller 2014; Hippke 2015), microlensing events (Han 2008; Liebig & Wambsganss 2010; Bennett et al. 2014), and asymmetric light curves due to plasma tori of hypothetical volcanic moons (Ben-Jaffel & Ballester 2014).

Indeed, Kepler-1625 b-i has recently been identified as an exomoon candidate (Heller 2018; Teachey et al. 2018) and is awaiting a conclusive confirmation. Moreover, Lewis et al. (2015) discuss that the *CoRoT* target SRc01 E2 1066 can be explained as a binary gas-giant planet, although the signal could also correspond to a single planet transiting a starspot (Erikson et al. 2012). Therefore, methods similar to those listed above could be applicable when searching for binary planets.

Our paper is organized as follows. In Section 2, we outline our RHD model. Section 3 describes our nominal simulation with the formation of binary planets. Planetary encounters are analyzed, as well as the influence of the gas disk. Subsequently, we test the stability of binary planets in several simplified models (without neighboring embryos; without the disk; etc.). We also study binary planet formation in a set of four additional simulations to verify the relevance of the process. In Section 4, we estimate the expected occurrence rate of binary planets in the exoplanetary population and we also discuss a possible role of binary planets in planetary sciences. Section 5 is devoted to conclusions.

1.1. Definitions

To avoid confusion, let us list several definitions that we use throughout the rest of the paper.

1. *Binary* is shorthand for a binary planet, not to be mistaken with binary stars etc.
2. *Transient* (also *transient binary* or *transient pair*) is a binary that forms by two-body encounters of planetary embryos (e.g., Astakhov et al. 2005), in our case with the assistance of the disk gravity as we shall demonstrate later. We choose the name *transient* because we find the typical lifetime of these binaries to be of the order of one stellarcentric orbital period.
3. *Hardening* (e.g., Hills 1975) is a process during which the orbital energy of a binary configuration is dissipated and the separation of binary components decreases.
4. *Stability* of a binary planet is discussed if it can survive more than one stellarcentric orbital period, which is usual after hardening. In principle, such a binary can be observed. We characterize *stability* by means of the lifetime over which the binary components remain gravitationally bound.
5. *Encounter* refers to a close encounter of two or more planetary embryos (single or binary), when they enter one another’s Hill sphere.
6. *Merger* refers to a physical collision of two embryos. In our approximation, we replace the colliding embryos by a single object, assuming perfect merger (mass and momentum conservation).
7. We denote orbital elements in the stellarcentric frame with a subscript “s” to distinguish them from the orbital elements of one binary component with respect to another

(e.g., a_s is the stellarcentric semimajor axis but a is the semimajor axis of the binary configuration).

2. Radiation Hydrodynamic Model

2.1. General Overview

The individual constituents of our model are as follows. First, we consider radiation transfer, which is essential to properly reproduce the disk structure (Bitsch et al. 2013) and to account for all components of the Type I torque acting on low-mass planets (e.g., Baruteau & Masset 2008; Kley & Crida 2008; Kley et al. 2009; Lega et al. 2014).

Second, we use a two-fluid approximation to include a disk of pebbles, which serves as a material reservoir for the accreting embryos (Ormel & Klahr 2010; Lambrechts & Johansen 2012; Morbidelli & Nesvorný 2012).

Third, we also take into account that pebbles heat the accreting embryos, which in turn heat the gas in their vicinity. The migration is then modified due to the thermal torque (Benéz-Llambay et al. 2015; Masset 2017) and its dynamical component—the hot-trail effect (Chrenko et al. 2017; Eklund & Masset 2017; Masset & Velasco Romero 2017)—which perturbs the embryos in such a way that their orbital eccentricities are excited. This is due to the epicyclic motion of the embryo, which causes variations in the azimuthally uneven distribution of the heated (and thus underdense) gas.

The numerical modeling is done with the FARGO_THORIN code⁴, which was introduced and described in detail in Chrenko et al. (2017). The code is based on FARGO (Masset 2000). The model is 2D (vertically averaged) but planets are evolved in 3D. A number of important vertical phenomena were implemented, although some with unavoidable approximations.

A new phenomenon implemented in this study is the vertical hot-trail effect described by Eklund & Masset (2017), which can excite orbital inclinations. Such excitation should not occur for an isolated and non-inclined orbit because it is quenched by the growth in eccentricity, which is faster (Eklund & Masset 2017); however, the vertical hot-trail effect operates when a non-negligible inclination is initially excited by some other mechanism. For example, it can become important in a system of multiple embryos where close encounters temporarily pump up the inclinations. The vertical hot trail then starts to counteract the usual inclination damping by bending waves (Tanaka & Ward 2004).

2.2. Governing Equations

Gas is treated as a viscous Eulerian fluid described by the surface density Σ , flow velocity \mathbf{v} on the polar staggered mesh, and the internal energy ϵ . The pebble disk is represented by an inviscid and pressureless fluid with its own surface density Σ_p and velocity \mathbf{u} . We assume two-way coupling between the two fluids by linear drag terms, with the Stokes number τ calculated for the Epstein regime.

The RHD partial differential equations read

$$\frac{\partial \Sigma}{\partial t} + \nabla \cdot (\Sigma \mathbf{v}) = 0, \quad (1)$$

⁴ The code is available at <http://sirrah.troja.mff.cuni.cz/~chrenko>.

$$\frac{\partial \mathbf{v}}{\partial t} + \mathbf{v} \cdot \nabla \mathbf{v} = -\frac{1}{\Sigma} \nabla P + \frac{1}{\Sigma} \nabla \cdot \overleftrightarrow{T} - \frac{\int \rho \nabla \phi \, dz}{\Sigma} + \frac{\Sigma_p \Omega_K}{\Sigma \tau} (\mathbf{u} - \mathbf{v}), \quad (2)$$

$$\frac{\partial \epsilon}{\partial t} + \nabla \cdot (\epsilon \mathbf{v}) = -P \nabla \cdot \mathbf{v} + Q_{\text{visc}} + Q_{\text{acc}} + \frac{2\sigma_B}{\tau_{\text{eff}}} (T_{\text{irr}}^4 - T^4) - 2H \nabla \cdot \mathbf{F}, \quad (3)$$

$$\frac{\partial \Sigma_p}{\partial t} + \nabla \cdot (\Sigma_p \mathbf{u}) = -\left(\frac{\partial \Sigma_p}{\partial t} \right)_{\text{acc}}, \quad (4)$$

$$\frac{\partial \mathbf{u}}{\partial t} + \mathbf{u} \cdot \nabla \mathbf{u} = -\frac{\int \rho_p \nabla \phi \, dz}{\Sigma_p} - \frac{\Omega_K}{\tau} (\mathbf{u} - \mathbf{v}), \quad (5)$$

where the individual quantities are the pressure P , viscous stress tensor \overleftrightarrow{T} (e.g., Masset 2002), gas volume density ρ , volume density of pebbles ρ_p , coordinate z perpendicular to the midplane, gravitational potential ϕ of the primary and the planets, Keplerian angular frequency Ω_K , viscous heating term Q_{visc} (Mihalas & Weibel Mihalas 1984), accretion heating term Q_{acc} related to the accretion sink term $(\partial \Sigma_p / \partial t)_{\text{acc}}$, Stefan–Boltzmann constant σ_B , effective vertical optical depth τ_{eff} (Hubeny 1990), irradiation temperature T_{irr} (Chiang & Goldreich 1997; Menou & Goodman 2004; Baillié & Charnoz 2014), midplane gas temperature T (the term $\propto T^4$ describes vertical cooling), vertical pressure scale height H , and radiative flux \mathbf{F} .

The ideal-gas state equation is used as the thermodynamic closing relation:

$$P = (\gamma - 1) \epsilon = \Sigma \frac{R}{\mu} T, \quad (6)$$

where γ is the adiabatic index, R is the universal gas constant, and μ is the mean molecular weight. Equation (6) has been widely used in numerical models to relax inferior isothermal approximations and to account for the disk thermodynamics (through the energy equation), which is important for accurate migration rates (e.g., Kley & Crida 2008; Kley et al. 2009; Lega et al. 2014). We also point out that the given state equation neglects the radiation pressure and phase transitions, which is a valid assumption in low-temperature disks (D’Angelo et al. 2003).

Finally, flux-limited diffusion and the one-temperature approximation are utilized to describe the in-plane radiation transport, leading to

$$\mathbf{F} = -D \nabla T = -\lambda_{\text{lim}} \frac{16\sigma_B T^3}{\rho_0 \kappa} \nabla T, \quad (7)$$

where D denotes the diffusion coefficient, λ_{lim} is the flux limiter according to Kley (1989), ρ_0 is the midplane volume density, and $\kappa(\rho, T)$ is the material opacity. We use the opacity by Bell & Lin (1994) for both the Rosseland and Planck opacities.

For completeness, we provide the accretion heating formula

$$Q_{\text{acc}} = \sum_i \frac{GM_{\text{em},i} \dot{M}_{\text{em},i}}{R_i S_{\text{cell}}}, \quad (8)$$

where the sum goes over all embryos with indices i , masses $M_{\text{em},i}$, self-consistently calculated pebble accretion rates $\dot{M}_{\text{em},i}$, and physical radii R_i . G is the gravitational constant and S_{cell} is the surface area of the cell that contains the respective embryo and in which the heat is liberated (Q_{acc} is zero in other cells).

2.3. Evolution of Planets and Inclination Damping

Planets are evolved on 3D orbits using the IAS15 integrator (Rein & Liu 2012; Rein & Spiegel 2015). Planetary collisions are treated as perfect mergers. The planet–disk interactions are calculated by means of the vertical averaging procedure of Müller et al. (2012). The planetary potential is adopted from Klahr & Kley (2006) and has the smoothing length $r_{\text{sm}} = 0.5R_H$, where R_H is the planet’s Hill sphere.

When computing the torque acting on an embryo, we do not exclude any part of the Hill sphere because we focus on low-mass embryos (Lega et al. 2014). Such an exclusion is required only when embryos exceed masses $\simeq 10M_{\oplus}$ and form a circumplanetary disk. This disk should not contribute to the gas-driven torque because it comoves with the embryo (Crida et al. 2008). Our model ignores the torques from pebbles (Benéz-Llambay & Pessah 2018) because we assume relatively low pebble-to-gas mass ratios (less than 0.001). But we point out that during accretion of pebbles, we account for the transfer of their mass and linear momentum onto the embryo.

An important ingredient when investigating 3D planetary orbits is the inclination damping (e.g., Cresswell et al. 2007). We include the damping by using the formula from Tanaka & Ward (2004). In our case, the damping acceleration perpendicular to the disk plane reads

$$a_z = \begin{cases} \beta \frac{\Sigma \Omega_K}{c_s^4} (2A_z^c v_z + A_z^s z \Omega_K), & I > I_0 \\ 0, & I \leq I_0 \end{cases} \quad (9)$$

where $\beta = 0.3$ (e.g., Pierens et al. 2013), $A_z^c = -1.088$, and $A_z^s = -0.871$ are fixed coefficients, c_s is the sound speed, v_z is the embryo’s vertical velocity, and z is its vertical separation from the midplane. Σ and Ω_K are evaluated along the embryo’s orbit.

In writing Equation (9), we introduce a simple modification of Tanaka & Ward’s formula. We assume that the inclination damping does not operate when the orbital inclination I is below a certain critical value I_0 . The motivation for this modification stems from the findings of Eklund & Masset (2017), who investigated the orbital evolution of a hot (accreting) planet in a 3D radiative disk. Not only did they find the excitation of the eccentricity due to the hot-trail effect, but they also showed that the effect has a vertical component that can excite the inclinations.

In our 2D model with accretion heating, the excitation of eccentricity is reproduced naturally. Regarding the inclinations, we simply assume that the hot-trail effect operates vertically as well and balances the inclination damping up to the value I_0 . For larger inclinations, the damping takes over and the standard formula for a_z applies. We consider I_0 to be a free parameter of

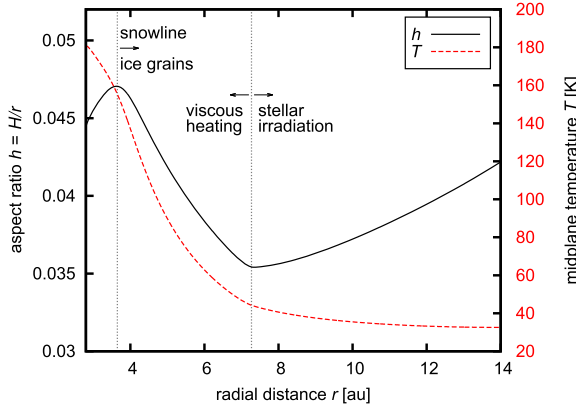


Figure 1. Radial profile of the aspect ratio $h(r) = H/r$ and temperature $T(r)$ in the disk used in our simulations. The right vertical dotted line marks the transition between the viscously heated and stellar irradiated regions, the latter exhibiting flaring of the disk. The left vertical dotted line corresponds to the water ice line, which is also a local maximum of the opacities of Bell & Lin (1994). The figure is taken from Chrenko et al. (2017).

the model and choose $I_0 = 10^{-3}$ rad $\simeq 0^\circ.057$, which is at the lower end of the results of Eklund & Masset (2017).

3. Simulations

3.1. Disk Model

The protoplanetary disk model used in all our RHD simulations is exactly the same as in Chrenko et al. (2017), including the initial and boundary conditions (de Val-Borro et al. 2006). The parameters⁵ characterizing the initial gas disk are the surface density $\Sigma = 750(r/(1 \text{ au}))^{-0.5} \text{ g cm}^{-2}$, kinematic viscosity $\nu = 5 \times 10^{14} \text{ cm}^2 \text{ s}^{-1}$, adiabatic index $\gamma = 1.4$, mean molecular weight $\mu = 2.4 \text{ g mol}^{-1}$, vertical opacity drop $c_{\kappa} = 0.6$, and disk albedo $A = 0.5$. The central star has an effective temperature $T_* = 4370 \text{ K}$, stellar radius $R_* = 1.5 R_{\odot}$, and mass $M_* = 1 M_{\odot}$. The domain stretches from $r_{\min} = 2.8 \text{ au}$ to $r_{\max} = 14 \text{ au}$ in radius and spans the entire azimuth, having a grid resolution of 1024×1536 (rings \times sectors).

The gas disk is numerically evolved to its thermal equilibrium and only after that is the coupled pebble disk introduced. Pebbles are parameterized by the radial pebble mass flux $\dot{M}_F = 2 \times 10^{-4} M_{\oplus} \text{ yr}^{-1}$ (Lambrechts & Johansen 2014), the Schmidt number $Sc = 1$, coagulation efficiency $\epsilon_p = 0.5$ (Lambrechts & Johansen 2014), bulk density $\rho_b = 1 \text{ g cm}^{-3}$, and turbulent stirring efficiency $\alpha_p = 1 \times 10^{-4}$ (e.g., Youdin & Lithwick 2007). To infer the pebble sizes, we assume the drift-limited growth regime (Birnstiel et al. 2012; Lambrechts & Johansen 2014), leading to pebble sizes of several centimeters.

For reference, Figure 1 shows the radial profiles of the aspect ratio $h(r) = H/r$ and temperature $T(r)$ of the equilibrium gas disk. The $h(r)$ profile has a maximum near 4 au, where the opacity peaks just before the sublimation of water ice (Bell & Lin 1994). Therefore the heat produced by viscous heating is not easily radiated away from this opaque region and the disk puffs up.

Near 7 au, the disk starts to flare because the vertical optical depth is small enough for the incoming radiation to penetrate

deeper and heat the disk. The transition to the flared outer parts produces a zone of convergent Type I migration for planetary embryos (Bitsch et al. 2013; Pierens 2015).

3.2. Nominal Simulation

Let us now discuss and analyze our nominal simulation in which binary planets were found to form. Initially, we set four embryos on circular orbits with stellarcentric semimajor axes $a_s = 5, 6.7, 8.4,$ and 10.1 au , inclinations $I_s = I_0 = 10^{-3} \text{ rad} \simeq 0^\circ.057$, and randomized longitudes. The initial mass of each embryo is $M_{\text{em}} = 3 M_{\oplus}$ and their orbital separations are equal to 16 mutual Hill radii:

$$R_{\text{mH},ij} = \frac{a_{s,i} + a_{s,j}}{2} \left(\frac{M_{\text{em},i} + M_{\text{em},j}}{3M_*} \right)^{1/3}. \quad (10)$$

Embryos are numbered 1, 2, 3, and 4 from the innermost outward.

Figure 2 shows the evolution of embryos over 140 kyr of the full RHD simulation with pebble accretion and respective heating. At first, the embryos undergo convergent migration toward their zero-torque radius. Without the heating torques, the embryos would concentrate near 7 au thanks to the contribution of the entropy-related corotation torque (Paardekooper & Mellema 2008), which is positive from $\simeq 4$ to 7 au in this particular disk model.

With the heating torques, however, the zero-torque radius is shifted further out because these torques are always positive (Benéz-Llambay et al. 2015). Moreover, the hot-trail effect quickly excites orbital eccentricities. Within $\simeq 2 \text{ kyr}$, the eccentricities reach $e_s \simeq 0.02$ for the innermost embryo and $e_s \simeq 0.04$ for the outermost.

The inclinations first remain constant near the prescribed I_0 value, with only small temporal excitations not exceeding $I_s \simeq 0^\circ.2$. Even these initially small inclinations are enough to modify the encounter geometries in such a way that the system becomes gradually stirred in the vertical direction. Once the system becomes closely packed, at about $\simeq 35 \text{ kyr}$ into the simulation, the mutual close encounters pump the inclinations significantly, typically to $I_s \simeq 1^\circ$ and even up to $I_s \simeq 2^\circ$. Planets can pass above or below each other because their vertical excursions are comparable to (or larger than) their Hill spheres. For example, the maximal vertical excursion of a $5 M_{\oplus}$ embryo at 10 au is $z_{\text{max}} \simeq 2R_{\text{H}}$ when $I_s = 2^\circ$.

Due to excited eccentricities, the embryos never form a stable resonant chain, in accordance with Chrenko et al. (2017). Moreover, the excited inclinations help the embryos to avoid collisions and mergers for a long period of time. Consequently, close encounters of embryos are frequent in the system. Between $\simeq 98 \text{ kyr}$ and $\simeq 114 \text{ kyr}$, strong unphysical oscillations of the stellarcentric orbital elements appear in Figure 2 for some of the embryos, indicating formation of gravitationally bound binary planets.⁶

⁵ A great number of the parameters listed in this section ($\nu, c_{\kappa}, A, T_*, R_*, \dot{M}_F, Sc, \epsilon_p, \rho_b, \alpha_p$) were not defined in Section 2 to keep it brief. To understand how these parameters enter the model, we refer the reader to Chrenko et al. (2017).

⁶ In Figure 2, we can also identify co-orbital configurations (1/1 resonances), for example for embryos 1 and 3 between 62.5 and 66 kyr. To keep the paper focused on binary planets, we refer the interested reader to other works discussing formation and detectability of co-orbital planets, e.g., Laughlin & Chambers (2002), Cresswell & Nelson (2008), Giuppone et al. (2012), Chrenko et al. (2017), Brož et al. (2018).

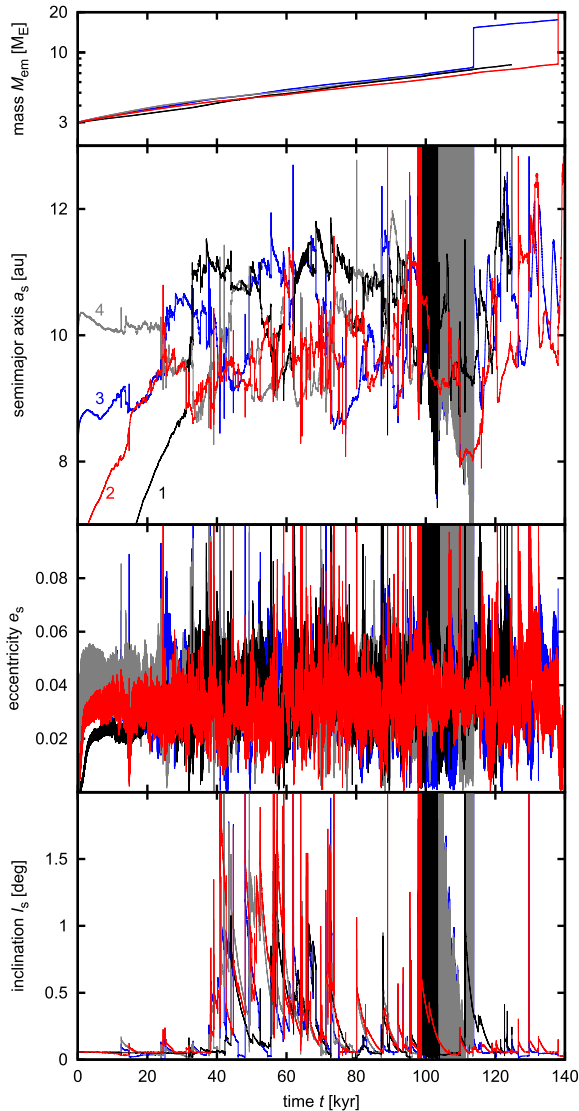


Figure 2. Temporal evolution of the embryo masses M_{em} (top), stellarcentric semimajor axes a_s (second row), eccentricities e_s (third row), and inclinations i_s (bottom) in the full RHD simulation with the gas disk, pebble disk, pebble accretion, and accretion heating. Initially, there are four migrating embryos, numbered from the innermost outward. The inclination starts at $i_0 = 10^{-3}$ rad; the inclination damping is switched off whenever $i \leq i_0$. The strong variations of the stellarcentric Keplerian elements between $\simeq 98$ kyr and $\simeq 114$ kyr are a consequence of binary planet formation. A member of the binary swaps for one of the accompanying embryos three times, as indicated by the change in color of the oscillating curves (from a narrow strip of red to black and to gray). The existence of the binary is ended abruptly by a merger (clearly related to the instantaneous mass increase in the $M_{em}(t)$ plot).

3.3. Gravitationally Bound Pairs of Embryos

To identify the events related to the binary formation in the simulation described above, we computed orbits of the relative motion among all possible pairs of embryos and selected those with $a < R_{mH}$, $e < 1$. The results are shown in Figure 3. Throughout the simulation, we found 65 time intervals during which at least two embryos are captured on a mutual elliptical

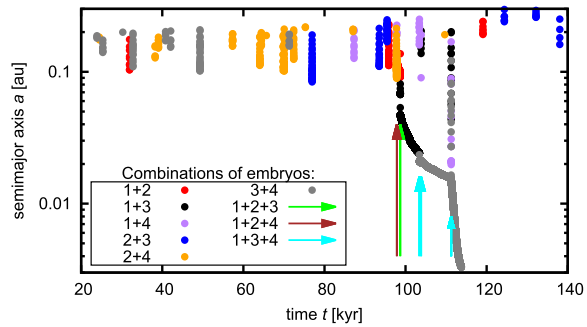


Figure 3. The record of all relative two-body orbits satisfying the conditions $a < R_{mH}$ and $e < 1$ in our nominal simulation. The filled circles mark the instantaneous semimajor axes and each pair of embryos is distinguished by color. The arrows are used to indicate when a gravitationally bound pair participates in a three-body encounter.

orbit, changing their relative orbital energy from initially positive to negative (and back to positive when the capture terminates). Subsequently, we also scanned the sample of bound pairs and looked for cases when a third embryo has its distance from a pair $d < R_{mH}$ to identify three-body (pair-embryo) encounters. These are highlighted in Figure 3 by arrows.

Analyzing the lifetime of the bound pairs, we found that most of them dissolve before finishing one stellarcentric orbit. However, we found a single case when several binary configurations existed consecutively for a prolonged period of time between $\simeq 98$ kyr and $\simeq 114$ kyr. This time interval is bordered by three-body encounters, which usually cause the binary separation to drop.

In summary, bound pairs can form in two-body encounters but they quickly dissolve unless they undergo a three-body encounter with one of the remaining embryos. The latter process is known as binary hardening (e.g., Hills 1975, 1990; Goldreich et al. 2002; Astakhov et al. 2005) and it occurs when an external perturber removes energy from a binary system, which then becomes more tightly bound. To distinguish between two types of events contributing to the formation of bound pairs, we call those formed in two-body encounters *transient* binaries because of their typically short dynamical lifetime.

Transient binaries have been the subject of many different studies, for example, in the three-body Hill problem (e.g., Simó & Stuchi 2000; Astakhov et al. 2005). Their formation is possible because the orbital energy of two bodies is no longer conserved when additional perturbers (e.g., the central star) are present (e.g., Cordeiro et al. 1999; Araujo et al. 2008). Our system is of course more complicated because additional gravitational perturbations arise from the gas disk. We will demonstrate in Section 3.4 that the gas indeed facilitates formation of transients.

One last question we address here is whether or not the occurrence of bound pairs in Figure 3 is related to the vertically stirred orbits of embryos. To find an answer, we looked for bound pairs (with $a < R_{mH}$, $e < 1$) in one of our previous simulations reported in Chrenko et al. (2017) (dubbed Case III), where the inclinations were damped in the standard way (Tanaka & Ward 2004). We found only six bound pairs (all transients) compared to 65 cases in our nominal simulation presented here. Therefore, the excited inclinations importantly

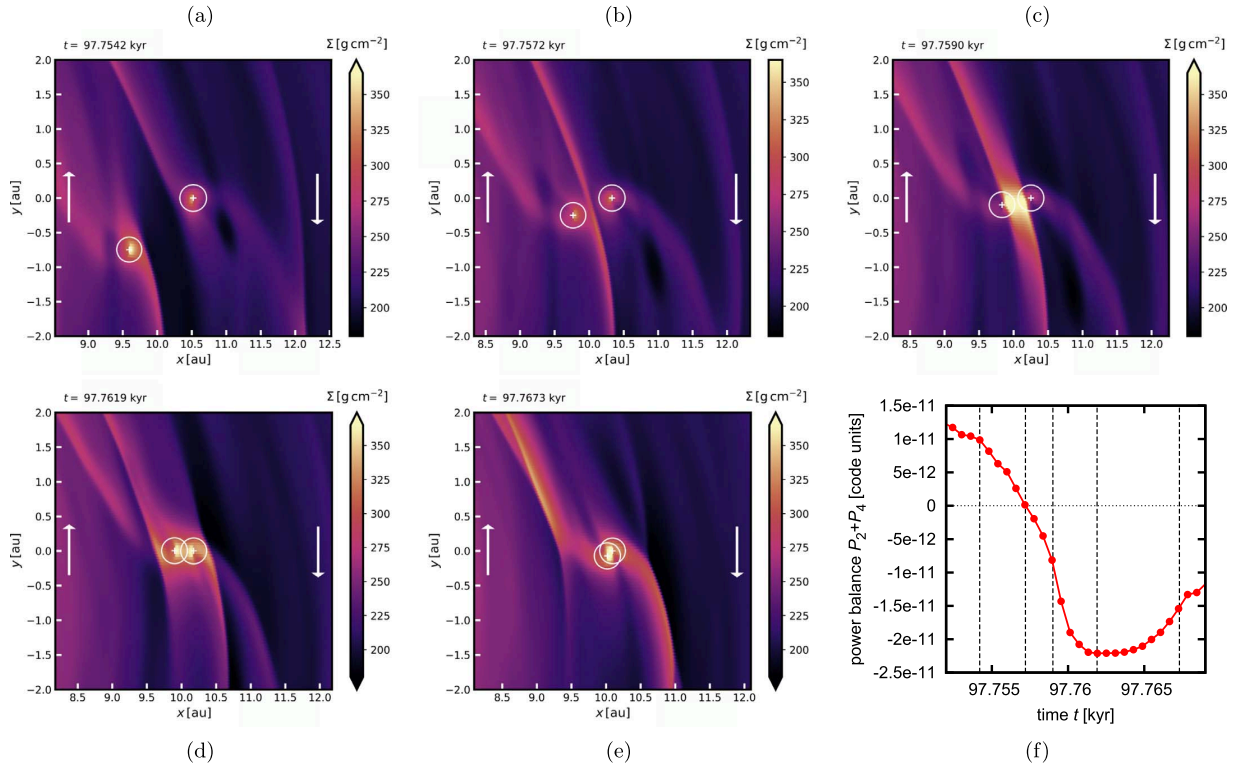


Figure 4. Formation of a transient binary during a two-body encounter of embryos 2 and 4. The first five panels (a)–(e) show the evolution of the perturbed surface density Σ . Locations of the embryos are marked by white crosses, their Hill spheres are indicated by white circles, and white arrows show the direction of the Keplerian shear in the reference frame corotating with embryo 2, which is placed at the center of each plot. The individual panels are labeled with the simulation time t . The final panel (f) shows the evolution of the total power of the gravitational forces exerted by the disk on embryos 2 and 4. The vertical dashed lines mark the simulation time corresponding to the snapshots of Σ in panels (a)–(e). An animation of the formation of the transient binary is available in the online Journal and covers $t \simeq 97.73$ – 97.8 kyr in simulation time.

(An animation of this figure is available.)

change the outcomes of embryo encounters in the gas disk and help to form transients.

3.4. Transient Binary Formation in a Two-body Encounter

Here we investigate the formation of a transient pair of embryos 2 and 4, which precedes the binary hardening events in our nominal simulation. The pair forms in a two-body interaction at $t \simeq 97.76$ kyr. To see whether the embryo–disk interactions assist in the process, we show in Figure 4 the evolution of the perturbed gas surface density Σ during the encounter.

Before the encounter (panel (a)), the usual structures can be seen in the disk. The hot (underdense) trail of the outer embryo 2 can be seen as a dark oval spot in the bottom right quadrant (it moves down and gets larger in time). The hot trail of the inner embryo 4 is less prominent and looks like an underdense gap attached to the embryo from inside.

As the embryos approach in panel (b), the outer spiral arm of the inner embryo 4 and the inner spiral arm of the outer embryo 2 join and overlap. The overlap forms a strong density wave positioned between the embryos. The overdensity increases as part of the wave becomes trapped between the Hill spheres of the two embryos in panel (c). From panel (c) to (d), the embryos cross this shared density wave.

In panel (d), the embryos are so close to each other that they effectively act on the disk as a single mass, and the previously shared spiral arm splits into an inner and an outer component with a small pitch angle. There are two more spirals with a larger pitch angle that are leftovers of the initial wakes launched by the embryos. In panel (e), all spirals blend into a single pair of arms. The embryos enter one another’s Hill sphere between panels (d) and (e) through the vicinity of the Lagrange points L_1 for the outer and L_2 for the inner embryo (Astakhov et al. 2005). The embryos are captured on a prograde binary orbit (in panel (e), embryo 4 orbits the central embryo 2 counterclockwise).

The spiral arm crossing that appears during the encounter is known to produce strong damping effects on the embryos (Papaloizou & Larwood 2000). It is thus likely that the gas supports the gravitational capture by dissipating the orbital energy. To quantify this effect, we measured the total gravitational force $\mathbf{F}_{g,i}$ exerted by the disk on each embryo and we calculated the mechanical power

$$P_i = \int_{\text{disk}} \mathbf{v}_i \cdot \mathbf{F}_{g,i} dS, \quad (11)$$

where \mathbf{v}_i is the velocity vector of the embryo and the integral goes over the entire disk. P_i directly determines the rate of

change of the orbital energy \dot{E}_i of each embryo (e.g., Cresswell et al. 2007).

Panel (f) of Figure 4 shows the total balance of the energy subtraction (or addition) for embryos 2 and 4, $P = P_2 + P_4$. The energy is transferred to the disk when $P < 0$ and subtracted from the disk when $P > 0$. It is obvious that throughout the closest approach (panels (b)–(e)), the orbital energy of the embryos dissipates and thus the influence of the gas disk on the formation of transients is confirmed.

3.5. Binary Planet Hardening in Three-body Encounters

The transient pair of embryos 2 and 4 does not dissolve; instead it is further stabilized in three-body encounters with the remaining embryos. Figure 5 shows these encounters in detail. First, the transient pair encounters embryo 1 at $t \simeq 97.85$ kyr. During this encounter, one component of the binary (embryo 4) becomes unbound and is deflected away, but the incoming embryo 1 takes its place in an exchange reaction so the binary continues to exist.

Similar situations occur at about $\simeq 98.69$ kyr, when the configuration 1 + 2 changes to 1 + 3, and at $\simeq 103.4$ kyr, when the configuration 1 + 3 changes to 3 + 4. Figure 5 also reveals that the binary becomes hardened with each encounter since the overlap between the $r(t)$ curves for the binary components becomes tighter.

An even clearer indication of binary hardening is provided by Figure 6, where we plot the temporal evolution of the orbital elements of the binary planet. The color of the curves changes each time there is a change in the composition of the binary. One can further notice that the exchange interactions produce sudden decreases of a and also of e . Between the exchange interactions, a decreases smoothly whereas e generally increases in an oscillatory manner. We will describe these variations later.

Considering the binary planet inclination, the transient binary 2 + 4 forms with a prograde orbit and a relatively low inclination. During the first three-body encounter, the binary is reconfigured to a retrograde orbit with the inclination oscillating between 100° and 170° . The inclination then slowly evolves toward 180° regardless of the swap encounters, which only diminish the amplitude of the oscillation.

The binary planet does not survive to the end of our simulation. At $\simeq 111.26$ kyr, it undergoes a three-body exchange interaction with embryo 1 during which their Hill spheres overlap for a prolonged period of time (see the spike in Figure 3 at $\simeq 111.26$ kyr). Consequently, the binary inclination is flipped from the retrograde configuration to $I = 80^\circ$. In this configuration, the binary undergoes a fast decrease of a , accompanied by an equally fast increase of e . Consequently, the binary planet ends its life in a merger into a single body.

3.6. Binary Planet Evolution without Perturbing Embryos

The lifetime of the hardened binary in our nominal simulation is long enough ($\sim 10^4$ yr) to be interesting. There are two basic questions that we shall now address. First, what is the evolution of such a binary if the surrounding embryos and their perturbations are ignored? And second, what causes the changes in the binary orbital elements between the three-body encounters in Figure 6?

To answer these questions, we discard the non-binary embryos and restart the simulation from the configuration of

the binary planet,⁷ gas, and pebbles corresponding to $t = 100$ kyr. Three models are numerically evolved for 45 kyr. The first one has the same setup as the initial simulation (apart from the ignored non-binary embryos). In the second one, the accretion heating is disabled but the mass of the binary components can still grow by pebble accretion. In the third one, we again switch off accretion heating and discard the pebble disk; the binary mass therefore remains constant.

The orbital evolution of the binary in these three cases is shown in Figure 7. The evolution of the inclination is more or less the same, regardless of the model, and converges toward a fully retrograde configuration. The semimajor axis decreases as a consequence of pebble accretion, which transports the linear momentum and mass onto the binary components, thus changing their orbital angular momentum. It is worth noting that if the pebble accretion and accretion heating are ignored, the isolated binary planet evolving in the radiative disk exhibits only minor orbital changes (once it adjusts to the removal of the surrounding embryos at the beginning of the restart).

The eccentricity substantially changes only in the model with accretion heating, otherwise it oscillates around its initial value or exhibits a slow secular variation. In other words, not only is the hot-trail effect important for exciting the eccentricities of individual embryos before the encounter phase, but it is also responsible for pumping the eccentricity of the binary up to an asymptotic value $e \simeq 0.75$.

These findings justify our incorporation of pebble accretion and accretion heating into the model because both phenomena affect the rate of change of the binary orbital elements. Pebble accretion diminishes the semimajor axis and accretion heating excites the eccentricity.

3.7. Binary Planet Evolution in the Disk-free Phase

When protoplanetary disks undergo dispersal due to photoevaporation, the emerging planetary systems may become unstable (e.g., Lega et al. 2013). Here we test whether the hardened binary planet could survive the gas removal phase and the subsequent orbital instabilities. Since the binary undergoes three-body encounters during the disk phase, they can also be expected after removal of the disk.

To investigate the evolution after the photoevaporation, we remove the fluid part of the model (i.e., gas and pebbles) instantly and continue with a pure N -body simulation. The orbits are integrated for an additional 10 Myr. To account for the chaotic nature of an N -body system with close encounters, we extract 48 orbital configurations of the embryos from between $\simeq 99.7$ kyr and $\simeq 102.4$ kyr of the nominal simulation and use them as the initial conditions for 48 independent integrations.

Our aim is to quantify the survival rate of binary planets. Figure 8 shows the evolution of the fraction $N_{\text{surv}}/N_{\text{tot}}$, where N_{surv} is the number of N -body systems still containing a binary planet at simulation time t and N_{tot} is the total number of systems (48). The dependence exhibits a steep decrease—the binary dissolves before 0.1 Myr of evolution in $\simeq 45\%$ of cases and before 1 Myr in $\simeq 76\%$ of cases. However, the trend for $t \geq 1$ Myr becomes rather flat. The binary planet survives the whole integration timespan in 15% of our runs.

⁷ The binary elements at the moment of restart are $a \simeq 0.035$ au, $e \simeq 0.66$, $I \simeq 2.6$ rad.

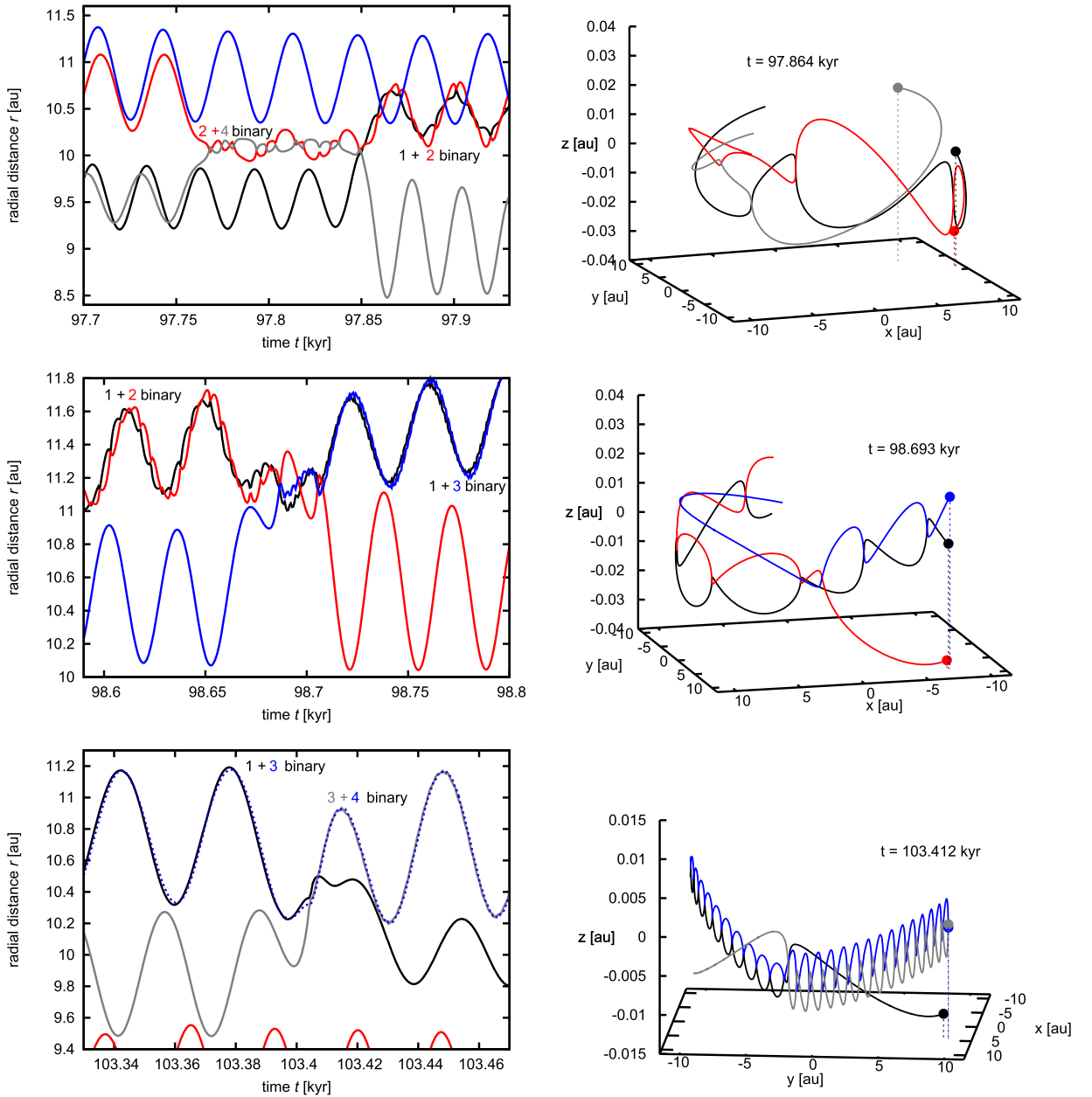


Figure 5. Details of important three-body encounters occurring in the nominal simulation, leading to reconfiguration and hardening of the binary planet. Each row shows a different encounter (and the first row also shows the transient binary of embryos 2 + 4 preceding the three-body encounters). We plot the temporal evolution of the radial distance r (left column) and also the orbital evolution in 3D Cartesian space (right column) in a short time interval around the respective encounters. The numbering and coloring of the bodies is the same as in Figure 2. Filled circles in the right column mark the positions of embryos at the simulation time t given by the labels. An animated version of the top row of Figure 5 is available in the online Journal. The animation spans $t \simeq 97.7\text{--}97.92$ kyr in simulation time, displaying the same tracks as in the static figure.

(An animation of this figure is available.)

We estimate the fraction of planetary systems f_{surv} in which the binary can survive the orbital instabilities. An estimate for young systems can be readily made by taking the final fraction of our integrations conserving the binary, yielding $f_{\text{surv},10 \text{ Myr}} \simeq 15\%$. To make an estimate for older systems, we performed a power-law extrapolation of the flat tail

of the distribution in Figure 8. The resulting extrapolation $0.22(t/(1 \text{ Myr}))^{-0.21}$ yields $f_{\text{surv},4.5 \text{ Gyr}} \simeq 4\%$ for $t = 4.5 \text{ Gyr}$ (i.e., comparable to the age of the solar system).

Let us briefly discuss the orbital architecture of the individual systems at the end of our integrations (Figure 9). The systems that retained the binary can be divided into two

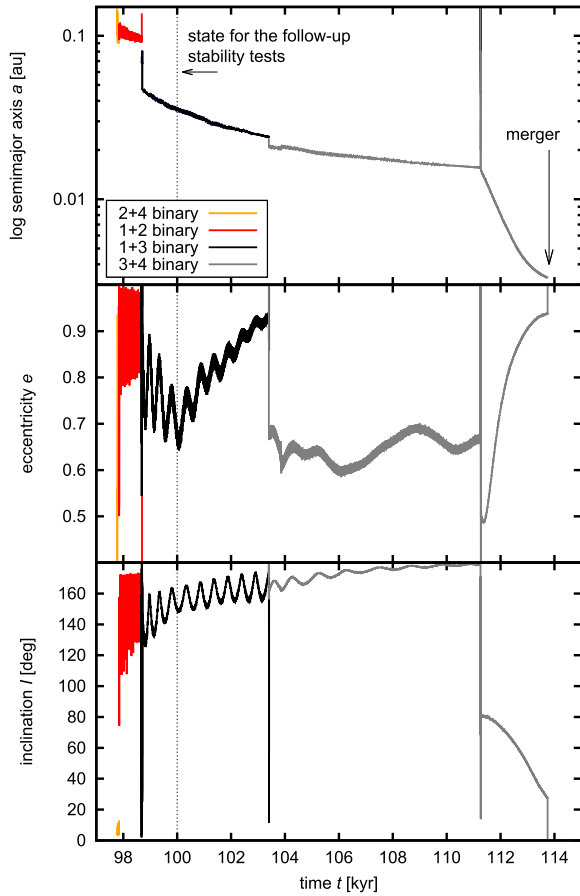


Figure 6. The temporal evolution of the orbital elements of the binary planet, namely the semimajor axis a (top), eccentricity e (middle), and inclination I (bottom). The color of the curves changes if different embryos become locked in the binary configuration during a three-body encounter (see Figure 5 for reference). The encounters can be recognized as sudden spikes and they typically lead to a sudden decrease of a and e . In the course of time, the binary becomes bound more tightly. The existence of the binary ends with a merger, marked by an arrow.

classes. The more common first class comprises five systems (simulation numbers 5, 12, 28, 34, 37) in which one of the binary components undergoes an early collision (at about ≈ 0.1 Myr) with one of the remaining embryos while maintaining the binary configuration. The collision reduces the multiplicity of the system and changes the mass ratio of the binary components from 1/1 to 2/1. The stability of such systems is obvious from Figure 9 because eccentricities are only marginally excited and the planets do not undergo orbital crossings.

The less frequent second class of orbital architectures (simulation numbers 17 and 38) includes systems in which no collision occurred yet the binary managed to survive close encounters. Orbits of the single embryos in these simulations are moderately eccentric and have orbital crossings with the binary. It is very likely that these systems would reconfigure and the binary would dissolve when integrating for $t > 10$ Myr. However, we

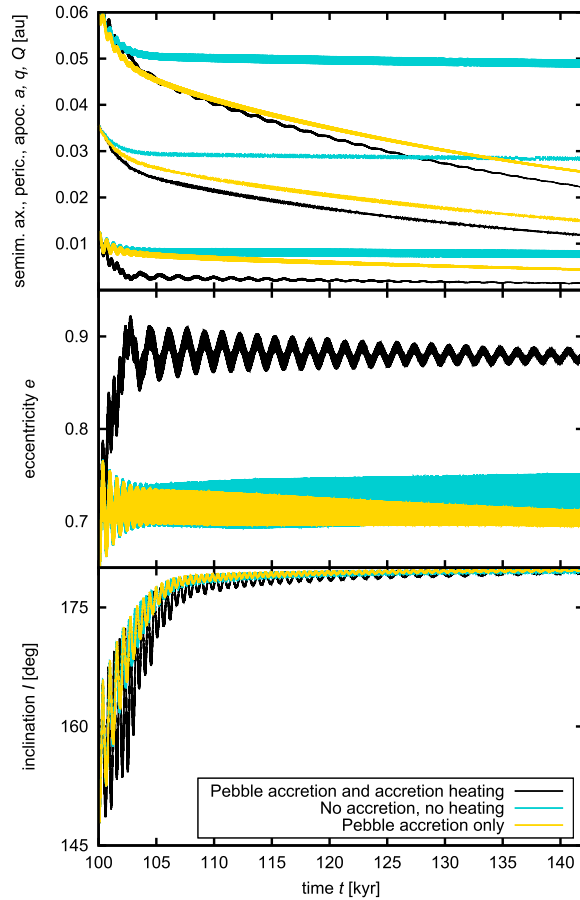


Figure 7. Stability test starting from the binary planet configuration corresponding to $t = 100$ kyr in Figure 6. In this test, the surrounding planetary embryos are removed. Therefore we study evolution of an isolated binary driven only by its interactions with the disk and not by close encounters. Three cases are shown: one with the complete RHD and two-fluid part of the model (black curve), one with pebble accretion but without accretion heating (gold curve), and one with neither pebble accretion nor heating (turquoise curve). Pebble accretion (i.e., mass growth) of the embryos generally causes the decrease in the semimajor axis. Accretion heating, on the other hand, is capable of pumping the eccentricity above the initial value.

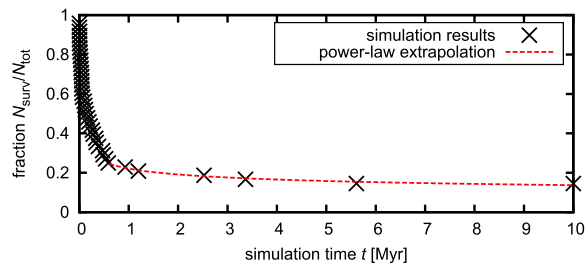


Figure 8. The fraction of N -body integrations in which the binary planet survives until simulation time t . The crosses mark the results of our integrations; the dashed curve is a power-law fit that is used as an extrapolation for $t > 10$ Myr.

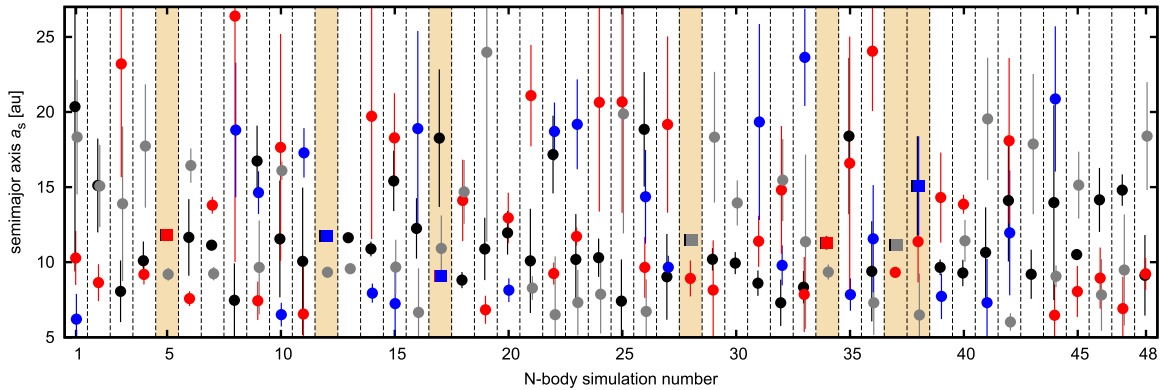


Figure 9. Orbital distribution of the planetary systems 10 Myr after removal of the disk. The horizontal axis shows the reference number of N -body simulations; individual cases are separated by the vertical dashed lines. The vertical axis shows the stellarcentric semimajor axis of planets displayed with symbols (the coloring is the same as in the previous figures). Single planets are marked by filled circles, binary planets are distinguished by filled squares (squares correspond to a_s of the binary barycenter). The systems that preserved the binary are also highlighted using a yellow background. The vertical bars of each symbol indicate the span of orbits from pericenter to apocenter (large bars correspond to eccentric orbits and smaller ones to more circular orbits).

believe that these two cases are accounted for by the power-law extrapolation when estimating f_{surv} for old systems.

3.8. Formation Efficiency

So far the analysis has been based on our nominal simulation. Although a broader study of the parametric space is difficult using RHD simulations, it is important to quantify how common it is for transients to become hardened and stabilized in three-body encounters. Also, it is desirable to test whether the result is sensitive to the choice of initial separations, embryo masses, and embryo multiplicity.

We perform four additional full RHD simulations in which we vary the initial conditions for embryos (the disk remains the same as in Section 3.1). Embryos start with different random longitudes, and inclinations are $I_s = I_0$. Two simulations (denoted I and II) are run with four embryos, each having $M_{\text{em}} = 3 M_{\oplus}$ again, but the innermost embryo is initially placed at $a_s = 6$ au and the remaining ones are spaced by 10 mutual Hill radii. Two simulations (denoted III and IV) include eight embryos with $M_{\text{em}} = 1.7 M_{\oplus}$, the innermost one being placed at $a_s = 5$ au and the others having initial separations of eight mutual Hill radii.

Simulations I and II cover 120 kyr of evolution. A common feature of these runs is a merger occurring relatively early (at ≈ 40 kyr and ≈ 51 kyr in simulations I and II, respectively), followed by a second merger (at ≈ 81 kyr and ≈ 94 kyr, respectively). Simulation III covers 180 kyr of evolution. There is a late violent sequence at ≈ 150 kyr during which two mergers occur and three embryos are scattered out of the simulated part of the disk.

In simulations I–III, only transient binaries are formed. However, we detect one case of a hardened binary in simulation IV, which covers 120 kyr of evolution. The simulation also contains 190 transients compared to 65 cases found in our nominal simulation, which implies that the increased multiplicity of the system (eight embryos instead of four) logically increases the frequency of embryo encounters.

Figure 10 shows the evolution of orbital elements of the binary configurations participating in binary hardening. First, a transient consisting of embryos 2 and 7 forms at about 122.5 kyr. After ≈ 1 kyr, it undergoes a three-body encounter

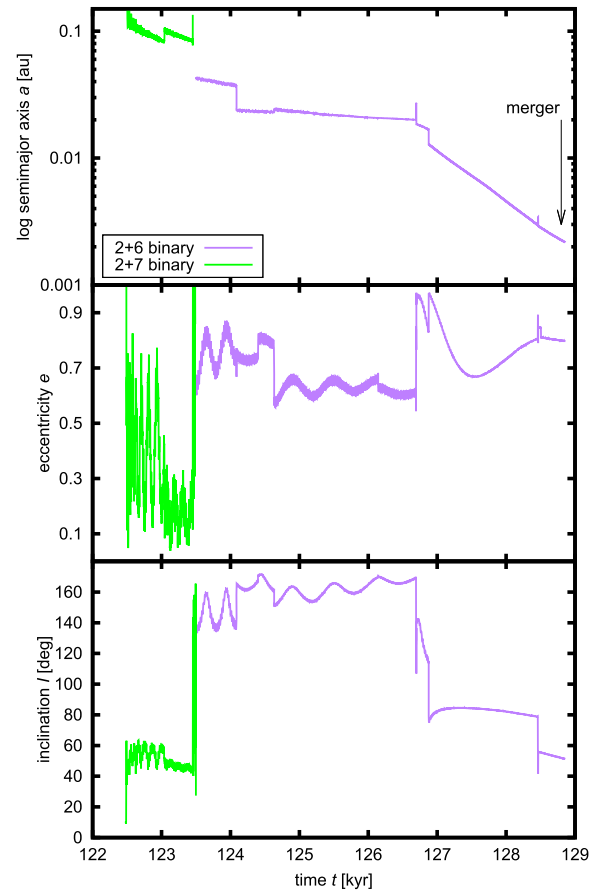


Figure 10. As in Figure 6, but for the binary configurations found in our additional simulation IV with eight embryos (initial $M_{\text{em}} = 1.7 M_{\oplus}$). The binary shown here undergoes similar evolution to that in Figure 6.

during which the configuration changes to embryos 2 and 6 and the semimajor axis of the binary decreases. Then the binary evolves for about 5 kyr due to pebble accretion and additional

three-body encounters. The secular rate of change of a is clearly related to the value of I , suggesting that the deposition of pebbles onto a prograde binary causes the separation to decrease faster than in a retrograde case. As in the nominal simulation, the binary separation shrinks until the binary merges.

Although the statistics of our five (one nominal and four additional) RHD simulations is still poor, we can nevertheless conclude that a binary planet with a considerable lifetime can form in at least some cases. We can also make a crude estimate of the formation efficiency f_{form} , which we define as the fraction of simulations in which a binary planet was formed and then hardened, obtaining $f_{\text{form}} \simeq 0.4$.

For simulations that formed such binaries, we also define the total time τ_{bp} for which the binary planet existed in the system (regardless of which embryos were bound). The binary in our nominal simulation existed for $\simeq 16$ kyr and the binary in simulation IV existed for $\simeq 6$ kyr in total. Taking the arithmetic mean of these two values, we obtain $\tau_{\text{bp}} \simeq 11$ kyr.

4. Discussing Binary Planets

4.1. Model Complexity and Limitations

The choice of the RHD model was not a priori motivated by studying the formation of binary planets. The initial motivation was to check how the evolution described in Chrenko et al. (2017) changes if the orbits of embryos become inclined due to the vertical hot-trail effect (only the horizontal hot trail was modeled in Chrenko et al. 2017). We found binary planet formation as an unexpected yet natural outcome of the model.

It is possible that a less complex model could be applied to scan the parametric space, e.g., by N -body integrations. But although there are many state-of-the-art N -body models of migration in multiplanet systems with disks (e.g., Cossou et al. 2013, 2014; Izidoro et al. 2017), none of them (to our knowledge) identified the formation of binary planets. This suggests that there might be issues preventing binary planet formation in such models.

We demonstrated in Section 3.4 that hydrodynamic effects are important during the formation of transient binaries by two-body encounters. The pair of approaching embryos creates perturbations in the disk that differ from perturbations arising from isolated embryos. The prescriptions for the disk torques that are currently used in N -body models (Cresswell & Nelson 2008; Paardekooper et al. 2010, 2011; Fendyke & Nelson 2014) cannot account for such effects because they were derived from models containing a single embryo, not an interacting pair. Moreover, such prescriptions do not account for the thermal torque and hot-trail effect.

We point out that our RHD model has some limitations as well. First, although the grid resolution leads to numerical convergence of the migration rate for low-mass planets (see, e.g., Lega et al. 2014; Brož et al. 2018, for discussions of resolution), it is not tuned to resolve binary configurations with the smallest orbital separations well enough. However, looking at the turquoise curve in Figure 7 (i.e., the case without additional perturbers), the marginal change of orbital elements indicates a very low level of numerical dissipation, safely negligible over a typical binary lifetime during the disk phase. Second, the vertical hot trail cannot be implemented in our 2D model in a self-consistent way. 3D simulations would be required to assess the importance of the vertical dimension,

which we neglect here. Finally, the magnitude of the thermal torques depends on the thermal diffusivity and therefore on the opacity (Masset 2017). However, we used a single opacity prescription and it remains unclear whether the described effects work the same way, e.g., in a low-density disk undergoing photoevaporation.

4.2. Formation Mechanism

We found that two-body encounters of planetary embryos in the gas disk can establish transient binaries. A binary planet with a considerable lifetime can form from a transient by a three-body encounter that provides the necessary energy dissipation to make the pair more tightly bound. Here we discuss whether there are other mechanisms suitable for formation of binary planets.

An additional possibility exists during the reaccumulation phase after a large impact of two embryos approaching on initially unbound trajectories, as discussed by Ryan et al. (2014). But this situation is highly unlikely. Head-on collisions usually disrupt the protoplanets in such a way that the reaccumulation forms a large primary and a low-mass disk, from which a satellite can be assembled but not a binary companion. Only a special grazing geometry with a large impact parameter can be successful (Ryan et al. 2014) and it can only produce binaries with separations of a few planetary radii due to the angular momentum deficit of such an encounter.

Finally, planets can be captured in a binary configuration by means of tidal dissipation. Ochiai et al. (2014) studied the evolution of three hot Jupiters around a host star and discovered that binary gas giants can form in $\sim 10\%$ of systems that undergo orbital crossings.

4.3. Mass of the Binary

In our hydrodynamic simulations, the components of binaries have comparable masses of several M_{\oplus} before they merge. But as we found in the follow-up gas-free N -body simulations, the system often stabilizes by a collision of one of the embryos with the binary. If the binary survives the collision, the mass ratio of the components increases to 2/1. Therefore it seems that, if born from a population of equal-mass embryos (as obtained in the oligarchic growth scenarios), binary planets would preferentially exist with the component mass ratio 1/1 or 2/1. This aspect of our model is related to the choice of the initial embryo masses and is of course too simplified to capture the outcome of models where accretion creates a range of embryo masses.

Although simulations with gas accretion onto the planets are beyond the scope of our paper, we believe that runaway accretion of gas onto the binary would disrupt it. We thus expect that the binary planets formed in three-body encounters cannot exceed the masses of giant planet cores. This could be ensured by the mechanism of pebble isolation (Lambrechts et al. 2014; Bitsch et al. 2018) or simply because binaries could form late, just before dispersal of the gas disk. However, it is possible that binary giant planets form later by the mechanism of tidal capture (Ochiai et al. 2014).

4.4. Tidal Evolution

Orbital evolution due to tidal dissipation is without doubt an important factor for the stability of binary planets. However, it

is difficult to assess the tidal effects at this stage because there are many unknown parameters. A large uncertainty lies in the parameter k_2/Q , where k_2 is the degree 2 Love number and Q is the tidal quality factor (e.g., Harris & Ward 1982). These parameters reflect the interior structure and thus they depend on the planetary composition (water-rich versus silicate-rich) and state (cold versus magma worlds), the latter of which changes on an uncertain timescale. Moreover, our model treats the planets as point-mass objects, and therefore we have no information about their rotation, which is important to determine the level of spin-orbital synchronicity. Additionally, similar masses of the binary components and their (possibly) retrograde and highly eccentric orbit make the analysis of tides even more complicated. For all these reasons, the model of tidal evolution of a binary planet should be sufficiently complex and should account for the internal structure and rheology (e.g., Boué et al. 2016; Walterová & Běhouňková 2017).

4.5. Occurrence Rate and Observability

We define the occurrence rate of binary planets f_{bp} as the fraction of planetary systems that are expected to contain at least one binary planet hardened by three-body encounters. An order-of-magnitude estimate can be obtained by dividing the timescale $\tau_{\text{bp}} \simeq 10^4$ yr for which these binary planets are typically present in our simulations (Section 3.8) by the lifetime of protoplanetary disks $\tau_{\text{disk}} \simeq 10^7$ yr (e.g., Fedele et al. 2010), correcting for the formation efficiency $f_{\text{form}} \simeq 0.4$ (Section 3.8) and for the fraction of the emerging planetary systems f_{stab} in which the binary planet can survive after dispersal of the gas disk (Section 3.7). This leads to

$$f_{\text{bp}} = f_{\text{form}} \frac{\tau_{\text{bp}}}{\tau_{\text{disk}}} f_{\text{stab}}. \quad (12)$$

We quantify two characteristic values for young planetary systems (using $f_{\text{stab},10 \text{ Myr}} \simeq 0.15$) and for old planetary systems (using $f_{\text{stab},4.5 \text{ Gyr}} \simeq 0.04$), leading to $f_{\text{bp},10 \text{ Myr}} \simeq 6 \times 10^{-5}$ and $f_{\text{bp},4.5 \text{ Gyr}} \simeq 2 \times 10^{-5}$. In other words, one out of $\simeq(2-5) \times 10^4$ planetary systems should contain a binary planet formed by two- and three-body encounters.

We emphasize that the estimate is highly uncertain because it is inferred from a small number of tests. Moreover, our simulations cover only a small region of the protoplanetary disk, the evolution timescale is still short compared to the disk's lifetime, and the number of embryos is relatively low. Last but not least, our estimate assumes that binaries only form by the processes identified in this work.

As pointed out in Section 1, the estimated occurrence rate should motivate a systematic search for binary planets in the observational data. For example, binary planets should be detectable by the Hunt for Exomoons with *Kepler* (HEK) project (Kipping et al. 2012). The sensitivity of this survey is $\simeq 40\%$ for binaries with Pluto-Charon mass ratios (Kipping et al. 2015).

4.6. Role in Planetary Systems

The possible existence of binary planets opens new avenues in planetary sciences. A study of long-term orbital dynamics and stability of binaries in various systems is needed (e.g., Donnison 2010), including an assessment of their tidal evolution. Binary planets are challenging for hydrodynamic modeling as well. Local high-resolution simulations of

interactions with the disk, pebble accretion, pebble isolation (e.g., Bitsch et al. 2018), and gas accretion (e.g., Lambrechts & Lega 2017) should be performed for binary planets (preferably in 3D) to understand the impact of these processes in detail.

In this paper, we reported various fates of binary planets (considering the set of gas-free N -body simulations). Frequently, one of the binary components underwent a collision with an equally large impactor, or the binary merged. The merger of the binary planet is a process that should be investigated (e.g., by the smoothed-particle hydrodynamics (SPH) method, Jutzi 2015).

A merger can occur in a situation when the binary orbit is inclined with respect to the global orbital plane, and the resulting body would then retain the initial angular momentum of the binary, forming a planet (or a giant planet core) with an angular tilt of the rotational axis. It might be worth investigating the relation of such an event to the origin of Uranus.

Moreover, the collision of the binary components would statistically occur at high impact angles. It is interesting that such impact angles and similar masses of the target and the impactor (although on unbound trajectories) were also used for a successful explanation of the impact origin of the Earth-Moon system (Canup 2012).

5. Conclusions

By means of 2D radiation hydrodynamic simulations with 3D planetary orbits, we described the formation of binary planets in a system of migrating super-Earths. A key ingredient of the model is the vertical hot-trail effect (Eklund & Masset 2017), which was incorporated by reducing the efficiency of the prescription for inclination damping (Tanaka & Ward 2004). We also accounted for the pebble disk, pebble accretion, and accretion heating, which naturally produces the horizontal hot-trail effect, providing excitation of eccentricity (Chrenko et al. 2017).

When convergent migration drives the planetary embryos together, the geometry of their encounters allows for vertical perturbations owing to the non-zero inclinations. The orbits become vertically stirred and dynamically hot, reaching inclinations up to $\simeq 2^\circ$.

Numerous transient binary planets form during the simulations by gas-assisted two-body encounters but such transients dissolve quickly. Binary planets with longer lifetimes $\sim 10^4$ yr form when a transient undergoes a three-body encounter with a third embryo. During this process of binary hardening, energy is removed from the binary orbit and the separation of components decreases. Also, three-body encounters often reconfigure the binary when one of the components swaps places with the encountered embryo. The existence of hardened binaries in our simulations typically ends with a merger of its components, which forms a giant planet core.

The role of the gas disk in binary planet formation is twofold. In two-body encounters, the disk can dissipate orbital energy of the embryos, thus aiding the gravitational capture. The dissipation is provided when the embryos cross a shared spiral arm. In three-body encounters, the disk torques hold the embryos closely packed and the hot-trail effect maintains the eccentricities and inclinations excited, increasing the probability that a transient will encounter another embryo before it dissolves.

We conducted numerical experiments to test the stability and evolution of binary planets in cases when pebble accretion is halted, or accretion heating is inefficient, or the disk dissipates. We found that pebble accretion causes a secular decrease of a of the binary whereas e increases due to the hot-trail effect.

For the binary to survive after dispersal of the disk, it is required that the surrounding embryos are removed or reconfigured dynamically. Quite often, a stable configuration is achieved when one of the components of the surviving binary undergoes a merger with another embryo, increasing the binary mass ratio from approximately 1/1 to 2/1.

We roughly estimated the expected fraction of planetary systems with binary planets to be $f_{bp} \simeq (2-6) \times 10^{-5}$, where the upper limit holds for young planetary systems and the lower limit holds for 4.5 Gyr old systems. In other words, a binary planet should be present in one planetary system out of $\simeq(2-5) \times 10^4$.

One can think of many new applications that the possible existence of binary planets brings. First, although binary planets have yet to be discovered, our estimate of their occurrence rate is encouraging for future observations. Second, the hydrodynamic interactions of binary planets with the disk may be different from those of a single planet and are worth investigating, preferably in 3D. Third, collisional models for planetary bodies that usually focus on unbound trajectories should also investigate colliding binaries to assess the possible outcomes.

The work of O.C. has been supported by Charles University (research program no. UNCE/SCI/023; project GA UK no. 128216; project SVV-260441) and by The Ministry of Education, Youth and Sports from the Large Infrastructures for Research, Experimental Development and Innovations project IT4Innovations National Supercomputing Center LM2015070. The work of O.C. and M.B. has been supported by the Grant Agency of the Czech Republic (grant No. 13-06083S). The work of D.N. has been supported by NASA XRP grant. Access to computing and storage facilities owned by parties and projects contributing to the National Grid Infrastructure MetaCentrum, provided under the programme “Projects of Large Research, Development, and Innovations Infrastructures” (CESNET LM2015042), is greatly appreciated. We thank Robin Canup and an anonymous referee for helpful comments on the paper.

ORCID iDs

Ondřej Chrenko  <https://orcid.org/0000-0001-7215-5026>

Miroslav Brož  <https://orcid.org/0000-0003-2763-1411>

David Nesvorný  <https://orcid.org/0000-0002-4547-4301>

References

- Araujo, R. A. N., Winter, O. C., Prado, A. F. B. A., & Vieira Martins, R. 2008, *MNRAS*, 391, 675
- Astakhov, S. A., Lee, E. A., & Farrelly, D. 2005, *MNRAS*, 360, 401
- Baillié, K., & Charnoz, S. 2014, *ApJ*, 786, 35
- Baruteau, C., & Masset, F. 2008, *ApJ*, 672, 1054
- Bell, K. R., & Lin, D. N. C. 1994, *ApJ*, 427, 987
- Benéz-Llambay, P., Masset, F., Koenigsberger, G., & Szulágyi, J. 2015, *Natur*, 520, 63
- Benéz-Llambay, P., & Pessah, M. E. 2018, *ApJL*, 855, L28
- Ben-Jaffel, L., & Ballester, G. E. 2014, *ApJL*, 785, L30
- Bennett, D. P., Batista, V., Bond, I. A., et al. 2014, *ApJ*, 785, 155
- Birstiel, T., Klahr, H., & Ercolano, B. 2012, *A&A*, 539, A148
- Bitsch, B., Crida, A., Morbidelli, A., Kley, W., & Dobbs-Dixon, I. 2013, *A&A*, 549, A124
- Bitsch, B., Morbidelli, A., Johansen, A., et al. 2018, *A&A*, 612, A30
- Boué, G., Correia, A. C. M., & Laskar, J. 2016, *CeMDA*, 126, 31
- Brown, M. E., van Dam, M. A., Bouchez, A. H., et al. 2006, *ApJL*, 639, L43
- Brož, M., Chrenko, O., Nesvorný, D., & Lambrechts, M. 2018, arXiv:1810.03385
- Brozović, M., Showalter, M. R., Jacobson, R. A., & Buie, M. W. 2015, *Icar*, 246, 317
- Canup, R. M. 2011, *AJ*, 141, 35
- Canup, R. M. 2012, *Sci*, 338, 1052
- Chiang, E. I., & Goldreich, P. 1997, *ApJ*, 490, 368
- Chrenko, O., Brož, M., & Lambrechts, M. 2017, *A&A*, 606, A114
- Christy, J. W., & Harrington, R. S. 1978, *AJ*, 83, 1005
- Cordeiro, R. R., Martins, R. V., & Leonel, E. D. 1999, *AJ*, 117, 1634
- Cossou, C., Raymond, S. N., Hersant, F., & Pierens, A. 2014, *A&A*, 569, A56
- Cossou, C., Raymond, S. N., & Pierens, A. 2013, *A&A*, 553, L2
- Cresswell, P., Dirksen, G., Kley, W., & Nelson, R. P. 2007, *A&A*, 473, 329
- Cresswell, P., & Nelson, R. P. 2008, *A&A*, 482, 677
- Crida, A., Sándor, Z., & Kley, W. 2008, *A&A*, 483, 325
- D’Angelo, G., Henning, T., & Kley, W. 2003, *ApJ*, 599, 548
- de Val-Borro, M., Edgar, R. G., Artymowicz, P., et al. 2006, *MNRAS*, 370, 529
- Donnison, J. R. 2010, *MNRAS*, 406, 1918
- Eklund, H., & Masset, F. S. 2017, *MNRAS*, 469, 206
- Erikson, A., Santerne, A., Renner, S., et al. 2012, *A&A*, 539, A14
- Fedele, D., van den Ancker, M. E., Henning, T., Jayawardhana, R., & Oliveira, J. M. 2010, *A&A*, 510, A72
- Fendyke, S. M., & Nelson, R. P. 2014, *MNRAS*, 437, 96
- Fraser, W. C., Bannister, M. T., Pike, R. E., et al. 2017, *NatAs*, 1, 0088
- Giuppone, C. A., Benéz-Llambay, P., & Beaugé, C. 2012, *MNRAS*, 421, 356
- Goldreich, P., Lithwick, Y., & Sari, R. 2002, *Natur*, 420, 643
- Han, C. 2008, *ApJ*, 684, 684
- Harris, A. W., & Ward, W. R. 1982, *AREPS*, 10, 61
- Heller, R. 2014, *ApJ*, 787, 14
- Heller, R. 2018, *A&A*, 610, A39
- Hills, J. G. 1975, *AJ*, 80, 809
- Hills, J. G. 1990, *AJ*, 99, 979
- Hippke, M. 2015, *ApJ*, 806, 51
- Hubeny, I. 1990, *ApJ*, 351, 632
- Izidoro, A., Ogiwara, M., Raymond, S. N., et al. 2017, *MNRAS*, 470, 1750
- Jutzi, M. 2015, *P&SS*, 107, 3
- Kipping, D. M. 2009, *MNRAS*, 392, 181
- Kipping, D. M., Bakos, G. Á, Buchhave, L., Nesvorný, D., & Schmitt, A. 2012, *ApJ*, 750, 115
- Kipping, D. M., Schmitt, A. R., Huang, X., et al. 2015, *ApJ*, 813, 14
- Klahr, H., & Kley, W. 2006, *A&A*, 445, 747
- Kley, W. 1989, *A&A*, 208, 98
- Kley, W., Bitsch, B., & Klahr, H. 2009, *A&A*, 506, 971
- Kley, W., & Crida, A. 2008, *A&A*, 487, L9
- Lambrechts, M., & Johansen, A. 2012, *A&A*, 544, A32
- Lambrechts, M., & Johansen, A. 2014, *A&A*, 572, A107
- Lambrechts, M., Johansen, A., & Morbidelli, A. 2014, *A&A*, 572, A35
- Lambrechts, M., & Lega, E. 2017, *A&A*, 606, A146
- Laughlin, G., & Chambers, J. E. 2002, *AJ*, 124, 592
- Lee, M. H., & Peale, S. J. 2006, *Icar*, 184, 573
- Lega, E., Crida, A., Bitsch, B., & Morbidelli, A. 2014, *MNRAS*, 440, 683
- Lega, E., Morbidelli, A., & Nesvorný, D. 2013, *MNRAS*, 431, 3494
- Lewis, K. M., Ochiai, H., Nagasawa, M., & Ida, S. 2015, *ApJ*, 805, 27
- Liebig, C., & Wambsganss, J. 2010, *A&A*, 520, A68
- Marchis, F., Descamps, P., Baek, M., et al. 2008, *Icar*, 196, 97
- Marchis, F., Hestroffer, D., Descamps, P., et al. 2006, *Natur*, 439, 565
- Margot, J. L., Nolan, M. C., Benner, L. A. M., et al. 2002, *Sci*, 296, 1445
- Masset, F. 2000, *A&AS*, 141, 165
- Masset, F. S. 2002, *A&A*, 387, 605
- Masset, F. S. 2017, *MNRAS*, 472, 4204
- Masset, F. S., & Velasco Romero, D. A. 2017, *MNRAS*, 465, 3175
- McKinnon, W. B., Stern, S. A., Weaver, H. A., et al. 2017, *Icar*, 287, 2
- Menou, K., & Goodman, J. 2004, *ApJ*, 606, 520
- Mihalas, D., & Weibel Mihalas, B. 1984, *Foundations of Radiation Hydrodynamics* (New York: Oxford Univ. Press)
- Morbidelli, A., & Nesvorný, D. 2012, *A&A*, 546, A18
- Müller, T. W. A., Kley, W., & Meru, F. 2012, *A&A*, 541, A123
- Nesvorný, D., Youdin, A. N., & Richardson, D. C. 2010, *AJ*, 140, 785
- Noll, K. S., Grundy, W. M., Stephens, D. C., Levison, H. F., & Kern, S. D. 2008, *Icar*, 194, 758

THE ASTROPHYSICAL JOURNAL, 868:145 (14pp), 2018 December 1

Chrenko, Brož, & Nesvorný

- Ochiai, H., Nagasawa, M., & Ida, S. 2014, *ApJ*, 790, 92
Ormel, C. W., & Klahr, H. H. 2010, *A&A*, 520, A43
Paardekooper, S.-J., Baruteau, C., Crida, A., & Kley, W. 2010, *MNRAS*, 401, 1950
Paardekooper, S.-J., Baruteau, C., & Kley, W. 2011, *MNRAS*, 410, 293
Paardekooper, S.-J., & Mellema, G. 2008, *A&A*, 478, 245
Papaloizou, J. C. B., & Larwood, J. D. 2000, *MNRAS*, 315, 823
Pierens, A. 2015, *MNRAS*, 454, 2003
Pierens, A., Cossou, C., & Raymond, S. N. 2013, *A&A*, 558, A105
Pravec, P., Scheirich, P., Kušnirák, P., et al. 2006, *Icar*, 181, 63
Pravec, P., Scheirich, P., Vokrouhlický, D., et al. 2012, *Icar*, 218, 125
Rein, H., & Liu, S.-F. 2012, *A&A*, 537, A128
Rein, H., & Spiegel, D. S. 2015, *MNRAS*, 446, 1424
Richardson, D. C., & Walsh, K. J. 2006, *AREPS*, 34, 47
Ryan, K., Nakajima, M., & Stevenson, D. J. 2014, AAS Meeting, 46, 201.02
Scheeres, D. J., Fahnestock, E. G., Ostro, S. J., et al. 2006, *Sci*, 314, 1280
Simó, C., & Stuchi, T. J. 2000, *PhyD*, 140, 1
Simon, A., Szatmáry, K., & Szabó, G. M. 2007, *A&A*, 470, 727
Simon, A. E., Szabó, G. M., Kiss, L. L., & Szatmáry, K. 2012, *MNRAS*, 419, 164
Sonnott, S., Mainzer, A., Grav, T., Masiero, J., & Bauer, J. 2015, *ApJ*, 799, 191
Tanaka, H., & Ward, W. R. 2004, *ApJ*, 602, 388
Teachey, A., Kipping, D. M., & Schmitt, A. R. 2018, *AJ*, 155, 36
Veillet, C., Parker, J. W., Griffin, I., et al. 2002, *Natur*, 416, 711
Walker, A. R. 1980, *MNRAS*, 192, 47P
Walsh, K. J., Richardson, D. C., & Michel, P. 2008, *Natur*, 454, 188
Walterová, M., & Běhouňková, M. 2017, *CeMDA*, 129, 235
Youdin, A. N., & Lithwick, Y. 2007, *Icar*, 192, 588

2.4 Paper IV: Oscillatory migration of accreting protoplanets driven by a 3D distortion of the gas flow

State of the art in 2019

In addition to Papers I–III and Eklund & Masset (2017) discussed above, several works were published to date which significantly contributed to the understanding of the heating torque and its influence on low-mass protoplanets. Masset (2017) presented a first theoretical framework in which he introduced the class of thermal torques to unify the cold-finger effect (Lega et al. 2014) and the heating torque (Benítez-Llambay et al. 2015). For a disk with a finite uniform thermal diffusivity χ , he applied the linear perturbation analysis to the set of shearing-sheet hydrodynamic equations with the addition of the one-temperature energy equation (see Sect. 1.1.2)

$$\frac{\partial \epsilon}{\partial t} + (\vec{v} \cdot \nabla) \epsilon = -P \nabla \cdot \vec{v} - \nabla \cdot \vec{F}_H + S, \quad (2.1)$$

where S can be decomposed to background source terms and the planet-induced source term S_p . The heat flux is

$$\vec{F}_H = -\chi \rho \nabla \left(\frac{\epsilon}{\rho} \right). \quad (2.2)$$

It is then possible to study linear disturbances in gas distribution created by the presence of a cold ($S_p = 0$) or hot ($S_p > 0$) planet, responsible for the cold-finger effect or the heating torque, respectively. It turns out that the density disturbance is positive for the cold planet, negative for the hot planet, and its overall shape is determined by a distortion due to the Keplerian shear. The density disturbance usually acquires the two-lobed shape discussed in Sect. 1.4.5.

The torque values obtained by Masset (2017) are

$$\Gamma_{\text{cold}} = -1.61 \frac{\gamma - 1}{\gamma} \frac{x_p}{\lambda_c} \Gamma_0, \quad (2.3)$$

and

$$\Gamma_{\text{heating}} = 1.61 \frac{\gamma - 1}{\gamma} \frac{x_p}{\lambda_c} \frac{L}{L_c} \Gamma_0, \quad (2.4)$$

where x_p is the distance of the planet to corotation with gas, the characteristic scale of the density disturbance is $\lambda_c = \sqrt{\chi/q\Omega_K\gamma}$, with the shear constant $q \simeq 3/2$, and the critical luminosity is $L_c = 4\pi GM_p \chi \rho_0 / \gamma$. In these expressions, γ is the adiabatic index and ρ_0 is the unperturbed gas density.

Follow-up studies extended the linear theory of thermal torques to include the vertical and horizontal hot-trail effect (Fromenteau & Masset 2019). Guilera et al. (2019) included the thermal torques in migration maps to demonstrate their importance for planet migration.

Although the linear perturbation theory is without doubts a useful tool for describing the heating torque (or the cold-finger effect) analytically, we shall see in the following that it does not provide a complete description of all possible flavours of the heating torque.

Aims and methods

Our studies of the heating torque presented in Papers I–III inevitably suffer from several drawbacks related to the 2D nature of **Thorin**:

- the vertical hot trail (inclination growth) cannot be self-consistently calculated;
- the assumption of the vertically isothermal gas distribution (used when evaluating the planet-disk gravitational interaction) is clearly violated above/below an accreting protoplanet;
- the 2D vertically integrated velocity field does not exactly reproduce the gas flow in midplane, thus the redistribution of hot gas might be inaccurate.

With the initial aim to validate our results from Papers I–III, we extended the public version of the **Fargo3d** code (Benítez-Llambay & Masset 2016) to include the energy equations for gas and radiation. We used the two-temperature approach (see Sect. 1.1.2) and we implemented viscous heating, radially ray-traced stellar irradiation, 3D radiative diffusion in the FLD approximation and parametric accretion heating from luminous protoplanets (pebble disk was not included). The **Ias15** integrator (Rein & Spiegel 2015) was interfaced to resolve N-body interactions. We also added OpenMP to the existing parallelisation of **Fargo3d** by MPI or CUDA.

From the physical point of view, our 3D RHD code is similar to the **Fargoca** code (Lega et al. 2014). However, there are at least two advantages of our code from the computational point of view. First, **Fargo3d** allows for a finer decomposition of the 3D computational domain (in the radial and vertical directions) while **Fargoca** only allows for a one-dimensional (radial) decomposition. Therefore, high resolution problems can be split to more MPI nodes using our code, which allows for a better scalability on CPU clusters. Second, the solution of linearised energy equations is obtained using the **IBiCGStab** (improved stabilised bi-conjugate gradient; Yang & Brent 2002) method which usually requires less CPU communications per time step compared to the SOR and it does not require any tuning of problem-dependent parameters (such as the over-relaxation parameter of SOR).

Simulations presented in Paper IV can be regarded as a follow-up to Benítez-Llambay et al. (2015). Generally, we present two types of simulations which share the same disk and planet parameters and they only differ in the opacity law. The opacity is either constant (as in Benítez-Llambay et al. 2015) or non-uniform (temperature-dependent; using the opacity table of Bell & Lin 1994). In most of our simulations, we study the heating torque acting on a single $3 M_{\oplus}$ protoplanet on a fixed circular orbit. The accretion mass doubling time which determines the luminosity of the

protoplanet is 100 kyr, comparable to the outcome of simulations with pebble accretion in Paper I. Our analysis focuses on a description of the perturbed gas flow near the planet in three dimensions (including the vertical direction).

Major results

3D DISTORTION OF THE GAS FLOW. Regardless of the opacity law, we found that the direction of the gas flow near the accreting protoplanet substantially changes with respect to a cold-planet situation. Specifically:

- Circulating streamlines passing by the protoplanet become bent towards the protoplanet (in the cold-planet situation, they are rather deflected away from the protoplanet).
- There are no horseshoe streamlines performing U-turns close to the Hill sphere (in the cold-planet situation, the stagnation point of the flow is typically within the Hill sphere, as well as several U-turns).
- In the horizontal direction, some streamlines, originating downstream the horseshoe region, become captured in the vicinity of the protoplanet, forming a retrograde spiral.
- The spiral-like flow propagates into the vertical direction, rising above the protoplanet. It forms a gas column, outflowing from the Hill sphere (in the cold-planet situation, there is usually a vertical inflow directed through the Hill sphere towards the protoplanet; Fung et al. 2015; Lambrechts & Lega 2017).

MECHANISMS OF THE FLOW DISTORTION. We identified two processes contributing to the flow distortion. The first one can be understood as follows: in the vicinity of a non-accreting protoplanet, gas accumulates within the potential well and the density and pressure exhibit local gradients that point towards the protoplanet. When the protoplanet becomes accreting and luminous, the pressure is not strongly perturbed while the density distribution develops two underdense lobes. Subsequently, there is a misalignment between the gradients of density and pressure, leading to a non-zero baroclinic term $\propto \nabla \rho \times \nabla P$ in the vorticity equation. The baroclinic vorticity production forces the flow to reconfigure.

The second process appears because the vertical temperature gradient above the accreting protoplanet is steep and can become superadiabatic. Therefore, the vicinity of the protoplanet becomes susceptible to convection and the vertical outflow is established.

FLOW INSTABILITY AND TORQUE OSCILLATIONS. In disks with vertically non-uniform opacities, the background vertical temperature gradients might be already on the verge of a superadiabatic stratification (Lin & Papaloizou 1980; Ruden & Pollack 1991). The accreting protoplanet then triggers convective instabilities that cannot be compensated for in a stationary manner and the gas flow becomes unstable. The set of spiral-like streamlines starts to circulate around the protoplanet in

a retrograde sense. Since the concentration of the overheated and thus underdense gas is amplified in the region of spiral-like streamlines, a single dominant underdense lobe is formed which follows the retrograde circulation around the protoplanet. This results in strong oscillations of the heating torque.

The torque variations lead to an oscillatory migration during which the protoplanet undergoes fast outward and inward excursions. They span $\sim 10^{-3}$ au and their direction changes approximately on the orbital timescale. The mean migration rate (averaged over multiple oscillations) remains almost unaffected by the heating torque. The heating torque therefore does not lead to outward migration in this case.

The amplitude of the oscillations scales with the opacity stratification above the protoplanet. For the temperature-dependent opacity laws $\kappa \propto T^\beta$, we found that the amplitude linearly decreases with β , but appears for all considered parameters in the range $\beta = 0.5\text{--}2$. If, on the other hand, the opacity is *radially non-uniform but vertically constant*, the flow instability and torque oscillations do not appear. This manifests the importance of the vertical structure and the vertical flow for the outcome of the heating torque.

IMPLICATIONS. Our findings have important implications because they show that the conclusions of Benítez-Llambay et al. (2015) and Masset (2017) do not provide a full description of the heating torque. Let us summarise the new pieces of the puzzle here.

First and foremost, the heating torque does not always have to be positive and does not always lead to outward migration. Second, explaining the response of the disk to planet accretion by the presence of horizontal underdense lobes (Benítez-Llambay et al. 2015) represents only a part of the whole picture; the vertical outflow of the overheated gas is equally important. Third, the linear perturbation theory of Masset (2017) does not predict the flow instability, nor the oscillatory heating torque. Fourth, the distortion of the horseshoe region close to the protoplanet suggests that the corotation torque might be modified in the presence of accretion heating as well. This has to be verified since Masset (2017) argued that the corotation torque should remain unaffected.

2.4.1 Reprint

Here we include the reprint of Paper IV.

Oscillatory migration of accreting protoplanets driven by a 3D distortion of the gas flow[★]

Ondřej Chrenko¹ and Michiel Lambrechts²¹ Institute of Astronomy, Charles University in Prague, V Holešovičkách 2, 18000 Prague 8, Czech Republic
e-mail: chrenko@sirrah.troja.mff.cuni.cz² Lund Observatory, Department of Astronomy and Theoretical Physics, Lund University, Box 43, 22100 Lund, Sweden

Received 21 February 2019 / Accepted 27 April 2019

ABSTRACT

Context. The dynamics of a low-mass protoplanet accreting solids is influenced by the heating torque, which was found to suppress inward migration in protoplanetary disks with constant opacities.

Aims. We investigate the differences in the heating torque between disks with constant and temperature-dependent opacities.

Methods. Interactions of a super-Earth-sized protoplanet with the gas disk are explored using 3D radiation hydrodynamic simulations.

Results. Accretion heating of the protoplanet creates a hot underdense region in the surrounding gas, leading to misalignment of the local density and pressure gradients. As a result, the 3D gas flow is perturbed and some of the streamlines form a retrograde spiral rising above the protoplanet. In the constant-opacity disk, the perturbed flow reaches a steady state and the underdense gas responsible for the heating torque remains distributed in accordance with previous studies. If the opacity is non-uniform, however, the differences in the disk structure can lead to more vigorous streamline distortion and eventually to a flow instability. The underdense gas develops a one-sided asymmetry which circulates around the protoplanet in a retrograde fashion. The heating torque thus strongly oscillates in time and does not on average counteract inward migration.

Conclusions. The torque variations make the radial drift of the protoplanet oscillatory, consisting of short intervals of alternating rapid inward and outward migration. We speculate that transitions between the positive and oscillatory heating torque may occur in specific disk regions susceptible to vertical convection, resulting in the convergent migration of multiple planetary embryos.

Key words. hydrodynamics – planets and satellites: formation – planet-disk interactions – protoplanetary disks

1. Introduction

Migration of protoplanets embedded in their natal gas disks is a key evolutionary step in the formation of each planetary system. Low-mass protoplanets, incapable of gap opening (Crida et al. 2006), undergo Type I migration under the influence of the gravitational torques exerted by the Lindblad spiral wakes (Goldreich & Tremaine 1979; Ward 1986) and by the gas in their corotation region (Ward 1991; Masset 2002; Tanaka et al. 2002; Paardekooper & Mellema 2006, 2008; Baruteau & Masset 2008; Masset & Casoli 2009; Paardekooper & Papaloizou 2009; Baruteau et al. 2011). Type I migration has a complicated relationship with disk structure and thermophysics (e.g. Kley & Crida 2008; Paardekooper et al. 2010, 2011; Lega et al. 2015). A detailed understanding of the underlying mechanism is therefore essential for the creation of realistic population synthesis models (e.g. Coleman & Nelson 2016).

A low-mass protoplanet evolving in a radiative disk has recently been shown to be subject to thermal torques (Lega et al. 2014; Benítez-Llambay et al. 2015; Masset & Velasco Romero 2017; Masset 2017) related to the thermal perturbations induced by the protoplanet in its vicinity. If the protoplanet itself is cold and non-luminous (Lega et al. 2014), the gas arriving in its potential well becomes heated, mostly as a result of compression (by means of the thermodynamic “PdV” term). The resulting temperature excess becomes smoothed out by radiative

transfer, so when the gas leaves the high-pressure region it lacks some of its internal energy – compared to the state before the compression – and therefore becomes colder and overdense. Two overdense lobes appear along the streamlines outflowing from the Hill sphere and their asymmetry makes the total torque acting on the protoplanet more negative, enhancing the inward migration. This process is known as the cold-finger effect (Lega et al. 2014).

In the opposite limit, the protoplanet is hot as a result of the solid material deposition during its formation (e.g. by pebble accretion; Ormel & Klahr 2010; Lambrechts & Johansen 2012). In such a case, the luminous protoplanet acts as a local heat source for the surrounding gas. Once the gas is heated, it becomes underdense compared to the situation without accretion heating. Benítez-Llambay et al. (2015) performed 3D radiation hydrodynamic simulations with the assumption of constant disk opacity and found that the hot protoplanet on a fixed circular orbit creates two underdense lobes of gas, again associated with the outflow from the Hill sphere. The rear lobe (positioned behind the protoplanet outwards from its orbit) is dominant, therefore there is an overabundance of gas ahead of the protoplanet and the resulting torque becomes more positive, supporting outward migration. The positive enhancement was named the heating torque. It was proposed to be an additional mechanism (along with other possibilities; see e.g. Rafikov 2002; Paardekooper & Mellema 2006; Morbidelli et al. 2008; Li et al. 2009; Yu et al. 2010; Kretke & Lin 2012; Bitsch et al. 2013; Fung & Chiang 2017; Brasser et al. 2018; Miranda & Lai 2018;

[★] Movie attached to Fig. 6 is available at <https://www.aanda.org>

McNally et al. 2019) capable of preventing the destruction of terrestrial-sized planetary embryos by an overly efficient inward migration (Korycansky & Pollack 1993; Ward 1997; Tanaka et al. 2002).

Moreover, the heating torque has important dynamical consequences for migrating protoplanets (Brož et al. 2018; Chrenko et al. 2018) because it can excite orbital eccentricities and inclinations by means of the hot-trail effect (Eklund & Masset 2017; Chrenko et al. 2017), which counteracts the otherwise efficient eccentricity and inclination damping by waves (Tanaka & Ward 2004; Cresswell et al. 2007).

Nevertheless, the heating torque has not been extensively studied in 3D radiative disks with non-uniform opacities. However, realistic opacity functions (Bell & Lin 1994; Semenov et al. 2003; Zhu et al. 2012) are of great significance for the disk structure and planet migration (e.g. Kretke & Lin 2012; Bitsch et al. 2013) and this study shows that the heating torque is affected as well.

In this paper, we reinvestigate the thermal torques acting on a low-mass protoplanet, with special emphasis on the heating torque in a disk with non-uniform opacity. We examine the streamlines near the protoplanet and point out the importance of their 3D distortion for redistribution of the hot underdense gas responsible for the heating torque.

2. Model

We consider a protoplanetary system consisting of a central protostar surrounded by a disk of coupled gas and dust in which a single protoplanet is embedded. The fluid part of the disk model accounts only for the gas, assuming the dust is a passive tracer that acts as the main contributor to the material opacity.

2.1. Governing equations

The disk is described using Eulerian hydrodynamics on a staggered spherical mesh centred on the protostar. The spherical coordinates consist of the radial distance r , azimuthal angle θ , and colatitude ϕ . Our model is built on top of the hydrodynamic module of FARGO3D¹ (Benítez-Llambay & Masset 2016), which solves the equations of continuity and momentum of a fluid

$$\frac{\partial \rho}{\partial t} + (\mathbf{v} \cdot \nabla) \rho = -\rho \nabla \cdot \mathbf{v}, \quad (1)$$

$$\frac{\partial \mathbf{v}}{\partial t} + (\mathbf{v} \cdot \nabla) \mathbf{v} = -\frac{\nabla P}{\rho} - \nabla \Phi + \frac{\nabla \cdot \mathbb{T}}{\rho} - [2\boldsymbol{\Omega} \times \mathbf{v} + \boldsymbol{\Omega} \times (\boldsymbol{\Omega} \times \mathbf{r})], \quad (2)$$

where ρ is the volume density, t is time, \mathbf{v} is the flow velocity vector (with the radial, azimuthal, and vertical components v_r , v_θ and v_ϕ), P is pressure, Φ is the gravitational potential of the protostar and the protoplanet, \mathbb{T} is the viscous stress tensor (Benítez-Llambay & Masset 2016), \mathbf{r} is the radius vector and $\boldsymbol{\Omega}$ is the angular velocity vector, which is non-zero because we work in the reference frame corotating with the protoplanet.

To account for the energy production, dissipation and transport in the disk, we implement the two-temperature energy equations for the gas and the radiation field according to the formulation of Bitsch et al. (2013):

$$\frac{\partial E_R}{\partial t} + \nabla \cdot \mathbf{F} = \rho \kappa_P [4\sigma T^4 - cE_R], \quad (3)$$

¹ Public version of the code is available at <http://fargo.in2p3.fr/>

$$\frac{\partial \epsilon}{\partial t} + (\mathbf{v} \cdot \nabla) \epsilon = -P \nabla \cdot \mathbf{v} - \rho \kappa_P [4\sigma T^4 - cE_R] + Q_{\text{visc}} + Q_{\text{art}} + Q_{\text{acc}}, \quad (4)$$

where E_R is the radiative energy, \mathbf{F} the radiation flux, κ_P the Planck opacity, σ the Stefan–Boltzmann constant, T the gas temperature, c the speed of light, ϵ the internal energy of the gas, and Q_{visc} the viscous heating term (Mihalas & Weibel Mihalas 1984). Furthermore, Q_{art} describes the heating due to the artificial viscosity (Stone & Norman 1992), and Q_{acc} the heat released when the protoplanet is accreting. Stellar irradiation is neglected in this paper for simplicity although our code is capable of including it as well.

The state equation of the ideal gas is used:

$$P = (\gamma - 1)\epsilon = (\gamma - 1)\rho c_V T, \quad (5)$$

where γ is the adiabatic index and c_V is the specific heat at constant volume, which can be expressed as $c_V = R/(\mu(\gamma - 1))$, where R is the universal gas constant and μ is the mean molecular weight.

The flux-limited diffusion approximation (FLD; Levermore & Pomraning 1981) is adopted to obtain a closure relation for the radiation flux,

$$\mathbf{F} = -\lambda_{\text{lim}} \frac{c}{\rho \kappa_R} \nabla E_R, \quad (6)$$

where κ_R is the Rosseland opacity and λ_{lim} is the flux limiter of Kley (1989). For the opacities, we assume that the Planck and Rosseland means are similar enough to be replaced with a single value κ . This is a valid assumption in the cold regions of protoplanetary disks that we aim to study (Bitsch et al. 2013). The detailed opacity law will be specified later in Sect. 2.3.

The accretion luminosity of the protoplanet is given by

$$L = \frac{GM_p \dot{M}_p}{R_p} = \frac{GM_p^2}{R_p \tau}, \quad (7)$$

where G is the gravitational constant, M_p is the mass of the protoplanet, \dot{M}_p is its accretion rate, and R_p is the radius of the protoplanet. In writing the second equality, we introduce the mass doubling time $\tau = M_p/\dot{M}_p$, which is a free parameter that controls the accretion rate in our model (see Sect. 2.2).

We assume that the radiation flux from the protoplanet is completely absorbed by the optically thick gas in the eight grid cells enclosing the protoplanet (Benítez-Llambay et al. 2015; Eklund & Masset 2017; Lambrechts & Lega 2017). The accretion heating, which is non-zero only within these cells, is then simply

$$Q_{\text{acc}} = \frac{L}{V}, \quad (8)$$

where V is the total volume of the heated cells.

The disk evolves in the combined gravitational potential of the central protostar and the embedded protoplanet:

$$\Phi = -\frac{GM_\star}{r} - \frac{GM_p}{d} f_{\text{sm}}, \quad (9)$$

where M_\star is the mass of the protostar and d is the cell-protoplanet distance. The planetary potential is smoothed to avoid numerical divergence at the protoplanet location ($d=0$)

O. Chrenko and M. Lambrechts: Oscillatory migration of accreting protoplanets driven by a 3D distortion of the gas flow

using the tapering cubic-spline function f_{sm} of Klahr & Kley (2006):

$$f_{\text{sm}} = \begin{cases} 1, & (d > r_{\text{sm}}), \\ \left[\left(\frac{d}{r_{\text{sm}}} \right)^4 - 2 \left(\frac{d}{r_{\text{sm}}} \right)^3 + 2 \frac{d}{r_{\text{sm}}} \right], & (d \leq r_{\text{sm}}), \end{cases} \quad (10)$$

where the smoothing length r_{sm} is a fraction of the Hill sphere radius of the protoplanet (see Sect. 2.2). Orbital evolution of the protoplanet is tracked using the IAS15 integrator (Rein & Spiegel 2015) from the REBOUND² package (Rein & Liu 2012), which we interfaced with FARGO3D.

Although FARGO3D is an explicit hydrodynamic solver, implementing Eqs. (3) and (4) in an explicit form would lead to a very restrictive Courant condition on the largest permitted time step length. To avoid such a time step limitation, it is advantageous to solve the energy equations in an implicit form. We thus follow the discretisation and linearisation proposed by Bitsch et al. (2013), with a minor modification introduced in Appendix A.

The solution of the implicit problem is obtained iteratively by minimizing the residual $\mathbf{r} \equiv \mathbf{A}\mathbf{x} - \mathbf{b}$, where \mathbf{A} is the matrix of the linear system, \mathbf{x} is the solution vector, and \mathbf{b} is the right-hand side vector. Our iterative solver uses the improved bi-conjugate stabilised method (IBiCGStab; Yang & Brent 2002) with the Jacobi preconditioning. The convergence criterion is $\|\mathbf{r}\|/\|\mathbf{b}\| < 10^{-4}$, where the norms are calculated in the L_2 space.

2.2. Initial conditions and parameters

Initial conditions describing the disk are adopted from Kley et al. (2009) and Lega et al. (2014). The surface density follows the power-law function $\Sigma = 484(r/1 \text{ au})^{-0.5} \text{ g cm}^{-2}$. The initial Σ is converted into the initial ρ assuming the disk is vertically isothermal. The velocity field is given by balancing the gravitational acceleration from the protostar, the acceleration due to the pressure gradient, and the centrifugal acceleration. We assign constant kinematic viscosity $\nu = 10^{15} \text{ cm}^2 \text{ s}^{-1}$ to the gas to mimic the angular momentum transport in the disk driven by physical effects outside the scope of this study (e.g. the turbulent eddy viscosity). The initial aspect ratio is $h = H/r = 0.05$, where H is the pressure scale height. The disk is therefore initially non-flaring but we point out that h evolves during the simulations. The adiabatic index is $\gamma = 1.43$ and the mean molecular weight is $\mu = 2.3 \text{ g mol}^{-1}$, corresponding to the solar mixture of the hydrogen and helium.

We assume a single embedded super-Earth with the mass $M_p = 3 M_\oplus$, orbiting on a circular orbit at the heliocentric distance of Jupiter: $a_p = a_J = 5.2 \text{ au}$. Unless otherwise specified, the orbit is held fixed in our simulations, i.e. the protoplanet is not allowed to migrate and the torque we measure is the static torque. The simulations are performed in the reference frame corotating with the protoplanet at the Keplerian angular frequency $\Omega_p \equiv \Omega_J = \sqrt{GM_\star/a_p^3}$ and the smoothing length for the tapering function of the gravitational potential f_{sm} is $r_{\text{sm}} = 0.5R_H$, where $R_H = a_p(M_p/(3M_\star))^{1/3}$ is the Hill sphere radius. We study both cases with and without planetary accretion, corresponding to the hot- and cold-protoplanet limit, respectively. In the simulations with the accretion, we assume the mass-doubling time $\tau = 100 \text{ kyr}$, which is a value within the range of the expected pebble accretion rates (Lambrechts & Johansen 2014;

Chrenko et al. 2017). The resulting luminosity of the protoplanet is $L \simeq 4.2 \times 10^{27} \text{ erg s}^{-1}$.

2.3. Opacities

Using the initial disk parameters, we setup two fiducial disk models that only differ in the material opacity function. The opacity is either constant or follows a slightly modified (see below) prescription of Bell & Lin (1994). To distinguish between the models, we use the abbreviations $\kappa_{\text{const-disk}}$ and $\kappa_{\text{BL-disk}}$, respectively. The exact value of the opacity in the $\kappa_{\text{const-disk}}$ is tuned to be the same as in the $\kappa_{\text{BL-disk}}$ at the location of the protoplanet a_p , leading to $\kappa_{\text{const}} \equiv \kappa_{\text{BL}}(r = a_p) = 1.11 \text{ cm}^2 \text{ g}^{-1}$.

The unmodified opacity from Bell & Lin (1994), which we denote $\kappa_{\text{BL}}^{\text{full}}(\rho(r, \theta, \phi), T(r, \theta, \phi))$, is a fitting law that sets κ as a function of the local gas density and temperature. The table spans several regimes corresponding to the presence (or absence) of dust or molecular species dominant in protoplanetary disks. Using $\kappa_{\text{BL}}^{\text{full}}$ in our simulations with the accretion heating of the protoplanet could cause strong local opacity gradients, because we expect the temperature perturbations to reach $\sim 10^1 \text{ K}$ at distances of one cell size from the centre of the protoplanet.

In practice, we apply the opacity law of Bell & Lin in a simplified way, using $\kappa_{\text{BL}}(\bar{\rho}(r, \phi), \bar{T}(r, \phi))$, where the bared quantities are azimuthally computed arithmetic means and the dependence on the θ -coordinate is therefore dropped. This helps us to distinguish the effects caused by the global structure of the disk from those related to the local κ - T - ρ feedback. To justify our approach, we verify in Appendix B that the unmodified opacity table $\kappa_{\text{BL}}^{\text{full}}$ of Bell & Lin (1994) does not change our conclusions.

The fiducial κ_{const} - and κ_{BL} -disks are discussed throughout the majority of the paper, with the exception of Sect. 3.6 where we study the dependence of the heating torque on the opacity gradient within the disk.

2.4. Grid resolution and boundary conditions

Migration of low-mass protoplanets critically depends on the grid resolution, we therefore combine the well-established disk extent and resolution from Lega et al. (2014; in the azimuthal and vertical direction) and Eklund & Masset (2017; in the radial direction). The disk radially stretches from $r_{\text{min}} = 3.12 \text{ au}$ to $r_{\text{max}} = 7.28 \text{ au}$ and is resolved by 512 rings. We prevent any vertical motions of the protoplanet in our simulations by assuming that the solution is symmetric with respect to the midplane. One of the disk boundaries in the colatitude is therefore located at the midplane ($\phi = \pi/2$); the vertical extent above the midplane is 7° . The colatitude is resolved by 64 zones. In the azimuth, we use only 1 sector in our preparatory simulations without the protoplanet and 1382 sectors in our simulations with the embedded protoplanet. The resulting local resolution is eight cells per R_H in the r - and ϕ -directions and three cells per R_H in the θ -direction (see also Appendix B.2 for a simple resolution test).

The azimuthal boundary conditions are periodic for all primitive quantities. The radial boundary conditions are symmetric for ρ , ϵ , and v_ϕ and reflecting for v_r . E_R is set to a zero gradient and v_θ is extrapolated using the same radial dependence as for the Keplerian rotation velocity. The boundary conditions in colatitude are symmetric for ρ , ϵ , v_r and v_θ , and reflecting for v_ϕ . E_R is symmetrised at the midplane boundary and set to $a_R T_0^4$ at the remaining boundary in the colatitude, where a_R is the radiation constant and $T_0 \equiv 5 \text{ K}$ is the ambient temperature that allows for vertical radiative cooling of the disk. Additionally,

² Public version of the code is available at <https://rebound.readthedocs.io/en/latest/>

wave-damping conditions of de Val-Borro et al. (2006) are imposed near the radial edges and also near the disk surface.

3. Simulations

3.1. Equilibrium disks

Since we use a non-isothermal equation of state and we also account for the energy production and transfer, the parametric setup of the disk, which was discussed so far, is not stationary. Therefore, before the simulations with the embedded protoplanet are conducted, we let both disks (κ_{const} -disk and κ_{BL} -disk) numerically evolve over a timescale of $100 P_{\text{orb}}$, where $P_{\text{orb}} = 2\pi/\Omega_J$.

The equilibrium state after the relaxation is presented in Fig. 1. We plot the radial profiles of the midplane temperature T , opacity κ , entropy $S = P/\rho^\gamma$ and aspect ratio $h = H/r$, where the pressure scale height is determined as $H = c_s/\Omega_K$ and the sound speed as $c_s = \sqrt{\gamma P/\rho}$.

The constant opacity of the κ_{const} -disk makes all the remaining radial dependences rather shallow. The aspect ratio is almost flat, only slightly increasing with the radial distance. In the κ_{BL} -disk, on the other hand, the opacity has a peak near 3.5 au, where the water ice evaporates for the given setup, and decreases at larger radii. Therefore, the efficiency of the disk cooling increases and simultaneously, the efficiency of the viscous heating diminishes with the dropping relative velocity of the shearing layers. Consequently, the aspect ratio radially decreases as the energy budget is not sufficient to puff up the disk. In such a disk, T and S profiles radially decrease more steeply compared to the κ_{const} -disk.

3.2. Torque evolution

Starting from the relaxed state of the disks, we copy the hydrodynamic quantities in the azimuthal direction to expand the resolution from a single sector to the desired 1382 sectors. The protoplanet is inserted and we simulate $30 P_{\text{orb}}$ of evolution while neglecting any accretion and accretion heating of the protoplanet. The aim of this part of the simulation is to allow the disk to adjust to the presence of a gravitational perturber and to acquire a converged value of the disk torque in the absence of the accretion heating, corresponding to the cold-protoplanet limit. For the κ_{BL} -disk, this part of the simulation is similar to the experiments in Lega et al. (2014). Subsequently, we continue the simulation for another $30 P_{\text{orb}}$ during which we let the planetary mass grow while releasing the accretion heat into the gas disk according to Eqs. (7) and (8).

Figure 2 shows the temporal evolution of the torque exerted on the protoplanet by the κ_{const} -disk and κ_{BL} -disk. During the phase without accretion heating, the torque converges to a stationary value during $10 P_{\text{orb}}$. The torque value in the κ_{BL} -disk is more positive compared to the κ_{const} -disk, which is because the steeper radial decline of the entropy in the κ_{BL} -disk enhances the positive entropy-driven part of the corotation torque (Paardekooper & Mellema 2006; Baruteau & Masset 2008).

When the accretion heating is activated in the κ_{const} -disk, a positive contribution is added to the torque, in accordance with the results of Benítez-Llambay et al. (2015). The torque slightly oscillates at first, but the amplitude of the oscillations decreases in time and becomes negligible at $t = 50 P_{\text{orb}}$.

On the contrary, when the accretion heating is activated in the κ_{BL} -disk, the outcome of the heating torque becomes very different. Strong oscillations of the disk torque are excited

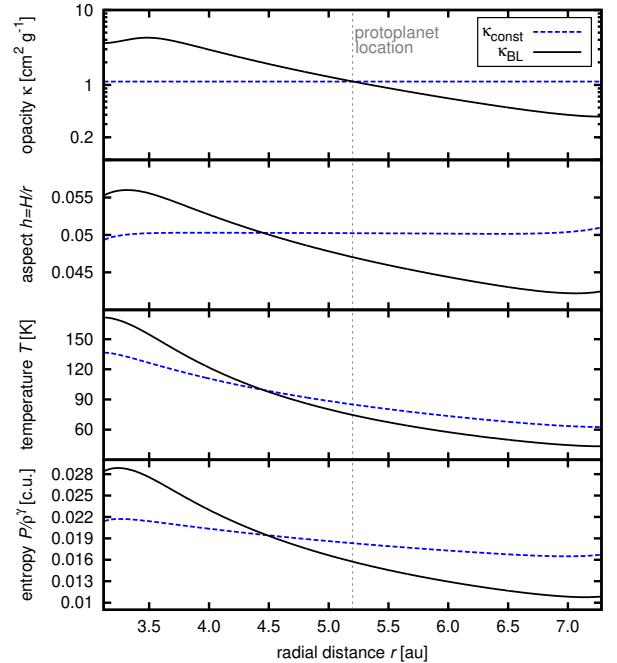


Fig. 1. Radial profiles of the characteristic quantities in the κ_{const} -disk (dashed blue curves) and the κ_{BL} -disk (solid black curves) after their numerical relaxation over $t = 100 P_{\text{orb}}$. From top to bottom panels: opacity κ , aspect ratio $h = H/r$, temperature T and entropy $S = P/\rho^\gamma$. Midplane values are displayed (or used to derive h). Dotted vertical line indicates the orbital distance of the protoplanet, $a_p = 5.2$ au.

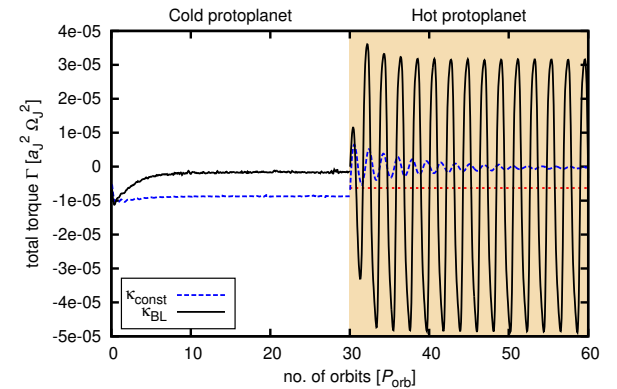


Fig. 2. Temporal evolution of the total torque exerted on the protoplanet ($M_p = 3 M_\oplus$) by the κ_{const} -disk (dashed blue curve) and the κ_{BL} -disk (solid black curve). For $t \leq 30 P_{\text{orb}}$, the protoplanet is not accreting. Its accretion and the respective heating are activated for $t > 30 P_{\text{orb}}$, as also highlighted by a yellow background. While the blue curve evolves as expected, i.e. gains a positive boost when the accretion heating is initiated (Benítez-Llambay et al. 2015), the black curve does not converge and instead exhibits strong oscillations between positive and negative values. The red horizontal dotted line shows the mean value of the oscillating black curve and demonstrates that the heating torque makes the total torque more negative in this case.

almost immediately and they do not vanish in time; instead, their amplitude remains the same. The arithmetic mean of the torque measured in the time interval $30\text{--}60 P_{\text{orb}}$ is $\bar{\Gamma} \simeq -6.3 \times 10^{-6} a_J^2 \Omega_J^2$, implying that the torque is more negative

O. Chrenko and M. Lambrechts: Oscillatory migration of accreting protoplanets driven by a 3D distortion of the gas flow

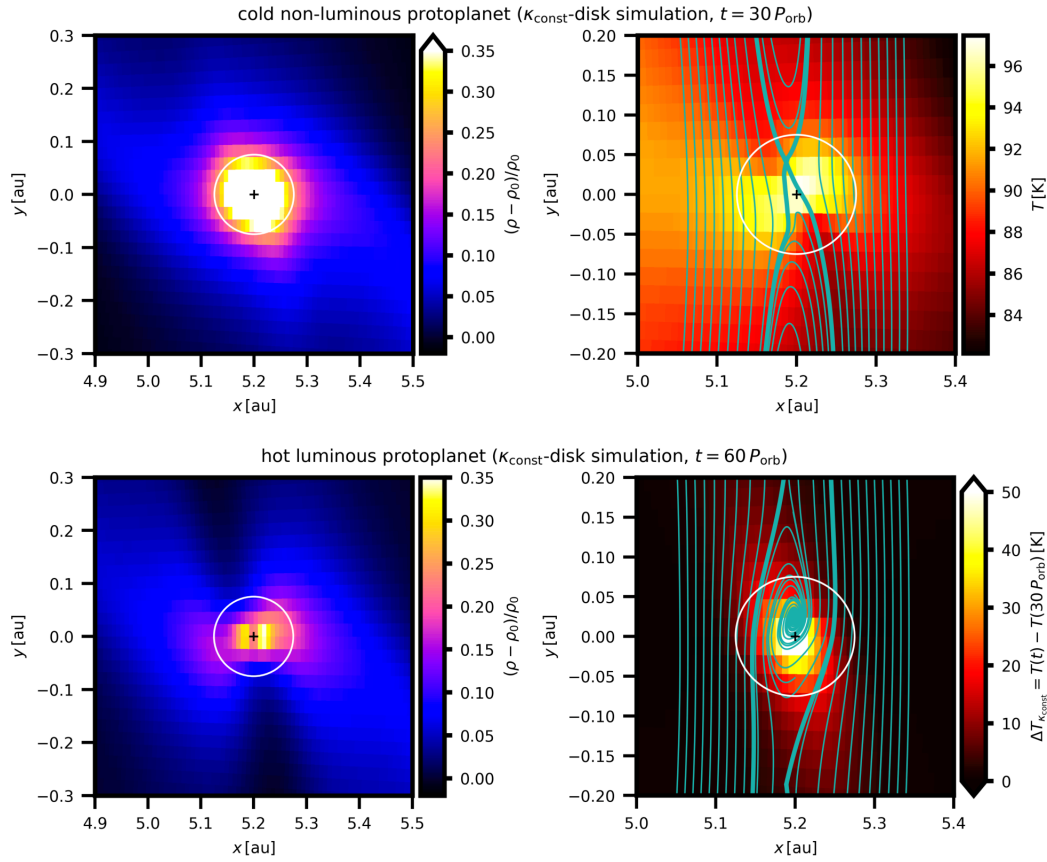


Fig. 3. Hydrodynamic quantities in the midplane of the κ_{const} -disk close to the protoplanet. *Top row:* cold protoplanet right before the accretion heating is initiated (at $t = 30 P_{\text{orb}}$). *Bottom row:* steady state of gas around the hot protoplanet (at $t = 60 P_{\text{orb}}$). The figure is constructed as a Cartesian projection of the spherical grid. The density maps (*left*) display the perturbation $(\rho - \rho_0)/\rho_0$ relative to the equilibrium disk ($t = 0 P_{\text{orb}}$), the temperature map for the cold protoplanet (*top right*) shows the absolute values, and the temperature map for the hot protoplanet (*bottom right*) shows the excess with respect to the cold protoplanet (by subtracting $T(t = 30 P_{\text{orb}})$ from $T(t = 60 P_{\text{orb}})$). The position of the protoplanet is marked with the cross, the extent of its Hill sphere is bordered by the circle. The green curves (*right*) show the topology of streamlines in the frame corotating with the protoplanet. In the inertial frame, the protoplanet would orbit counterclockwise. The streamlines outwards from its orbit thus depict the flow directed from $y > 0$ to $y < 0$; the inward streamlines are oriented in the opposite direction. A detailed view of the streamlines is provided in Fig. 5 where we also sort them according to their type.

compared to the situation without accretion heating (the mean torque in the interval $20\text{--}30 P_{\text{orb}}$ is $\bar{\Gamma} \approx -1.6 \times 10^{-6} a_J^2 \Omega_J^2$). The amplitude of the variations with respect to the mean value is $\approx \pm 3.9 \times 10^{-5} a_J^2 \Omega_J^2$ and the oscillation period is $\approx 2.1 P_{\text{orb}}$.

The torque oscillations are unexpected and we therefore focus throughout the rest of the paper on finding the physical mechanism that excites them. The occurrence of oscillations suggests that the gas distribution around the protoplanet is changing during the simulation, as we can demonstrate using the integral expression for the disk torque,

$$\Gamma = \int_{\text{disk}} (\mathbf{r}_p \times \mathbf{F}_g)_\perp dV, \quad (11)$$

where \mathbf{r}_p is the radius vector of the protoplanet, \mathbf{F}_g is the gravitational force of a disk element, the vertical component of the cross product is considered, and we integrate over the disk volume. Only a non-zero azimuthal component of \mathbf{F}_g can lead to a non-vanishing cross product in the integral, and therefore any oscillations of Γ must be related to a variation of $F_{g,\theta}$. In other words, there must be an azimuthal asymmetry in the gas distribution with respect to the protoplanet for the torque to be non-zero

and only a temporal redistribution of the asymmetry can cause a torque oscillation.

Our strategy throughout the remainder of Sect. 3 is the following: first, we focus on the κ_{const} -disk simulation in Sect. 3.3. Although similar simulations were analysed by Benítez-Llambay et al. (2015), our aim is to focus on the 3D gas flow that has not yet been described. Our findings are then expanded for the κ_{BL} -disk simulation in Sect. 3.4 where we relate the gas redistribution to the oscillatory behaviour of the torque. Section 3.5 is devoted to identifying the key physical mechanisms that affect the gas flow. In Sect. 3.6, we vary the disk opacity gradient and study its impact on the torque oscillation. Finally, we relax the assumption of a fixed orbit and explore how the protoplanet migrates in Sect. 3.7.

3.3. Steady state of the heated gas

In this section, the κ_{const} -disk simulation is analysed.

3.3.1. Midplane

Figure 3 compares the midplane density and temperature distribution around the cold and hot protoplanet. We display the state

of the simulation at $t = 30$ (i.e. at the final stage of the phase without accretion heating) and $60 P_{\text{orb}}$ (i.e. at the final stage of the phase with accretion heating). The latter represents the steady state of gas around the accreting protoplanet and we verified that such a distribution is achieved early (at $t \approx 31 P_{\text{orb}}$) and does not greatly evolve afterwards.

For the non-luminous protoplanet, the gas state is in agreement with [Lega et al. \(2014; see their Fig. 10 for a comparison\)](#). The density distribution is not spherically symmetric with respect to the protoplanet but there are two patches of slightly overdense gas along the outflow from the Hill sphere known as the cold fingers (explained in Sect. 1). The temperature drop inside the fingers is clearly apparent from the top-right panel of Fig. 3.

When the protoplanet becomes luminous, the gas distribution is modified and the heating torque arises. Following [Benítez-Llambay et al. \(2015\)](#) and [Masset \(2017\)](#), one can imagine the response of the gas to the heating from the protoplanet as follows: first, an underdense disturbance appears close to the protoplanet, with a characteristic scale length given by the linear perturbation model of [Masset \(2017\)](#):

$$\lambda_c = \sqrt{\frac{\chi}{q\Omega_p\gamma}}, \quad (12)$$

where χ is the thermal diffusivity and q is a dimensionless measure of the disk shear ($q = 3/2$ for a Keplerian disk). Second, the low-density gas is distorted by the shear motions. The rotation of the inner disk with respect to the protoplanet is faster and the low-density gas thus propagates ahead of the protoplanet. The motion of the outer disk lags behind the protoplanet and so does the hot perturbation. As a result, two hot lobes with decreased density are formed along the streamlines outflowing from the Hill sphere, as described by [Benítez-Llambay et al. \(2015\)](#). The size of the lobes is inherently asymmetric because the corotation between the protoplanet and the sub-Keplerian gas is radially shifted inwards, therefore the outer rear lobe is usually larger and the heating torque should be positive.

Such an advection-diffusion interplay is indeed observed in Fig. 3, where we find the typical two-lobed distribution of hot underdense gas around the luminous protoplanet and the positive boost of the total torque (Fig. 2) confirms that the outer lobe is slightly more pronounced. The bottom-right panel reveals the magnitude and spatial extent of the temperature excess, as well as its skewed shape in the direction of the disk shear.

However, we make a new observation here concerning the streamlines of the flow that are overlaid in the temperature maps. It is obvious that the hot perturbation significantly changes the topology of the flow with respect to the cold-protoplanet case. U-turn streamlines no longer appear in the depicted part of the disk, the direction of the circulating streamlines changes as they pass the protoplanet, and a new set of spiral-like retrograde streamlines appears.

3.3.2. Vertical plane

It is known that vertical motions play an important role in the structure of circumplanetary envelopes (e.g. [Tanigawa et al. 2012; Fung et al. 2015; Ormel et al. 2015; Cimerman et al. 2017; Lambrechts & Lega 2017; Kurokawa & Tanigawa 2018; Popovas et al. 2019](#)). Since previous studies of the heating torque did not investigate the vertical perturbations, we therefore do so here. Figure 4 shows the gas temperature and the velocity field in the vertical plane intersecting the location of the protoplanet. When the protoplanet is cold, there is a vertical stream of gas

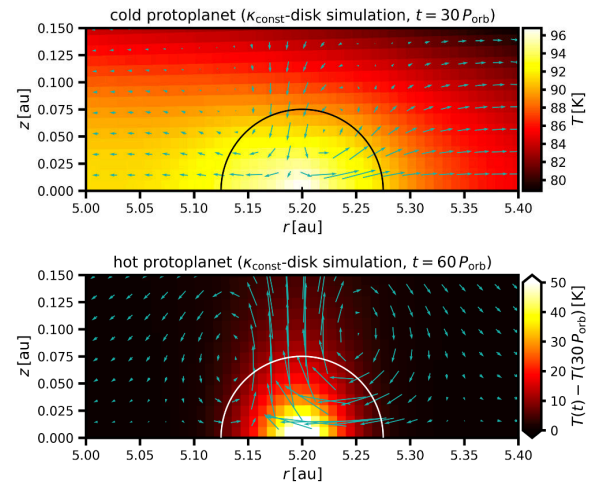


Fig. 4. Temperature map around the cold protoplanet at $t = 30 P_{\text{orb}}$ (top) and temperature excess around the hot protoplanet at $t = 60 P_{\text{orb}}$ (bottom) in the κ_{const} -disk. The vertical plane (perpendicular to the disk midplane) is displayed. The green arrows show the vertical velocity vector field.

descending towards the protoplanet and escaping as an outflow through the midplane, in accordance with e.g. [Lambrechts & Lega \(2017\)](#).

However, in the presence of accretion heating the direction of the gas flow above the protoplanet is reverted; it forms an outflowing column while the midplane flow becomes directed towards the protoplanet. Two overturning cells appear on each side of the vertical column (although it is important to point out that no such cells are apparent in the full 3D flow which is discussed later). We notice that the hot perturbation is not spherically symmetric but rather elongated in the direction of the column, indicating that the envelope is not hydrostatic.

3.3.3. Two- and three-dimensional streamline topology

So far, we have described two new findings that were not incorporated in the existing descriptions of the heating torque ([Benítez-Llambay et al. 2015; Masset 2017](#)): the distortion of the streamline topology and the reversal of the vertical motions. The flow direction is directly linked to the heating torque because it determines the redistribution of the hot gas by advection and thus contributes to the shape of the underdense regions. Therefore, we focus on the streamline topology in this section.

The streamlines are calculated using the explicit first-order Euler integrator and the trilinear interpolation of the velocity field. The interpolation allows us to obtain the velocity vector at an arbitrary location within the spherical grid. The size of the integration step is chosen so that the length integrated during a single propagation does not exceed 0.1 of the shortest cell dimension.

We construct 2D and 3D projections of the streamline topologies. For the 2D projections, the streamlines are generated exactly at the midplane where $v_\phi = 0$ and although they provide a useful visualisation, we emphasise that by construction they carry no information about the adjacent vertical flows. For the 3D projections, the streamlines are generated slightly above the midplane (at $\phi = \pi/2 - 0.005$ rad) to take into account non-zero v_ϕ .

Figure 5 shows 2D and 3D streamlines in the κ_{const} -disk, again for the exact same simulation stages as in Figs. 3 and 4. In the plots, we distinguish the following types of streamline: first,

O. Chrenko and M. Lambrechts: Oscillatory migration of accreting protoplanets driven by a 3D distortion of the gas flow

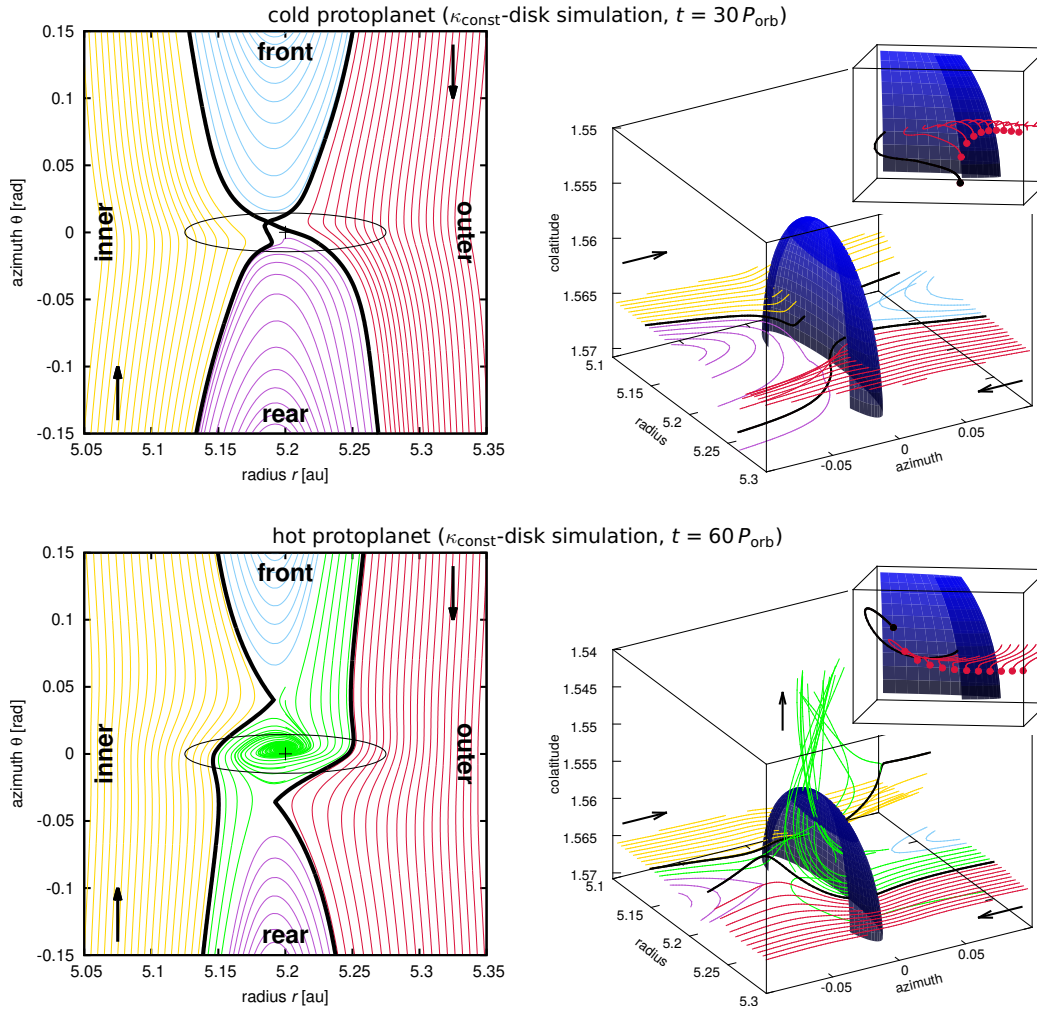


Fig. 5. Detailed streamline topology in the κ_{const} -disk simulation. *Top row:* cold protoplanet at $t = 30 P_{\text{orb}}$. *Bottom row:* hot protoplanet at $t = 60 P_{\text{orb}}$. Rectangular projection in the spherical coordinates is used to display the disk midplane near the protoplanet (*left*) and the actual 3D flow (*right*). The colour of the curves distinguishes individual sets of streamlines: inner circulating (yellow), outer circulating (red), front horseshoe (light blue), rear horseshoe (purple) and other (green). The thick black lines highlight the critical circulating streamlines closest to the protoplanet. The black cross and the ellipse mark the location and Hill sphere of the protoplanet; the black arrows indicate the flow direction with respect to the protoplanet. In 3D figures (*right*), the dark blue hemisphere corresponds to the Hill sphere above the midplane. Additionally, the insets in the corners of the 3D figures provide a close-up of the upstream outer circulating streamlines viewed from a slightly different angle. The endpoints indicate where the flow exits the depicted part of the space and highlight if the initially coplanar streamlines descend towards the protoplanet (*top*) or rather rise vertically (*bottom*). We emphasise that the streamlines in the 3D figures are generated above the midplane and do not directly correspond to those in the 2D figures.

there are circulating streamlines that do not cross the corotation with the protoplanet. To imagine the direction of the relative motion, we point out that the gas on inner circulating streamlines moves faster than the protoplanet, whereas the gas on outer circulating streamlines lags behind the protoplanet. Second, there are horseshoe streamlines that make a single U-turn and cross the corotation once at each side of the protoplanet. Such streamlines ahead of the orbital motion of the protoplanet form the front horseshoe region and those located behind the protoplanet belong to the rear horseshoe region. To outline the separatrices between the horseshoe and circulating regions, we highlight the critical inner and outer circulating streamlines that are located closest to the protoplanet. Finally, some of our plots contain streamlines that do not fall in any of the aforementioned categories.

When the protoplanet is non-luminous, the 2D midplane streamlines in Fig. 5 do not exhibit any unexpected features. The stagnation point (X-point) of the flow is located within the Hill sphere, which is also intersected by both horseshoe and circulating streamlines. In 3D, we notice that upon making their U-turn, the horseshoe streamlines vertically descend towards the midplane, as already pointed out by Fung et al. (2015) or Lambrechts & Lega (2017). A similar descent is also exhibited by some of the circulating streamlines closest to the protoplanet.

For the hot protoplanet, we now obtain a clear picture of the streamline distortion. In the midplane, the following changes appear:

- Circulating streamlines cross a smaller portion of the Hill sphere. When passing the protoplanet, they are bent towards it (unlike near the non-luminous protoplanet where they are

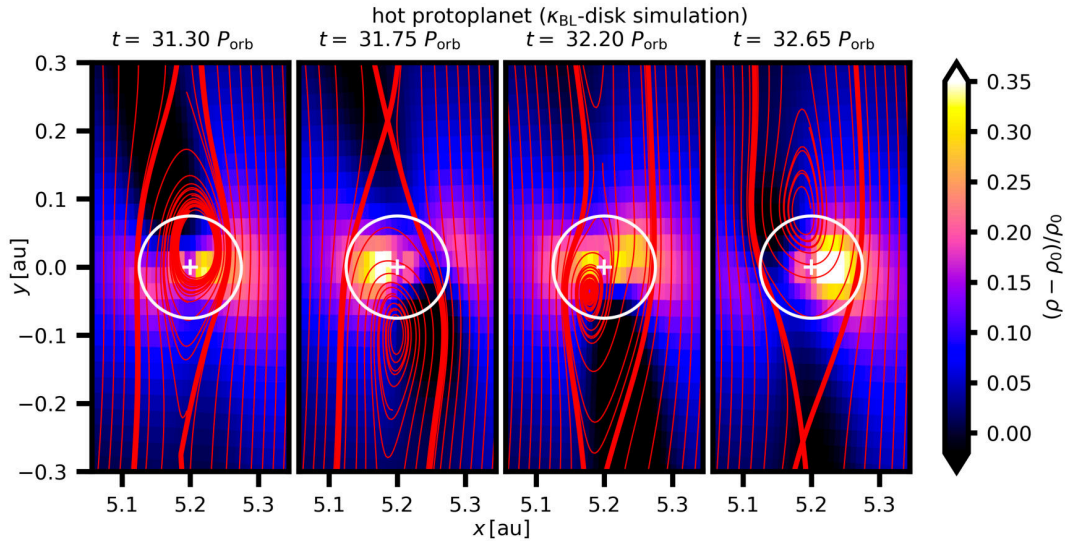


Fig. 6. Evolution of the perturbed midplane gas density in the κ_{BL} -disk simulation. The corresponding simulation time t is given by labels. Individual snapshots represent the state of gas when the total torque acting on the protoplanet is minimal (*left*), maximal (*third*), and oscillating in between (*second and right*). The streamlines are overplotted for reference. The figure is also available as an [online](#) movie, showing the temporal evolution from $t = 30\text{--}33 P_{\text{orb}}$.

rather deflected away), which is especially apparent for the critical circulating streamlines.

- The classical horseshoe streamlines detach from the Hill sphere and make their U-turns at greater azimuthal separations.
- Part of the streamlines originating in the downstream horseshoe regions is captured inside the Hill sphere where it rotates around the protoplanet in a retrograde fashion. In 3D, the distortion has the following additional features:
 - The “captured” streamlines are uplifted and form a spiral-like vertical column, outflowing and escaping from the Hill sphere.
 - When the circulating streamlines pass the protoplanet and become perturbed, they are also uplifted. This behaviour is the exact opposite of that seen in the cold-protoplanet situation.

3.4. Instability of the heated gas

We now return to the κ_{BL} -disk simulation for which we discovered the strong oscillations of the heating torque (Fig. 2).

3.4.1. Evolving underdense lobes

Investigating the evolution of the gas density, we find that the position and size of the underdense lobes never become stationary, as shown in Fig. 6 (see also the [online](#) movie). The figure shows a sequence of snapshots corresponding to $t = 31.3, 31.75, 32.20$ and $32.65 P_{\text{orb}}$.

The first panel depicts the state when the total torque reaches its first minimum during the beginning of the oscillatory phase. There is a dominant underdense lobe located ahead of the protoplanet while the rear lobe almost disappears. Such a distribution can be easily related to the strong negative torque: the excess of the gas mass behind the protoplanet (and the paucity of mass ahead of it) leads to an azimuthal pull acting against the orbital motion, imposing a negative torque.

When the torque is reversing from negative to positive (second panel), both lobes are similarly pronounced. The rear one

seems to be located closer to the protoplanet. The third panel corresponds to the torque maximum. The rear lobe is dominant and thus the overabundance of the gas ahead of the protoplanet makes the torque positive. The final panel shows the state when the oscillating torque is approximately halfway from positive to negative. The gas distribution indeed looks like a counterpart to the second panel since both lobes are again apparent but the front one is now closer to the protoplanet.

The gas redistribution is clearly related to the topology of the streamlines and to the position of the spiral-like flow. We notice that the centre of the captured streamlines undergoes retrograde (“clockwise”) rotation around the protoplanet. One underdense lobe is always associated with this rotating flow. Apparently, the redistribution of the hot gas by advection tends to favour the lobe which is intersected by the majority of the captured streamlines at a given time. In the first panel of Fig. 6, for example, the hot gas is transported more efficiently into the front lobe, creating a strong front-rear asymmetry between the lobes. In the third panel, the situation is exactly the opposite and the rear lobe is more pronounced.

We point out that the continuous variations of the hot lobes and their alternating dominance are unexpected features of the heating torque which was previously thought to be strictly positive (Benítez-Llambay et al. 2015).

3.4.2. Evolving 2D and 3D streamline topology

We again explore the streamline topology and its changes related to the redistribution of the hot gas. Figure 7 shows the midplane streamlines near the protoplanet for a selection of simulation times between $t = 31.3$ and $32.15 P_{\text{orb}}$. The former corresponds to the torque minimum, the latter to the torque maximum. The time intervals between the individual panels are not uniform but are rather selected to highlight the most interesting transitions.

The sequence reveals the following features:

- In panel a, the streamlines are similar to the steady-state κ_{const} -disk case (bottom of Fig. 5) in several ways, mostly in the detachment of the classical horseshoe streamlines and in the existence of the retrograde streamlines captured from

O. Chrenko and M. Lambrechts: Oscillatory migration of accreting protoplanets driven by a 3D distortion of the gas flow

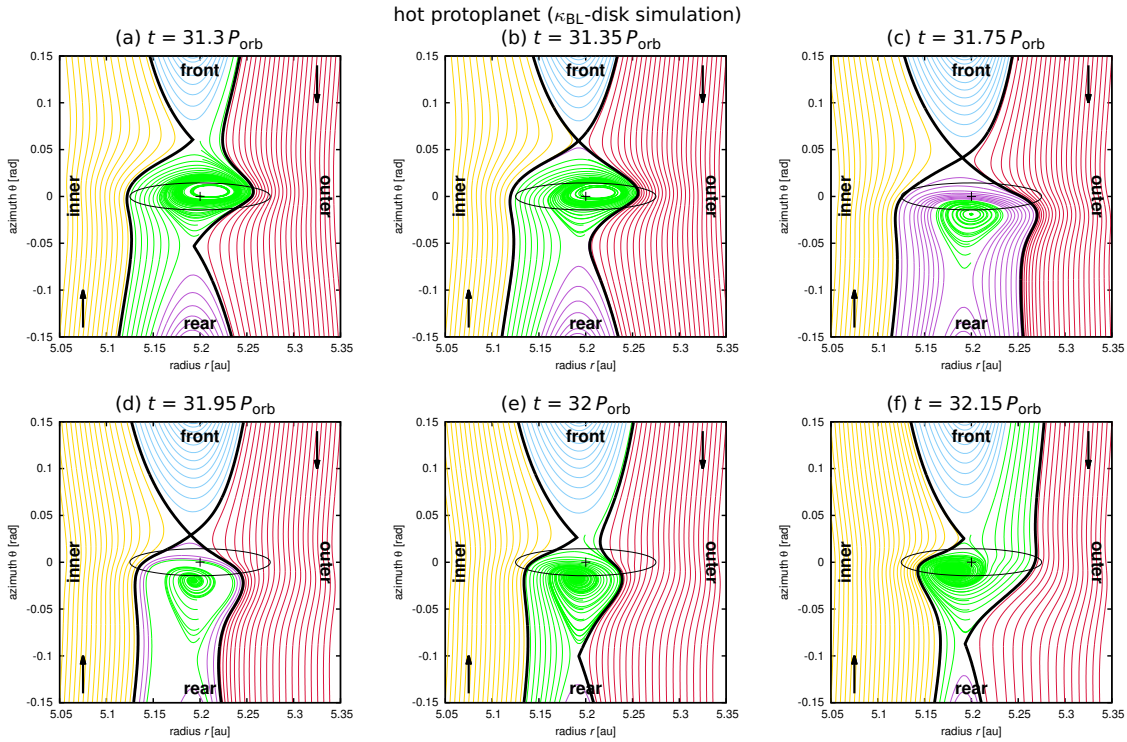


Fig. 7. Midplane streamline topology in the κ_{BL} -disk simulation. The panels are labelled by the simulation time. The individual types of streamlines are the same as in Fig. 5. The sequence (a–f) represents the transition between the states corresponding to the minimum and maximum of the torque, respectively (see Fig. 2 to relate the panels to the torque evolution).

downstream horseshoe regions. But there are also important differences: there are none inner circulating streamlines intersecting the Hill sphere and moreover, a larger part of the captured streamlines originate in the rear horseshoe region while the front horseshoe region is almost disconnected.

- In panel b, the front horseshoe region becomes entirely disconnected. The captured streamlines originate exclusively in the rear horseshoe region.
- In panel c, the outer circulating streamlines also stop crossing the Hill sphere. Some of the streamlines that were captured in b now overshoot the protoplanet and make a U-turn ahead of it. The centre around which the captured streamlines enclose becomes shifted behind the protoplanet.
- In panel d, the front X-point moves closer to the Hill sphere and so do the front horseshoe streamlines. The rear horseshoe region becomes radially narrower and the number of U-turn streamlines overshooting the protoplanet diminishes.
- In panel e, the front horseshoe region reconnects with the captured streamlines.
- In panel f, the captured streamlines originate mostly in the front horseshoe region while the rear horseshoe region is evolving towards its disconnection, similarly to what we saw for the front horseshoe region in panels a and b. The centre of the captured streamlines moves inwards from the protoplanet (and will continue to propagate ahead).

Figure 8 shows three selected snapshots of 3D streamlines ($t = 31.3, 31.75$ and $32.15 P_{\text{orb}}$) when the oscillating torque is at its minimum (top), grows halfway towards the maximum (middle), and reaches it (bottom). Clearly, the reshaping of the streamline topology that we described for the midplane

propagates in a complicated way into the vertical direction as well:

- In the first panel, the spiraling streamlines of the vertical column are more or less centred above the protoplanet and as they rise above the midplane they penetrate the majority of the Hill sphere.
- In the second panel, we see the overshooting rear horseshoe streamlines making their U-turns within the Hill sphere. The vertical column of captured streamlines is displaced to the rear of the Hill sphere. As the captured streamlines spiral up, the column tilts towards the Hill sphere. The outer circulating streamlines are strongly uplifted towards colatitudes above the Hill sphere.
- In the third panel, some uplifted outer circulating streamlines penetrate into the vertical column and by this reconfiguration, the column reconnects with the front horseshoe region while the rear one starts to disconnect.

3.5. Physical processes distorting the gas flow

In previous sections, we revealed that the gas heating from an accreting protoplanet changes the topology of the flow. Perturbed streamlines have a tendency to bend towards the protoplanet and also to rise vertically. If the perturbations become strong enough, the streamlines can form a vertical spiral. In this section, we investigate the physical processes responsible for such a streamline distortion.

In Sect. 3.5.1, we theorise that the streamline distortion is a result of vorticity perturbations arising because the vigorous accretion heating renders the circumplanetary gas baroclinic.

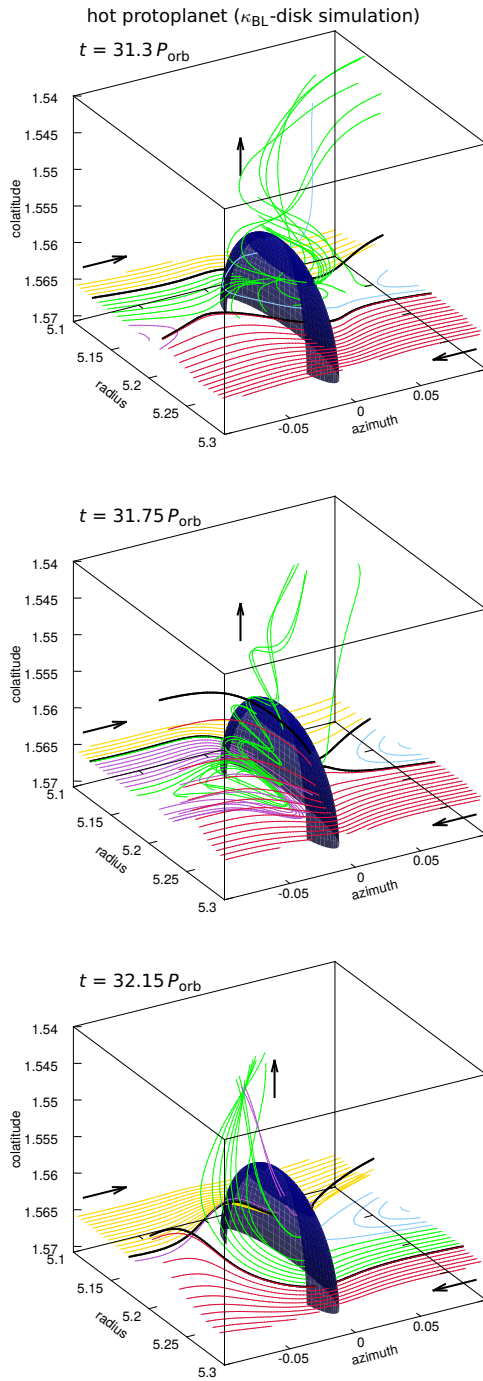


Fig. 8. Three-dimensional streamlines in the κ_{BL} -disk simulation. Each snapshot is labelled by the simulation time. The panels correspond to the minimum (*top*) and maximum (*bottom*) torque and to the state in between (*middle*).

Confirmation is provided for the steady state of the κ_{const} -disk simulation in Sects. 3.5.2 and 3.5.3. Finally, Sect. 3.5.4 demonstrates that the vertical temperature gradient above the accreting protoplanet is superadiabatic and we also highlight differences between the κ_{const} -disk and the κ_{BL} -disk.

3.5.1. Vorticity evolution

The spiral-like structure of the captured streamlines and the bending of nearby circulating streamlines suggests that the vorticity of the flow is modified when the protoplanet becomes hot. The vorticity can be defined via the relation

$$\omega_{\text{a}} \equiv \omega_{\text{r}} + 2\Omega \equiv \nabla \times \mathbf{v} + 2\Omega, \quad (13)$$

where ω_{a} is the absolute vorticity and ω_{r} is the relative vorticity in the reference frame corotating with the protoplanet.

Evolution of ω_{r} is described by the vorticity equation in the corotating frame (see Appendix C)

$$\frac{D\omega_{\text{r}}}{Dt} = (\omega_{\text{a}} \cdot \nabla) \mathbf{v} - \omega_{\text{a}} (\nabla \cdot \mathbf{v}) + \frac{\nabla \rho \times \nabla P}{\rho^2}, \quad (14)$$

where D/Dt denotes the Lagrangian derivative. In writing the equation, we neglected the effects of viscous diffusivity (large Reynolds number limit) but otherwise the equation is general.

Regarding the terms on the right-hand side, the first one describes the tendency of vortex tubes to become twisted due to velocity field gradients and the second one characterises the stretching or contraction of vortex tubes due to flow expansion or compression. These first two terms, usually called the twisting and stretching terms, are only important if there is non-zero absolute vorticity already existing in the flow and they can cause its redistribution.

The remaining term on the right-hand side is the baroclinic term. It vanishes in barotropic flows where the pressure and density gradients are always parallel, but since our model is not barotropic, $\nabla \rho$ and ∇P can be misaligned, leading to vorticity production or destruction since their cross product can be non-zero. Because ρ near the accreting protoplanet exhibits asymmetric perturbations while P remains roughly spherically symmetric, one can expect non-zero baroclinic perturbations to arise. The respective non-zero vorticity then enhances circulation around a given point of the continuum, twisting the streamlines with respect to the situation unperturbed by accretion heating.

3.5.2. Baroclinic vorticity generation

It is not a priori evident which source term is the most important for the vorticity evolution in our simulations. In Fig. 9, we study the variations of ω_{r} and the source terms of Eq. (14) along a single outer circulating streamline. We compare the situation near the cold and hot protoplanet in the κ_{const} -disk.

Downstream, before the streamline encounters the protoplanet, the situation is similar for the compared cases: the azimuthal and radial vorticity components $\omega_{r,\theta}$ and $\omega_{r,r}$ are negligible, while the polar component $\omega_{r,\phi}$ is non-zero and positive. The positive value of $\omega_{r,\phi}$ corresponds to the inherent vorticity in a flow with the Keplerian shear: taking $v_r = 0$, $v_\phi = 0$ and $v_\theta = \sqrt{GM}/r - \Omega r$, one obtains $\omega_{r,\phi} = -0.5\Omega_{\text{K}}(r) + 2\Omega$. At the same time, the source terms are zero because far from the protoplanet there are no strong velocity gradients, no compression and $\nabla \rho$ and ∇P are aligned.

To relate the vorticity variation with the streamline distortion close to the protoplanet, let us carry out a thought experiment, considering the fact that the vorticity describes the tendency of the flow to circulate around some point in space. First we focus on the hot-protoplanet case which is the most important for us. First we imagine an observer moving along the critical outer circulating streamline, corresponding to the outer thick black curve

O. Chrenko and M. Lambrechts: Oscillatory migration of accreting protoplanets driven by a 3D distortion of the gas flow

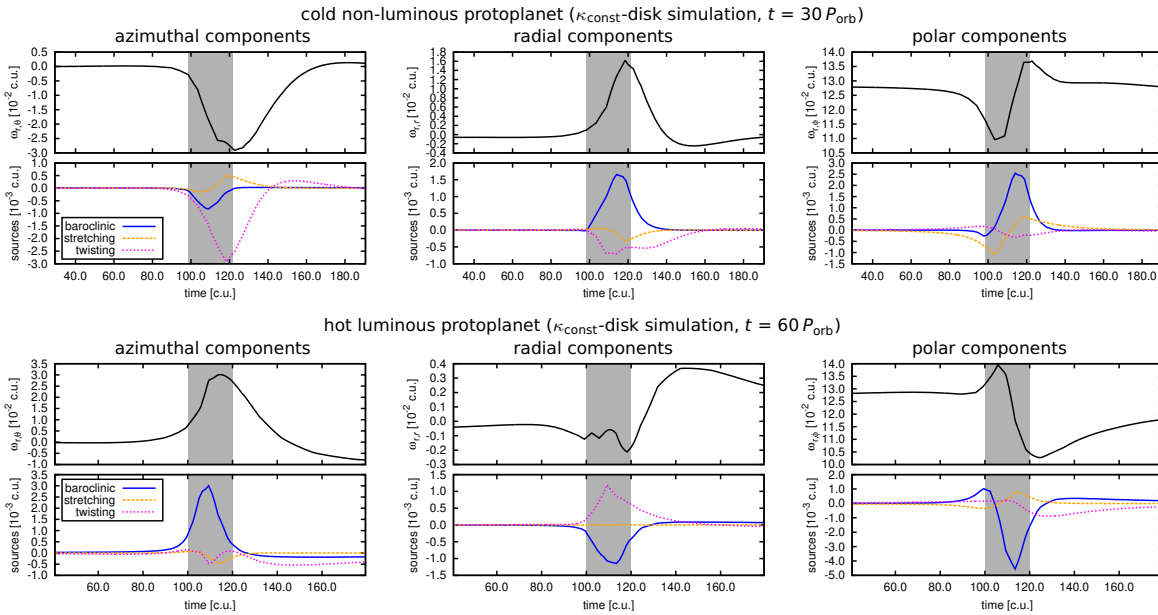


Fig. 9. Evolution of the relative vorticity (*first and third row*) and balance of the vorticity source terms (*second and fourth row*) along a single streamline in the κ_{const} -disk simulation. The streamlines for these measurements are chosen from the 3D sets displayed in Fig. 5. For the hot protoplanet (*bottom two rows*) the extremal outer circulating streamline is selected, and for the cold protoplanet (*top two rows*) we select an outer circulating streamline with a comparable Hill sphere crossing time. Azimuthal (*left*), radial (*middle*), and polar (*right*) components of the vorticity (black solid curve), and the baroclinic term (blue solid curve), stretching term (orange dashed curve), and twisting term (magenta dotted curve) are displayed using scaled code units. The grey rectangle marks the Hill sphere crossing. We point out that the source terms represent the rate of change of the vorticity and also that the vertical range is not kept fixed among individual panels.

in the bottom right panel of Fig. 5. The observer moves with the flow, predominantly in the $-\theta$ direction. For this experiment, we dub the directions θ , $-\theta$, r , $-r$, ϕ and $-\phi$ as behind, ahead, outwards, inwards, down, and up, respectively. Considering only the streamlines of Fig. 5 originating at $r > r_p$, they initially define a plane at constant $\phi = \pi/2 - 0.005$ rad and the observer propagates through that plane. When the flow reaches the Hill sphere, the observer studies the instantaneous displacement of nearby gas parcels which corresponds to the deformation of the surface defined by neighbouring streamlines.

According to the bottom panels of Fig. 9, the observer measures $\omega_{r,\theta} > 0$ when crossing the Hill sphere. Thus $\omega_{r,\theta}$ points against the direction of the motion of the observer, forcing the circulation in the local (r, ϕ) plane. The nearby gas parcels must obey the following right-hand rule: when the thumb points in the direction of $\omega_{r,\theta}$, wrapping fingers determine the direction of circulation. From the point of view of the observer, an outer gas parcel falls downwards to the midplane and an inner gas parcel rises upwards. This is exactly in accordance with Fig. 5 where streamlines passing the protoplanet are uplifted from the $\phi = \pi/2 - 0.005$ rad plane and the kick gets stronger with decreasing separation from the protoplanet.

$\omega_{r,r}$ only slightly oscillates during the Hill sphere crossing but becomes positive (although relatively small) upstream. Using again the same considerations as above, $\omega_{r,r}$ points outwards from the observer after crossing the Hill sphere, promoting circulation in the (θ, ϕ) plane. Using the right-hand rule, a gas parcel ahead of the observer falls downwards and a gas parcel behind the observer rises upwards. In Fig. 5, this is reflected by the streamline topology when the red streamlines rising after the Hill sphere passage suddenly start to fall back towards the midplane.

As for the remaining vorticity component $\omega_{r,\phi}$, it remains positive during the Hill sphere crossing but acquires a positive

boost at first and a more prominent negative perturbation afterwards. The later diminishes the circulation related to shear in the (r, θ) plane. This is only possible if gas parcels near the observer become displaced towards trajectories with smaller shear velocities. In Fig. 5, the streamline topology indeed exhibits such a behaviour because when the red streamlines (and similarly green and yellow ones) pass the protoplanet, they are being bent towards it.

Looking at the source terms, it is obvious that the baroclinic term is responsible for perturbing $\omega_{r,\theta}$ and $\omega_{r,\phi}$, while counteracting the twisting term contributing to $\omega_{r,r}$. The importance of the baroclinic term for the flow approaching the hot protoplanet is thus confirmed. Moreover, the perturbation is indeed 3D as each of the studied components is important for the resulting streamline topology.

Comparing the hot-protoplanet case to the cold-protoplanet case, we notice that the evolution of $\omega_{r,\theta}$ and $\omega_{r,\phi}$ is roughly anti-symmetric, as is the evolution of the baroclinic source term. This is consistent with our finding that streamlines near the cold protoplanet are distorted in the opposite manner (they fall towards the midplane and deflect away from the protoplanet). In other words, the baroclinic behaviour of the vicinity of the protoplanet is reverted between the cold- and hot-protoplanet case.

3.5.3. Baroclinic region

Although we do not repeat the vorticity analysis for the remaining sets of streamlines, it is clear that features of the streamline distortion can be explained by the baroclinic generation of the vorticity. To further support this claim, we compare in Fig. 10 the map of the baroclinic term near the cold and hot protoplanet in the κ_{const} -disk. We plot the polar component of the baroclinic term $(\nabla\rho \times \nabla P)_\phi / \rho^2$ in the midplane. Since the midplane flow is

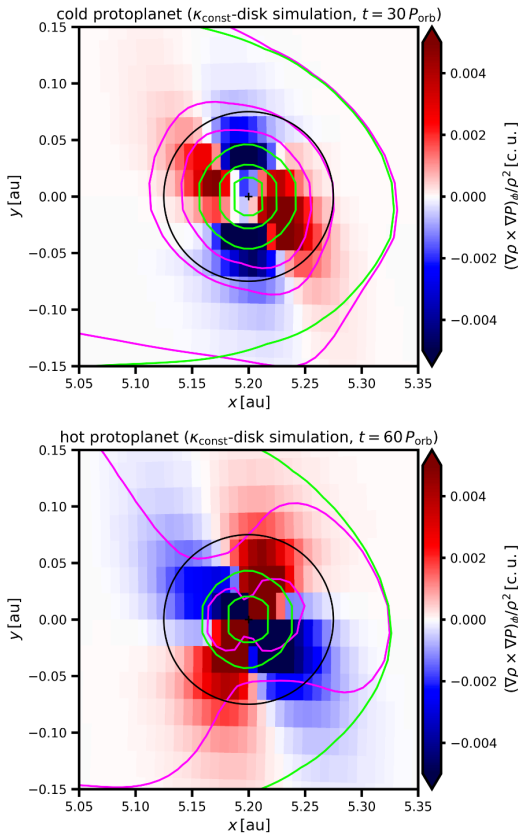


Fig. 10. Maps of the ϕ -component of the baroclinic term in the κ_{const} -disk simulation. The purple isocontours depict several levels of the constant volume density and the green isocontours correspond to the isobars. The levels of the contours are kept fixed between the panels.

effectively 2D (because $v_\phi = 0$ in midplane), only the polar component of ω_ϕ is non-zero and thus also the polar component of the baroclinic term is the most important one.

Figure 10 reveals that the gas is baroclinic near both the cold and hot protoplanet, but for the latter case, the map becomes approximately antisymmetric compared to the cold-protoplanet case, slightly rotated in the retrograde sense and the baroclinic region is more extended.

The existence of the baroclinic region can be explained using the isocontours of constant volume density and isobars. For a barotropic gas ($\nabla\rho \parallel \nabla P$), any nearby isocontours of constant ρ and P should have the same shape. Wherever the isocontours depart from one another, it means that the local gradients of ρ and P are misaligned and that the baroclinic term is non-zero.

Looking at the cold-protoplanet case, the isobars and contours of constant density are nearly spherically symmetric. However, we notice that each density isocontour exhibits two bumps and appears to be stretched in the direction where the gas outflows from the Hill sphere. Clearly, these bumps are associated with the cold-finger perturbation that appears in the same location (see Fig. 3). Since the cold fingers are filled with overdense gas, they perturb the local density gradient, causing it to point towards them. At the same time, the isobars remain approximately spherically symmetric.

When the protoplanet is hot, the cold fingers are replaced with hot underdense perturbations. Therefore, the local density

gradient tends to point away from them. We can see that this is indeed true because the density isocontours do not exhibit bumps, but rather concavities across the overheated region (compare with Fig. 3). Clearly, this is the reason why the baroclinic map for the hot protoplanet appears reverted compared to the cold protoplanet.

Summarising these findings, we see that the thermal perturbations associated either with the cold-finger effect or the heating torque make the circumplanetary region baroclinic. But the influence on the vorticity evolution is the opposite when comparing the cold- and hot-protoplanet cases.

3.5.4. Vertical convection

Although the baroclinic distortion of the gas flow is a robust mechanism, it does not provide a simple explanation as to why the κ_{BL} -disk simulation exhibits gas instability whereas the κ_{const} -disk simulation remains stable. We now explore the vertical stability of both disks against vertical convection, considering only the hot-protoplanet limit.

To do so, we employ the Schwarzschild criterion,

$$|\nabla_{\text{rad},\phi}| > |\nabla_{\text{ad},\phi}| \Leftrightarrow \frac{|\nabla_{\text{rad},\phi}|}{|\nabla_{\text{ad},\phi}|} - 1 > 0, \quad (15)$$

where the subscript “rad” denotes the vertical³ temperature gradient found in our simulations and the subscript “ad” denotes the temperature gradient that an adiabatic gas would establish. The ∇ symbol stands for the logarithmic gradient $d\log T/d\log P$, yielding $|\nabla_{\text{ad},\phi}| = (\gamma - 1)/\gamma$ for the adiabatic case.

The Schwarzschild criterion is not necessarily a universal way to determine if the disk is unstable to convection. The reason is that convective destabilisations in protoplanetary disks are opposed by diffusive effects (e.g. Held & Latter 2018) and shear motions (Rüdiger et al. 2002). However, to our knowledge there are no convective criteria that would take into account the disk perturbation by the protoplanet, therefore we choose to use the Schwarzschild criterion for its simplicity, keeping the limitations in mind.

Figure 11 shows the vertical velocity field and balance of the Schwarzschild criterion in the vertical direction of the κ_{const} -disk and κ_{BL} -disk. Each panel shows a different simulation time and vertical plane. For the κ_{const} -disk, we display $t = 60 P_{\text{orb}}$ and the vertical plane intersecting the location of the protoplanet, whereas for the κ_{BL} -disk, each plane approximately intersects the centre around which the captured streamlines of Fig. 6 circulate at the given simulation time ($t = 31.3, 31.75, 32.2$ and $32.65 P_{\text{orb}}$). In other words, we choose the vertical planes where we expect the most prominent vertical outflow.

The first thing we point out is that the background differs between the studied disks. The background of the κ_{BL} -disk is slightly superadiabatic, contrary to the κ_{const} -disk. The difference arises as a result of the opacity laws. As derived by Lin & Papaloizou (1980) and Ruden & Pollack (1991), one can make a qualitative estimate for optically thick regions unperturbed by the protoplanet

$$\left(\frac{|\nabla_{\text{rad},\phi}|}{|\nabla_{\text{ad},\phi}|} - 1 \right)_{\text{background}} = \frac{1/(4-\beta)}{(\gamma-1)/\gamma} - 1, \quad (16)$$

³ We use the colatitude ϕ to study the vertical gradients because the curvature of spherical coordinates near the midplane does not significantly depart from the true vertical direction.

O. Chrenko and M. Lambrechts: Oscillatory migration of accreting protoplanets driven by a 3D distortion of the gas flow

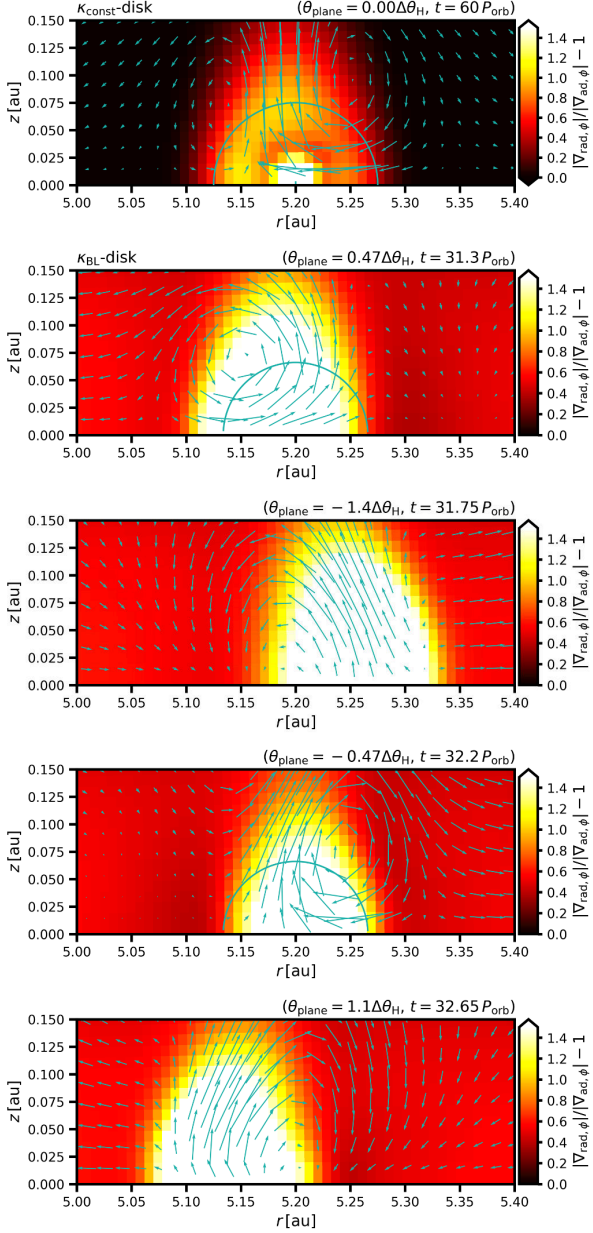


Fig. 11. Balance of the Schwarzschild criterion in the vertical planes of the κ_{const} -disk (top) and the κ_{BL} -disk (remaining panels). The individual vertical planes are chosen to track the most prominent vertical flow at the given simulation time t (see the main text) and their azimuthal separations from the protoplanet location are given by panel labels (using multiples of the azimuthal span $\Delta\theta_{\text{H}}$ of the Hill sphere radius). The colour maps evaluate Eq. (15). Positive values indicate superadiabatic vertical temperature gradients. The vertical velocity vector field is overlaid in the plots. The half-circles mark the overlap of a given plane with the Hill sphere (the planes in panels 3 and 5 do not overlap with the Hill sphere).

where β is the power-law index of the $\kappa \propto T^\beta$ dependence. In the κ_{const} -disk, $\beta = 0$ and thus $|\nabla_{\text{rad},\phi}|/|\nabla_{\text{ad},\phi}| - 1 \simeq -0.17$. In the κ_{BL} -disk, the Bell & Lin (1994) opacity law in the given temperature range corresponds to water-ice grains and exhibits $\beta = 2$,

therefore $|\nabla_{\text{rad},\phi}|/|\nabla_{\text{ad},\phi}| - 1 \simeq 0.67$. These estimated values are in a good agreement with the background values of Fig. 11.

The background itself is not convective because vertical convection is usually not self-sustainable unless there is a strong heat deposition within the disk (e.g. Cabot 1996; Stone & Balbus 1996; Klahr et al. 1999; Lesur & Ogilvie 2010) which, however, can be provided by the hot accreting protoplanet in our case. Indeed, looking at the κ_{const} -disk in Fig. 11 (top), the region where we previously identified the most significant temperature excess due to planetary luminosity (compare with Fig. 4) is superadiabatic and the corresponding vertical outflow can be considered convective.

In the κ_{BL} -disk simulation, the temperature gradient departs from the adiabatic one even more, and additionally, the excess is no longer centred above the protoplanet itself but rather spans its vicinity. This can be seen from the varying azimuthal coordinate of the displayed vertical planes and also from the radial offset of the highly superadiabatic region in panels 3 and 5.

We summarise the section by speculating that the κ_{BL} -disk simulation becomes destabilised because the hot disturbance created by the accreting protoplanet is subject to vertical buoyant forces acting over a more extended region (compared to the κ_{const} -disk). The reason is that the hot disturbance is imposed over an already superadiabatic background. The uplift of the material cannot be compensated for in a stationary manner and eventually the vertical outflow becomes offset with respect to the protoplanet and starts to change its position in a cyclic manner. However, such a description is rather qualitative and precise conditions for triggering the instability should be explored in future works.

3.6. Torque oscillation versus opacity gradient

We now perform a partial exploration of the parametric space by varying the opacity gradient within the disk. The aim is twofold: first, we would like to support the claim of the previous Sect. 3.5.4 of the importance of the vertical stratification for the torque oscillations. Second, it is desirable to show that the appearance of torque oscillations in the κ_{BL} -disk is not coincidental and that it can be recovered for a wider range of parameters.

We construct six additional disk models with artificial opacity laws that (i) conserve the opacity value at the protoplanet location ($1.11 \text{ cm}^2 \text{ g}^{-1}$) and (ii) lead to opacity gradients which are intermediate between the κ_{const} - and κ_{BL} -disks. The latter property accounts for the highly unconstrained size distribution of solid particles in protoplanetary disks which manifests itself in a large parametric freedom of the power-law slope of the opacity profile (e.g. Piso et al. 2015).

The first additional set of disks utilises the opacity law which we dub T -dependent:

$$\kappa(\bar{T}(r, \phi)) = \kappa_0 \bar{T}^\beta. \quad (17)$$

Similarly to the Bell & Lin (1994) opacity in the water-ice regime, it is exclusively a function of temperature. The temperature \bar{T} is again azimuthally averaged to disentangle the influence of global opacity gradients (which we focus on) from those related to accretion heating of the protoplanet. We examine the values $\beta = 1.5$, 1, and 0.5 to span the range between $\beta = 0$ (κ_{const} -disk) and 2 (κ_{BL} -disk). The constant of proportionality κ_0 is always chosen to recover $\kappa = 1.11 \text{ cm}^2 \text{ g}^{-1}$ at $r = a_p$ and $\phi = \pi/2$ in an equilibrium disk. We find $\kappa_0 \simeq 0.0016$, 0.014, and $0.122 \text{ cm}^2 \text{ g}^{-1}$ for the respective values of β .

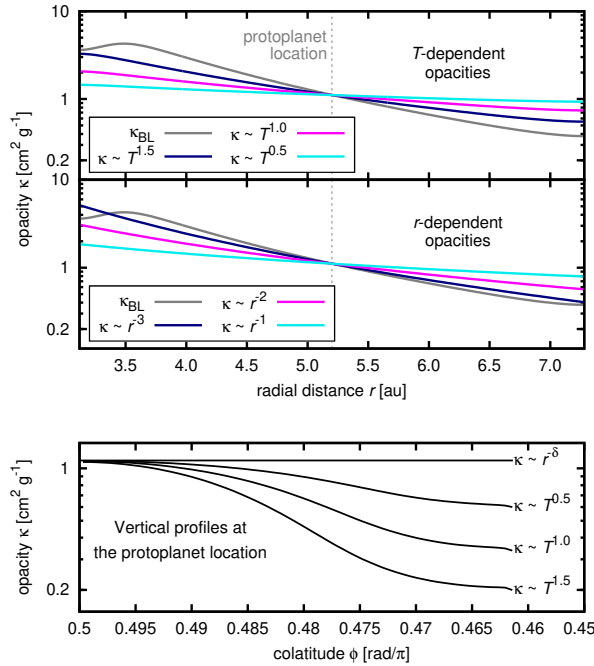


Fig. 12. Radial (*top two panels*) and vertical (*bottom*) opacity profiles in equilibrium disks which we use to study the torque dependence on the opacity gradients. In the top panels, the individual cases are distinguished by colour and labelled in the legend. The profile of the κ_{BL} -disk (solid grey curve) is plotted for comparison. The bottom panel corresponds to the protoplanet location and demonstrates that only the disks with T -dependent opacities develop a vertical opacity gradient (which is not allowed for r -dependent opacities by construction).

The opacity law used for the second additional set of disks, referred to as r -dependent, is

$$\kappa(r) = 1.11 \left(\frac{r}{a_p} \right)^{-\delta} \text{ cm}^2 \text{ g}^{-1}, \quad (18)$$

and we choose $\delta = 3, 2,$ and 1 (because $\delta = 4$ leads to an opacity profile similar to the κ_{BL} -disk). The motivation for choosing this purely radially dependent opacity law is to distinguish between effects caused by radial and vertical opacity gradients. The latter does not appear when $\kappa = \kappa(r)$.

The opacity profiles of these disks in radiative equilibrium are summarised in Fig. 12 which reveals that all radial opacity gradients (top two panels) are indeed shallower compared to the κ_{BL} -disk. However, all disks with r -dependent opacities have zero vertical opacity gradient by construction (bottom panel), unlike disks with T -dependent opacities which vertically decrease.

The torque measurements are performed in the same way as in our previous experiments and the results are given in Fig. 13. For disks with T -dependent opacities (top), we find that the torque oscillations appear for all investigated values of β . The oscillation amplitude on the other hand decreases linearly with β and the period becomes slightly shorter as well. In case of r -dependent opacities (bottom), the torque evolution does not strongly depend on δ and exhibits marginal and vanishing oscillations, as in the κ_{const} -disk case.

Since the only qualitative difference between the disks with T -dependent and r -dependent opacities is in the vertical opacity

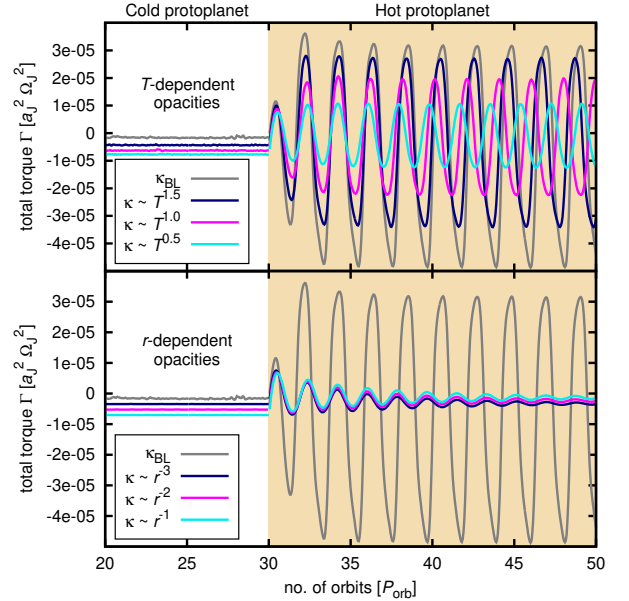


Fig. 13. Torque evolution in disks described in Fig. 12. *Top panel:* disks with T -dependent opacities. *Bottom panel:* disks with r -dependent opacities. The individual cases are distinguished by colour and labelled in the legend. The evolution from the κ_{BL} -disk simulation (solid grey curve) is given for reference. In the top panel, the torque amplitude diminishes with the power-law index of the opacity law, yet the oscillations appear in all studied cases. In the bottom panel, we find that oscillations are rapidly damped.

gradient, our torque measurements confirm the importance of the vertical structure for the torque oscillations. The torque oscillates wherever the vertical opacity profile favours superadiabatic vertical stratification and the oscillation amplitude scales with the strength of the opacity-temperature coupling. In the absence of the vertical opacity gradient, the oscillations are not established.

3.7. Evolution of a migrating protoplanet

The previous simulations were conducted assuming a fixed orbit for the protoplanet and the static torque was examined. Here we explore whether or not our findings can be readily applied to a dynamical case when the protoplanet is allowed to radially migrate and its semimajor axis evolves. In this section, we focus only on the κ_{BL} -disk in which we found the flow instability.

Starting from $t = 30 P_{\text{orb}}$, we release the protoplanet and run the simulation until $t = 60 P_{\text{orb}}$. Figure 14 compares the obtained dynamical torque with the previous result of our static experiments. It is obvious that the oscillating character of the torque is retained and therefore the instability of the flow operates near a moving protoplanet as well. There are differences both in the amplitude and phase of the torque oscillations, but the mean value of the torque over the simulated period of time is $\bar{\Gamma} \approx -1.3 \times 10^{-6} a_J^2 \Omega_J^2$. Although this value is slightly more positive than the static heating torque ($\bar{\Gamma} \approx -6.3 \times 10^{-6} a_J^2 \Omega_J^2$), it is almost the same as the torque acting on the cold protoplanet ($\bar{\Gamma} \approx -1.6 \times 10^{-6} a_J^2 \Omega_J^2$). We thus confirm that in the κ_{BL} -disk, the heating torque does not add any considerable positive contribution to the mean torque but causes it to strongly oscillate instead.

The bottom panel of Fig. 14 shows the actual evolution of the semimajor axis of the protoplanet. On average, the protoplanet

O. Chrenko and M. Lambrechts: Oscillatory migration of accreting protoplanets driven by a 3D distortion of the gas flow

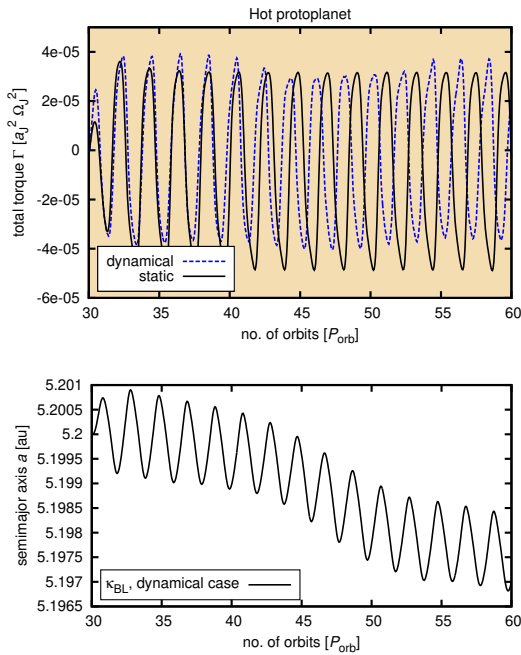


Fig. 14. *Top:* comparison of the static (solid black curve) and dynamical torque (dashed blue curve) acting on the hot protoplanet in the κ_{BL} -disk. *Bottom:* evolution of the semimajor axis in the κ_{BL} -disk when the protoplanet is allowed to migrate. The migration is inward and oscillatory.

slowly migrates inward but this drift is not smooth. The protoplanet exhibits fast periodic inward and outward excursions on an orbital timescale. The migration rate of these individual excursions (not to be confused with the mean migration rate stated above) is $\dot{a} \sim (10^{-3} \text{ au})/P_{\text{orb}}$.

Finally, we note that the mean migration rate is not constant, which also corresponds to the varying offset of the dynamical torque with respect to the static torque in Fig. 14. It is likely that the unstable gas distribution around the protoplanet is further affected by the protoplanet’s radial drift.

4. Discussion

This section discusses the applicability of our results, draws links to some previous studies, and speculates about possible implications for planet formation. Additionally, we outline possibilities for future work. Although most of them are beyond the scope of this paper, we at least present several additional simulations in Appendix B to verify the correctness of our model (we study the impact of the luminosity increase, grid resolution, opacity treatment, and computational algorithm on the evolution of torque oscillations).

4.1. Relation to previous works

Our results revealed unexpected perturbations of the gas flow in the vicinity of the protoplanet undergoing strong accretion heating, one of them being the vertical outflow. The resolution of our simulations was originally tailored for studying the torque and may lack some accuracy close to the protoplanet where the outflow occurs. Follow-up studies should therefore use simulations with a high-resolution protoplanetary envelope, similarly

to Tanigawa et al. (2012); Fung et al. (2015); Ormel et al. (2015); Lambrechts & Lega (2017) for example.

It is likely that a critical combination of the opacity κ and luminosity L for a given planetary mass M_p exists for which the vertical outflow is triggered, similarly to the dependences of the heating torque explored by Benítez-Llambay et al. (2015). Popovas et al. (2018, 2019) studied the stability of the circumplanetary envelope during pebble accretion and found that the gas within the Bondi sphere exhibits 3D convective motions, assuming $L \simeq 1.4 \times 10^{26} \text{ erg s}^{-1}$, $M_p = 0.95 M_{\oplus}$ and $\kappa = 1 \text{ cm}^2 \text{ g}^{-1}$. Lambrechts & Lega (2017) also explored a set of (L, κ, M_p) parameters and their impact on the structure of the circumplanetary envelope. They found the inner region of the envelope to depart from hydrostatic equilibrium when the luminosity exceeds $L = 10^{27} \text{ erg s}^{-1}$ around a $M_p = 5 M_{\oplus}$ core within a $\kappa = 1 \text{ cm}^2 \text{ g}^{-1}$ environment, but they did not identify any vertical outflow. The outflow in our simulations appears for higher L and smaller M_p compared to Lambrechts & Lega (2017). We can therefore assume that our parameters cross the critical ones.

Regarding the baroclinic perturbations, although they are known to produce vortical instabilities in protoplanetary disks (Klahr & Bodenheimer 2003; Petersen et al. 2007a,b; Lesur & Papaloizou 2010; Raettig et al. 2013; Barge et al. 2016), they have rarely been considered in relation to hot protoplanets. For example, Owen & Kollmeier (2017) claim that hot protoplanets can excite large-scale baroclinic vortices but we do not identify any of those in our simulations. Instead, we find baroclinic perturbations to be responsible for 3D distortion of the gas flow near the protoplanet.

4.2. Implications for the formation of planetary systems

Although the heating torque has previously been thought to be strictly positive and also efficient in high-opacity locations of protoplanetary disks, our paper shows that it can exhibit more complicated behaviour if the temperature dependence of the disk opacity is taken into account. We identified an oscillatory mode of the heating torque in the disk region with $\kappa \propto T^2$ and we demonstrated that it can operate even for shallower dependences such as $\kappa \propto T^{0.5}$, albeit with a decreased amplitude. This behaviour resembles the nature of baroclinic and convective disk instabilities which usually operate in the most opaque regions with the steepest entropy gradients but become less effective elsewhere (e.g. Pfeil & Klahr 2019).

It is worth noting that our simulations neglected the effect of stellar irradiation. Stellar-irradiated disks tend to have vertical temperature profiles that are closer to being isothermal (e.g. Flock et al. 2013), unlike disk models used in this work which have rather adiabatic or slightly superadiabatic vertical temperature gradients. On the other hand, even the irradiated disks often contain shadowed regions protected against stellar irradiation; for example behind the puffed-up inner rim (e.g. Dullemond et al. 2001) or between the viscously heated inner disk and a flared irradiated outer disk (e.g. Bitsch et al. 2013). In such regions, the oscillatory migration could still operate.

For the aforementioned reasons, it is likely that transition zones might exist in protoplanetary disks, separating regions where protoplanets migrate under the influence of the standard positive heating torque and where they undergo oscillatory migration. Migration at the edges of such zones could be convergent, leading to a pileup of protoplanets.

⁴ Greater number of parameters were discussed in Popovas et al. (2018, 2019) but we quote those closest to this paper.

5. Conclusions

By means of 3D radiation-hydrodynamic simulations, we investigated the heating torque (Benítez-Llambay et al. 2015) acting on a luminous $3 M_{\oplus}$ protoplanet heated by accretion of solids. The aim was to compare the torque evolution and physics in a disk with non-uniform opacities (Bell & Lin 1994) with the outcome of a constant-opacity simulation.

We discovered that the gas flow near the protoplanet is perturbed by two mechanisms:

1. The gas advected past the protoplanet becomes hot and underdense. Consequently, a misalignment is created between the gradients of density and pressure within the Hill sphere of the protoplanet. The baroclinic term of the vorticity equation ($\sim \nabla \rho \times \nabla P$) then becomes non-zero and modifies the vorticity of the flow.
2. The efficient heat deposition in the midplane makes the vertical temperature gradient superadiabatic, thus positively enhancing vertical gas displacements.

The streamline topology exhibits a complex 3D distortion. The most important feature are spiral-like streamlines rising vertically above the hot protoplanet, forming an outflow column of gas escaping the Hill sphere.

In the constant-opacity disk, the vertical outflow is centralised above the protoplanet; it temporarily captures streamlines from both horseshoe regions and such a state is found to be stationary over the simulation time scale. The distribution of the hot gas then remains in accordance with findings of Benítez-Llambay et al. (2015), having a two-lobed structure, and so does the resulting positive heating torque.

In the disk with non-uniform opacity, $\kappa \propto T^2$ (typically outside the water-ice line), we find the superadiabatic temperature gradient to be steeper and the distorted gas flow to be unstable. The vertical spiral flow becomes offset with respect to the protoplanet and periodically changes its position, spanning the edge of the Hill sphere in a retrograde fashion. Its motion is followed by the underdense gas and the resulting heating torque strongly oscillates in time. The interplay can be characterised by the following sequence:

1. A stage when most of the captured streamlines originate in the rear horseshoe region and their spiral-like structure is offset ahead of the protoplanet. Therefore the hot gas cumulates ahead of the protoplanet, a dominant underdense lobe is formed there, and the torque becomes negative, reaching the minimum of its oscillation.
2. A stage when the front horseshoe region becomes completely isolated from the captured streamlines. Some of the rear horseshoe streamlines start to overshoot the protoplanet and make U-turns ahead of it. At the same time, the spiral-like structure recedes behind the protoplanet. The lobe from stage 1 starts to decay while a rear lobe starts to grow and the torque changes from negative to positive.
3. Antisymmetric situation to stage 1, when most of the captured streamlines originate in the front horseshoe region, the dominant lobe trails the protoplanet and the torque is positive, reaching the maximum of its oscillation.
4. Antisymmetric situation to stage 2, when the torque decreases from positive to negative and the cycle repeats.

Such an advective redistribution of the hot underdense gas is sustained over the simulation timescale.

We also studied the dependence of the torque oscillations on the opacity gradient and found that they can appear even for $\kappa \propto T^{0.5}$, although their amplitude linearly decreases with the power-law slope of the $\kappa(T)$ dependence. We also demonstrated that

the oscillations would vanish in a disk with zero vertical opacity gradient.

If the protoplanet is allowed to migrate, its mean migration rate is nearly unaffected but the radial drift is not smooth; it is rather oscillatory, consisting of brief inward and outward radial excursions with a characteristic rate of $\dot{a} \sim 10^{-4} \text{ au yr}^{-1}$.

We discussed possible implications of the oscillating heating torque for planet formation and pointed out that it can affect the global evolution of hot migrating low-mass protoplanets. During their migration through disk regions with varying opacities it might be possible for the protoplanets to switch between the standard positive heating torque of Benítez-Llambay et al. (2015) and the positive/negative torque oscillations discovered in this paper.

Acknowledgements. The work of O.C. has been supported by Charles University (research program no. UNCE/SCI/023; project GA UK no. 624119; project SVV-260441), by the Grant Agency of the Czech Republic (grant No. 18-06083S) and by The Ministry of Education, Youth and Sports from the Large Infrastructures for Research, Experimental Development and Innovations project IT4Innovations National Supercomputing Centre LM2015070. Access to computing and storage facilities owned by parties and projects contributing to the National Grid Infrastructure MetaCentrum, provided under the programme “Projects of Large Research, Development, and Innovations Infrastructures” (CESNET LM2015042), is greatly appreciated. O.C. would like to thank M. Brož and B. Bitsch for useful discussions and also E. Lega who kindly provided her numerical code FARGOCA for comparison simulations. The authors are grateful to an anonymous referee whose insightful ideas helped to improve the manuscript.

References

- Barge, P., Richard, S., & Le Dizès, S. 2016, *A&A*, 592, A136
 Baruteau, C., & Masset, F. 2008, *ApJ*, 672, 1054
 Baruteau, C., Fromang, S., Nelson, R. P., & Masset, F. 2011, *A&A*, 533, A84
 Bell, K. R., & Lin, D. N. C. 1994, *ApJ*, 427, 987
 Benítez-Llambay, P., & Masset, F. S. 2016, *ApJS*, 223, 11
 Benítez-Llambay, P., Masset, F., Koenigsberger, G., & Szulágyi, J. 2015, *Nature*, 520, 63
 Bitsch, B., Crida, A., Morbidelli, A., Kley, W., & Dobbs-Dixon, I. 2013, *A&A*, 549, A124
 Brasser, R., Matsumura, S., Muto, T., & Ida, S. 2018, *ApJ*, 864, L8
 Brož, M., Chrenko, O., Nesvorný, D., & Lambrechts, M. 2018, *A&A*, 620, A157
 Cabot, W. 1996, *ApJ*, 465, 874
 Chrenko, O., Brož, M., & Lambrechts, M. 2017, *A&A*, 606, A114
 Chrenko, O., Brož, M., & Nesvorný, D. 2018, *ApJ*, 868, 145
 Cimerman, N. P., Kuiper, R., & Ormel, C. W. 2017, *MNRAS*, 471, 4662
 Coleman, G. A. L., & Nelson, R. P. 2016, *MNRAS*, 457, 2480
 Cresswell, P., Dirksen, G., Kley, W., & Nelson, R. P. 2007, *A&A*, 473, 329
 Crida, A., Morbidelli, A., & Masset, F. 2006, *Icarus*, 181, 587
 de Val-Borro, M., Edgar, R. G., Artymowicz, P., et al. 2006, *MNRAS*, 370, 529
 Dullemond, C. P., Dominik, C., & Natta, A. 2001, *ApJ*, 560, 957
 Eklund, H., & Masset, F. S. 2017, *MNRAS*, 469, 206
 Flock, M., Fromang, S., González, M., & Commerçon, B. 2013, *A&A*, 560, A43
 Fung, J., & Chiang, E. 2017, *ApJ*, 839, 100
 Fung, J., Artymowicz, P., & Wu, Y. 2015, *ApJ*, 811, 101
 Goldreich, P., & Tremaine, S. 1979, *ApJ*, 233, 857
 Held, L. E., & Latter, H. N. 2018, *MNRAS*, 480, 4797
 Klahr, H., & Kley, W. 2006, *A&A*, 445, 747
 Klahr, H. H., & Bodenheimer, P. 2003, *ApJ*, 582, 869
 Klahr, H. H., Henning, T., & Kley, W. 1999, *ApJ*, 514, 325
 Kley, W. 1989, *A&A*, 208, 98
 Kley, W., & Crida, A. 2008, *A&A*, 487, L9
 Kley, W., Bitsch, B., & Klahr, H. 2009, *A&A*, 506, 971
 Korycansky, D. G., & Pollack, J. B. 1993, *Icarus*, 102, 150
 Kretke, K. A., & Lin, D. N. C. 2012, *ApJ*, 755, 74
 Kurokawa, H., & Tanigawa, T. 2018, *MNRAS*, 479, 635
 Lambrechts, M., & Johansen, A. 2012, *A&A*, 544, A32
 Lambrechts, M., & Johansen, A. 2014, *A&A*, 572, A107
 Lambrechts, M., & Lega, E. 2017, *A&A*, 606, A146
 Lega, E., Crida, A., Bitsch, B., & Morbidelli, A. 2014, *MNRAS*, 440, 683
 Lega, E., Morbidelli, A., Bitsch, B., Crida, A., & Szulágyi, J. 2015, *MNRAS*, 452, 1717
 Lesur, G., & Ogilvie, G. I. 2010, *MNRAS*, 404, L64

O. Chrenko and M. Lambrechts: Oscillatory migration of accreting protoplanets driven by a 3D distortion of the gas flow

- Lesur, G., & Papaloizou, J. C. B. 2010, *A&A*, 513, A60
- Levermore, C. D., & Pomraning, G. C. 1981, *ApJ*, 248, 321
- Li, H., Lubow, S. H., Li, S., & Lin, D. N. C. 2009, *ApJ*, 690, L52
- Lin, D. N. C., & Papaloizou, J. 1980, *MNRAS*, 191, 37
- Masset, F. S. 2002, *A&A*, 387, 605
- Masset, F. S. 2017, *MNRAS*, 472, 4204
- Masset, F. S., & Casoli, J. 2009, *ApJ*, 703, 857
- Masset, F. S., & Velasco Romero, D. A. 2017, *MNRAS*, 465, 3175
- McNally, C. P., Nelson, R. P., Paardekooper, S.-J., & Benítez-Llambay, P. 2019, *MNRAS*, 484, 728
- Mihalas, D., & Weibel Mihalas, B. 1984, *Foundations of Radiation Hydrodynamics* (New York: Oxford University Press)
- Miranda, R., & Lai, D. 2018, *MNRAS*, 473, 5267
- Morbidelli, A., Crida, A., Masset, F., & Nelson, R. P. 2008, *A&A*, 478, 929
- Ormel, C. W., & Klahr, H. H. 2010, *A&A*, 520, A43
- Ormel, C. W., Shi, J.-M., & Kuiper, R. 2015, *MNRAS*, 447, 3512
- Owen, J. E., & Kollmeier, J. A. 2017, *MNRAS*, 467, 3379
- Paardekooper, S.-J., & Mellema, G. 2006, *A&A*, 459, L17
- Paardekooper, S.-J., & Mellema, G. 2008, *A&A*, 478, 245
- Paardekooper, S.-J., & Papaloizou, J. C. B. 2009, *MNRAS*, 394, 2283
- Paardekooper, S.-J., Baruteau, C., Crida, A., & Kley, W. 2010, *MNRAS*, 401, 1950
- Paardekooper, S.-J., Baruteau, C., & Kley, W. 2011, *MNRAS*, 410, 293
- Petersen, M. R., Julien, K., & Stewart, G. R. 2007a, *ApJ*, 658, 1236
- Petersen, M. R., Stewart, G. R., & Julien, K. 2007b, *ApJ*, 658, 1252
- Pfeil, T., & Klahr, H. 2019, *ApJ*, 871, 150
- Piso, A.-M. A., Youdin, A. N., & Murray-Clay, R. A. 2015, *ApJ*, 800, 82
- Popovas, A., Nordlund, Å., Ramsey, J. P., & Ormel, C. W. 2018, *MNRAS*, 479, 5136
- Popovas, A., Nordlund, Å., & Ramsey, J. P. 2019, *MNRAS*, 482, L107
- Raettig, N., Lyra, W., & Klahr, H. 2013, *ApJ*, 765, 115
- Rafikov, R. R. 2002, *ApJ*, 572, 566
- Rein, H., & Liu, S.-F. 2012, *A&A*, 537, A128
- Rein, H., & Spiegel, D. S. 2015, *MNRAS*, 446, 1424
- Ruden, S. P., & Pollack, J. B. 1991, *ApJ*, 375, 740
- Rüdiger, G., Arlt, R., & Shalybkov, D. 2002, *A&A*, 391, 781
- Semenov, D., Henning, T., Helling, C., Ilgner, M., & Sedlmayr, E. 2003, *A&A*, 410, 611
- Stone, J. M., & Balbus, S. A. 1996, *ApJ*, 464, 364
- Stone, J. M., & Norman, M. L. 1992, *ApJS*, 80, 753
- Tanaka, H., & Ward, W. R. 2004, *ApJ*, 602, 388
- Tanaka, H., Takeuchi, T., & Ward, W. R. 2002, *ApJ*, 565, 1257
- Tanigawa, T., Ohtsuki, K., & Machida, M. N. 2012, *ApJ*, 747, 47
- Ward, W. R. 1986, *Icarus*, 67, 164
- Ward, W. R. 1991, in Lunar and Planetary Inst. Technical Report, Vol. 22, Lunar and Planetary Science Conference
- Ward, W. R. 1997, *ApJ*, 482, L211
- Yang, L. T., & Brent, R. P. 2002, in Proceedings of the Fifth Conference on Algorithm and Architectures for Parallel Processing., ed. W. Zhou, X. Chi, A. Goscinski, & G. Li (IEEE), 324
- Yu, C., Li, H., Li, S., Lubow, S. H., & Lin, D. N. C. 2010, *ApJ*, 712, 198
- Zhu, Z., Hartmann, L., Nelson, R. P., & Gammie, C. F. 2012, *ApJ*, 746, 110

Appendix A: Modifications of the numerical scheme

We implemented Eqs. (3) and (4) into FARGO3D using their discrete form derived by Bitsch et al. (2013; see their Appendix B). We introduce a minor modification of the numerical scheme, which allows for all the source terms to be accounted for in a single substep. Using the same notation as in Bitsch et al. (2013), the relation between the temperature and radiative energy at $t + \Delta t$ is

$$T^{n+1} = \eta_1 + \eta_2 E_R^{n+1}, \quad (\text{A.1})$$

and we redefine

$$\eta_1 = \frac{T^n + 12\Delta t \frac{\kappa_P}{c\nu} \sigma (T^n)^4 + \Delta t \frac{Q_{\epsilon\text{-indep}}}{\rho c\nu}}{1 + 16\Delta t \frac{\kappa_P}{c\nu} \sigma (T^n)^3 + \Delta t (\gamma - 1) \nabla \cdot \mathbf{v}}, \quad (\text{A.2})$$

$$\eta_2 = \frac{\Delta t \frac{\kappa_P}{c\nu} c}{1 + 16\Delta t \frac{\kappa_P}{c\nu} \sigma (T^n)^3 + \Delta t (\gamma - 1) \nabla \cdot \mathbf{v}}. \quad (\text{A.3})$$

There are two changes with respect to Bitsch et al. (2013). First, the compressional heating is included via the last term in the denominator of Eqs. (A.2) and (A.3). Second, the $Q_{\epsilon\text{-indep}}$ term is a sum of all heat sources that do not depend on ϵ (or T); in our case $Q_{\epsilon\text{-indep}} = Q_{\text{visc}} + Q_{\text{art}} + Q_{\text{acc}}$. We note that when necessary, the stellar irradiation term can also be easily included in $Q_{\epsilon\text{-indep}}$ but it is neglected in this work.

Appendix B: Supporting simulations

In this appendix, we summarize several additional simulations designed to confirm the robustness of our conclusions.

B.1. Simulation with a smoothly increasing luminosity of the protoplanet

In our main simulations, we usually start the phase with accretion heating abruptly, by instantaneously increasing the luminosity of the protoplanet from $L=0$ to the value corresponding to the mass doubling time $\tau = 100$ kyr. Such a sudden appearance of a strong heat source might produce an unexpected behaviour and instabilities by itself. In order to exclude any undesirable behaviour, we repeat the κ_{BL} -disk simulation with accretion heating of the protoplanet, but now we linearly increase L from zero at $t = 30 P_{\text{orb}}$ to its maximal value over the time interval of $10 P_{\text{orb}}$.

Figure B.1 shows the measured torque evolution. Clearly, the gradual increase of L has no impact on the final character of the torque, and the oscillations related to the flow reconfigurations inevitably appear.

B.2. Simulation with an increased azimuthal resolution

The resolution in our simulations is motivated by works of Lega et al. (2014) and Eklund & Masset (2017). Although we do not perform extended convergence tests of our own, the resolution should be sufficient to recover a realistic torque value and also a realistic advection-diffusion redistribution of the hot gas near the protoplanet.

However, once the circumplanetary flow becomes unstable, it is no longer clear if the chosen resolution is sufficient. For example, one might argue that the coverage of the Hill sphere by the grid cells in the azimuthal direction is too poor. Here we present

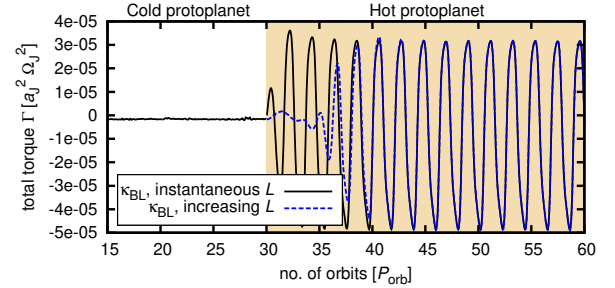


Fig. B.1. Torque evolution in the κ_{BL} -disk with instantaneously increased luminosity of the protoplanet L (solid black curve; same as in Fig. 2) compared to the κ_{BL} -disk with smoothly increasing L (dashed blue curve). Even before L reaches its maximum value in the latter case, the curves start to overlap. After $t = 40 P_{\text{orb}}$, the agreement is almost exact.

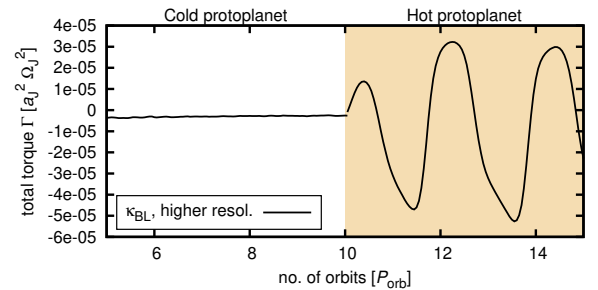


Fig. B.2. Torque evolution obtained in the κ_{BL} -disk simulation with an increased azimuthal resolution of 2764 cells. The time span of the individual phases is shortened to save computing time. The instability in the presence of the accretion heating is however recovered again.

an experiment in which we double the number of the grid cells in the azimuthal direction in order to obtain the same coverage of the Hill sphere in all directions. We perform the κ_{BL} -disk simulation again, however we shorten the phase without accretion heating to $10 P_{\text{orb}}$ and the phase with accretion heating to $5 P_{\text{orb}}$.

The result is shown in Fig. B.2 and demonstrates that the torque oscillations are recovered even when the increased resolution is used. However, the amplitude of the torque oscillations slightly changes, implying that the resolution dependence should be explored more carefully in the future.

B.3. Simulation with the unmodified Bell & Lin opacity table

The simulations of the κ_{BL} -disk presented in this paper are performed with a simplified opacity law of Bell & Lin (1994) (explained in Sect. 2.2). Here we test how the results change if the unmodified opacity law $\kappa_{\text{BL}}^{\text{full}}$ is used and the dependence on the local values of T and ρ is retained.

Figure B.3 compares the torque evolution in our standard κ_{BL} -disk with that in a $\kappa_{\text{BL}}^{\text{full}}$ -disk. Clearly, the instability occurs in both disks, regardless of whether or not the input values for the opacity function are azimuthally averaged. The only difference is in the torque amplitude which is larger in the $\kappa_{\text{BL}}^{\text{full}}$ -disk.

The increased amplitude occurs because if T locally rises, so does the material opacity ($\kappa_{\text{BL}}^{\text{full}} \propto T^2$ in the given disk region). Subsequently, the radiative cooling of the hot gas becomes less efficient and T rises even more. As a result, the underdense perturbations related to any temperature excess are more pronounced, leading to the larger amplitude of the torque oscillations.

O. Chrenko and M. Lambrechts: Oscillatory migration of accreting protoplanets driven by a 3D distortion of the gas flow

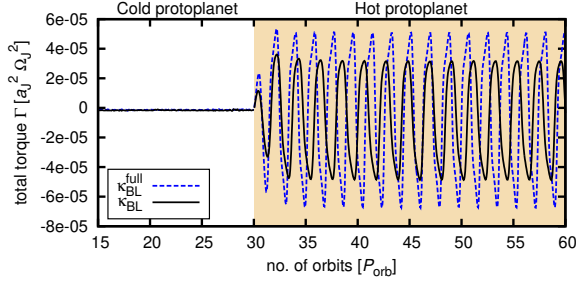


Fig. B.3. Comparison of the torque evolutions obtained in the κ_{BL} -disk (solid black curve; same as in Fig. 2) and the $\kappa_{\text{BL}}^{\text{full}}$ -disk (dashed blue curve). The first model inputs azimuthally averaged values of ρ and T to the opacity function of Bell & Lin (1994), while the latter uses local values of ρ and T . Both cases lead to the instability of the circumplanetary flow, but they differ in the amplitude of the torque oscillations.

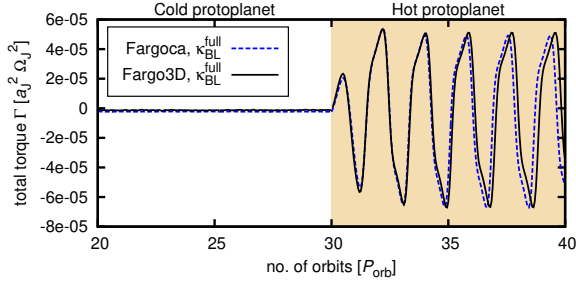


Fig. B.4. Comparison of the torque evolutions obtained with two independent codes FARGO3D (solid black curve) and FARGOCA (dashed blue curve). The unmodified $\kappa_{\text{BL}}^{\text{full}}$ opacity table of Bell & Lin (1994) was used in this case.

B.4. Code comparison

With the aim to confirm that our implementation of the energy equations in FARGO3D is correct and also that the instability of the circumplanetary flow does not arise due to numerical artefacts, we present a comparison simulation obtained with an independent and well-tested radiation hydrodynamic code FARGOCA (Lega et al. 2014). The simulation is performed with the unmodified $\kappa_{\text{BL}}^{\text{full}}$ opacity law of Bell & Lin (1994).

Figure B.4 compares the torque evolution found using our code with the one obtained with FARGOCA. We can see that the converged torque for the cold protoplanet is in a satisfactory agreement.

When the accretion heating is initiated, the same oscillatory trend is observed with both codes. The curves overlap at first; later they start to depart in terms of the oscillation phase. However, the amplitude remains the same.

Since the converged torques are in agreement and the instability is recovered, we conclude that the differences that we identify in Fig. B.4 arise only because our radiation module in FARGO3D relies on a slightly different numerical scheme (see Appendix A) compared to FARGOCA.

Appendix C: Vorticity equation in the corotating frame

For the convenience of the reader, we provide a step-by-step derivation of the vorticity equation. Starting with Eq. (2), we apply the curl on both sides. In the following, we neglect the viscous term (large Reynolds number limit).

The following identities of the vector calculus will be utilised:

$$(\mathbf{a} \cdot \nabla) \mathbf{a} = \frac{1}{2} \nabla (\mathbf{a} \cdot \mathbf{a}) + (\nabla \times \mathbf{a}) \times \mathbf{a}, \quad (\text{C.1})$$

$$\nabla \times (\mathbf{a} \times \mathbf{b}) = \mathbf{a} (\nabla \cdot \mathbf{b}) - \mathbf{b} (\nabla \cdot \mathbf{a}) + (\mathbf{b} \cdot \nabla) \mathbf{a} - (\mathbf{a} \cdot \nabla) \mathbf{b}, \quad (\text{C.2})$$

$$\nabla \cdot (\nabla \times \mathbf{a}) = 0, \quad (\text{C.3})$$

$$\nabla \times (\nabla f) = \mathbf{0}, \quad (\text{C.4})$$

where the last identity holds for scalar functions that are at least twice continuously differentiable.

The curl of the advection term yields

$$\nabla \times [(\mathbf{v} \cdot \nabla) \mathbf{v}] = \nabla \times \left[\frac{1}{2} \nabla (\mathbf{v} \cdot \mathbf{v}) + (\nabla \times \mathbf{v}) \times \mathbf{v} \right] = \nabla \times [\boldsymbol{\omega}_r \times \mathbf{v}], \quad (\text{C.5})$$

where we used Eq. (C.1) in writing the first equality, Eq. (C.4) to remove the $\sim \mathbf{v} \cdot \mathbf{v}$ term, and we defined the relative vorticity in the corotating frame $\boldsymbol{\omega}_r = \nabla \times \mathbf{v}$. Using Eqs. (C.2) and (C.3), we further obtain

$$\nabla \times [(\mathbf{v} \cdot \nabla) \mathbf{v}] = \boldsymbol{\omega}_r (\nabla \cdot \mathbf{v}) + (\mathbf{v} \cdot \nabla) \boldsymbol{\omega}_r - (\boldsymbol{\omega}_r \cdot \nabla) \mathbf{v}. \quad (\text{C.6})$$

The curl of the pressure term leads to

$$\nabla \times \left(\frac{\nabla P}{\rho} \right) = -\frac{1}{\rho^2} \nabla \rho \times \nabla P, \quad (\text{C.7})$$

because $\nabla \times (\nabla P) = \mathbf{0}$ (Eq. (C.4)).

When dealing with the gravitational term, it is useful to realise that the centrifugal acceleration can be expressed as $\boldsymbol{\Omega} \times (\boldsymbol{\Omega} \times \mathbf{r}) = \nabla \Phi_c$, with the centrifugal potential $\Phi_c = -\frac{1}{2} r_{\perp}^2 \Omega^2$. The curl of a combined force term, $\nabla \times [\nabla (\Phi + \Phi_c)]$, is zero owing to Eq. (C.4).

Finally, we take the curl of the Coriolis acceleration:

$$\nabla \times (2\boldsymbol{\Omega} \times \mathbf{v}) = 2 [\boldsymbol{\Omega} (\nabla \cdot \mathbf{v}) - (\boldsymbol{\Omega} \cdot \nabla) \mathbf{v}], \quad (\text{C.8})$$

where we removed terms $\sim \nabla \cdot \boldsymbol{\Omega}$, $\sim \nabla \boldsymbol{\Omega}$ because $\boldsymbol{\Omega}$ in our simulations is constant.

Recollecting all the terms, we can write the relative vorticity equation

$$\frac{\partial \boldsymbol{\omega}_r}{\partial t} + (\mathbf{v} \cdot \nabla) \boldsymbol{\omega}_r = \frac{D \boldsymbol{\omega}_r}{Dt} = (\boldsymbol{\omega}_a \cdot \nabla) \mathbf{v} - \boldsymbol{\omega}_a (\nabla \cdot \mathbf{v}) + \frac{\nabla \rho \times \nabla P}{\rho^2}, \quad (\text{C.9})$$

where we defined the absolute vorticity in the inertial frame $\boldsymbol{\omega}_a = \boldsymbol{\omega}_r + 2\boldsymbol{\Omega}$.

Conclusions

By means of numerical RHD simulations in 2D and 3D, we explored migration of low-mass ($M_p \sim 10^0 M_\oplus$) protoplanets due to their interactions with a gas disk during their ongoing accretion of pebbles. We focused on evolution in the giant-planet formation zone and we investigated the influence of the heating torque (Benítez-Llambay et al. 2015) triggered by pebble accretion. We found several important implications for the early phases of formation of planetary systems.

Eccentricity excitation by the hot-trail effect

In addition to the heating torque, accretion heating leads to eccentricity excitation by means of the hot-trail effect (Chrenko et al. 2017; Eklund & Masset 2017). The effect arises because the gravitational pull of asymmetrically distributed hot underdense gas near accreting protoplanets accelerates them on their epicycle, creating a positive feedback between the acceleration and the eccentricity growth. The eccentricity growth is terminated approximately for $e \sim h$ when the tidal damping starts to dominate again.

In a closely packed system of super-Earths undergoing convergent migration, eccentricities excited by the hot-trail effect ($e \simeq 0.03$) prevent resonant locking and allow the protoplanets to interact in a series of close encounters. These repeated encounters can potentially lead to collisions, resulting in a direct and fast formation of giant planet cores. Merger events tend to be preceded by 3-body encounters (Brož et al. 2018).

Formation of binary planets

Motivated by findings of Eklund & Masset (2017) who pointed out that the hot-trail effect excites inclinations as well, we re-investigated the evolution of multiple $3 M_\oplus$ protoplanets with an artificially reduced efficiency of the inclination damping. We found that such conditions facilitate formation of binary planets during close encounters (Chrenko et al. 2018). Transient binary planets (dissolving on an orbital timescale) are formed when two protoplanets enter their mutual Hill sphere and their orbital energy is dissipated in gas density waves. Binary planets with a prolonged lifetime are formed when a transient binary undergoes hardening in a three-body interaction with some other protoplanet. Our study of the stability of binaries predicts that one binary planet should be observable in a sample of $\simeq (2-5) \times 10^4$ planetary systems, which is a low occurrence, but still traceable in future observational campaigns.

RHD simulation with a swarm of planetary embryos

We also performed a simulation with many ($N = 120$) Mars-mass embryos ($M_p = 0.1 M_\oplus$) to push the applicability of RHD simulations to even earlier evolutionary

phases (usually studied with N-body techniques). We found that such a swarm of embryos matures through a relatively low number of merger events (Brož et al. 2018). The most massive bodies remain on low inclinations which allows them to grow by pebble accretion more efficiently compared to the smaller embryos that are stirred to larger inclinations, offset with respect to the pebble feeding zone. This finding confirms the mechanism of the viscously stirred pebble accretion described by Levison et al. (2015) using N-body models.

3D gas flow instability around accreting planets

In our 3D simulations (Chrenko & Lambrechts 2019), we investigated how the heating torque differs between disks with constant and non-uniform (temperature-dependent) opacities. Regardless of the opacities, accretion heating leads to baroclinic and convective perturbations which distort the direction of the flow in the vicinity of the protoplanet. A retrograde spiral-like flow of gas appears near the protoplanet which is fed from downstream horseshoe regions, rises in the direction perpendicular to the disk midplane, and outflows from the Hill sphere above/below the protoplanet.

For temperature-dependent opacities $\kappa \propto T^\beta$ with $\beta = 0.5-2$, the perturbed flow eventually becomes unstable. The instability redistributes underdense gas responsible for the heating torque into a one-sided lobe circulating around the protoplanet. The circulation causes strong oscillations of the resulting torque. The migration is then oscillatory as well, with inward/outward excursions at a rate $\sim 10^{-4}$ au yr $^{-1}$ (for $\beta = 2$). The mean migration rate remains almost unaffected by the heating torque which, in this specific case, does not promote outward migration. We suggest that transition zones might exist in protoplanetary disks where accreting planets switch between the standard positive heating torque and the oscillatory mode. An accumulation of planets may be expected at these transitions.

Code development

In order to perform the aforementioned RHD simulations, it was necessary to develop appropriate computational tools. For the purpose of our 2D modelling, we extended the 2D HD code `Fargo` (Masset 2000) by including the 1-temperature energy equation for gas, accretion heating, stellar irradiation, horizontal radiative diffusion, and viscous heating. We also implemented a two-fluid approximation to describe the pebble disk as an additional fluid, coupled with the gas disk via a two-way linear drag term. The `Ias15` integrator was interfaced with the code to study planetary orbits in 3D and also to allow for a precise integration of close encounters and detection of collisions. A simple coagulation/drift model was implemented to describe the initial state of the pebble disk and we developed a numerical method to account for pebble accretion by planets. The resulting code named `Thorin` was

made publicly available³.

Our 3D code contains less physical modules than `Thorin` but compares well to state-of-the-art codes used in the field of planet-disk interactions (such as `Fargoca`; Lega et al. 2014). It was built on top of the `Fargo3d` code (Benítez-Llambay & Masset 2016) into which we implemented the energy equations for gas and radiation in the 2-temperature approximation. Viscous heating, accretion heating, 3D flux-limited radiation diffusion, and radially ray-traced stellar irradiation were accounted for. The `Ias15` integrator was used again but accretion onto planets was only parametric in this case.

Future work and outlook

This thesis unveiled several new implications for observed exoplanetary systems (i.e. the hot-trail effect excites eccentricities which can explain the paucity of resonant orbits; binary planets should be rare but detectable in future). Nevertheless, it would be fruitful to focus our future work on connecting our RHD models with observations more tightly.

Concerning exoplanetary systems, we would like to improve our RHD simulations to be suitable for regions near inner rims of disks. It is believed that an accumulation and interactions of migrating protoplanets near the inner rim might result in formation of close-in super-Earths (Cossou et al. 2014; Izidoro et al. 2017; Lambrechts et al. 2019). However, implications of the heating torque and the hot-trail effect for this scenario are yet to be assessed. Similarly, it remains to be decided whether the protoplanets pile up at the inner rim (e.g. Miranda & Lai 2018) or rather penetrate into the inner cavity (e.g. Brasser et al. 2018).

Regarding the Solar System, we are currently investigating an alternative scenario of terrestrial planet formation. It assumes that terrestrial planets accreted early while they were still embedded in a gas disk. In our framework, only the Earth–Moon system might have potentially formed later by a single Moon-forming impact, needed to match radiometric constraints (Canup 2012, 2019). Our preliminary results show that if there was a reversal (outward gradient) of the gas density profile in the inner disk (similarly to Ogihara et al. 2015, albeit related to a viscosity transition in our case), embryos in the terrestrial zone would undergo convergent migration, forming terrestrial planets by mutual collisions, with a contribution of pebble accretion.

Finally, since this thesis demonstrated the importance of the heating torque and the hot-trail effect, it would be worthwhile to implement these phenomena in N-body integrators with prescribed migration because, despite their limitations, they allow for a faster and more extended exploration of the parametric space. Overall, we believe that our results will lead to an improvement of planet population synthesis.

³See <http://sirrah.troja.mff.cuni.cz/~chrenko/> for the source code, documentation and user's guide.

Bibliography

- [1] Adachi, I., Hayashi, C., & Nakazawa, K. 1976, *Progress of Theoretical Physics*, 56, 1756
- [2] Adams, F. C., Lada, C. J., & Shu, F. H. 1987, *ApJ*, 312, 788
- [3] ALMA Partnership, Brogan, C. L., Pérez, L. M., et al. 2015, *ApJ*, 808, L3
- [4] André, P., Di Francesco, J., Ward-Thompson, D., et al. 2014, in *Protostars and Planets VI*, ed. H. Beuther, R. S. Klessen, C. P. Dullemond, & T. Henning, 27
- [5] André, P. & Montmerle, T. 1994, *ApJ*, 420, 837
- [6] André, P., Ward-Thompson, D., & Barsony, M. 1993, *ApJ*, 406, 122
- [7] Andrews, S. M., Huang, J., Pérez, L. M., et al. 2018, *ApJ*, 869, L41
- [8] Andrews, S. M. & Williams, J. P. 2005, *ApJ*, 631, 1134
- [9] Andrews, S. M. & Williams, J. P. 2007, *ApJ*, 671, 1800
- [10] Andrews, S. M., Wilner, D. J., Hughes, A. M., Qi, C., & Dullemond, C. P. 2009, *ApJ*, 700, 1502
- [11] Andrews, S. M., Wilner, D. J., Hughes, A. M., Qi, C., & Dullemond, C. P. 2010, *ApJ*, 723, 1241
- [12] Ansdell, M., Williams, J. P., van der Marel, N., et al. 2016, *ApJ*, 828, 46
- [13] Armitage, P. J. 2010, *Astrophysics of Planet Formation*
- [14] Armitage, P. J. 2011, *ARA&A*, 49, 195
- [15] Armitage, P. J. 2015, arXiv e-prints, arXiv:1509.06382
- [16] Artymowicz, P. 1993, *ApJ*, 419, 166
- [17] Artymowicz, P. 1993, *ApJ*, 419, 155
- [18] Avenhaus, H., Quanz, S. P., Garufi, A., et al. 2018, *ApJ*, 863, 44
- [19] Bae, J., Hartmann, L., Zhu, Z., & Nelson, R. P. 2014, *ApJ*, 795, 61
- [20] Bai, X.-N. & Stone, J. M. 2010, *ApJ*, 722, 1437
- [21] Baillié, K., Charnoz, S., & Pantin, E. 2016, *A&A*, 590, A60
- [22] Balbus, S. A. 2011, *Magnetohydrodynamics of Protostellar Disks*, ed. P. J. V. Garcia, 237–282
- [23] Balbus, S. A. & Hawley, J. F. 1998, *Reviews of Modern Physics*, 70, 1
- [24] Baruteau, C., Crida, A., Paardekooper, S.-J., et al. 2014, *Protostars and Planets VI*, 667
- [25] Baruteau, C. & Masset, F. 2008, *ApJ*, 672, 1054
- [26] Baruteau, C. & Masset, F. 2008, *ApJ*, 678, 483
- [27] Baruteau, C. & Masset, F. 2013, in *Lecture Notes in Physics*, Berlin Springer Verlag, Vol. 861, *Lecture Notes in Physics*, Berlin Springer Verlag, ed. J. Souchay, S. Mathis, & T. Tokieda, 201
- [28] Batygin, K. 2015, *MNRAS*, 451, 2589
- [29] Beckwith, S. V. W., Sargent, A. I., Chini, R. S., & Guesten, R. 1990, *AJ*, 99, 924
- [30] Bell, K. R. & Lin, D. N. C. 1994, *ApJ*, 427, 987

- [31] Ben-Jaffel, L. & Ballester, G. E. 2014, *ApJ*, 785, L30
- [32] Benítez-Llambay, P., Masset, F., Koenigsberger, G., & Szulágyi, J. 2015, *Nature*, 520, 63
- [33] Benítez-Llambay, P. & Masset, F. S. 2016, *ApJS*, 223, 11
- [34] Benítez-Llambay, P. & Pessah, M. E. 2018, *ApJ*, 855, L28
- [35] Bennett, D. P., Batista, V., Bond, I. A., et al. 2014, *ApJ*, 785, 155
- [36] Beurle, K., Murray, C. D., Williams, G. A., et al. 2010, *ApJ*, 718, L176
- [37] Biele, J., Ulamec, S., Maibaum, M., et al. 2015, *Science*, 349, 1.9816
- [38] Binney, J. & Tremaine, S. 2008, *Galactic Dynamics: Second Edition*
- [39] Birnstiel, T., Dullemond, C. P., & Brauer, F. 2010, *A&A*, 513, A79
- [40] Birnstiel, T., Dullemond, C. P., Zhu, Z., et al. 2018, *ApJ*, 869, L45
- [41] Birnstiel, T., Klahr, H., & Ercolano, B. 2012, *A&A*, 539, A148
- [42] Bitsch, B., Crida, A., Morbidelli, A., Kley, W., & Dobbs-Dixon, I. 2013, *A&A*, 549, A124
- [43] Bitsch, B., Izidoro, A., Johansen, A., et al. 2019, *A&A*, 623, A88
- [44] Bitsch, B. & Kley, W. 2010, *A&A*, 523, A30
- [45] Bitsch, B., Morbidelli, A., Johansen, A., et al. 2018, *A&A*, 612, A30
- [46] Bitsch, B., Raymond, S. N., & Izidoro, A. 2019, *A&A*, 624, A109
- [47] Blandford, R. D. & Payne, D. G. 1982, *MNRAS*, 199, 883
- [48] Blum, J., Gundlach, B., Krause, M., et al. 2017, *MNRAS*, 469, S755
- [49] Blum, J. & Münch, M. 1993, *Icarus*, 106, 151
- [50] Blum, J. & Wurm, G. 2000, *Icarus*, 143, 138
- [51] Blum, J. & Wurm, G. 2008, *ARA&A*, 46, 21
- [52] Bohren, C. F. & Huffman, D. R. 1983, *Absorption and scattering of light by small particles*
- [53] Borucki, W. J., Koch, D., Basri, G., et al. 2010, *Science*, 327, 977
- [54] Bouvier, J., Alencar, S. H. P., Harries, T. J., Johns-Krull, C. M., & Romanova, M. M. 2007, in *Protostars and Planets V*, ed. B. Reipurth, D. Jewitt, & K. Keil, 479
- [55] Brasser, R., Matsumura, S., Muto, T., & Ida, S. 2018, *ApJ*, 864, L8
- [56] Brauer, F., Dullemond, C. P., & Henning, T. 2008, *A&A*, 480, 859
- [57] Brouwer, D. & Clemence, G. M. 1961, *Methods of celestial mechanics*
- [58] Brož, M., Chrenko, O., Nesvorný, D., & Lambrechts, M. 2018, *A&A*, 620, A157
- [59] Buchhave, L. A., Latham, D. W., Johansen, A., et al. 2012, *Nature*, 486, 375
- [60] Calvet, N. & Gullbring, E. 1998, *ApJ*, 509, 802
- [61] Calvet, N., Patino, A., Magris, G. C., & D'Alessio, P. 1991, *ApJ*, 380, 617
- [62] Camenzind, M. 1990, *Reviews in Modern Astronomy*, 3, 234
- [63] Canup, R. M. 2012, *Science*, 338, 1052
- [64] Canup, R. M. 2019, in *Lunar and Planetary Science Conference, Lunar and Planetary Science Conference*, 2044
- [65] Casoli, J. & Masset, F. S. 2009, *ApJ*, 703, 845

-
- [66] Chambers, J. E. 2016, *ApJ*, 825, 63
- [67] Chiang, E. & Youdin, A. N. 2010, *Annual Review of Earth and Planetary Sciences*, 38, 493
- [68] Chiang, E. I. & Goldreich, P. 1997, *ApJ*, 490, 368
- [69] Chrenko, O., Brož, M., & Lambrechts, M. 2017, *A&A*, 606, A114
- [70] Chrenko, O., Brož, M., & Nesvorný, D. 2018, *ApJ*, 868, 145
- [71] Chrenko, O. & Lambrechts, M. 2019, *A&A*, 626, A109
- [72] Coleman, G. A. L. & Nelson, R. P. 2014, *MNRAS*, 445, 479
- [73] Coleman, G. A. L. & Nelson, R. P. 2016, *MNRAS*, 457, 2480
- [74] Connolly, H. C. & Jones, R. H. 2016, *Journal of Geophysical Research (Planets)*, 121, 1885
- [75] Cossou, C., Raymond, S. N., Hersant, F., & Pierens, A. 2014, *A&A*, 569, A56
- [76] Cossou, C., Raymond, S. N., & Pierens, A. 2013, *A&A*, 553, L2
- [77] Cresswell, P., Dirksen, G., Kley, W., & Nelson, R. P. 2007, *A&A*, 473, 329
- [78] Cresswell, P. & Nelson, R. P. 2008, *A&A*, 482, 677
- [79] Crida, A., Morbidelli, A., & Masset, F. 2006, *Icarus*, 181, 587
- [80] Cuzzi, J. N., Estrada, P. R., & Davis, S. S. 2014, *ApJS*, 210, 21
- [81] Cuzzi, J. N., Hogan, R. C., Paque, J. M., & Dobrovolskis, A. R. 2001, *ApJ*, 546, 496
- [82] Cuzzi, J. N., Hogan, R. C., & Shariff, K. 2008, *ApJ*, 687, 1432
- [83] D’Angelo, G., Henning, T., & Kley, W. 2003, *ApJ*, 599, 548
- [84] Dauphas, N. & Chaussidon, M. 2011, *Annual Review of Earth and Planetary Sciences*, 39, 351
- [85] Dittrich, K., Klahr, H., & Johansen, A. 2013, *ApJ*, 763, 117
- [86] Dobbs-Dixon, I., Cumming, A., & Lin, D. N. C. 2010, *ApJ*, 710, 1395
- [87] Draine, B. T. 2006, *ApJ*, 636, 1114
- [88] Draine, B. T. & Lee, H. M. 1984, *ApJ*, 285, 89
- [89] Drażkowska, J., Alibert, Y., & Moore, B. 2016, *A&A*, 594, A105
- [90] Dubrulle, B., Morfill, G., & Sterzik, M. 1995, *Icarus*, 114, 237
- [91] Dullemond, C. P., Birnstiel, T., Huang, J., et al. 2018, *ApJ*, 869, L46
- [92] Dullemond, C. P., Dominik, C., & Natta, A. 2001, *ApJ*, 560, 957
- [93] Dullemond, C. P. & Monnier, J. D. 2010, *ARA&A*, 48, 205
- [94] Dutrey, A., Semenov, D., Chapillon, E., et al. 2014, in *Protostars and Planets VI*, ed. H. Beuther, R. S. Klessen, C. P. Dullemond, & T. Henning, 317
- [95] Eklund, H. & Masset, F. S. 2017, *MNRAS*, 469, 206
- [96] Ercolano, B. & Pascucci, I. 2017, *Royal Society Open Science*, 4, 170114
- [97] Fang, M., van Boekel, R., Wang, W., et al. 2009, *A&A*, 504, 461
- [98] Fedele, D., van den Ancker, M. E., Henning, T., Jayawardhana, R., & Oliveira, J. M. 2010, *A&A*, 510, A72
- [99] Fendyke, S. M. & Nelson, R. P. 2014, *MNRAS*, 437, 96
- [100] Filacchione, G., Capaccioni, F., Ciarniello, M., et al. 2016, *Icarus*, 274, 334
- [101] Flaherty, K. M., Hughes, A. M., Rose, S. C., et al. 2017, *ApJ*, 843, 150

- [102] Flaherty, K. M., Hughes, A. M., Rosenfeld, K. A., et al. 2015, *ApJ*, 813, 99
- [103] Flock, M., Fromang, S., González, M., & Commerçon, B. 2013, *A&A*, 560, A43
- [104] Flock, M., Fromang, S., Turner, N. J., & Benisty, M. 2016, *ApJ*, 827, 144
- [105] Flock, M., Nelson, R. P., Turner, N. J., et al. 2017, *ApJ*, 850, 131
- [106] Fraser, W. C., Bannister, M. T., Pike, R. E., et al. 2017, *Nature Astronomy*, 1, 0088
- [107] Fromang, S. & Nelson, R. P. 2005, *MNRAS*, 364, L81
- [108] Fromenteau, S. & Masset, F. S. 2019, *MNRAS*, 485, 5035
- [109] Fung, J., Artymowicz, P., & Wu, Y. 2015, *ApJ*, 811, 101
- [110] Fung, J. & Chiang, E. 2017, *ApJ*, 839, 100
- [111] Goldreich, P. & Lynden-Bell, D. 1965, *MNRAS*, 130, 97
- [112] Goldreich, P. & Tremaine, S. 1979, *ApJ*, 233, 857
- [113] Goldreich, P. & Tremaine, S. 1980, *ApJ*, 241, 425
- [114] Goodman, J. & Pindor, B. 2000, *Icarus*, 148, 537
- [115] Goodman, J. & Rafikov, R. R. 2001, *ApJ*, 552, 793
- [116] Greaves, J. S. & Rice, W. K. M. 2010, *MNRAS*, 407, 1981
- [117] Greenberg, R., Wacker, J. F., Hartmann, W. K., & Chapman, C. R. 1978, *Icarus*, 35, 1
- [118] Greene, T. P., Wilking, B. A., Andre, P., Young, E. T., & Lada, C. J. 1994, *ApJ*, 434, 614
- [119] Guilera, O. M., Cuello, N., Montesinos, M., et al. 2019, *MNRAS*, 486, 5690
- [120] Guillot, T., Ida, S., & Ormel, C. W. 2014, *A&A*, 572, A72
- [121] Gullbring, E., Hartmann, L., Briceño, C., & Calvet, N. 1998, *ApJ*, 492, 323
- [122] Gundlach, B. & Blum, J. 2015, *ApJ*, 798, 34
- [123] Güttler, C., Blum, J., Zsom, A., Ormel, C. W., & Dullemond, C. P. 2010, *A&A*, 513, A56
- [124] Hagihara, Y. 1972, *Celestial mechanics*. Vol.2, pt.1: Perturbation theory; Vol.2, pt.2: Perturbation theory
- [125] Haisch, Karl E., J., Lada, E. A., & Lada, C. J. 2001, *ApJ*, 553, L153
- [126] Hallam, P. D. & Paardekooper, S. J. 2018, *MNRAS*, 481, 1667
- [127] Hartigan, P., Edwards, S., & Ghandour, L. 1995, *ApJ*, 452, 736
- [128] Hartmann, L., Calvet, N., Gullbring, E., & D'Alessio, P. 1998, *ApJ*, 495, 385
- [129] Hayashi, C. 1981, *Progress of Theoretical Physics Supplement*, 70, 35
- [130] Heller, R. 2014, *ApJ*, 787, 14
- [131] Helling, C., Winters, J. M., & Sedlmayr, E. 2000, *A&A*, 358, 651
- [132] Henning, T. & Semenov, D. 2013, *Chemical Reviews*, 113, 9016
- [133] Herczeg, G. J. & Hillenbrand, L. A. 2008, *ApJ*, 681, 594
- [134] Hernández, J., Hartmann, L., Megeath, T., et al. 2007, *ApJ*, 662, 1067
- [135] Hildebrand, R. H. 1983, *QJRAS*, 24, 267
- [136] Hills, J. G. 1975, *AJ*, 80, 809
- [137] Hogerheijde, M. R., Bergin, E. A., Brinch, C., et al. 2011, *Science*, 334, 338

- [138] Hollenbach, D. J., Yorke, H. W., & Johnstone, D. 2000, in *Protostars and Planets IV*, ed. V. Mannings, A. P. Boss, & S. S. Russell, 401–428
- [139] Howard, A. W., Marcy, G. W., Bryson, S. T., et al. 2012, *ApJS*, 201, 15
- [140] Howell, L. H. & Greenough, J. A. 2003, *Journal of Computational Physics*, 184, 53
- [141] Huang, J., Andrews, S. M., Pérez, L. M., et al. 2018, *ApJ*, 869, L43
- [142] Hubeny, I. 1990, *ApJ*, 351, 632
- [143] Ida, S. & Guillot, T. 2016, *A&A*, 596, L3
- [144] Ida, S. & Makino, J. 1993, *Icarus*, 106, 210
- [145] Ida, S., Yamamura, T., & Okuzumi, S. 2019, *A&A*, 624, A28
- [146] Isella, A., Carpenter, J. M., & Sargent, A. I. 2009, *ApJ*, 701, 260
- [147] Isella, A., Huang, J., Andrews, S. M., et al. 2018, *ApJ*, 869, L49
- [148] Isella, A. & Natta, A. 2005, *A&A*, 438, 899
- [149] Izidoro, A., Ogiwara, M., Raymond, S. N., et al. 2017, *MNRAS*, 470, 1750
- [150] Izidoro, A., Raymond, S. N., Morbidelli, A., Hersant, F., & Pierens, A. 2015, *ApJ*, 800, L22
- [151] Jacquet, E., Balbus, S., & Latter, H. 2011, *MNRAS*, 415, 3591
- [152] Jäger, C., Dorschner, J., Mutschke, H., Posch, T., & Henning, T. 2003, *A&A*, 408, 193
- [153] Jiménez, M. A. & Masset, F. S. 2017, *MNRAS*, 471, 4917
- [154] Johansen, A., Klahr, H., & Henning, T. 2006, *ApJ*, 636, 1121
- [155] Johansen, A. & Lambrechts, M. 2017, *Annual Review of Earth and Planetary Sciences*, 45, 359
- [156] Johansen, A., Mac Low, M.-M., Lacerda, P., & Bizzarro, M. 2015, *Science Advances*, 1, 1500109
- [157] Johansen, A., Oishi, J. S., Mac Low, M.-M., et al. 2007, *Nature*, 448, 1022
- [158] Johansen, A. & Youdin, A. 2007, *ApJ*, 662, 627
- [159] Johansen, A., Youdin, A., & Klahr, H. 2009, *ApJ*, 697, 1269
- [160] Johnson, J. A., Aller, K. M., Howard, A. W., & Crepp, J. R. 2010, *PASP*, 122, 905
- [161] Jones, M. G., Pringle, J. E., & Alexander, R. D. 2012, *MNRAS*, 419, 925
- [162] Kama, M., Bruderer, S., Carney, M., et al. 2016, *A&A*, 588, A108
- [163] Kama, M., Min, M., & Dominik, C. 2009, *A&A*, 506, 1199
- [164] Kane, S. R., Ciardi, D. R., Gelino, D. M., & von Braun, K. 2012, *MNRAS*, 425, 757
- [165] Kenyon, S. J. & Hartmann, L. 1987, *ApJ*, 323, 714
- [166] Kipping, D. M. 2009, *MNRAS*, 392, 181
- [167] Kipping, D. M., Bakos, G. Á., Buchhave, L., Nesvorný, D., & Schmitt, A. 2012, *ApJ*, 750, 115
- [168] Klahr, H. & Kley, W. 2006, *A&A*, 445, 747
- [169] Klahr, H., Pfeil, T., & Schreiber, A. 2018, *Instabilities and Flow Structures in Protoplanetary Disks: Setting the Stage for Planetesimal Formation*, 138

- [170] Klahr, H. H. & Bodenheimer, P. 2003, *ApJ*, 582, 869
- [171] Kleine, T. & Walker, R. J. 2017, *Annual Review of Earth and Planetary Sciences*, 45, 389
- [172] Kley, W. 1989, *A&A*, 208, 98
- [173] Kley, W. 1999, *MNRAS*, 303, 696
- [174] Kley, W., Bitsch, B., & Klahr, H. 2009, *A&A*, 506, 971
- [175] Kley, W. & Crida, A. 2008, *A&A*, 487, L9
- [176] Kley, W. & Nelson, R. P. 2012, *ARA&A*, 50, 211
- [177] Kokubo, E. & Ida, S. 1998, *Icarus*, 131, 171
- [178] Kokubo, E. & Ida, S. 2000, *Icarus*, 143, 15
- [179] Kolb, S. M., Stute, M., Kley, W., & Mignone, A. 2013, *A&A*, 559, A80
- [180] Königl, A. 1991, *ApJ*, 370, L39
- [181] Königl, A. & Salmeron, R. 2011, *The Effects of Large-Scale Magnetic Fields on Disk Formation and Evolution*, ed. P. J. V. Garcia, 283–352
- [182] Korycansky, D. G. & Pollack, J. B. 1993, *Icarus*, 102, 150
- [183] Kretke, K. A. & Lin, D. N. C. 2012, *ApJ*, 755, 74
- [184] Kuiper, R., Klahr, H., Dullemond, C., Kley, W., & Henning, T. 2010, *A&A*, 511, A81
- [185] Kuiper, R. & Klessen, R. S. 2013, *A&A*, 555, A7
- [186] Kurtovic, N. T., Pérez, L. M., Benisty, M., et al. 2018, *ApJ*, 869, L44
- [187] Lada, C. J. 1987, in *IAU Symposium*, Vol. 115, *Star Forming Regions*, ed. M. Peimbert & J. Jugaku, 1
- [188] Lada, C. J., Muench, A. A., Luhman, K. L., et al. 2006, *AJ*, 131, 1574
- [189] Lada, C. J. & Wilking, B. A. 1984, *ApJ*, 287, 610
- [190] Lambrechts, M. & Johansen, A. 2012, *A&A*, 544, A32
- [191] Lambrechts, M. & Johansen, A. 2014, *A&A*, 572, A107
- [192] Lambrechts, M., Johansen, A., & Morbidelli, A. 2014, *A&A*, 572, A35
- [193] Lambrechts, M. & Lega, E. 2017, *A&A*, 606, A146
- [194] Lambrechts, M. & Morbidelli, A. 2016, in *AAS/Division for Planetary Sciences Meeting Abstracts*, 48, 105.08
- [195] Lambrechts, M., Morbidelli, A., Jacobson, S. A., et al. 2019, *arXiv e-prints*, arXiv:1902.08694
- [196] Lega, E., Crida, A., Bitsch, B., & Morbidelli, A. 2014, *MNRAS*, 440, 683
- [197] Lega, E., Morbidelli, A., Bitsch, B., Crida, A., & Szulágyi, J. 2015, *MNRAS*, 452, 1717
- [198] Lega, E., Morbidelli, A., & Nesvorný, D. 2013, *MNRAS*, 431, 3494
- [199] Levermore, C. D. & Pomraning, G. C. 1981, *ApJ*, 248, 321
- [200] Levison, H. F., Kretke, K. A., & Duncan, M. J. 2015, *Nature*, 524, 322
- [201] Levison, H. F., Kretke, K. A., Walsh, K. J., & Bottke, W. F. 2015, *Proceedings of the National Academy of Science*, 112, 14180
- [202] Levison, H. F., Morbidelli, A., Gomes, R., & Backman, D. 2007, in *Protostars and Planets V*, ed. B. Reipurth, D. Jewitt, & K. Keil, 669

- [203] Levison, H. F., Thommes, E., & Duncan, M. J. 2010, *AJ*, 139, 1297
- [204] Li, H., Lubow, S. H., Li, S., & Lin, D. N. C. 2009, *ApJ*, 690, L52
- [205] Lin, D. N. C., Bodenheimer, P., & Richardson, D. C. 1996, *Nature*, 380, 606
- [206] Lin, D. N. C. & Ida, S. 1997, *ApJ*, 477, 781
- [207] Lin, D. N. C. & Papaloizou, J. 1979, *MNRAS*, 186, 799
- [208] Lin, D. N. C. & Papaloizou, J. 1980, *MNRAS*, 191, 37
- [209] Lin, D. N. C. & Papaloizou, J. 1985, in *Protostars and Planets II*, ed. D. C. Black & M. S. Matthews, 981
- [210] Lissauer, J. J. 1987, *Icarus*, 69, 249
- [211] Liu, B. & Ormel, C. W. 2018, *A&A*, 615, A138
- [212] Lubow, S. H. & Ida, S. 2010, *Planet Migration*, ed. S. Seager, 347–371
- [213] Lynden-Bell, D. & Pringle, J. E. 1974, *MNRAS*, 168, 603
- [214] Lyra, W., Johansen, A., Zsom, A., Klahr, H., & Piskunov, N. 2009, *A&A*, 497, 869
- [215] Malhotra, R. 1993, *Nature*, 365, 819
- [216] Malygin, M. G., Kuiper, R., Klahr, H., Dullemond, C. P., & Henning, T. 2014, *A&A*, 568, A91
- [217] Manara, C. F., Fedele, D., Herczeg, G. J., & Teixeira, P. S. 2016, *A&A*, 585, A136
- [218] Manara, C. F., Morbidelli, A., & Guillot, T. 2018, *A&A*, 618, L3
- [219] Manara, C. F., Rosotti, G., Testi, L., et al. 2016, *A&A*, 591, L3
- [220] Mann, A. W., Gaidos, E., Lépine, S., & Hilton, E. J. 2012, *ApJ*, 753, 90
- [221] Mann, R. K. & Williams, J. P. 2010, *ApJ*, 725, 430
- [222] Masset, F. 2000, *A&AS*, 141, 165
- [223] Masset, F. S. 2001, *ApJ*, 558, 453
- [224] Masset, F. S. 2008, in *EAS Publications Series*, Vol. 29, *EAS Publications Series*, ed. M.-J. Goupil & J.-P. Zahn, 165–244
- [225] Masset, F. S. 2011, *Celestial Mechanics and Dynamical Astronomy*, 111, 131
- [226] Masset, F. S. 2017, *MNRAS*, 472, 4204
- [227] Masset, F. S. & Benítez-Llambay, P. 2016, *ApJ*, 817, 19
- [228] Masset, F. S. & Casoli, J. 2009, *ApJ*, 703, 857
- [229] Masset, F. S. & Casoli, J. 2010, *ApJ*, 723, 1393
- [230] Masset, F. S., D’Angelo, G., & Kley, W. 2006, *ApJ*, 652, 730
- [231] Masset, F. S., Morbidelli, A., Crida, A., & Ferreira, J. 2006, *ApJ*, 642, 478
- [232] Masset, F. S. & Papaloizou, J. C. B. 2003, *ApJ*, 588, 494
- [233] Mathis, J. S., Rumpl, W., & Nordsieck, K. H. 1977, *ApJ*, 217, 425
- [234] Matsumura, S., Brasser, R., & Ida, S. 2017, *A&A*, 607, A67
- [235] Mayor, M. & Queloz, D. 1995, *Nature*, 378, 355
- [236] McCaughrean, M. J. & O’dell, C. R. 1996, *AJ*, 111, 1977
- [237] Menou, K. & Goodman, J. 2004, *ApJ*, 606, 520
- [238] Meyer-Vernet, N. & Sicardy, B. 1987, *Icarus*, 69, 157

- [239] Mihalas, D. & Weibel Mihalas, B. 1984, *Foundations of radiation hydrodynamics* (Oxford University Press, New York)
- [240] Miranda, R. & Lai, D. 2018, *MNRAS*, 473, 5267
- [241] Molyarova, T., Akimkin, V., Semenov, D., et al. 2017, *ApJ*, 849, 130
- [242] Morbidelli, A., Bottke, W. F., Nesvorný, D., & Levison, H. F. 2009, *Icarus*, 204, 558
- [243] Morbidelli, A., Crida, A., Masset, F., & Nelson, R. P. 2008, *A&A*, 478, 929
- [244] Morbidelli, A., Lambrechts, M., Jacobson, S., & Bitsch, B. 2015, *Icarus*, 258, 418
- [245] Morbidelli, A. & Nesvorný, D. 2012, *A&A*, 546, A18
- [246] Mulders, G. D., Pascucci, I., & Apai, D. 2015, *ApJ*, 814, 130
- [247] Müller, T. W. A., Kley, W., & Meru, F. 2012, *A&A*, 541, A123
- [248] Muzerolle, J., Calvet, N., Briceño, C., Hartmann, L., & Hillenbrand, L. 2000, *ApJ*, 535, L47
- [249] Muzerolle, J., D'Alessio, P., Calvet, N., & Hartmann, L. 2004, *ApJ*, 617, 406
- [250] Muzerolle, J., Hartmann, L., & Calvet, N. 1998, *AJ*, 116, 2965
- [251] Muzerolle, J., Luhman, K. L., Briceño, C., Hartmann, L., & Calvet, N. 2005, *ApJ*, 625, 906
- [252] Najita, J. R. & Kenyon, S. J. 2014, *MNRAS*, 445, 3315
- [253] Nakagawa, Y., Sekiya, M., & Hayashi, C. 1986, *Icarus*, 67, 375
- [254] Natta, A., Testi, L., Comerón, F., et al. 2002, *A&A*, 393, 597
- [255] Nesvorný, D. & Morbidelli, A. 2012, *AJ*, 144, 117
- [256] Nesvorný, D., Vokrouhlický, D., Bottke, W. F., Noll, K., & Levison, H. F. 2011, *AJ*, 141, 159
- [257] Nesvorný, D., Youdin, A. N., & Richardson, D. C. 2010, *AJ*, 140, 785
- [258] Niemann, H. B., Atreya, S. K., Bauer, S. J., et al. 2005, *Nature*, 438, 779
- [259] Noll, K. S., Grundy, W. M., Stephens, D. C., Levison, H. F., & Kern, S. D. 2008, *Icarus*, 194, 758
- [260] Ochiai, H., Nagasawa, M., & Ida, S. 2014, *ApJ*, 790, 92
- [261] Ogihara, M., Kobayashi, H., Inutsuka, S.-i., & Suzuki, T. K. 2015, *A&A*, 579, A65
- [262] Ormel, C. W. 2017, in *Astrophysics and Space Science Library*, ed. M. Pessah & O. Gressel, Vol. 445, 197
- [263] Ormel, C. W. & Klahr, H. H. 2010, *A&A*, 520, A43
- [264] Ormel, C. W. & Kobayashi, H. 2012, *ApJ*, 747, 115
- [265] Ossenkopf, V. 1991, *A&A*, 251, 210
- [266] Paardekooper, S.-J., Baruteau, C., Crida, A., & Kley, W. 2010, *MNRAS*, 401, 1950
- [267] Paardekooper, S.-J., Baruteau, C., & Kley, W. 2011, *MNRAS*, 410, 293
- [268] Paardekooper, S. J. & Mellema, G. 2004, *A&A*, 425, L9
- [269] Paardekooper, S.-J. & Mellema, G. 2006, *A&A*, 459, L17
- [270] Paardekooper, S.-J. & Mellema, G. 2008, *A&A*, 478, 245
- [271] Paardekooper, S.-J. & Papaloizou, J. C. B. 2008, *A&A*, 485, 877

- [272] Paardekooper, S.-J. & Papaloizou, J. C. B. 2009, MNRAS, 394, 2283
- [273] Paardekooper, S.-J. & Papaloizou, J. C. B. 2009, MNRAS, 394, 2297
- [274] Padgett, D. L., Brandner, W., Stapelfeldt, K. R., et al. 1999, AJ, 117, 1490
- [275] Pan, L., Padoan, P., Scalo, J., Kritsuk, A. G., & Norman, M. L. 2011, ApJ, 740, 6
- [276] Papaloizou, J. C. B. & Larwood, J. D. 2000, MNRAS, 315, 823
- [277] Parker, A. H. & Kavelaars, J. J. 2010, ApJ, 722, L204
- [278] Pascucci, I., Testi, L., Herczeg, G. J., et al. 2016, ApJ, 831, 125
- [279] Pérez, L. M., Benisty, M., Andrews, S. M., et al. 2018, ApJ, 869, L50
- [280] Pérez, L. M., Carpenter, J. M., Chandler, C. J., et al. 2012, ApJ, 760, L17
- [281] Pérez, L. M., Chandler, C. J., Isella, A., et al. 2015, ApJ, 813, 41
- [282] Pfeil, T. & Klahr, H. 2019, ApJ, 871, 150
- [283] Picogna, G., Stoll, M. H. R., & Kley, W. 2018, A&A, 616, A116
- [284] Pierens, A., Cossou, C., & Raymond, S. N. 2013, A&A, 558, A105
- [285] Pierens, A. & Raymond, S. N. 2016, MNRAS, 462, 4130
- [286] Pinte, C., Dent, W. R. F., Ménard, F., et al. 2016, ApJ, 816, 25
- [287] Podio, L., Kamp, I., Codella, C., et al. 2013, ApJ, 766, L5
- [288] Pollack, J. B., Hollenbach, D., Beckwith, S., et al. 1994, ApJ, 421, 615
- [289] Pollack, J. B., Hubickyj, O., Bodenheimer, P., et al. 1996, Icarus, 124, 62
- [290] Pringle, J. E. 1981, ARA&A, 19, 137
- [291] Quintana, E. V., Barclay, T., Raymond, S. N., et al. 2014, Science, 344, 277
- [292] Rafikov, R. R. 2002, ApJ, 572, 566
- [293] Ramsey, J. P. & Dullemond, C. P. 2015, A&A, 574, A81
- [294] Rasio, F. A. & Ford, E. B. 1996, Science, 274, 954
- [295] Rein, H. & Liu, S.-F. 2012, A&A, 537, A128
- [296] Rein, H. & Spiegel, D. S. 2015, MNRAS, 446, 1424
- [297] Rigliaco, E., Natta, A., Testi, L., et al. 2012, A&A, 548, A56
- [298] Robitaille, T. P., Whitney, B. A., Indebetouw, R., Wood, K., & Denzmore, P. 2006, ApJS, 167, 256
- [299] Rogers, L. A. 2015, ApJ, 801, 41
- [300] Rosotti, G. P., Juhasz, A., Booth, R. A., & Clarke, C. J. 2016, MNRAS, 459, 2790
- [301] Rowe, J. F., Bryson, S. T., Marcy, G. W., et al. 2014, ApJ, 784, 45
- [302] Ruden, S. P. & Pollack, J. B. 1991, ApJ, 375, 740
- [303] Ryan, K., Nakajima, M., & Stevenson, D. J. 2014, in AAS/Division for Planetary Sciences Meeting Abstracts, 46, 201.02
- [304] Safronov, V. S. 1969, *Evoliutsiia doplanetnogo oblaka*.
- [305] Salinas, V. N., Hogerheijde, M. R., Bergin, E. A., et al. 2016, A&A, 591, A122
- [306] Sándor, Z., Lyra, W., & Dullemond, C. P. 2011, ApJ, 728, L9
- [307] Schneider, A. D., Dullemond, C. P., & Bitsch, B. 2018, A&A, 617, L7
- [308] Schoonenberg, D., Liu, B., Ormel, C. W., & Dorn, C. 2019, arXiv e-prints, arXiv:1906.00669

- [309] Schoonenberg, D. & Ormel, C. W. 2017, *A&A*, 602, A21
- [310] Semenov, D., Henning, T., Helling, C., Ilgner, M., & Sedlmayr, E. 2003, *A&A*, 410, 611
- [311] Shakura, N. I. & Sunyaev, R. A. 1973, *A&A*, 500, 33
- [312] Simon, A., Szatmáry, K., & Szabó, G. M. 2007, *A&A*, 470, 727
- [313] Simon, A. E., Szabó, G. M., Kiss, L. L., & Szatmáry, K. 2012, *MNRAS*, 419, 164
- [314] Simon, J. B., Armitage, P. J., Li, R., & Youdin, A. N. 2016, *ApJ*, 822, 55
- [315] Simon, J. B., Beckwith, K., & Armitage, P. J. 2012, *MNRAS*, 422, 2685
- [316] Spencer, J. R. & Nimmo, F. 2013, *Annual Review of Earth and Planetary Sciences*, 41, 693
- [317] Spilker, L. 2019, *Science*, 364, 1046
- [318] Spruit, H. C. 1996, in *NATO Advanced Science Institutes (ASI) Series C*, ed. R. A. M. J. Wijers, M. B. Davies, & C. A. Tout, Vol. 477, 249–286
- [319] Stern, S. A., Bagenal, F., Ennico, K., et al. 2015, *Science*, 350, aad1815
- [320] Stern, S. A., Spencer, J. R., Weaver, H. A., et al. 2019, arXiv e-prints, arXiv:1901.02578
- [321] Stewart, S. T. & Leinhardt, Z. M. 2009, *ApJ*, 691, L133
- [322] Stognienko, R., Henning, T., & Ossenkopf, V. 1995, *A&A*, 296, 797
- [323] Stone, J. M. & Norman, M. L. 1992, *ApJS*, 80, 753
- [324] Suzuki, T. K., Muto, T., & Inutsuka, S.-i. 2010, *ApJ*, 718, 1289
- [325] Tanaka, H., Takeuchi, T., & Ward, W. R. 2002, *ApJ*, 565, 1257
- [326] Tanaka, H. & Ward, W. R. 2004, *ApJ*, 602, 388
- [327] Tazzari, M., Testi, L., Ercolano, B., et al. 2016, *A&A*, 588, A53
- [328] Teachey, A. & Kipping, D. M. 2018, *Science Advances*, 4, eaav1784
- [329] Teague, R., Guilloteau, S., Semenov, D., et al. 2016, *A&A*, 592, A49
- [330] Terquem, C. E. J. M. L. J. 2003, *MNRAS*, 341, 1157
- [331] Tiscareno, M. S., Nicholson, P. D., Cuzzi, J. N., et al. 2019, *Science*, 364, aau1017
- [332] Tomasko, M. G., Archinal, B., Becker, T., et al. 2005, *Nature*, 438, 765
- [333] Toomre, A. 1964, *ApJ*, 139, 1217
- [334] Tsiganis, K., Gomes, R., Morbidelli, A., & Levison, H. F. 2005, *Nature*, 435, 459
- [335] Valenti, J. A., Basri, G., & Johns, C. M. 1993, *AJ*, 106, 2024
- [336] Vicente, S. M. & Alves, J. 2005, *A&A*, 441, 195
- [337] Voshchinnikov, N. V. 2004, *Astrophysics and Space Physics Reviews*, 12, 1
- [338] Wada, K., Tanaka, H., Suyama, T., Kimura, H., & Yamamoto, T. 2009, *ApJ*, 702, 1490
- [339] Walsh, K. J., Morbidelli, A., Raymond, S. N., O’Brien, D. P., & Mandell, A. M. 2011, *Nature*, 475, 206
- [340] Ward, W. R. 1986, *Icarus*, 67, 164
- [341] Ward, W. R. 1989, *ApJ*, 336, 526

-
- [342] Ward, W. R. 1991, in Lunar and Planetary Inst. Technical Report, Vol. 22, Lunar and Planetary Science Conference
- [343] Ward, W. R. 1997, *Icarus*, 126, 261
- [344] Ward, W. R. 1997, *ApJ*, 482, L211
- [345] Ward, W. R. & Hahn, J. M. 1994, *Icarus*, 110, 95
- [346] Weidenschilling, S. J. 1977, *MNRAS*, 180, 57
- [347] Weidenschilling, S. J. 1977, *Ap&SS*, 51, 153
- [348] Weidenschilling, S. J. 1980, *Icarus*, 44, 172
- [349] Weidenschilling, S. J. & Marzari, F. 1996, *Nature*, 384, 619
- [350] Weidling, R., Güttler, C., Blum, J., & Brauer, F. 2009, *ApJ*, 696, 2036
- [351] Wetherill, G. W. & Stewart, G. R. 1989, *Icarus*, 77, 330
- [352] Whipple, F. L. 1972, in *From Plasma to Planet*, ed. A. Elvius, 211
- [353] Williams, J. P. 2012, *Meteoritics and Planetary Science*, 47, 1915
- [354] Williams, J. P. & Best, W. M. J. 2014, *ApJ*, 788, 59
- [355] Williams, J. P. & Cieza, L. A. 2011, *ARA&A*, 49, 67
- [356] Windmark, F., Birnstiel, T., Güttler, C., et al. 2012, *A&A*, 540, A73
- [357] Woitke, P., Min, M., Pinte, C., et al. 2016, *A&A*, 586, A103
- [358] Yang, C. C., Johansen, A., & Carrera, D. 2017, *A&A*, 606, A80
- [359] Yang, L. T. & Brent, R. P. 2002, in *Proceedings of the Fifth Conference on Algorithm and Architectures for Parallel Processing.*, ed. W. Zhou, X. Chi, A. Goscinski, & G. Li (IEEE), 324–328
- [360] Youdin, A. N. & Goodman, J. 2005, *ApJ*, 620, 459
- [361] Youdin, A. N. & Lithwick, Y. 2007, *Icarus*, 192, 588
- [362] Zhang, K., Bergin, E. A., Blake, G. A., Cleeves, L. I., & Schwarz, K. R. 2017, *Nature Astronomy*, 1, 0130
- [363] Zhang, S., Zhu, Z., Huang, J., et al. 2018, *ApJ*, 869, L47
- [364] Zhu, Z., Hartmann, L., & Gammie, C. 2009, *ApJ*, 694, 1045
- [365] Zhu, Z., Hartmann, L., Nelson, R. P., & Gammie, C. F. 2012, *ApJ*, 746, 110
- [366] Zsom, A., Ormel, C. W., Güttler, C., Blum, J., & Dullemond, C. P. 2010, *A&A*, 513, A57

List of publications

Publications of the dissertation research:

- **Chrenko, O.**, Brož, M., & Lambrechts, M. 2017, *Eccentricity excitation and merging of planetary embryos heated by pebble accretion*, A&A, 606, A114
- Brož, M., **Chrenko, O.**, Nesvorný, D., & Lambrechts, M. 2018, *Dynamics of multiple protoplanets embedded in gas and pebble discs and its dependence on Σ and ν parameters*, A&A, 620, A157
- **Chrenko, O.**, Brož, M., & Nesvorný, D. 2018, *Binary planet formation by gas-assisted encounters of planetary embryos*, ApJ, 868, 145
- **Chrenko, O.** & Lambrechts, M. 2019, *Oscillatory migration of accreting protoplanets driven by a 3D distortion of the gas flow*, A&A, 626, A109

Previous publications:

- **Chrenko, O.**, Brož, M., Nesvorný, D., Tsiganis, K., & Skoulidou, D. K. 2015, *The origin of long-lived asteroids in the 2:1 mean-motion resonance with Jupiter*, MNRAS, 451, 2399

Conference contributions:

- **Chrenko, O.**, & Brož, M. 2015, *Planetesimals embedded in a gaseous disc vs mean-motion resonances*, in AAS/Division for Planetary Sciences Meeting Abstracts, 47, 418.02
- **Chrenko, O.**, & Brož, M. 2016, *Building the giant planet cores by convergent migration of pebble-accreting embryos*, in AAS/Division for Planetary Sciences Meeting Abstracts, 48, 318.03
- Brož, M., & **Chrenko, O.** 2016, *Gap opening after merger events of 3-Earth-mass protoplanets*, in AAS/Division for Planetary Sciences Meeting Abstracts, 49, 413.06
- **Chrenko, O.**, Brož, M., & Lambrechts, M. 2017, *Evolution of migrating protoplanets heated by pebble accretion*, in AAS/Division for Planetary Sciences Meeting Abstracts, 49, 500.05
- **Chrenko, O.**, Brož, M., & Nesvorný, D. 2018, *Evolution of multiplanet systems in 2D and 3D radiative disks*, in IAU General Assembly Abstracts, 30, IAUS345

